CHALMERS

Towards Improved Scale-Resolving Modeling and Simulations of Turbulent Flows

MAGNUS CARLSSON

Department of Mechanics and Maritime Sciences
CHALMERS UNIVERSITY OF TECHNOLOGY
Göteborg, Sweden December 2022

THESIS FOR THE DEGREE OF DOCTOR OF PHILOSOPHY IN THERMO AND FLUID DYNAMICS

Towards Improved Scale-Resolving Modeling and Simulations of Turbulent Flows

MAGNUS CARLSSON

Department of Mechanics and Maritime Sciences
Division of Fluid Mechanics
CHALMERS UNIVERSITY OF TECHNOLOGY

Göteborg, Sweden December 2022

Towards Improved Scale-Resolving Modeling and Simulations of Turbulent Flows
MAGNUS CARLSSON
ISBN 978-91-7905-740-4

Doktorsavhandlingar vid Chalmers tekniska högskola
Ny serie nr. 5206
ISSN 0346-718X
Department of Mechanics and Maritime Sciences
Division of Fluid Mechanics
Chalmers University of Technology
SE-412 96 Göteborg
Sweden
Telephone: +46 (0)31-772 1000

Chalmers Reproservice
Göteborg, Sweden December 2022

Towards Improved Scale-Resolving Modeling and Simulations of Turbulent Flows
MAGNUS CARLSSON
Department of Mechanics and Maritime Sciences
Division of Fluid Mechanics
Chalmers University of Technology

ABSTRACT

Scale-resolving simulations are viewed as powerful means for predicting complex turbulent flows, as often encountered in aeronautical applications. However, since turbulent scales span over a considerable range from the smallest Kolmogorov scales to the largest of equivalence to configuration size, scale-resolving computations are often demanding on computational resources and, furthermore, on the underlying numerical methods used in the simulations. Nonetheless, hybrid RANS (Reynolds-Averaged Navier-Stokes)-LES (Large-Eddy Simulation) techniques are considered computationally accurate and affordable for aeronautical industry applications.

This thesis explores and develops numerical methods suitable for hybrid RANS-LES. These methods are implemented in the Computational Fluid Dynamics (CFD) solver M-Edge.

A low-dissipative, low-dispersive numerical scheme was analyzed and verified in subsonic LES of turbulent channel flow and Decaying Isotropic Turbulent (DIT). It was shown that numerical dissipation and dispersion needs to be carefully tuned, in order to accurately predict resolved turbulent stresses and the correct decay of turbulent kinetic energy. The reported results are in good agreement with reference DNS and experimental data. The numerical scheme was further adapted and analyzed for compressible flow, where good agreement with reference DNS and experimental data is achieved for hybrid RANS-LES of supersonic turbulent channel flow and supersonic baseflow.

The optimized numerical scheme was then examined in hybrid RANS-LES computations of developing turbulent channel flow. In order to mitigate the grey area the LES zone, synthetic turbulence was applied at the RANS-LES interface using the Synthetic Eddy Method (SEM) and the Synthetic Turbulence Generator (STG). It was shown that using upstream turbulent statistics from a precursor LES or RANS, the recovery length of the skin friction coefficient can be reduced with improved mitigation of the grey area.

A new implicit gradient reconstruction scheme was developed, which is suitable for node-centered solvers. It was shown that the reconstruction scheme achieves fourth-order scaling on highly irregular anisotropic grids for an analytical academic case.

The Navier-Stokes Characteristic Boundary Condition (NSCBC) was implemented and verified for transport of an analytical vortex. It was shown that special boundary treatment is needed for transporting turbulent structures through the boundary with minimal reflections.

Keywords: Numerical methods, High-order gradient reconstruction, Scale-resolving simulation, Turbulence modelling, Hybrid RANS-LES, Synthetic Turbulence, Compressible flow

To my family.

Acknowledgements

I would like to thank my supervisors who gave my the opportunity to pursue a PhD: Lars Davidson at Chalmers, Shia-Hui Peng at FOI and Sebastian Arvidson at Saab Aeronautics. Your support and guidance have been invaluable during the years.

I would like to thank Peter Eliasson and Per Weinerfelt at Saab Aeronautics for providing support regarding the flow solver M-Edge and for the theoretical input on my work. It was always a pleasure to visit you to discuss numerical schemes and discretizations, and mathematics in general. I look forward to continuing the collaboration with you as future colleagues.

I would like to thank all my colleagues at Chalmers for creating an enjoyable work atmosphere. Special thanks to Niklas Hidman for helping me stay in shape by dragging me through the surrounding running trails during lunch breaks in a pace I cannot keep up with, and Gonzalo Montero Villar (Hernandez, Rodriguez, di Maria and all your other family names) for our overlapping work and all interesting discussions we had. I have never enjoyed discussing with someone I have disagreed with this much before.

Furthermore, I would like to thank the following people that I have been in contact with during the PhD: Stefan Wallin at KTH, Stockholm, for showing interest in my work and providing great input and support regarding the length scale based commutation term and turbulence modelling in general. Axel Probst and your colleagues at the German Aerospace Centre (DLR), Göttingen, for having me as a guest researcher May-June 2022. The discussions I had with you regarding numerics, hybrid RANS-LES methods among other things served as a great inspiration and I consider my visit to Göttingen a highlight of my PhD. Alistair Revell at the University of Manchester, for considering having me as a guest researcher in spring 2020. Sadly, a certain pandemic ended those plans.

Finally, I would like to thank my friends and family for the support and especially acknowledge my girlfriend Sara for putting up with my irrational working hours and sometimes lack of acknowledgement.

This work has been funded by the Swedish Governmental Agency for Innovation Systems (VINNOVA), the Swedish Defence Materiel Administration (FMV) and the Swedish Armed Forces within the National Aviation Research Programme (NFFP, Contract No. 2017–04887) and Saab Aeronautics. The simulations were performed on resources provided by the Swedish National Infrastructure for Computing (SNIC) at Chalmers Centre for Computational Science and Engineering (C3SE).

Magnus Carlsson
Göteborg, December 2022

NOMENCLATURE

Greek letters

ρ	density
σ_{ij}	viscous stress tensor
μ	dynamic viscosity
ν	kinematic viscosity
Δ	local filter-width
ε	dissipation rate

Roman letters

u_i	i^{th} component of the velocity vector
x_i	i^{th} component of the position vector
p	pressure
e_0	total energy
κ	thermal conductivity
T	temperature
C_P	specific heat at constant pressure
C_V	specific heat at constant volume
R	universal gas constant
γ	heat capacity ratio
P_r	Prandtl number
c	speed of sound
t_{ij}	turbulent stress tensor
k	turbulent kinetic energy

Abbreviations

CFD	Computational Fluid Dynamics
NSCBC	Navier-Stokes Characteristic Boundary Condition
RANS	Reynolds Averaged Navier-Stokes
LES	Large Eddy Simulation
ELES	Embedded LES
DNS	Direct Numerical Simulation
HRLM	Hybrid RANS-LES Modeling
STG	Synthetic Turbulence Generator
SEM	Synthetic Eddy Method
DES	Detached Eddy Simulation
(D)DES	Delayed-DES
(I)DDES	Improved-DDES

THESIS

This thesis consists of an extended summary and the following appended papers:

Paper A M. Carlsson, L. Davidson, S.H. Peng, and S. Arvidson. "Investigation of Low-dissipation Low-dispersion Schemes for Incompressible and Compressible Flows in Scale-Resolving Simulations". Submitted for journal publication

Paper B M. Carlsson, L. Davidson, S.H. Peng, and S. Arvidson. "Investigation of Turbulence Injection Methods in Compressible Flow Solvers in Large Eddy Simulation". *2022 AIAA SciTech Forum.* Jan. 2022. DOI: `10.2514/6.2022-0483`

Paper C M. Carlsson, L. Davidson, S.H. Peng, and S. Arvidson. "Higher Order Gradients on Unstructured Meshes Using Compact Formulation for Node-Centered Schemes". *2022 AIAA Aviation Forum.* June 2022. DOI: `10.2514/6.2022-4156`

Paper D M. Carlsson, S. Wallin, L. Davidson, S.H. Peng, and S. Arvidson. "Seamless Interface Methods for Grey-Area Mitigation in Scale-Resolving Hybrid RANS-LES". *DLES13 2022.* 2022

Paper E M. Carlsson, L. Davidson, S.H. Peng, and S. Arvidson. *Implementation of Nonreflecting Inlet and Outlet Boundary Conditions in the Subsonic Regime for a Node-Based Compressible Solver.* Tech. rep. Chalmers University of Technology, Göteborg, Sweden, Technical Report, 2021

Other publications related to this thesis:

Paper F S. Arvidson, M. Carlsson, and S. Nilsson. "Effect of LES Length Scale and Numerical Scheme in Hybrid RANS-LES of Free Shear Layer Flows". *International Council of Aeronauutical Sciences (ICAS), Stockholm.* 2022

Division of Work

All papers were written by M. Carlsson. L. Davidson, S-H. Peng and S. Arvidson provided support and valuable input in the writing and preparation of the manuscripts. L. Davidson has been the main supervisor for this thesis. All implementations of methods in the flow solver M-Edge, simulations, analysis and interpretation of results were performed by M. Carlsson. The development of the numerical scheme presented in Paper A was performed by M. Carlsson, with guidance and support from the co-authors. The formulation of the injection methods in Paper B was done by M. Carlsson with valuable input from S-H. Peng. The implicit gradient reconstruction scheme, presented in Paper C, was derived and developed by M. Carlsson. Theoretical input was provided by S-H. Peng. The stand-alone script for the gradient scheme was written by M. Carlsson. The proposal of the length scale based commutation term in Paper D was formulated by M. Carlsson in collaboration with S. Wallin, where S. Wallin provided theoretical guidance and support. The implementation of the NSCBC in Paper E was done by M. Carlsson.

Contents

Part I
Extended Summary

The scope of this thesis is the development of methods used in hybrid RANS-LES modeling. A low-dissipative, low-dispersive numerical scheme is evaluated in Paper A, where it is calibrated and verified in hybrid RANS-LES of turbulent channel flow and Decaying Isotropic Turbulent (DIT). It was concluded that numerical dissipation needs to be carefully reduced, in order to accurately resolve relevant turbulent scales while still achieving a converged solution. The predictions are further improved by the enhanced dispersive properties of the scheme. The numerical scheme was then adopted to and applied in compressible flows, such as a classical shock tube case and in hybrid RANS-LES of supersonic baseflow, where good results with respect to analytical results and experiments are achieved.

In Paper B, an embedded hybrid RANS-LES approach is verified using synthetic turbulence, in order to introduce turbulent fluctuations into a LES domain. Three different methods to inject the synthetic fluctuation into the LES domain was investigated. It was concluded that introducing synthetic fluctuations at the RANS-LES interface can effectively mitigate the grey-area region for turbulent channel flow, where the proposed turbulence injection method gives the best result for developing turbulent channel flow and developing boundary layer flow.

In order to further increase the numerical accuracy, a new implicit gradient reconstruction scheme was proposed in paper C. The reconstruction scheme achieves fourth-order scaling on irregular, highly anisotropic mixed-element grids for an analytical academic case.

In Paper D, a new seamless hybrid RANS-LES approach was derived and evaluated for free shear layer flows. The method exploits the commutation error at RANS-LES interfaces, where a commutation error term based on the hybrid length-scale is applied to reduce the grey-area in the vicinity of the RANS-LES interface. Improved results with respect to experiment are achieved in hybrid RANS-LES of mixing shear layer flows.

To avoid nonphysical reflections in scale-resolving simulations, the boundaries of a truncated flow domain needs to be able to handle incoming and outgoing numerical or physical waves. The Navier-Stokes Characteristic Boundary Condition (NSCBC) was implemented and verified for transporting an analytical vortex through the boundaries in paper E.

This thesis is organized as follows. An introduction is given Chapter 1 where hybrid RANS-LES methods are introduced with an aeronautical perspective. A survey of turbulent inflow boundary conditions is given, along with numerical methods commonly used in hybrid RANS-LES. The turbulence modeling approaches and the numerical methods used in this thesis are presented in Chapters 2 and 3, respectively. Chapter 4 further validates the turbulence modeling approaches and numerical methods used for additional test cases. A summary of the appended papers is given in Chapter 5. Finally, Chapter 6 summarizes the outcomes of the thesis work.

Chapter 1

Introduction

Aviation industries have over the years made tremendous effort dedicating to innovation and development of technologies in order to reduce environmental footprint with reduced life-cycle costs of aeronautical systems. Computer-based techniques, which have been increasingly implemented to support aircraft design and performance analysis, have shown great potentials in supplementing costly wind-tunnel and flight tests. Indeed, multidisciplinary design optimization is now becoming possible in industrial applications, by incorporating model-based tools/approaches in design procedure, and advanced flow simulation strategies in performance analysis. The techniques as such have been implemented in research and development of novel and innovative aeronautical products to support the realization of the targets in line with e.g. ACARE 2020 [1] and FlightPath 2050 [2].

In conjunction with different functionalities, Computational Fluid Dynamics (CFD) form the core and the fundamental platform of flow simulations. To address turbulent flows commonly encountered in aeronautical applications, the methods used today for aerodynamic design are mainly based on steady-state RANS (Reynolds-Averaged Navier-Stokes) simulations, which often provide reliable results for steady flows and attached boundary layers. In dealing with complex aerodynamic flows characterized by, for example, massive flow separation and unsteady vortex motion, RANS methods become often inaccurate. In many applications, resolved turbulence is required to support reliable analysis of, e.g., aeroacoustic noise generation. Obviously, it is desirable to introduce accurate and reliable modelling and simulation methods, such as advanced turbulence modelling and improved numerical schemes, in order to enable scale-resolving simulations in an industrial environment. It is recognized that, by definition, spectral effects are lost in Reynolds-averaging of conventional RANS methods, which are unable to produce scale-resolving predictions. On the other hand, the use of LES (Large-Eddy Simulation) methods remains unfeasible in complex aeronautical applications in the foreseeable future. As highlighted in the NASA CFD vision [3], nonetheless, Hybrid RANS-LES and wall-modeled LES offers the best prospects for industry applications.

With improved flow simulation techniques, accurate predictions of complex unsteady fluid flows can be made, i.e. separated flows which can lead to system disturbances and structural fatigue. Hybrid RANS-LES techniques are considered to be sufficiently accurate and computationally affordable for the aeronautical industry. Industrially adapted hybrid RANS-LES modelling (HRLM) techniques thus have the potential to improve product quality, give a more efficient design process with shorter time-to-market for new products and products with a reduced environmental impact.

1.1 Modeling of Turbulent Flows

Turbulence is a three-dimensional, chaotic and unsteady phenomenon governed by the Navier-Stokes equations. It is present in most flows in nature and in engineering applications, for example, the flows around cars, airplanes, trains as well as and flows in a ventilated room or in a combustion chamber. Turbulence appears when the inertial force dominates significantly over the viscous force, which are characterized by high Reynolds numbers. Its chaotic nature makes it difficult to estimate or solve analytically, and often numerical simulations are required. Turbulent flows are considered to consist of swirling structures of different sizes, which are usually referred to as eddies.

These eddies are characterized by three different scales: a length scale, a time scale and a velocity scale. The kinetic energy of these eddies can be statistically quantified by studying the energy spectrum illustrated in Fig. 1.1, where the energy of eddies with a certain length scale is described by the inverse of their length scale, the wave number $\kappa \propto 1/l$.

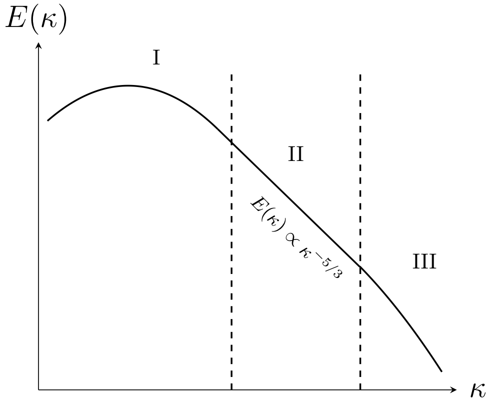

Figure 1.1: *Energy spectrum. I: Large scale energy containing eddies, II: Inertial subrange and III: Dissipative range.* $E(\kappa)$ *is the turbulent kinetic energy and* κ *is the wave nuber.*

The energy spectrum is divided into three sub-regions. Eddies in region I shown in Fig. 1.1 are the most energy-containing eddies and extract energy from the mean flow. They have a length scale proportional to the geometry of the problem being studied, but are unstable and will eventually break down into smaller eddies. Part of the energy extracted from the largest scales is transferred to the smaller scales. This process is repeated and the energy transfer to the smaller scales is referred to as the cascade process.

Eddies in region II (presented in Fig. 1.1), the inertial sub-range, have become statistically isotropic, i.e. they have no preferred direction, and exhibits a $\kappa^{-5/3}$ decay in the energy spectrum. The eddies located in the dissipative range, indicated by region III in Fig. 1.1, are described by the Kolmogorv scales. Here, the turbulent kinetic energy is transferred to thermal heat through viscous dissipation. Energy conservation dictates that the energy dissipation from the small eddies to heat in region III must be in the order of the rate of energy transfer from large eddies in region I.

The complex non-linear interaction described above is reflected by turbulence modeling. The common techniques in turbulence modeling are presented in Fig. 1.2, where the region resolution of the corresponding modeling technique is indicated in the turbulent kinetic energy spectrum. Different modeling techniques aim to model and/or resolve different parts of the spectrum. Direct numerical simulation (DNS) is the most accurate method available for investigating fundamental physics of turbulent flows. In DNS, the Navier-Stokes equations are solved numerically without any turbulence model. This gives an exact solution of the flow field in time and space. However, in order to resolve all the turbulent scales, the local grid size and time step need to be in the order of the Kolmogorov scales. This is extremely costly in terms of computer resources for domains with large dimensions or at large Reynolds number, and this approach currently remains out of reach for most engineering applications.

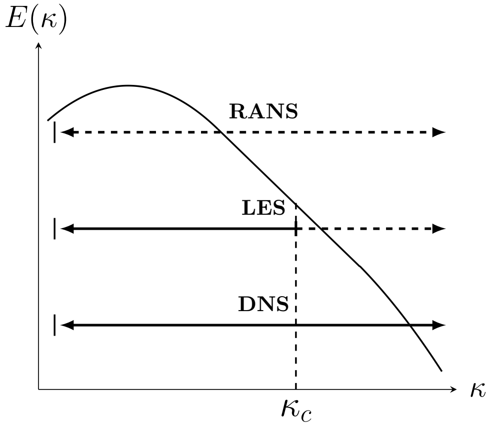

Figure 1.2: *Spectrum for turbulent kinetic energy. Turbulence modeling techniques are indicated with horizontal lines, where dashed indicates modeled part and solid indicates resolved part. Vertical dashed line indicates the location of the cut-off frequency κ_c.*

The computational methods associated with the lowest computational cost, but the least general method, is the RANS family, which model all turbulent scales by Reynolds-averaging the Navier-Stokes equations. The time-averaging needs to be sufficiently large in comparison with the turbulent time scale. Of different RANS methodologies, the most commonly used are eddy viscosity based models (EVM), which approximate the turbulent stresses using a linear relation of the mean strain-rate tensor and an eddy viscosity, and Reynolds stress models (RSM), in which aims to either solve the transport equations for the turbulent stresses or to formulate the turbulent stress tensor in a non-linear algebraic form. RANS models work well in flows where the time variation in the mean flow is of much lower frequency than the turbulence itself, but may fail when the mean flow quantities are strongly affected by large scale turbulent eddies.

Different from RANS, LES methods are based on the spatial filtering of the Navier-Stokes equations. LES aims to model the effect of sub-grid small scales that are more isotropic, while the large scale motions are explicitly computed. The spatial filtering introduces a cut-off frequency κ_c, as indicated in Fig. 1.2, which is inversely proportional to the local cell size Δ. The small scales are commonly described as Sub-Grid-Scales (SGS), and the filter-width should be chosen so that κ_c is in the inertial sub-range (see region II in Fig. 1.1) for accurate LES predictions. Compared to the full statistical averaging in RANS, the LES resolves the large scale turbulent interactions, and information about velocity, pressure fluctuations as well as e.g. two-point correlations are possible to obtain. However, while being much more computationally affordable than DNS, LES suffer from the requirement that the near-wall energetic eddies to a large part need to be resolved, which is still beyond the realistic computational limit for most engineering applications.

Hybrid RANS-LES modeling

Due to the excessive computational demand by LES and DNS, common practices for CFD-based workflows in the aeronautical industry still utilize steady RANS, although HRLM are increasingly adopted for certain classes of simulations in which swirling and separated flows are dominant. The key feature of HRLM is the RANS-type behavior in the vicinity of a solid boundary and a LES-type behavior joint with the RANS-modelled wall layer. In the HRLM framework, the most commonly used methods include the family of detached eddy simulation (DES) [4, 5, 6], which was extended by boundary-layer shielding, e.g. delayed DES (DDES) [7] and further wall modelling improvements in the improved DDES (IDDES) [8]. The DES-type of methods blend between the different modes through a hybrid length scale, which is adapted to the RANS length scale in the RANS region and to the LES length scale in the LES region. Alternative HRLM includes the partially integrated transport modeling (PITM) method [9, 10], the partially averaged Navier-Stokes (PANS) method [11, 12], and the scale adaptive simulation (SAS) [13]. Unlike in DES, the PANS formulation introduces a resolution parameter in terms of the ratio between the modeled and the total turbulent kinetic energy (resolved plus modeled). Another HRLM is for example the algebraic HYB0-model [14, 15], which blends between a mixing-length RANS model and a Smagorinsky LES model through an empirical blending function.

In embedded LES (ELES) or other zonal hybrid RANS-LES approaches a LES zone, embedded in the RANS region, is introduced to resolve the turbulent flow in regions of particular interest. The aim is to increase accuracy and to reduce the computational effort. The Zonal Detached Eddy Simulation (ZDES) [16, 17] is an example of such approaches. In connection to the RANS-modelled turbulence feeding into the LES region at the RANS-LES interface, the resolved turbulence in the LES region neighboring the interface is often delayed. This is the so-called ”grey-area problem”, which is not only present in zonal modeling approaches but also in non-zonal hybrid RANS-LES computations as well.

In LES, when the Navier–Stokes equations are subjected to spatially varying filter widths, it is recognized that the filtering operation and the standard finite volume spatial discretization does not commute [18], i.e. one introduces extra error terms called commutation errors. It was also shown in the hybrid RANS-LES context that these commutation residues may be potentially significant in regions with a filter width varying between RANS and LES scales [19, 20], which may further delay the transition from RANS to LES. In the PANS context, these commutation errors were explicitly accounted in simulations with temporal resolution variation [21], which was shown to promote the production of resolved turbulence. This was further investigated in [22, 23, 24], where the commutation residue term is active between the RANS and LES regions over and prescribed interface. It has been proven that that the commutation residue term can significantly accelerate the transition from modeled to resolved turbulence.

1.2 Simulation Methods and Accuracy

Synthetic Turbulence

The grey-area problem can be further mitigated by introducing resolved turbulence based on the statistics of the upstream modeled RANS turbulence. The most general approach is to synthesize artificial turbulence based on turbulent length scales and time scales from the mean RANS flow field using a so-called synthetic turbulence generator (STG). An ideal STG should be able to inject turbulent structures that are realistic for the specific problem under study. This involves satisfying the desired mean velocity profile, Reynolds stress tensor, turbulent kinetic energy spectrum, and correct phase information [25].

A family of STG methods attempt to synthesize a turbulent velocity field through the use of a spectral approach [26], where the fluctuating velocity field is represented by a Fourier series expansion. The intensity of the fluctuations can be computed from a modified von Karman spectrum and second-order statistics can be imposed through a Cholesky-decomposition-based tensor scaling approach [27, 28]. Temporal correlation of the fluctuation may be imposed by applying a time-filter [29] or a modified position vector scaled with the bulk velocity of the flow [28].

Another family of approaches is the Synthetic Eddy methods (SEM) [30, 31], where the turbulent field is superimposed by virtual vortical structures. These vortical structures or eddies are randomly generated and convected through a fictional domain, usually taken a box, giving both spatial and temporal correlation to the fluctuations, which are allowed to induce perturbations to cells in their neighbourhood. The SEM is able to predict statistical input data but fails to reproduce realistic spectral properties and yields a fluctuating velocity field with non-zero divergence [32]. Improvement was made to the original SEM, by which it was extended to give a divergence-free (DF-SEM)[32] fluctuating velocity field, and a generalization of the fictional domain in order to remove the dependency of the box [33], simplifying the implementation for complex geometries.

Numerical Accuracy

Proper resolution of the LES mode in HRLM requires a minimal dissipative and minimal dispersion numerical scheme. In scale-resolving computations, the accuracy and the order of the numerical method dictates the capabilities of resolving relevant length and time scales for turbulent flows, where higher-order methods (higher than second-order) are popular. Higher-order methods can be achieved by increasing the discretization stencil with additional neighbor points or by assuming a high-order polynomial for each cell. For complex geometries, which are typical for problems in the aeronautical applications, unstructured grids are often used to provide a quick discreization of the flow domain. For an unstructured flow solver, managing this type of grids poses a severe challenge due to the fact that the cells can have arbitrary shape and number of neighbours. Examples of higher-order methods for unstructured grids are higher-order finite-volume [34, 35], discontinuous galerkin [36], spectral volume [37, 38] or spectral difference [39, 40]. For an industrially capable CFD-package using second-order schemes, incorporating the changes adapting to higher-order methods require often substantial changes.

A low-dissipative finite-volume scheme suitable for unstructured compressible solvers was developed by Probst et al. [41], where the added numerical dissipation was effectively reduced and demonstrated with improved turbulence-resolving capabilities for wall-bounded flows. To further improve the capabilities of the numerical scheme, a low-dissipation and low-dispersion (LD2) scheme was formulated by Löwe et al. [42] and Probst et al. [43], where a higher order extrapolation of the face fluxes is used to control and reduce the numerical dispersion errors. The shock capturing capabilities of the numerical scheme is important, and should not interfere with the scale-resolving properties. In the original formulation by Jameson, a sensor similar to the second derivative of the pressure was formulated to identify shock waves [44]. A different variant of sensor targeting to minimize excessive dissipation in shock/turbulence interaction in LES was formulated by Ducros [45]. The sensor is a slight modification to Jameson's sensor and involves the local flow vorticity to identify regions with resolved turbulence.

1.3 Motivation and Objectives

This thesis has been motivated by the needs of aerodynamic industries, targeting improved simulation accuracy and increased computational efficiency for complex turbulent flows present in aeronautical applications. Although hybrid RANS-LES methods have been developed and implemented over the past two decades, the coherence and joint behavior of numerical schemes, synthetic turbulence injection and modeling techniques remain challenging and interesting research topics that need to pay special attention in order to increase the simulation robustness and accuracy in industrial applications. Additionally, the methodology needs to be able to handle different flow regimes, ranging from subsonic, transonic to supersonic and even hypersonic flows.

The general targets of this thesis is to improve the feasibility of scale-resolving modelling approaches in terms of both computational accuracy and computational efficiency for robust numerical analysis of aerodynamic flows. More specifically, the thesis work has been dedicated to development, implementation and evaluation of the following technical aspects for predicting unsteady aeronautical flows serving industrial applications:

- Robust numerical methods adapted for improved turbulence-resolving capabilities with hybrid RANS-LES methods.

- Synthetic Turbulence Generator (STG) methods adapted in scale-resolving simulations using zonal hybrid RANS-LES methods (including embedded LES) for improved feasibility and for potential industrial use.

- Improved RANS-LES interface methodology with seamless scale- and arbitrary geometry adaptation.

The methodology described above have been implemented into the flow solver M-Edge, which is the CFD package deployed in a set of industries, academia and research institutes (including Saab and FOI in Sweden). It is expected the method developed from the work will be exploited by industries to improve current aircraft designs and meet requirements on future aircraft platforms, and even in academic education for knowledge transfer.

Chapter 2

Modeling of Turbulent Flows

This chapter introduces the governing equations for turbulent flows. First, the form of Navier-Stokes equations which are solved for Direct Numerical Simulation (DNS) are presented. These equations need to be filtered in order to reduce the spatial and temporal resolution requirements, to make scale-resolving simulations more accessible to the industry. The filtered Navier-Stokes equations are presented, along with the turbulence modelWing methods used in this thesis. A description of the CFD solver used in this thesis then follows, with a detailed outline of the relevant numerical methods used for scale-resolving simulations.

2.1 Governing Equations of Fluid Motions

The Navier-Stokes equations for unsteady compressible flow reads

$$\frac{\partial \rho}{\partial t} + \frac{\partial (\rho u_i)}{\partial x_i} = 0 \tag{2.1}$$

$$\frac{\partial (\rho u_i)}{\partial t} + \frac{\partial (\rho u_i u_j)}{\partial x_j} = -\frac{\partial p}{\partial x_i} + \frac{\partial \sigma_{ij}}{\partial x_j} \tag{2.2}$$

$$\frac{\partial (\rho e_0)}{\partial t} + \frac{\partial (\rho e_0 u_j)}{\partial x_j} = -\frac{\partial (p u_j)}{\partial x_j} + \frac{\partial}{\partial x_j}\left[\kappa \frac{\partial T}{\partial x_j} + u_i \sigma_{ij}\right] \tag{2.3}$$

where the thermal conductivity κ is set to $\kappa = C_P \mu / P_r$, C_P is the specific heat capacity for constant pressure, μ is the molecular viscosity and P_r is the Prandtl number. The total energy is computed as $e_0 = e + u_i u_i/2$. For a perfect gas we have the internal energy $e = C_V T$, $C_V = R/(\gamma - 1)$, $\gamma = C_P/C_V$, where C_V is the specific heat capacity for constant volume, T is the temperature, R is the gas constant and γ is the heat capacity ratio. The equation of state reads

$$p = (\gamma - 1)\left[\rho e_0 - \frac{1}{2}\rho u_i u_i\right] \tag{2.4}$$

A Newtonian fluid is assumed and the viscous stress tensor is modeled as

$$\sigma_{ij} = \mu\left(\frac{\partial u_i}{\partial x_j} + \frac{\partial u_j}{\partial x_i} - \frac{2}{3}\frac{\partial u_k}{\partial x_k}\delta_{ij}\right) \tag{2.5}$$

To solve this set of equations (2.1)-(2.3) for turbulent flows in DNS, all relevant spatial and temporal scales in the flow field need to be resolved. This means that the grid needs to be fine enough to resolve features on the order of the Kolmogorov length scale

$$\eta = (\nu^3/\varepsilon)^{\frac{1}{4}} \tag{2.6}$$

where ν is the kinematic viscosity and ε is the dissipation rate. Likewise, the time step needs to be fine enough to resolve temporal dynamics on the order of the Kolmogorov time scale

$$\tau = (\nu/\varepsilon)^{\frac{1}{2}} \tag{2.7}$$

These resolution requirements for DNS impose a computational cost for industrial flows at high Reynolds numbers which is not feasible today and in the foreseeable future [46]. By filtering the Navier-Stokes equations (2.1) - (2.3), the resolution requirement is reduced. However, this filtering introduces additional unknown terms. Hence, modeling techniques such as, namely, turbulence modeling, are implemented to close the set of equations. The typical filtering process and the filtered Navier-Stokes equations used in this thesis are outlined below.

2.2 Modeling Methodologies

The RANS equations are derived by using time-averaging, which can for an arbitrary quantity Φ be expressed as

$$\overline{\Phi} = \frac{1}{T}\int_T \Phi \mathrm{d}t, \quad \Phi = \overline{\Phi} + \Phi' \tag{2.8}$$

where the instantaneous variable Φ is decomposed into a time-averaged part $\overline{\Phi}$ and a fluctuating part Φ'. Note that T is the time-averaging period in Eq. (2.8) that needs to be sufficiently large.

In LES, a spatial filter is applied instead. This can for a top-hat filter based on the finite volume method be expressed for the quantity Φ in 1D as:

$$\overline{\Phi}(x,t) = \frac{1}{\Delta x}\int_{x-0.5\Delta x}^{x+0.5\Delta x} \Phi(\xi,t)d\xi, \quad \Phi = \overline{\Phi} + \Phi' \tag{2.9}$$

Here, $\overline{\Phi}$ corresponds to a large scale fluctuating part (or resolved part) and Φ' corresponds to sub filter scale fluctuating part. In Eq. (2.9), an implicit filter is used through the finite volume discretisation, where the local control volume on the computational grid represents the spatial filter. In addition to the time-averaging in Eq. (2.8) and the spatial filtering in Eq. (2.9), the compressible Navier-Stokes equations contains also Favré filtered [47] quantities. The Favré filter is defined by

$$\widetilde{\Phi} = \frac{\overline{\Phi\rho}}{\overline{\rho}}, \quad \Phi = \widetilde{\Phi} + \Phi'' \tag{2.10}$$

Here, $(\bar{\cdot})$ means time-averaged quantities when RANS is applied and spatially-averaged quantities when LES is applied. The Favré filtering is denoted by $(\tilde{\cdot})$.

After filtering, the compressible Navier-Stokes equations ((2.1) - (2.3)) become

$$\frac{\partial\overline{\rho}}{\partial t} + \frac{\partial(\overline{\rho}\tilde{u}_i)}{\partial x_i} = 0 \tag{2.11}$$

$$\frac{\partial \overline{\rho}\tilde{u}_i}{\partial t} + \frac{\partial(\overline{\rho}\tilde{u}_i\tilde{u}_j)}{\partial x_j} = -\frac{\partial \overline{p}}{\partial x_i} - \frac{\partial \mathcal{T}_{ij}}{\partial x_j} \tag{2.12}$$

$$\frac{\partial(\overline{\rho}\tilde{e}_0)}{\partial t} + \frac{\partial(\overline{\rho}\tilde{e}_0\tilde{u}_j)}{\partial x_j} = -\frac{\partial(\overline{p}\tilde{u}_j)}{\partial x_j} + \frac{\partial \mathcal{H}_j}{\partial x_j} \tag{2.13}$$

where $\mathcal{T}_{ij}$ is the total stress tensor $\mathcal{T}_{ij} \equiv \overline{\rho}\tau_{ij} - \tilde{\sigma}_{ij}$, and $\mathcal{H}_j = q_j^t + \kappa\partial\tilde{T}/\partial x_j + \mathcal{T}_{ij}\tilde{u}_j$ are the sum of heat flux plus work done by viscous stresses . The Favré averaged viscous stress tensor is approximated as

$$\tilde{\sigma}_{ij} = \mu\left(\frac{\partial \tilde{u}_i}{\partial x_j} + \frac{\partial \tilde{u}_j}{\partial x_i} - \frac{2}{3}\frac{\partial \tilde{u}_k}{\partial x_k}\delta_{ij}\right) \tag{2.14}$$

The filtered kinetic energy $k \equiv \tau_{ii}/2$ should be included in the expression for total energy $\tilde{e}_0 = e + \tilde{u}_i\tilde{u}_i/2 + k$ due to the filtering process. The equation of state is then given by

$$\overline{p} = (\gamma - 1)\left[\overline{\rho}\tilde{e}_0 - \overline{\rho}\frac{1}{2}\tilde{u}_k\tilde{u}_k - \overline{\rho}k\right] \tag{2.15}$$

The filtering process has introduced two additional unknowns that need to be modeled, the turbulent stresses and the turbulent heat flux

$$\tau_{ij} = \widetilde{u_i u_j} - \tilde{u}_i\tilde{u}_j \tag{2.16}$$

$$q_j^t = -C_P\overline{\rho}\left(\widetilde{u_j T} - \tilde{T}u_j\right) \tag{2.17}$$

A common approach is to use the Boussinesq approximation, where an eddy viscosity μ_t is introduced to relate the turbulent stresses to the mean flow. The assumption is that the turbulent shear stress is proportional to the rate of mean strain rate

$$\tau_{ij} = -\mu_t\left(\frac{\partial \tilde{u}_i}{\partial x_j} + \frac{\partial \tilde{u}_j}{\partial x_i} - \frac{2}{3}\frac{\partial \tilde{u}_k}{\partial x_k}\delta_{ij}\right) + \frac{2}{3}\delta_{ij}\overline{\rho}k \tag{2.18}$$

and the turbulent heat flux is modeled as a diffusion term

$$q_j^t = C_P\frac{\mu_t}{Pr_t}\frac{\partial \tilde{T}}{\partial x_j} \tag{2.19}$$

Obviously, for models based on the Boussinesq assumption, the key has been to find an expression of the eddy viscosity to close the equation system of turbulence flows. Many different models for the turbulent viscosity μ_t of varying complexities exists in the literature, in the following sections the turbulence models used in this thesis are outlined.

2.2.1 Reynolds-Averaged-Navier-Stokes (RANS)

The Spalart-Allmaras model

The one-equation model of Spalart and Allmaras (SA) was especially developed for applications of aerodynamic flows and is empirically built as follows [48, 49]:

$$\frac{\partial(\overline{\rho}\tilde{\nu})}{\partial t} + \frac{\partial(\overline{\rho}\tilde{u}_j\tilde{\nu})}{\partial x_j} = C_{b1}\overline{\rho}\tilde{\nu}\widetilde{S} + \frac{1}{\sigma}\left[\frac{\partial}{\partial x_j}\left((\mu + \overline{\rho}\tilde{\nu})\frac{\partial \tilde{\nu}}{\partial x_j}\right) + C_{b2}\frac{\partial \tilde{\nu}}{\partial x_j}\frac{\partial \overline{\rho}\tilde{\nu}}{\partial x_j}\right] - C_{w1}\overline{\rho}f_w\left(\frac{\tilde{\nu}}{l_{RANS}}\right)^2 \tag{2.20}$$

where the quantities on the right-hand side correspond to, respectively, production, diffusion, cross diffusion and destruction. The length scale appearing in the destruction term is computed as the distance to the wall $l_{RANS} = d_w$. The eddy viscosity is defined as

$$\mu_t = \overline{\rho}\tilde{\nu} f_{\nu 1} \tag{2.21}$$

In order to ensure that $\tilde{\nu}$ equals $\kappa y u_\tau$ in the log-layer, buffer layer and viscous sublayer, a damping function $f_{\nu 1}$ is defined as

$$f_{\nu 1} = \frac{\chi^3}{\chi^3 + c_{v1}^3} \quad \text{with} \quad \chi = \frac{\tilde{\nu}}{\nu} \tag{2.22}$$

The quantity $\widetilde{S}$ in the production term corresponds to a modified vorticity such that it maintains its log-layer behaviour ($\widetilde{S} = \frac{u_\tau}{\kappa y}$)

$$\widetilde{S} = \tilde{\Omega} + \frac{\tilde{\nu}}{\kappa^2 l_{RANS}^2} f_{v2} \tag{2.23}$$

which is accomplished with the function

$$f_{v2} = 1 - \frac{\chi}{1 + \chi f_{v1}} \tag{2.24}$$

In Eq. (2.23) the magnitude of the vorticity tensor is computed as

$$\tilde{\Omega} = \sqrt{2\tilde{\Omega}_{ij}\tilde{\Omega}_{ij}}, \quad \tilde{\Omega}_{ij} = \frac{1}{2}\left(\frac{\partial \tilde{u}_i}{\partial x_j} - \frac{\partial \tilde{u}_j}{\partial x_i}\right) \tag{2.25}$$

In order to obtain a faster decaying behaviour of the destruction term in the outer region of the boundary layer, a function f_w is utilised

$$f_w(g) = g\left(\frac{1 + c_{w3}^6}{g^6 + c_{w3}^6}\right), \quad g = r + g_{w2}(r^6 + r), \quad r = \frac{\nu}{\widetilde{S}\kappa^2 l_{RANS}^2} \tag{2.26}$$

where g act as a limiter that prevents large values of f_w. Both r and f_w are equal 1 in the log-layer and decrease in the outer region. Constants of the model are

$$\begin{gathered} c_{b1} = 0.1355, \quad c_{b2} = 0.622, \quad \sigma = 2/3, \quad \kappa = 0.41, \\ c_{w1} = \frac{c_{b1}}{\kappa^2} + \frac{1 + c_{b2}}{\sigma}, \quad c_{w2} = 0.3, \quad c_{w2} = 2, \quad c_{v1} = 7.1 \end{gathered} \tag{2.27}$$

The Shear Stress Transport (SST) k-ω model

The two-equation SST k-ω model by Menter [50] was developed for improving predictions of aeronautical flows with strong adverse pressure gradients and separation. The model is a blending of the standard k-ε [51] model in the outer part of the boundary layer and the Wilcox k-ω model [52] in the near-wall part. The k-ε model is transformed into k-ω

formulation, resulting in a cross diffusion term and modified coefficients, which is then blended with the near-wall $k-\omega$ via a blending function. The model follows:

$$\begin{aligned}
\frac{\partial(\overline{\rho}k)}{\partial t}+\frac{\partial(\overline{\rho}\tilde{u}_jk)}{\partial x_j} &= \frac{\partial}{\partial x_j}\left[(\mu+\sigma_k\mu_t)\frac{\partial k}{\partial x_j}\right]+P_k-\overline{\rho}\sqrt{k^3}/l_{RANS}\\
\frac{\partial(\overline{\rho}\omega)}{\partial t}+\frac{\partial(\overline{\rho}\tilde{u}_j\omega)}{\partial x_j} &= \frac{\partial}{\partial x_j}\left[(\mu+\sigma_\omega\mu_t)\frac{\partial \omega}{\partial x_j}\right]+\gamma\frac{\overline{\rho}}{\mu_t}P_k-\beta\overline{\rho}\omega^2+2(1-F_1)\frac{\overline{\rho}\sigma_{\omega 2}}{\omega}\frac{\partial k}{\partial x_j}\frac{\partial \omega}{\partial x_j}
\end{aligned} \tag{2.28}$$

The RANS length scale is computed as $l_{RANS}=\sqrt{k}/(C_\mu\omega)$ with $C_\mu=0.09$. The production term in (2.28) reads as:

$$P_k=\min(\mu_t\tilde{S}^2, 10\cdot C_\mu\overline{\rho}k\omega) \tag{2.29}$$

Here $\tilde{S}$ is the magnitude of the strain rate tensor:

$$\tilde{S}=\sqrt{2\tilde{S}_{ij}\tilde{S}_{ij}},\quad \tilde{S}_{ij}=\frac{1}{2}\left(\frac{\partial\tilde{u}_i}{\partial x_j}+\frac{\partial\tilde{u}_j}{\partial x_i}\right) \tag{2.30}$$

In line with the shear-stress transport idea, the eddy viscosity is formulated

$$\mu_t=\overline{\rho}\frac{a_1k}{\max(a_1\omega,\tilde{S}F_2)} \tag{2.31}$$

which complies with $\overline{u'v'}\leq a_1k$, with $a_1=0.31$. This is in accordance with the Bradshaw assumption, and will reduce the turbulence level around stagnation regions and in adverse pressure gradient boundary layers compared to a standard eddy-viscosity model and the prediction of separated flows is improved. In Eq. (2.28) F_1 and F_2 denote the SST blending functions which read as follows:

$$\begin{aligned}
F_1=\tanh\left(\arg_1^4\right),\quad \arg_1 &= \min\left(\max\left[\frac{\sqrt{k}}{C_\mu\omega d_w},\frac{500\nu}{d_w^2\omega}\right],\frac{4\overline{\rho}\sigma_{\omega 2}k}{CD_{k\omega}d_w^2}\right),\\
F_2=\tanh\left(\arg_2^2\right),\quad \arg_2 &= \max\left(\frac{2\sqrt{k}}{C_\mu\omega d_w},\frac{500\nu}{d_w^2\omega}\right),\\
CD_{k\omega} &= \max\left(\frac{2\overline{\rho}\sigma_{\omega 2}}{\omega}\frac{\partial k}{\partial x_j}\frac{\partial \omega}{\partial x_j},10^{-10}\right)
\end{aligned} \tag{2.32}$$

The model constants of the k-ε and k-ω turbulence models are computed by a blend via $\gamma=\gamma_1F_1+\gamma_2(1-F_1)$:

$$\begin{gathered}
\gamma_1=5/9,\quad \beta_1=0.075,\quad \sigma_{k1}=0.85,\quad \sigma_{\omega 1}=0.5\\
\gamma_2=0.44,\quad \beta_2=0.0828,\quad \sigma_{k2}=1.0,\quad \sigma_{\omega 2}=0.856
\end{gathered} \tag{2.33}$$

2.2.2 Scale-Resolving Modeling

Large Eddy Simulation

In LES the large scales of turbulent flows are resolved, whereas the scales smaller than the local grid resolution are modeled. A popular and simple expression of computing ν_t in Eq. (2.18) is the Smagorinsky model [53]

$$\begin{aligned} \nu_{sgs} &= (C_S\Delta)^2|\tilde{S}| \\ |\tilde{S}| &\equiv \sqrt{2\tilde{S}_{ij}\tilde{S}_{ij}} \end{aligned} \tag{2.34}$$

where the local filter-width, Δ, is taken as the cubic root of local cell volume

$$\Delta = (\delta V_I)^{1/3} \tag{2.35}$$

The model constant C_S is recognized flow-dependent, taking a values typically in the range of (0.1,0.2). This model implies incorrect scaling close to walls. This is usually alleviated by using a damping function that gives the correct near-wall behaviour. However, the damping functions usually requires the skin-friction velocity in proximity of wall surface as input parameters, possibly leading to complex implementation issues for flow separation where the friction velocity becomes zero.

The Wall-Adapting Local Eddy-Viscosity (WALE) [54] model addresses this issue by providing a more complex expression in terms of resolved spatial derivatives, that automatically fulfills the near-wall scaling. The subgrid viscosity is defined as

$$\begin{aligned} \nu_{sgs} &= (C_m\Delta)^2\frac{(\mathcal{S}^d_{ij}\mathcal{S}^d_{ij})^{3/2}}{(\tilde{S}_{ij}\tilde{S}_{ij})^{5/2}+(\mathcal{S}^d_{ij}\mathcal{S}^d_{ij})^{5/4}} \\ \mathcal{S}^d_{ij} &= \frac{1}{2}\left(\frac{\partial\tilde{u}_i}{\partial x_l}\frac{\partial\tilde{u}_l}{\partial x_j}+\frac{\partial\tilde{u}_j}{\partial x_l}\frac{\partial\tilde{u}_l}{\partial x_i}\right)-\frac{1}{3}\frac{\partial\tilde{u}_m}{\partial x_l}\frac{\partial\tilde{u}_l}{\partial x_m}\delta_{ij} \end{aligned} \tag{2.36}$$

A common value for the model constant for wall bounded flow is $C_m = 0.325$ [54].

A differential operator based on the singular values of the velocity gradient tensor was proposed in [55] as a basis for an improved SGS eddy-viscosity model. The σ-model was shown to generate zero eddy-viscosity for any two-dimensional or two-component flows, an attractive feature that can unlock Kelvin-Helmholz instabilities and trigger resolved turbulence in free shear layer flows. Similar to the WALE model, it has the proper behavior in near-wall regions. The σ-model reads:

$$\begin{aligned} \nu_{sgs} &= (C_\sigma\Delta)^2 S_\sigma \\ S_\sigma &= \frac{\sigma_3(\sigma_1-\sigma_2)(\sigma_2-\sigma_3)}{\sigma_1^2} \end{aligned} \tag{2.37}$$

where $\sigma_1 \leq \sigma_2 \leq \sigma_3 \leq 0$ are the singular values of the velocity gradient tensor. In quasi two-dimensional flow regions, S_σ is close to zero, which ensures the decrease of the eddy viscosity in shear layers by rapidly reducing the sub-grid viscosity. The constant $C_\sigma = 1.35$ is chosen according to Nicoud et al. [55].

Hybrid RANS-LES

A variety of hybrid RANS-LES methods has been developed for the past 25 years. The idea is to exploit the computational efficiency in RANS and the computational accuracy in LES. The hybrid methods produces RANS-type behavior in the vicinity of a solid boundary, where RANS models have successively proven to accurately model attached boundary layers using a moderately coarse mesh. The HRLM switches to LES mode in off-wall regions and in region with separated flow, where LES models have proven to be able to effectively predict unsteady flow features.

Many methods are available in the literature, where the most well-known is the Detached Eddy Simulation (DES) [56, 5, 7, 8] family of models. Two different hybrid methods are used throughout this thesis, the Delayed-DES (DDES) for attached boundary layers where flow separation triggers the generation of resolved turbulence, and the Improved-DDES (IDDES) [8] for boundary layer flows with turbulent inflow content.

Detached Eddy Simulation (DES)

The DES [56] model modifies the underlying RANS model length scale (l_{RANS}) given in Eq. (2.20) for SA and Eq. (2.28) for SST, where l_{RANS} is replaced by

$$l_{DES} = \min(l_{RANS}, l_{LES}) \tag{2.38}$$

where

$$l_{LES} = C_{DES}\Psi\Delta \tag{2.39}$$

is the LES length scale. Here, C_{DES} is a modeling constant calibrated in simulations of decaying isotropic turbulence and Ψ is a correction function to avoid (an unphysical) low Reynolds number damping in the LES region [8]. This correction is not needed for the SST model [57] ($\Psi = 1$), since no low Reynolds number damping functions are present. Δ is the local filter width. In the original DES it is defined as

$$\Delta_{max} = \max(\Delta_x, \Delta_y, \Delta_z) \tag{2.40}$$

For an unstructured solver with a dual-grid, Δ_{max} in Eq. (2.40) can be ambiguous for cells not aligned with the coordinate directions. In the edge-based solver, such as M-Edge which is used in this work, it is approximated as the maximum edge length of a dual-cell (see Fig. 3.1).

In the near wall region the model reduces to the RANS model, whereas far away from the wall, $l_{RANS} \gg \Delta$ leading to $l_{DES} = l_{LES}$ and the model acts as a subgrid scale model. The formulation of the length scale in Eq. (2.38) caused premature switching from RANS to LES, known as grid-induced sepration (GIS). The grid-induced separation is caused by the DES model extending the LES region into the boundary layer, where the grid is not fine enough to resolve the turbulent stresses which leads to a reduction of the modeled skin friction and possibly an unphysical flow separation.

Delayed DES (DDES)

The GIS problem was addressed in the formulation of Delayed DES (DDES) [7], where the DES-length scale in Eq. (2.38) was redefined as

$$l_{DDES} = l_{RANS} - f_d \max(0, l_{RANS} - L_{LES}) \tag{2.41}$$

where L_{LES} is given in Eq. (2.39) and f_d is a shielding function

$$f_d = 1 - \tanh\left([C_1 r_d]^{C_2}\right) \tag{2.42}$$

which takes on the value unity in the LES region and zero elsewhere. This function aims to prevent LES content from penetrating into the RANS modeled boundary layer. The function r_d reads

$$r_d = \frac{\nu_t + \nu}{\kappa^2 d_w^2 \sqrt{\frac{1}{2}(\tilde{S}^2 + \tilde{\Omega}^2)}} \tag{2.43}$$

which is similar to r in Eq. (2.26) for the SA-model and should identify the outer wake of a boundary layer, where the grid is fine enough to resolve the turbulent stresses.

Improved DDES (IDDES)

For the simulation of wall bounded flows with synthetic turbulence injection in this thesis work, the Improved Delayed DES (IDDES) [8] is employed. The IDDES blends two branches, a DDES-like branch and a WMLES-like branch. The DDES-like branch should become active only when the inflow conditions do not have any turbulent content. The WMLES-like branch is intended to be active only when the inflow conditions used in the simulation are unsteady and impose some turbulent content. An additional criteria on the WMLES-like branch is that the grid is fine enough to resolve boundary-layer dominant eddies. The blending function between the RANS mode and the LES mode reads:

$$l_{IDDES} = \tilde{f}_d(1 + f_e) l_{RANS} + (1 - \tilde{f}_d) l_{LES} \tag{2.44}$$

Here, $\tilde{f}_d$ is a function that blends between DDES and WMLES, and f_e is a function to enhance the RANS length scale in the vicinity of the RANS-LES interface in order to reduce the log-layer mismatch. The LES length scale in (2.44) is given by Eq. (2.39) but the the local filter-width Δ is replaced by

$$\Delta_{dw} = \min(\max[C_{dw} d_w, C_{dw} \Delta_{max}, \Delta_{wn}], \Delta \max) \tag{2.45}$$

The purpose of Δ_{dw} in Eq. (2.45) is to give a correct log-layer behaviour in WMLES without the need to alter the value of the modeling constant C_{DES} adapted to decaying grid turbulence. In Eq. (2.45), $C_w = 0.15$ and Δ_{wn} is the characteristic wall-normal cell size. For an unstructured edge-based solver, this quantity is not defined in a straightforward way. In this thesis, it is approximated by taking the difference between the maximum and the minimum cell face value of the wall distance d_w for a given cell. The cell face value is computed by the average of the two connecting nodes for a given edge.

2.3 Improvements to Modelling

2.3.1 LES Length Scale

In the original formulation of the DES model, the the local filter width Δ in Eq. (2.39) is set to the maximum cell dimension Δ_{max}. It has been shown in several studies that Δ_{max} often gives an excess SGS viscosty for flow cases involving free shear layers in LES mode (e.g. [58, 24]). An alternative length scale to alleviate this problem was formulated by Shur et. al [58], where the length scale $\tilde{\Delta}_\omega$ is based on the local vorticity direction in the flow. For a hexahedral cell $\tilde{\Delta}_\omega$ is formulated as

$$\tilde{\Delta}_\omega = \frac{1}{\sqrt{3}} \max_{n,m} \|\mathbf{I}_n - \mathbf{I}_m\|, \quad \mathbf{I}_n = \mathbf{n}_\omega \times (\mathbf{r}_n - \mathbf{r}), \quad \mathbf{n}_\omega = \frac{\boldsymbol{\omega}}{\|\boldsymbol{\omega}\|} \tag{2.46}$$

where $\mathbf{n}_\omega$ is the unit vector aligned with the vorticity vector. This approach adapts the filter width to the local orientation of eddies, thus helping to reduce the problem of delayed transition from RANS to LES in the initial region of the shear layer. The factor $\frac{1}{\sqrt{3}}$ is needed to recover Δ_{max} for cubic cells in isotropic turbulence.

However, as pointed out in [58], replacing Δ_{max} with $\tilde{\Delta}_\omega$ is not enough to fully unlock the Kelvin-Helmholtz instability. To further force the reduction of the turbulent SGS viscosity in free shear layers the F_{KH} function is added to $\tilde{\Delta}_\omega$ to give

$$\Delta_{SLA} = \tilde{\Delta}_\omega F_{KH}(\langle VTM \rangle) \tag{2.47}$$

The F_{KH} function is based on a Vortex Tilting Measure (VTM) with the aim to detect Kelvin-Helmholtz like structures and rapidly reduce the LES filter width. The Vortex Tilting Measure and F_{KH} are given:

$$VTM = \frac{\sqrt{6}\|(\tilde{\mathbf{S}} \cdot \boldsymbol{\omega}) \times \boldsymbol{\omega}\|}{\boldsymbol{\omega}^2 \sqrt{3tr(\tilde{\mathbf{S}}^2) - [tr(\tilde{\mathbf{S}})]^2}} \max(0.2\nu/\nu_t, 1) \tag{2.48}$$

$$F_{KH} = \max(F_{KH}^{min}, \min[F_{KH}^{max}, F_{KH}^{min} + \frac{F_{KH}^{max} - F_{KH}^{min}}{a_2 - a_1}(\langle VTM \rangle) - a_1]) \tag{2.49}$$

where $tr(\cdot)$ is the trace operator, $F_{KH}^{max} = 1.0$ and F_{KH}^{min}, a_1 and a_2 are adjustable empirical parameters which are set to 0.1, 0.15 and 0.3 respectively [58]. Local VTM values are averaged over the current and closest neighboring cells, in order to make Δ_{SLA} behave as Δ_{max} in developed 3D turbulence. $\langle VTM \rangle$ is close to zero in the quasi-2D regions of the flow, whereas in regions with fully developed turbulence it is of the order of 1.0. The Vortex Tilting Measure $\langle VTM \rangle$ in in this thesis is computed as a volume average of the neighbouring cells. The function F_{KH} takes values between zero and one, where one is its natural value and a reduction towards zero takes place in flows where Kelvin-Helmholtz like structures are detected. By achieving this additional reduction of the turbulent SGS viscosity compared to $\tilde{\Delta}_\omega$, the two dimensional Kelvin-Helmholtz structures are able to break up and form three dimensional turbulent structures.

2.3.2 Zonal Interface Methods

In a zonal approach, a RANS and a LES region is separated by a prescribed interface. A schematic of a zonal approach with the prescribed RANS-LES interface is presented in Fig. 2.1. Here, an upstream region is treated in RANS but further downstream a focusing LES region is defined in order to get a better prediction of the flow field. However, if no special care is taken at the prescribed interface, there will be a severe delay in the development of resolved turbulence in the LES region since all turbulent scales are modeled in the RANS region, which is usually called a grey-area transition region. In order to trigger the equations to resolve turbulence and reduce the RANS-to-LES transition region, synthetic turbulent fluctuations can be superimposed onto the RANS mean flow field at the prescribed interface.

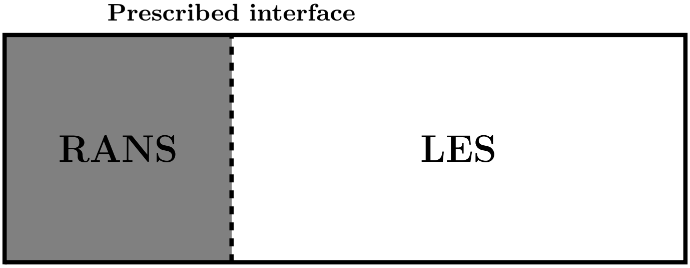

Figure 2.1: *Schematic of RANS and LES regions in zonal hybrid RANS-LES (embedded LES) with wall-normal RANS-LES interface indicated.*

Synthetic Turbulence

The synthetic turbulence methods considered in this theses are the Synthetic-Eddy Method by Jarrin et al. [31] and the Synthetic Turbulence Generator (STG) by Shur et al. [28]. A brief outline of the theory and the implementation of these methods are given in the following sections.

Synthetic Eddy Method (SEM)

The velocity fluctuations for the SEM are generated by a fixed number, N, of artificial eddys and have the representation

$$v'_j(\mathbf{x},t) = \frac{1}{\sqrt{N}} \sum_{k=1}^{N} \varepsilon_j^k f_\sigma(\mathbf{x} - \mathbf{x}^k) \tag{2.50}$$

where $\mathbf{x}^k$ are the locations of the eddies, ε_j^k are their respective intensities (with $\langle \varepsilon_j \rangle = 0$ and $\langle \varepsilon_j^2 \rangle = 1$). The shape function $f_\sigma(\mathbf{x} - \mathbf{x}^k)$ sets the velocity distribution of the eddy located at $\mathbf{x}^k$ and is given by

$$f_\sigma(\mathbf{x} - \mathbf{x}^k) = \sqrt{\frac{V_B}{\sigma^3}} f\left(\frac{x - x^k}{\sigma}\right) f\left(\frac{y - y^k}{\sigma}\right) f\left(\frac{z - z^k}{\sigma}\right) \tag{2.51}$$

where V_B is the volume of the box of eddies explained below, σ is a parameter that controls the size of the vortical structures and f is a shape function chosen to satisfy the normalization condition

$$\frac{1}{V}\iiint f^2(\mathbf{x}',\sigma)\mathrm{d}\mathbf{x}' = 1 \tag{2.52}$$

A function that satisfies this condition is a tent function [31]

$$f(x) = \begin{cases} \sqrt{\frac{3}{2}}(1-|x|) & \text{if } |x|<1 \\ 0 & \text{otherwise} \end{cases} \tag{2.53}$$

but is in this study taken as a truncated Gaussian according to

$$f(x) = \begin{cases} \frac{1}{\sqrt{\sqrt{\pi}C\,\mathrm{erf}(1/C)}}\exp\left(-\frac{1}{2C^2}|x|^2\right) & \text{if } |x|<1 \\ 0 & \text{otherwise} \end{cases} \tag{2.54}$$

with $C = 1/3$. The shape functions for Eqs. (2.53) and (2.54) are shown in Fig. 2.2. The length scale σ is estimated using information from a RANS model and the maximum local mesh size [31]

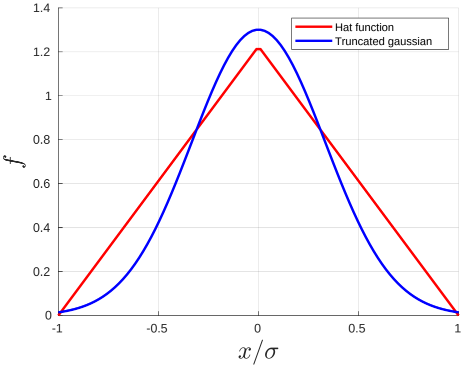

Figure 2.2: *SEM shape functions.*

$$\sigma = \max\left[\min(l_{RANS},\kappa\delta),\Delta_{max})\right] \tag{2.55}$$

where l_{RANS} is a RANS length scale and δ is the thickness of a boundary layer considered. The virtual eddies are randomly generated in, and convected through, a virtual domain around a given synthetic-forcing region. The virtual domain is given by a box and is generated around the forcing region $S = \{\mathbf{x}_1,\mathbf{x}_2,...,\mathbf{x}_s\}$, where the minimum and maximum coordinates are defined by

$$x_{i,\min} = \max_{\mathbf{x}\in S}(x_i - \sigma(\mathbf{x})) \quad \text{and} \quad x_{i,\max} = \max_{\mathbf{x}\in S}(x_i + \sigma(\mathbf{x})) \tag{2.56}$$

In order to ensure that the density of eddies inside of the box of eddies is constant and that the synthetic turbulent field is statistically covered by the eddies, the number of eddies is set as $N = \max(V_B/\sigma^3)$. Note the formulation of Eq. (2.56) generates a padding around the forcing domain S of the maximum eddy size σ. This padding is ignored in the vicinity of a wall or a periodic boundary. If an eddy overlaps a periodic boundary, the eddy position is mirrored to the other side of the periodic boundary in order to impose a periodic fluctuating velocity field. Time correlation of the fluctuating velocity field are imposed by updating the positions of the eddies using the integrated bulk velocity

$$\mathbf{x}^k(t + \Delta t) = \mathbf{x}^k(t) + \mathbf{U}_b \Delta t \tag{2.57}$$

where the integration of $\mathbf{U}_b$ is carried out over the interface S. Eddies that leave the box are randomly regenerated at the inlet side of the virtual box, given by the streamwise direction.

Synthetic Turbulence Generator (STG)

The velocity fluctuations for the STG [28] are computed by superimposing N Fourier modes:

$$\mathbf{v}'(\mathbf{x}, t) = \sqrt{6} \sum_{n=1}^{N} \sqrt{q^n} \left[\boldsymbol{\sigma}^n \cos(k^n \mathbf{d}^n \cdot \mathbf{x}' + \phi^n) \right] \tag{2.58}$$

where n denotes the mode number, $\mathbf{d}^n$ is the random vector that is uniformly distributed over a unit sphere and $\boldsymbol{\sigma}^n$ is a unit vector normal to $\mathbf{d}^n$ ($\boldsymbol{\sigma}^n \cdot \mathbf{d}^n = 0$) [26, 29]. These are given by

$$\mathbf{d}^n = \begin{bmatrix} \sin(\Theta^n)\cos(\Phi^n) \\ \sin(\Theta^n)\sin(\Phi^n) \\ \cos(\Theta^n) \end{bmatrix}, \quad \boldsymbol{\sigma}^n = \begin{bmatrix} \cos(\Phi^n)\cos(\Theta^n)\cos(\eta^n) - \sin(\Phi)\sin(\eta^n) \\ \sin(\Phi^n)\cos(\Theta^n)\cos(\eta^n) + \cos(\Phi)\sin(\eta^n) \\ -\sin(\Theta^n)\cos(\eta^n) \end{bmatrix} \tag{2.59}$$

where Φ^n, $\Theta^n = \arccos(1 - 2\gamma^n)$ and η^n are random angles with uniform distributions and intervals given in Table 2.1. Here, the uniformly distributed random phase angle ϕ^n in Eq. (2.58) is also shown.

Table 2.1: Intervals for uniformly distributed random variables.

variable	Φ^n	γ^n	η^n	ϕ^n
interval	$[0, 2\pi)$	$[0, 1)$	$[0, 2\pi)$	$[0, 2\pi)$

The normalized mode amplitude q^n is computed using a modified von Karman spectrum [28] according to

$$q^n = \frac{E(k^n)\Delta k^n}{\sum_{n=1}^{N} E(k^n)\Delta k^n}, \quad \sum_{n=1}^{N} q^n = 1 \tag{2.60}$$

where k^n is the wave number magnitude of the vector $\mathbf{d}^n$. Note that the random variables in Table 2.1 is only computed once. A modified position vector $\mathbf{x}'$ in Eq. (2.58) is introduced to impose time-correlation. Assuming that the streamwise direction is aligned with the x-direction, the position vector is expressed as

$$\mathbf{x}' = \begin{bmatrix} \frac{2\pi}{k^n \max(l_e(\mathbf{x}))}(x - U_b t) \\ y \\ x \end{bmatrix} \tag{2.61}$$

The bulk velocity U_b is integrated over the RANS-LES interface. $l_e(\mathbf{x})$ corresponds to the length scale of the most energy-containing mode and is given by $l_e(\mathbf{x}) = \min(2d_w(\mathbf{x}), C_t l_{RANS})$. $C_t = 3.0$ is an empirical constant and l_{RANS} is the local RANS length scale. The set of wave numbers k^n is fixed and is common for the entire RANS-LES interface. A geometric series is used

$$k^n = k_{\min}(1+\alpha)^{n+1}, \ n = 1, 2, ..., N, \ \alpha = 0.01 \tag{2.62}$$

to decrease the number of modes compared to a uniform distribution. The number of modes N in Eq. (2.58) is then obtained by

$$N = \mathrm{ceil}\left(\frac{\ln(k_{max}/k_{min})}{\ln(1+\alpha)+1}\right) \tag{2.63}$$

where $k_{min} = \pi/\max(l_e(\mathbf{x}))$, and $k_{max} = 1.5\max(2\pi/l_{cut}(\mathbf{x}))$. $l_{cut}(\mathbf{x})$ is computed as

$$l_{cut} = 2\min(0.3\Delta_{max} + 0.1d_w(\mathbf{x}), \Delta_{max}) \tag{2.64}$$

which corresponds to the length scale of the smallest scales that can be resolved by the grid.

Anisotropic Fluctuations

The velocity fluctuations in Eqs. (2.50) or (2.58) satisfy the restrictions $\langle v_i' \rangle = 0$ and $\langle v_i' v_j' \rangle = \delta_{ij}$, where $\langle \cdot \rangle$ denotes time averaging. In order to impose the correct Reynolds stress statistics [59] at the interface, the actual fluctuations $u_j'(\mathbf{x}, t)$ are computed from

$$u_j'(\mathbf{x}, t) = a_{ij} v_j'(\mathbf{r}, t) \tag{2.65}$$

where a_{ij} is the Cholesky-decomposed Reynolds stress tensor:

$$a_{ij} = \begin{bmatrix} \sqrt{R_{11}} & 0 & 0 \\ R_{21}/a_{11} & \sqrt{R_{22} - a_{21}^2} & 0 \\ R_{31}/a_{11} & (R_{32} - a_{21}a_{31})/a_{22} & \sqrt{R_{33} - a_{31}^2 - a_{32}^2} \end{bmatrix} \tag{2.66}$$

a_{ij} determines the magnitude of the velocity fluctuation as a function of the estimated Reynolds stresses $R_{ij} = \langle u_i' u_j' \rangle$, taken as the RANS modeled stresses at the RANS-LES interface.

Turbulence Injection Methods

The synthetic turbulence methods provide a fluctuating velocity field that is well defined in both space and time. If the LES domain starts directly at the inflow boundary, the fluctuating velocity signal may be imposed as a Dirichlet boundary condition according to

$$\mathbf{u}(\mathbf{x}, t) = \overline{\mathbf{u}}(\mathbf{x}, t) + \mathbf{u}'(\mathbf{x}, t) \tag{2.67}$$

where $\mathbf{u}(\mathbf{x}, t)$ is the boundary value of the velocity, $\overline{\mathbf{u}}(\mathbf{x}, t)$ is the mean velocity profile at the boundary and $\mathbf{u}'(\mathbf{x}, t)$ fluctuating velocity given by Eq. (2.65). However, if the synthetic turbulence is supposed to be injected in an embedded hybrid RANS-LES framework as in Fig. 2.1, where a forcing region is defined to drive the steady RANS velocity to an unsteady resolved turbulent velocity, Equation (2.67) can not be readily applied in a straight forward way.

This problem is addressed in Paper B [60], where suitable source terms are derived and investigated in developing turbulent channel flow and spatially developing boundary layer flow. The source terms are found by performing an expansion of the instantaneous velocity field according to

$$\tilde{u}_i \rightarrow \overline{u}_i + u'_i \tag{2.68}$$

in Eqs. (2.11)-(2.13), where $\tilde{u}_i$ is the mean flow and u'_i is an added synthetic part. These source terms are active only in the forcing region, taken as a wall-normal plane in Paper B, that provide a physically consistent way to impose fluctuations at an embedded RANS-LES interface. The interested reader is referred to Paper B for details about the derivation, below we state the results for the corresponding source terms.

Injection Method 1

Method 1 (M1) represents the injected fluctuations by considering the contribution from the convective flux [61, 22]. The additional source term associated to the fluctuations and stemming from the convective term is

$$\mathbf{Q}_C = S_n \begin{bmatrix} \overline{\rho} V' \\ \overline{\rho}(\tilde{u}_i V' + u'_i(\tilde{V} + V')) \\ \overline{\rho}\tilde{H} V' + \overline{\rho}(\frac{1}{2}(2\tilde{u}_i u'_i + u'_i u'_i))(\tilde{V} + V') \end{bmatrix} \tag{2.69}$$

where $\tilde{H} = \tilde{E} + \overline{p}/\overline{\rho}$ is the total enthalpy, $V' = n_i u'_i$, $\tilde{V} = n_i \tilde{u}_i$ and u'_i is taken from Eq. (2.65). Here, S_n is the projected cell area in a plane with normal n_i. The source term in Eq. (2.69) is added to the equations (2.11) - (2.13) to the cells that intersects the prescribed interface.

Injection Method 2

Method 2 (M2) is a volume source term stemming from the time derivative [62, 63], the contribution reads

$$\mathbf{Q}_T = \frac{\partial(\overline{\rho} u'_i)}{\partial t} \Delta V \tag{2.70}$$

where ΔV is the cell volume. In the work by Schmidt et al. [62], they introduced a ratio of the synthetically generated velocity fluctuations u'_i and the integral time scale T instead of applying a temporal derivative in order to express the source term. However, this requires knowledge about the integral time scale T, which may not be readily available. In the work by Probst [63], the term in Eq. (2.70) was discretized using the same time discretization scheme as the underlying flow solver. For a second-order backward difference scheme, this requires the fluctuations at previous times $u_i'^{n}$ and $u_i'^{n-1}$. It is argued that using the previous fluctuations from the synthetic turbulence generator may decouple the predicted flow solution from the target synthetic field, and are instead computed as the predicted fluctuations of the flow solver, namely $u_i'^n = u_i^n - \langle u_i \rangle$ and $u_i'^{n-1} = u_i^{n-1} - \langle u_i \rangle$, respectively. This requires time-averaged mean values $\langle u_i \rangle$, which are computed as a running-time average. The approach by Probst is adopted in this thesis.

Injection Method 3

Method 3 (M3) introduces fluctuations by superimposing both previous methods. That is, the contribution from the source terms given by Eq. (2.69) and (2.70) are added to the continuity, momentum and total energy equations, see Eqs. (2.11) - (2.13). By considering the contribution from both the time derivative and convection term, Method 3 should present a more complete formulation than Methods 1 and 2.

2.3.3 Improved Seamless Interface Method

The zonal interface method described in Section 2.3.2 is an effective hybrid RANS-LES approach when the prescribed interface can be readily defined, e.g. in flow cases where an attached boundary layer is located upstream of a region with flow separation induced by geometric settings to which the interface can often be referred. A sudden change in the geometry, e.g. a cavity or an obstacle, induces the flow separation and the LES region can easily be identified with prescribed RANS-LES interface beforehand, at which synthetic turbulenc can be added if needed. On the other hand, flows where the separation is subjected to adverse pressure gradient [17] or smooth-body separation [64], the location of the interface may become subtle.

A seamless hybrid RANS-LES interface method is investigated in Paper D [65], which requires no a prior knowledge of the RANS-LES interface location that is implicitly incorporated in the modelling formulation. The method aims to express the transfer of kinetic energy from the modeled turbulent scales to the resolved turbulent scales through an energy conservation principle based on the variation of the local hybrid length scale with the intention to accelerate the RANS-to-LES transition.

In regions of variable resolution, the transfer of energy between modeled RANS and resolved LES turbulence is quantified by a commutation residue term, originally formulated by Girimaji and Wallin [21]. They proposed a model for this term related to PANS and indicated extensions to length scale based models such as DES. We seek to exploit and extend this formulation for DES-based models aiming at entailing a more rapid transition between unresolved and resolved turbulent scales in the vicinity of a RANS-LES interface.

The energy balance in the spectral space is illustrated in Fig. 2.3 with $\kappa_c \propto 1/l_{ref}$ as the spectral cut-off wave number dividing the turbulence energy into the resolved and unresolved parts, k_r and k, respectively. For constant resolution, where κ_c is constant in space/time, the energy cascade σ is responsible for the energy exchange between the resolved and unresolved scales. With variable l_{ref}, κ_c can vary in time or space and correspondingly the position of the interface between k_r and k will change. This leads to an additional mechanism of energy exchange between k_r and k. Following Girimaji and Wallin [21], this energy exchange can be described by a commutation residue term, P_{Tr},

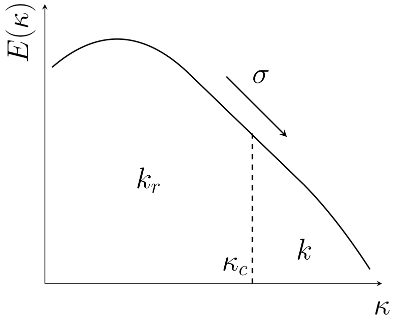

Figure 2.3: *Illustration of energy spectrum with cut-off wave number.*

in terms of the variation of the hybrid length scale l_{ref}:

$$P_{Tr} = \frac{2}{3}\frac{k}{l_{ref}}\frac{Dl_{ref}}{Dt} \tag{2.71}$$

In the DES concept, l_{ref} can be taken as any of the DES length scales (e.g. l_{DES} in Eq. (2.38), l_{DDES} in Eq. (2.41) or l_{IDDES} in Eq. (2.44)). The commutation residue term P_{Tr} in Eq. (2.71) acts as a source/sink term in the equations for k and ω, see Eq. (2.28). In the case of decreasing l_{ref}, energy is transferred from the unresolved (RANS) to the resolved (LES) scales and $P_{Tr} < 0$. Energy conservation dictates that the energy transfer rate, P_{Tr}, removed from the unresolved scales must be added to the resolved scales. The energy transfer to/from the resolved scales is modelled as a diffusion term in the momentum equation [21]

$$\mu_{Tr} = \frac{\overline{\rho} P_{Tr}}{S^2} \tag{2.72}$$

where $S = \sqrt{2\tilde{S}_{ij}\tilde{S}_{ij}}$. It must be emphasized that μ_{Tr} and μ_t represent different physics and should not be mixed up. For numerical solution they can be added through:

$$\mu_t^* = \mu_t + \mu_{Tr} \tag{2.73}$$

where μ_t^* replaces μ_t in Eq. (2.18). When resolution improves in space/time, energy is transferred from unresolved to resolved turbulence. This is brought by a negative μ_{Tr}. A limit $\mu_{Tr} \geq -\mu_t$ is introduced to ensure positive total turbulent diffusion.

Chapter 3

Numerical Methods for Scale-Resolving Simulations

The CFD solver used in the thesis work is the M-Edge code, which is an edge- and node-based Navier-Stokes flow solver applicable for both structured and unstructured grids [66, 67]. The finite volume discretisation of a node is obtained by applying the integral formulation of the filtered governing equations (2.11)-(2.13) to a control volume surrounding node i,

$$\delta V_i \frac{\partial q_i}{\partial t} + \sum_{j=1}^{n_i} F_{ij} \delta S_{ij} + \sum_{j=1}^{n_i} G_{ij} \delta S_{ij} = \delta V_i Q_i \tag{3.1}$$

where δV_i is the control-volume surrounding node i, $q_i = (\rho, \rho u, \rho v, \rho w, \rho E)^T$ are the unknown conservative variables at node i, F_{ij} and G_{ij} are the cell face convective and viscous fluxes, respectively, between nodes i and j, δS_{ij} is the cell face area connecting the dual control volumes of the nodes, and Q_i is the source term computed directly at the node. The dual grid control-volumes are computed from a primary grid. A visualisation of the dual and primary grids is shown in Fig. 3.1. The main numerical methods adopted in this thesis are outlined in the following sections.

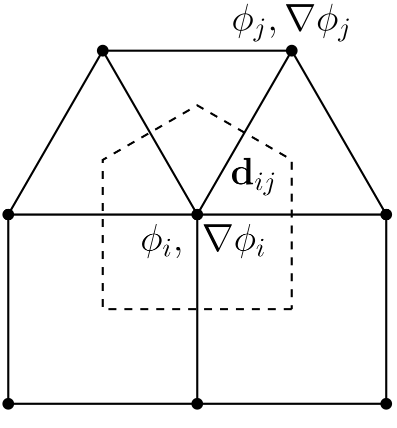

Figure 3.1: *Notation for dual grid control-volumes for a finite-volume discretization. The dual grid is generated from a node-centered unstructured grid.*

3.1 Temporal Discretization

For time-accurate unsteady simulations Eq. (3.1) is integrated in time using a second-order backward difference scheme. A dual-time stepping methodology exploiting an explicit low-storage multistage Runge-Kutta scheme [44] is used to advance the solution between physical time steps. The convective, diffusive and source terms in Eq. (3.1) are lumped into the residual

$$\delta V \frac{\partial q}{\partial t} + R(q) = 0 \tag{3.2}$$

where the physical time derivative is discretized as

$$\frac{\partial q}{\partial t} = \frac{3q^{n+1} - 4q^{n} + q^{n}}{2\Delta t} \tag{3.3}$$

where Δt is the physical time step. Equation (3.2) is converted to a steady state problem for each physical time step, where a dual-time derivative is introduced

$$\frac{\partial q^*}{\partial \tau} = -R^*(q^*) \tag{3.4}$$

and the residual is modified with the physical time derivative incorporated

$$R^*(q^*) = R(q^*) + \frac{3q^* - 4q^n + q^{n-1}}{2\Delta t} \tag{3.5}$$

The left hand side of Eq. (3.4) is driven to zero at each physical time step and the time accuracy according to Eq. (3.3) is achieved when sufficient convergence is reached. An m-stage Runge–Kutta scheme is used for time advancement in dual-time

$$\begin{aligned} q^{(0)} &= q^{(k)} \\ q^{(k,m)} &= q^{(0)} - \alpha_m \frac{\Delta\tau}{\delta V} R^*(q^{(k,m-1)}) \\ &\vdots \\ q^{(k+1)} &= q^{(k,m)} \end{aligned} \tag{3.6}$$

where $\Delta\tau$ is the pseudo-time step and α_m is the coefficients according to the Runge-Kutta scheme. Convergence is achieved after $k+1$ inner-iterations, $q^{(k+1)} \approx q^{n+1}$, usually after the residual in Eq. (3.4) has dropped two to three orders of magnitude. A three-stage RK scheme is used to solve the steady-state problem, where the coefficients with good smoothing properties are given by [66]

$$\alpha_1 = \frac{2}{3}, \quad \alpha_2 = \frac{2}{3}, \quad \alpha_3 = 1 \tag{3.7}$$

Note that the order of the daul-time stepping scheme with coefficients chosen as Eq. (3.7) is first-order. However, this does not degrade the solution quality since since the RK scheme, based on the local time step, is adopted to drive the solution converged to a steady state at each physical time step. The convergence of the local time-stepping scheme is further accelerated by using implicit residual smoothing and full-approximation storage (FAS) multigrid [44].

3.2 Spatial Discretization

The convective fluxes are discretized according to the second-order central skew-symmetric energy preserving formulation of Kok [68], together with a Jameson-Schmidt-Turkel (JST) artifical matrix dissipation [69, 70]

$$F_{ij} = \tilde{F}_{ij}(q_L, q_R) - D_{ij}(q) \tag{3.8}$$

where q_L, q_R are extrapolated face values according to a central scheme for reducing dispersion errors [42], the subscripts L and R refer to the left and right states at the cell face ij. D_{ij} is the JST artificial viscosity term needed for numerical stability, since the central skew-symmetric formulation by Kok does not provide any numerical dissipation to the scheme.

The boundary conditions are implemented in a weak formulation, in which a set of temporary flow variables are computed and used in the calculations of the boundary flux added to the residual. The residual then updates all unknown variables including the boundary values [71]. The viscous fluxes are discretized with a compact second-order central scheme.

3.2.1 Numerical Dissipation

The artificial viscosity in Eq. (3.8) is given in the JST scheme [72, 69], which is constructed as a blend of second- and fourth-order artificial dissipation according to

$$D_{ij}(q) = |A|_{ij} \left[\varepsilon_{ij}^{(2)}(q_i - q_j) - \varepsilon_{ij}^{(4)}(L(q_i) - L(q_j))\right] \tag{3.9}$$

Here, $|A|_{ij} = \left|\frac{\partial F}{\partial q}\right|_{ij}$ is the convective flux Jacobian and L is the undivided Laplacian. In the original "scalar dissipation" formulation of the JST-scheme, $|A|_{ij}$ is taken as the spectral radius basd on the eigenvalues of $|A|_{ij} = |u| + c$, where u and c are the velocity and the speed of sound, respectively. The terms involving the parameters $\varepsilon_{ij}^{(2)}$ and $\varepsilon_{ij}^{(4)}$ correspond to second- and fourth-order dissipation, respectively. The fourth-order dissipation should be active in smooth regions of the flow in order to provide good convergence to a steady state, but should vanish in the vicinity of shock waves as it will produce oscillations. The second-order dissipation term can mitigate oscillations and should be switched on by a sensor that can detected shock waves, as it will lead to degraded accuracy if it is active elsewhere.

The scalar dissipation formulation of $|A|_{ij}$ provides good convergence properties for steady simulations, usually in steady RANS simulations, but may add too much numerical dissipation and dampen actual physical waves (for example resolved turbulence) in scale-resolving simulations. In this thesis work, a matrix valued artificial dissipation formulation is exploited, where the dissipation for each equation is scaled by the respective eigenvalue of $|A|_{ij}$. The convective flux Jacobian in Eq. (3.9) is computed and diagonalized according to Langer [73]:

$$|A|_{ij} = R_{ij}|\Lambda|_{ij}R_{ij}^{-1} \tag{3.10}$$

where $|\Lambda|_{ij}$ is the diagonal eigenvalue matrix, R_{ij} and R_{ij}^{-1} are the left and right eigenvector matrices, respectively, based on the conservative variables. The parameter $\varepsilon_{ij}^{(4)}$ is taken as the difference between a global constant $\kappa^{(4)}$ and $\varepsilon_{ij}^{(2)}$

$$\varepsilon_{ij}^{(4)} = \max[0.0, \kappa^{(4)} - \varepsilon_{ij}^{(2)}] \tag{3.11}$$

such that in presence of shocks the higher differences are switched off in order to prevent oscillations. Typical values of $\kappa^{(4)}$ in Eq. (3.11) are in the range of 1/32 to 1/64 for RANS applictations [73] in order to provide good convergence properties to a steady state solution. However, as shown by Probst et al. [43] and Carlsson et al. [74], these values are not suitable for scale-resolving simulations and will severely dissipate resolved turbulence. LES of decaying grid turbulence and turbulent channel flow indicate that 1/512 to 1/1024 is a suitable range for $\kappa^{(4)}$ to allow a good trade off between convergence and numerical accuracy in scale-resolving simulations.

The second order dissipation coefficient $\varepsilon_{ij}^{(2)}$ is chosen as

$$\varepsilon_{ij}^{(2)} = \min[\kappa^{(2)} \max(\Psi_i, \Psi_j), 0.5] \tag{3.12}$$

where $\kappa^{(2)}$ is a constant and Ψ_i is a shock-capturing sensor. Note that the choice of $\varepsilon_{ij}^{(2)} = 1/2$, $\varepsilon_{ij}^{(4)} = 0$ gives a pure first-order upwind scheme in Eq. 3.9, which motivates the limit of 0.5 in Eq. (3.12).

Shock Capturing Methods

In the presence of shock waves, the flow solver should be able to distinguish discontinuities in the flow field. The standard pressure-based sensor by Jameson [72]

$$\Psi_i = \frac{|\sum_{k=1}^{m_0} (\tilde{p}_i - \tilde{p}_k)|}{\sum_{k=1}^{m_0} (\tilde{p}_i + \tilde{p}_k)} \tag{3.13}$$

identifies regions with large pressure differences, e.g. shock waves, and returns a value close to unity. The numerical scheme is then reduced to a first-order scheme through Eqs. (3.12) and (3.9). This is necessary according to Godunov [75], since any monotonicity preserving numerical scheme in the presence of shock waves can be at most first-order accurate. For regions with a smooth but continuously varying flow field the sensor given by Eq. (3.13) is usually switched off and the scheme follows the fourth-order dissipation in Eq. (3.9).

A different sensor targeted for minimizing excessive dissipation in shock/turbulence interaction in LES was proposed by Ducros [54]. The sensor is a modification to Jameson's sensor and is formulated by multiplying Ψ of Eq. (3.13) with a local function Φ_i defined by

$$\Phi_i = \frac{(\nabla \cdot \mathbf{u})^2}{(\nabla \cdot \mathbf{u})^2 + (\nabla \times \mathbf{u})^2 + \epsilon} \tag{3.14}$$

where ϵ is a numerical parameter included to avoid division by zero. The sensor includes the dilation and rotation of the flow field. Thus, regions with resolved turbulence will reduce the added dissipation. The second-order dissipation is then reformulated as

$$\varepsilon_{ij}^{(2)} = \min[\kappa^{(2)} \max(\Psi_i \Phi_i, \Psi_j \Phi_j), 0.5] \tag{3.15}$$

It was shown to effectively distinguish between shocks and compressible turbulence [54].

Low-Mach-Number Preconditioning

Low speed preconditioning is often introduced in CFD solvers for compressible flows to reduce the stiffness in the solution procedure for low speed flows with large disparity between the speed of sound and the local velocity. The positive definite preconditioning matrix P is based on Turkel's preconditioning method [76], where it implemented, for example, for the steady state Equations (3.4)

$$P^{-1} \frac{\partial q^*}{\partial \tau} + R^*(q^*) = 0 \quad \Leftrightarrow \quad \frac{\partial q^*}{\partial \tau} + P R^*(q^*) = 0 \tag{3.16}$$

The preconditioning matrix multiplies the entire residual vector. It is noted that it modifies the speed of sound into an artificial speed of sound close to the local velocity. For time-accurate scale-resolving simulations of low speed flows it is crucial to introduce low speed preconditioning to reduce numerical dissipation, see e.g. [74, 41].

3.2.2 Numerical Dispersion

The skew-symmetric energy preserving formulation deploys a particular discretization of the convective terms in the mean flow equations such that good dispersion properties are obtained. The averaged cell face values in the convective numerical flux are formulated as

$$\tilde{F}_{ij} = \begin{bmatrix} (\overline{\rho u})_{ij} \\ (\overline{\rho u}\bar{u} + \bar{p}I)_{ij} \\ (\overline{\rho u}\tilde{E} + \widetilde{pu})_{ij} \end{bmatrix} = \begin{bmatrix} \frac{1}{2}(\rho_L u_L + \rho_R u_R) \\ \frac{1}{2}(\rho_L u_L + \rho_R u_R)\frac{1}{2}(u_L + u_R) + \frac{1}{2}(p_L + p_R)I \\ \frac{1}{2}(\rho_L u_L + \rho_R u_R)\left[\frac{1}{2}(u_L u_R) + \frac{C_L C_R}{\gamma(\gamma-1)}\right] + \frac{1}{2}(u_L p_R + u_R p_L) \end{bmatrix} \tag{3.17}$$

The reader is referred to [42, 68] for the particular choice of averaging ($(\bar{\cdot})$ and $(\tilde{\cdot})$) in Eq. (3.17). For the conventional central flux the subscripts L, R are given by the nodal values at node i and j, respectively. In the low-dispersion scheme by Löwe et al. [42], the left and right face values of the velocity u and pressure p are extrapolated from the left and right node values, respectively, by using the gradient of the variable in the nodes, i.e.

$$\begin{aligned} u_L =& u_i + \alpha \nabla u_i \cdot \mathbf{d}_{ij}, \quad u_R = u_j - \alpha \nabla u_j \cdot \mathbf{d}_{ij} \\ p_L =& p_i + \alpha \nabla p_i \cdot \mathbf{d}_{ij}, \quad p_R = p_j - \alpha \nabla p_j \cdot \mathbf{d}_{ij} \end{aligned} \tag{3.18}$$

where $\mathbf{d}_{ij}$ is the distance vector between the two nodes. In this thesis work, the gradients are evaluated with a Green-Gauss' approximation, see Eq. (3.20), unless otherwise stated. α is a parameter that can be chosen to reduce the dispersion error for a specific range of wave numbers. Note that the the speed of sound and density is not extrapolated in the original scheme, since the effects of extrapolation of these quantities are small as reported by Löwe et al. [42]. However, this formulation was only evaluated for subsonic flow cases.

For compressible flow cases involving shock waves, as shown Paper A, it is recommended to extrapolate both density and speed of sound as well

$$\begin{aligned} \rho_L &= \rho_i + \alpha \nabla \rho_i \cdot \mathbf{d}_{ij}, \quad \rho_R = \rho_j - \alpha \nabla \rho_j \cdot \mathbf{d}_{ij} \\ c_L &= c_i + \alpha \nabla c_i \cdot \mathbf{d}_{ij}, \quad c_R = c_j - \alpha \nabla c_j \cdot \mathbf{d}_{ij} \end{aligned} \tag{3.19}$$

in order to reduce the oscillations in presence of a normal shock, especially for the temperature.

3.3 Gradient Reconstruction

Three different gradient reconstruction methods are outlined in this section. The first two are conventional explicit gradient reconstruction methods widely used in CFD codes. The third method is a new implicit gradient reconstruction method developed in Paper C [77]. A summary of these methods is given below.

3.3.1 Explicit Gradient Reconstruction

The divergence theorem (or Green-Gauss) gradient scheme is a popular method for discretizing the gradient operator in second-order accurate finite volume methods. On unstructured grids the discrete version of the divergence theorem is applied to estimate the nodal gradient of a function ϕ at node i according to

$$\nabla_i \phi \approx \frac{1}{\delta V_i} \sum_{j=1}^{n_i} \phi_{ij} \delta S_{ij} \tag{3.20}$$

where $\phi_{ij} = \frac{(\phi_i + \phi_j)}{2}$. The Green-Gauss gradient in Eq. (3.20) is second-order accurate on structured grids but may lose accuracy on skewed and anisotropic unstructured grids.

A more robust method is the least squares based (LSQ) method, which is a technique unrelated to the grid topology. The method relies on a stencil which identifies relevant neighbouring points for use in the gradient reconstruction. A linear system is solved to estimate the coefficients of a polynomial expansion around node i. Depending on the number of neighbours included to estimate the coefficients of the polynomial expansion, the resulting linear system may become over determined. The nodal gradients can be approximated for an assumed second-order polynomial [78, 79, 80] as

$$\begin{bmatrix} w_{i1}\Delta x_{i1} & w_{i1}\Delta y_{i1} & w_{i1}\Delta x_{i1}^2 & w_{i1}\Delta x_{i1}\Delta y_{i1} & w_{i1}\Delta y_{i1}^2 \\ \vdots & \vdots & \vdots & \vdots & \vdots \\ w_{ij}\Delta x_{ij} & w_{ij}\Delta y_{ij} & w_{ij}\Delta x_{ij}^2 & w_{ij}\Delta x_{ij}\Delta y_{ij} & w_{ij}\Delta y_{ij}^2 \\ \vdots & \vdots & \vdots & \vdots & \vdots \\ w_{iN_b}\Delta x_{iN_b} & w_{iN_b}\Delta y_{iN_b} & w_{iN_b}\Delta x_{iN_b}^2 & w_{iN_b}\Delta x_{iN_b}\Delta y_{iN_b} & w_{iN_b}\Delta y_{iN_b}^2 \end{bmatrix} \begin{bmatrix} \frac{\partial \phi}{\partial x}(\mathbf{x_i}) \\ \frac{\partial \phi}{\partial y}(\mathbf{x_i}) \\ \vdots \end{bmatrix} = \begin{bmatrix} w_{i1}(\phi(\mathbf{x_i}) - \phi(\mathbf{x_1})) \\ \vdots \\ w_{ij}(\phi(\mathbf{x_i}) - \phi(\mathbf{x_j})) \\ \vdots \\ w_{iN_b}(\phi(\mathbf{x_i}) - \phi(\mathbf{x_{N_b}})) \end{bmatrix} \tag{3.21}$$

where $\Delta x_{ij}, \Delta y_{ij}$ are distances between node i and a neighbouring node j and are given as

$$\Delta x_{ij} = x_i - x_j, \quad \Delta y_{ij} = y_i - y_j \tag{3.22}$$

The explicit least-squares problem in Eq. (3.21) can be efficiently solved using QR-factorization. In order to improve the condition number of the linear system, the weight in Eq. (3.21) is usually computed using the inverse distance according to

$$w_{ij} = \frac{1}{d_{ij}}, \; d_{ij} = \sqrt{(x_i - x_j)^2 + (y_i - y_j)^2} \tag{3.23}$$

To increase the order and accuracy of the gradient reconstruction scheme in Eq. (3.21), one can include neighbours to nearest neighbours. However, the compact formulation (by only including nearest neighbours according to Fig. 3.1) is then lost and the implementations on an unstructured grid may become increasingly complicated.

3.3.2 Implicit Gradient Reconstruction

In Paper C, a higher-order accurate gradient scheme is formulated to increase the reconstructed gradient accuracy while still maintaining the compact stencil in Fig. 3.1. The coefficients of a higher-order polynomial can be estimated by assuming knowledge of not only the values but also the gradient values of the neighbouring nodes. In numerical analysis this is referred to as Hermite interpolation. The coefficients of the polynomial are estimated by summing over j nearest neighbours to node i. This leads to the following set of equations, where the gradient values are implicitly connected:

$$\begin{bmatrix} \Delta x_{i1} & \Delta y_{i1} & \Delta x_{i1}^2 & \Delta x_{i1}\Delta y_{i1} & \Delta y_{i1}^2 & \cdots \\ \vdots & \vdots & \vdots & \vdots & \vdots & \ddots \\ \Delta x_{iN_b} & \Delta y_{iN_b} & \Delta x_{iN_b}^2 & \Delta x_{iN_b}\Delta y_{iN_b} & \Delta y_{iN_b}^2 & \cdots \\ 1 & 0 & 2\Delta x_{i1} & \Delta y_{i1} & 0 & \cdots \\ \vdots & \vdots & \vdots & \vdots & \vdots & \ddots \\ 1 & 0 & 2\Delta x_{iN_b} & \Delta y_{iN_b} & 0 & \cdots \\ 0 & 1 & 0 & \Delta x_{i1} & 2\Delta y_{i1} & \cdots \\ \vdots & \vdots & \vdots & \vdots & \vdots & \ddots \\ 0 & 1 & 0 & \Delta x_{iN_b} & 2\Delta y_{iN_b} & \cdots \end{bmatrix} \begin{bmatrix} L_{i,x}\frac{\partial \phi}{\partial x}(\mathbf{x_i}) \\ L_{i,y}\frac{\partial \phi}{\partial y}(\mathbf{x_i}) \\ \vdots \end{bmatrix} = \begin{bmatrix} \phi(\mathbf{x_i}) - \phi(\mathbf{x_1}) \\ \vdots \\ \phi(\mathbf{x_i}) - \phi(\mathbf{x_{N_b}}) \\ L_{i,x}\frac{\partial \phi}{\partial x}(\mathbf{x_1}) \\ \vdots \\ L_{i,x}\frac{\partial \phi}{\partial x}(\mathbf{x_{N_b}}) \\ L_{i,y}\frac{\partial \phi}{\partial y}(\mathbf{x_1}) \\ \vdots \\ L_{i,y}\frac{\partial \phi}{\partial y}(\mathbf{x_{N_b}}) \end{bmatrix} \tag{3.24}$$

In order to increase the robustness and the condition number of the gradient scheme in Eq. (3.24), normalized distances are introduced according to

$$\Delta x_{ij} = \frac{x_j - x_i}{L_{i,x}}, \quad \Delta y_{ij} = \frac{y_j - y_i}{L_{i,y}} \tag{3.25}$$

The choice of these factors are crucial to avoid growth of the condition number of the reconstruction matrix with grid refinement [81]. Different formulations were investigated in Paper C, the following factors showed robust performance on highly irregular and anisotropic grids with high aspect-ratio:

$$L_{i,x} = \max_j |x_j - x_i|, \quad L_{i,y} = \max_j |y_j - y_i| \tag{3.26}$$

The local system of equations in Eq. (3.24) can effectively be solved using QR-factorization. Coefficients that are connecting gradient values are collected at the left hand side and summed over the entire grid to form a global system of equations

$$P_{2D} \begin{bmatrix} \frac{\partial \phi}{\partial x} \\ \frac{\partial \phi}{\partial y} \end{bmatrix} = Q_{2D} \begin{bmatrix} \phi \\ \phi \end{bmatrix} \tag{3.27}$$

which has to be solved every solution iteration.

Chapter 4

Verification and Validation

This chapter summarizes the selected test cases used for calibration and evaluation of the methods presented in Chapters 2 and 3. In relation to numerical schemes, gradient reconstruction and scale-resolving modelling, the verification and validation conducted are briefly highlighted with computations of relevant test cases. All simulations have been performed with the unstructured compressible flow solver M-Edge, unless otherwise stated.

4.1 Verification and Validation of Numerical Schemes

In this section, computations of several test cases are presented for the evaluation of the performance of a proposed low-dispersive and low-dissipative numerical scheme adapted for compressible flows, the LD2C scheme. The scheme has been further verified on the basis of the LD2 scheme proposed by Probst et al. [43] and examined for incompressible flows. The related numerical parameters for both schemes are shown in Table 4.1.

Table 4.1: Numerical parameters for the LD2 scheme and the LD2C scheme adapted further to compressible flows.

Scheme	$\kappa^{(2)}$	$\kappa^{(4)}$	$\alpha_u,\ \alpha_p$	$\alpha_\rho,\ \alpha_c$
LD2	0	1/1024	1/3	0
LD2C	5	1/512	1/3	1/3

The value of the shock capturing parameter $\kappa^{(2)}$ and the extrapolation parameter α in Eqs. (3.18) and (3.19) in the compressible flow adapted scheme (denoted the LD2C scheme) was established in a shock-tube case in Paper A. The turbulence-resolving properties of the numerical scheme and calibration of the modeling constant C_{DES} are investigated in simulation of DIT in Section 4.1.1. The turbulence-resolving capabilities of the numerical scheme in wall-bounded flows in subsonic and supersonic conditions are investigated in Section 4.1.2 using IDDES. The LD2C scheme is further evaluated in hybrid RANS-LES of the supersonic baseflow case in Section 4.1.3.

4.1.1 Decaying Isotropic Turbulence

To asses the scale-resolving properties of the numerical scheme for incompressible isotropic turbulence using the LES mode of the SA (Eq. (2.20)) and SST (Eq. (2.28)) turbulence models, the isotropic grid-generated turbulence measured by Comte-Bellot and Corssin [82] is simulated as a temporal decay on an equidistant isotropic mesh.

The computational domain is a $2\pi \times 2\pi \times 2\pi$ cube discretized with N^3 equal sized Cartesian control volumes, using three different grid resolutions: $N = \{32, 64, 128\}$. The initial velocity distribution with zero mean velocity is obtained from the experimental energy distribution for $\tilde{t} = 0$ using an inverse Fourier transformation in a tool provided by Prof. Strelets at St. Petersburg Technical University. The other thermodynamic variables are initiated to uniform fields to simulate an initial turbulent Mach number of $M_t = 0.1$.

The turbulence modeling quantities are initialized as follows. The initial eddy viscosity field is computed from the Smagorinsky model (2.34) using the initial flucutating field. The SA-viscosity $\tilde{\nu}$ is then computed iteratively using a Newton solver to fulfil $\nu_t = f_{v1}\tilde{\nu}$. For the SST-model, the specific dissipation is computed using the Bradshaw [83] assumption: $\omega = S/\sqrt{C_\mu}$ with $C_\mu = 0.09$. The modeled kinetic energy k is then computed as $k = \nu_t \omega$.

Periodic boundary conditions are applied in all directions. The computed results are compared with the experiment by comparing the three dimensional spectrum at times $\tilde{t} \in \{0.87, 2.0\}$. The results on three different grids for SA-based and SST-based LES modes are shown in Fig. 4.1 using the LD2C-scheme in Table 4.1. For this case low Mach-number preconditioning is used but the shock capturing constant $\kappa^{(2)}$ is switched off.

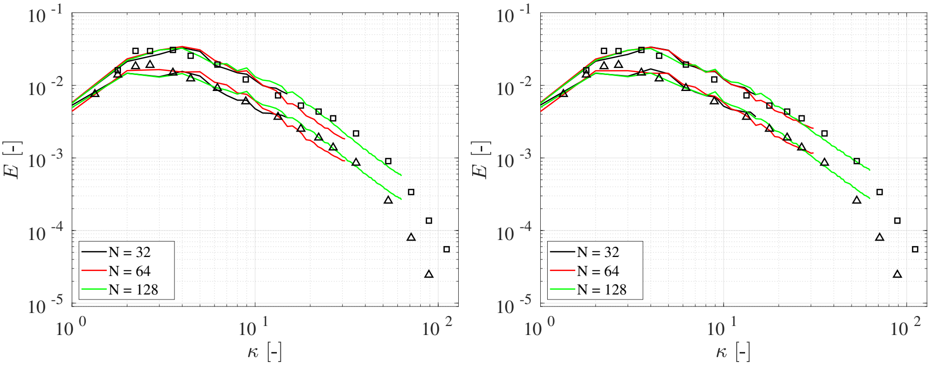

(a) *SA LES.* (b) *SST LES.*

Figure 4.1: *Decaying isotropic turbulence (DIT) using LES mode of hybrid RANS-LES model. Compared with experiments [82] at non-dimensional times* $\tilde{t} = 0.87$ (□) *and* $\tilde{t} = 2.0$ (△).

The modeling constant for the SA-based LES model is set to the standard value $C_{DES} = 0.65$ [7], where the presented spectra in Fig. 4.1a are in good agreement with the experiment. Results for the SST-based LES model is shown in Fig. 4.1b. Here, the model is run in its $k - \varepsilon$ mode using the standard value $C_{DES,k-\varepsilon} = 0.61$ [57]. The experimental spectra is well captured on all three grids. The SST model was also run in its $k - \omega$ mode with $C_{DES,k-\omega} = 0.78$ (not shown), giving nearly identical results as in Fig. 4.1b. The results shown in Fig. 4.1 indicate that the LD2C scheme can accurately predict the correct decay of isotropic turbulence without the need to recalibrate the standard values of the modeling constant C_{DES} for the underlying turbulence models.

4.1.2 Fully Developed Channel Flow

Fully-developed turbulent channel flow is a a useful test case commonly employed for examining the capabilities of resolving turbulence in wall-bounded flows. The test case is employed for the implementation, examination and validation of the numerical scheme and turbulence models using WRLES and the WMLES branch of IDDES. In order to evaluate the methodology for aeronautical applications both subsonic and supersonic conditions and a wide Reynolds number range of the fully-developed turbulent channel flow are simulated.

The computational domain is a rectangular box of height 2δ (y), a length of $2\pi\delta$ (x), and a width of $\pi\delta$ (z), where δ is the half-channel height. Periodic boundary conditions are applied in the streamwise and the spanwise directions. To replicate the same wall boundary conditions as the reference DNS [84, 85], no-slip adiabatic conditions are applied in the subsonic cases and no-slip isothermal conditions are applied in the supersonic cases.

To compensate for the lack of a pressure gradient $\partial p/\partial x$ driving the flow in the streamwise direction, the flow is driven by a forcing term f, which enforces a specific massflow through the channel in order to achieve a target Reynolds number based on the bulk velocity Re_b. The target bulk Reynolds number is chosen to satisfy a corresponding Reynolds number based on the friction velocity Re_τ, where the target Re_τ is derived from DNS results or correlations. Subsonic or supersonic conditions are controlled by specifying the bulk Mach number M_b. The operating Re_b, Re_τ and M_b are defined as in Coleman et al. [86]

$$Re_b = \frac{\overline{\rho}_b \overline{u}_b \delta}{\overline{\mu}_w}, \quad M_b = \frac{\overline{u}_b}{\overline{c}_w}, \quad Re_\tau = \frac{\overline{\rho}_w u_\tau \delta}{\overline{\mu}_w} \tag{4.1}$$

where $\overline{\mu}_w$ is dynamic viscosity at the wall, $\overline{c}_w$ is the speed of sound at the wall and $u_\tau = \sqrt{\tau_w/\overline{\rho}_w}$ is the friction velocity. Details on the computational arrangement of the turbulent channel flow simulations are given in Table 4.2. Wall-resloved (WR) indicates the WALE model given by Eq. (2.36) and wall-modeled (WM) indicates the WMLES branch of IDDES, where both the SA and SST models are considered. WM-Compressible (WMC) indicates that the case is supersonic.

Table 4.2: Summary of channel flow test cases and corresponding grid properties.

Case	Re_b	M_b	Re_τ	n_x	n_y	n_z	r	Δx^+	Δy^+	Δz^+
WR-395	6875	0.15	395	81	97	97	1.1	31	0.37-20	13
WM-395	6875	0.15	395	64	75	64	1.14	40	0.47-38	20
WM-2400	52500	0.15	2400	64	102	64	1.14	239	0.45-219	120
WM-18000	483000	0.15	18000	64	132	64	1.14	1795	0.45-1697	898
WMC-500	7667	1.5	500	64	78	64	1.14	50	0.45-46	25
WMC-1015	17000	1.5	1015	64	90	64	1.14	101	0.47-97	51
WMC-1015F	17000	1.5	1015	128	118	128	1.11	50	0.5-40	25
WMC-5000	100000	1.5	5000	64	112	64	1.14	518	0.5-515	259

Subsonic Channel Flow

The numerical settings according to the LD2-scheme (using low Mach number preconditioning) in Table 4.1 are evaluated in the nearly incompressible subsonic regime. A random initial velocity field is generated by imposing synthetic fluctuations (STG, see Section 2.3.2) in a $y - z$ plane in the middle of the channel for one convective time units (CTU $= \delta/U_b$). The flow is then allowed to develop for two CTU and then averaged over ten CTU. Time averaged quantities are then averaged in the streamwise and and spanwise directions.

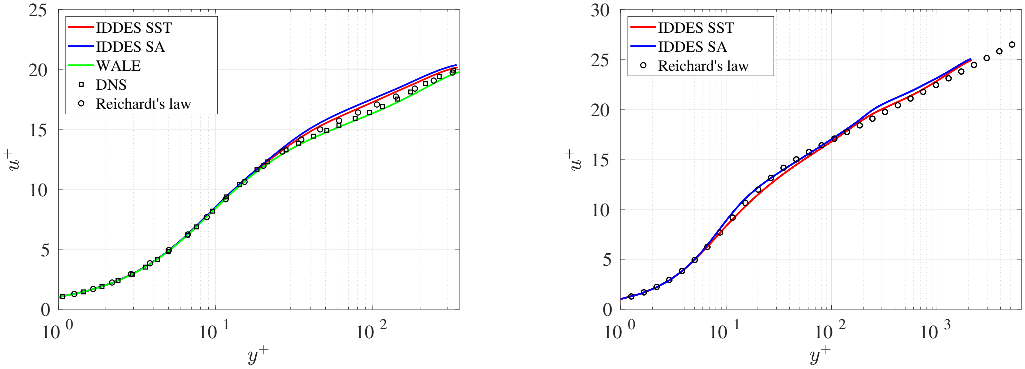

(a) *Velocity profile, WR-395 and WM-395.* (b) *Velocity profile, WM-2400.*

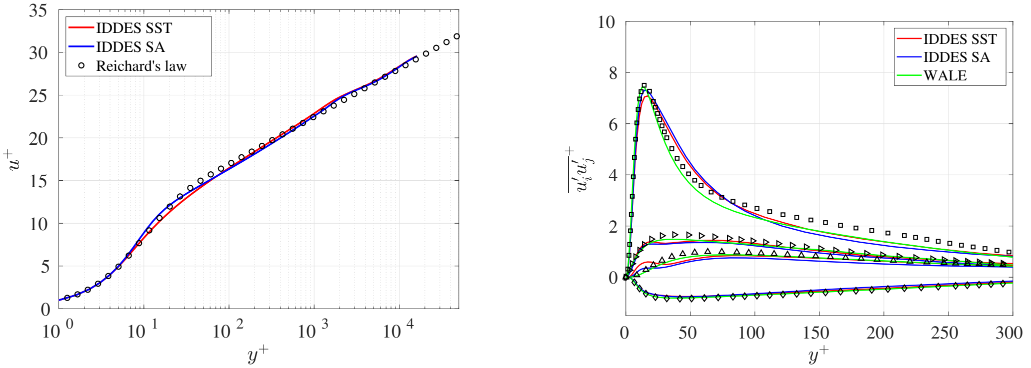

(c) *Velocity profile, WM-18000.* (d) *Total stresses, WR-395 and WM-395.*

Figure 4.2: *Fully developed subsonic channel flow at different Re_τ using WRLES and Hybrid RANS-LES IDDES. Turbulence model sensitivity. Results compared with DNS [84] and Reichardt's law [87].* □ : $\overline{u'u'}^+$, △ : $\overline{v'v'}^+$, ▷: $\overline{w'w'}^+$, ◇ : $\overline{u'v'}^+$ *from DNS data [84].*

Figure 4.2 presents the mean velocity profile for the subsonic cases at different Reynolds numbers and the total stresses (modeled plus resolved stresses) at $Re_\tau = 395$. Excellent agreement with reference DNS [84] for the velocity profile (Fig. 4.2a) and the total stresses (Fig. 4.2d) is achieved using the WALE model at $Re_\tau = 395$, where the peak of the streamwise stress $\overline{u'u'}^+$ is very well captured. The velocity profile is slightly overpredicted for the case using IDDES, where the effect is largest for the SA model. The velocity profile for the higher Reynolds number are in general well captured in comparison with the correlation by Reichardt [87], where a small log-layer mismatched can be observed at the RANS-LES interface (at around $y^+ \approx 200$ for $Re_\tau = 2400$ as shown in Fig. 4.2b and $y^+ \approx 2000$ for $Re_\tau = 18000$ as shown in Fig. 4.2c).

Supersonic Channel Flow

In the supersonic channel flow simulations the bulk Mach number is set to $M_b = 1.5$. No low Mach number preconditioning is used. In this case, both the LD2 and the LD2C schemes are evaluated. The same meshing strategy, initialization of flow field and averaging as in the incompressible cases are used. The Reynolds numbers for cases WMC-500 and WMC-1015 in Table 4.2 are chosen according to the DNS data available by Modesti et al. [85]. The Reynolds number for WMC-5000 was estimated using fully developed RANS to establish the relation between Re_b and Re_τ, since no reference DNS data was found by the author for this combination of higher Reynolds number and Mach number. However, by using proper velocity profile transformation the accuracy of the simulation can be estimated by using incompressible scaling laws.

As discussed by Coleman et al. [86], the so-called Van Driest transformation [88] can be employed for supersonic boundary layers in accounting for mean property variations in compressible turbulent wall-bounded flows. That means that the density weighted velocity profile and Reynolds stresses

$$u^+_{vD} = \int_0^{u^+} \sqrt{\frac{\bar{\rho}}{\bar{\rho}_w}} \mathrm{d}\tilde{u}^+, \quad \overline{u'_i u'_j}^+_{vD} = \frac{\bar{\rho}}{\bar{\rho}_w} \overline{u'_i u'_j}^+ \tag{4.2}$$

are expected to follow their incompressible counterparts.

Figure 4.3 presents the mean velocity profile for the cases WMC-500, WMC-1015 and WMC-5000 and the total stresses WMC CMP-1015 using SST-IDDES. Details about the grids used are given in Table 4.2. The results are similar to the subsonic case, the LD2 and LD2C schemes predicts the velocity profile very well in comparison to DNS data for cases WMC-500 and WMC-1015 (Figs. 4.3a and 4.3b), which collapses onto Reichardt's incompressible scaling law. Thus, the good agreement for the LD2 and LD2C schemes with the aforementioned law for the higher Reynolds number in WMC-5000 (Fig. 4.3c) is considered accurate.

However, the Reynolds stresses shown in Fig. 4.4b are not captured as well as in the incompressible case (Fig. 4.2d) for the LD2 and LD2C schemes using the same meshing strategy. For example, the peak value of the streamwise normal stress $\overline{u'u'}^+_{vD}$ is under predicted in comparison to the DNS result. In order to investigate the grid sensitivity, a finer grid is generated (see WMC-1015F in Table 4.2) with doubled grid resolution in the streamwise and spanwise directions, and a slightly finer resolution in the wall normal direction ($r = 1.11$). As shown in Figs. 4.4a and 4.4b, both the prediction of the velocity profile and the Reynolds stresses are improved.

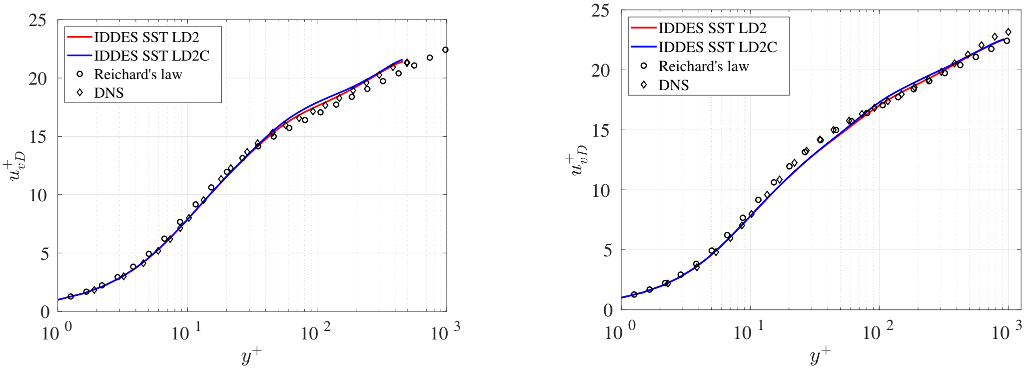

(a) *Velocity profile, WMC-500.* (b) *Velocity profile, WMC-1015.*

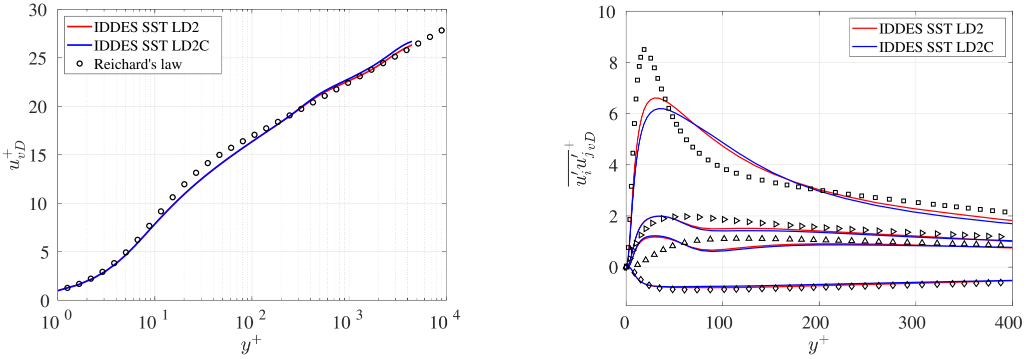

(c) *Velocity profile, WMC-5000.* (d) *Total stresses, WMC-1015.*

Figure 4.3: *Fully developed supersonic channel flow at different Re_τ using Hybrid RANS-LES SST-IDDES. Results compared with DNS [85] and Reichardt's law [87].* □ : $\overline{u'u'}^+_{vD}$, △ : $\overline{v'v'}^+_{vD}$, ▷: $\overline{w'w'}^+_{vD}$, ◇ : $\overline{u'v'}^+_{vD}$ *from DNS data [85].*

4.1.3 Supersonic Baseflow

A supersonic flow downstream of a blunt-based cylinder is characterized by expansion waves triggered by the sharp turn of the flow over the base corner. A separation bubble with a low pressure recirculation region contained by a shear layer is formed behind the base. The shear layer undergoes recompression and reattaches at the downstream end of the separation bubble along the symmetry axis. Due to the recompression, a shock wave is formed. A visualisation of the computational domain and the flow field is shown in Fig. 4.5. This kind of flow is commonly found behind high-speed projectiles, and the low pressure region behind the base can cause drag which can be a major part of the total drag. Thus, the modelling needs to be able to accurately predict the base pressure, along with other relevant properties such as the size of the recirculation bubble and turbulent properties subject to strong compressibilty effects. For this flow, experimental data are available from the study by Herrin and Dutton [89]. This test case was chosen to evaluate the LD2C scheme in a flow with strong turbulence/shock-wave interaction.

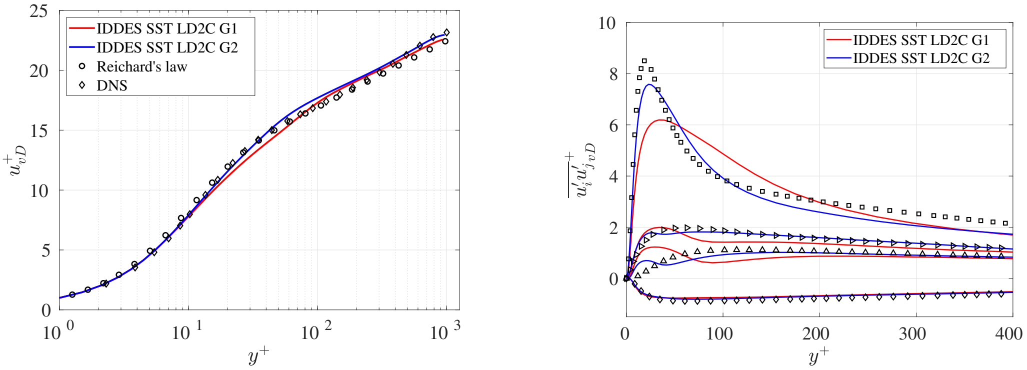

(a) *Velocity profile, WMC-1015F.*

(b) *Total stresses, WMC-1015F.*

Figure 4.4: *Fully developed supersonic channel flow for cases WMC-1015 (G1) WMC-1015F (G2) using Hybrid RANS-LES SST-IDDES. Results compared with DNS [85] and Reichardt's law [87].* $\square : \overline{u'u'}^+_{vD}$, $\triangle : \overline{v'v'}^+_{vD}$, $\triangleright : \overline{w'w'}^+_{vD}$, $\diamond : \overline{u'v'}^+_{vD}$ *from DNS data [85].*

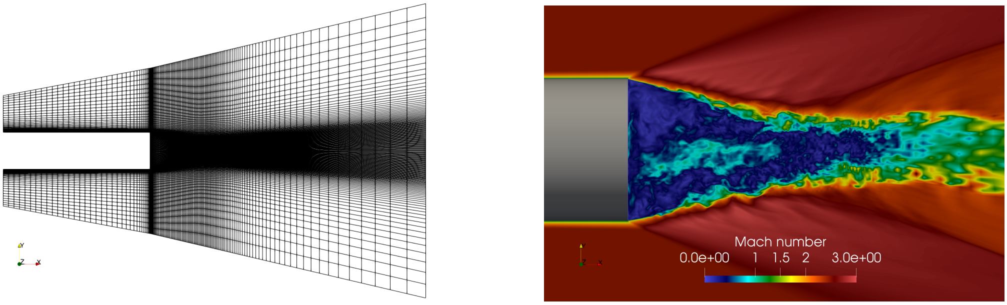

Figure 4.5: *Supersonic base flow. Illustration of computational domain (left) and visualization of flow field in the near wake of the cylinder (right). Simulation results acquired using LD2C on the finest grid.*

Table 4.3: Summary of supersonic base flow grid properties. N_θ indicates number of cells used in the azimuthal direction.

Grid	N_{cells}	N_θ	Type
G1	$1.82 \cdot 10^6$	128	Baseline
G2	$2.06 \cdot 10^6$	96	Refined shear layer
G3	$8.51 \cdot 10^6$	176	Refined shear layer/wake region

The flow includes a trailing wake of a circular cylinder with adiabatic walls aligned with a uniform supersonic flow, with a free stream Mach number of $M_\infty = 2.46$. The Reynolds number based on the free stream velocity U_∞, base radius R and free stream viscosity ν is set to $Re_R = 1.632 \cdot 10^6$. Three different grids are considered. A baseline grid with

$N_{cells} = 1.82 \times 10^6$ cells (G1) is used, which was designed by FOI in the DESider project [90]. Two new grids were generated[1], a grid with improved resolution in the shear layer consisting of $N_{cells} = 2.06 \times 10^6$ cells (G2), which was designed to match the resolution used in Guseva et al. [91]. The third grid considered contains $N_{cells} = 8.51 \times 10^6$ cells (G3), where several cells in the axial and radial directions have also been added in the recirculation region downstream the base.

The simulations are performed using the SA-DDES, where the length scale $\Delta = \Delta_{SLA}$ (see Eqs. (2.39) and (2.41)) is chosen in order to trigger an early development of resolved fluctuation in the separated shear layer. A time step of $\Delta t = 0.018R/U_\infty$ is used in the computation. After 10000 time steps, the flow is averaged for 20000 time steps. However, it is observed that the mean flow is still slightly asymmetric after time averaging, which is diminished by further averaging the solution in the azimuthal direction.

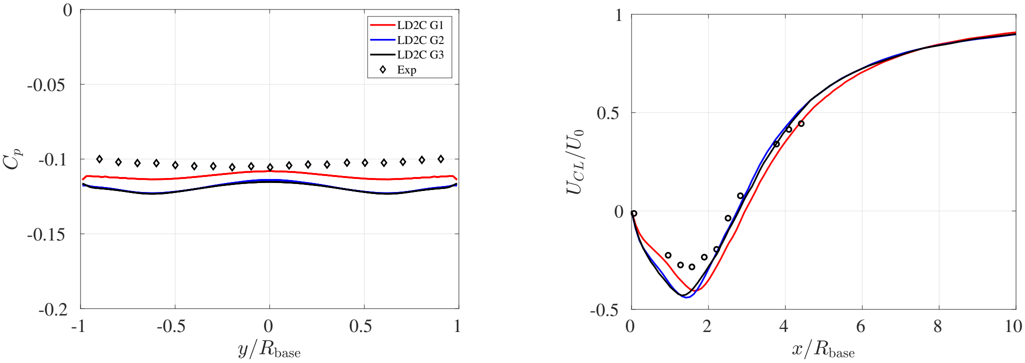

(a) *Base pressure.*

(b) *Centerline velocity.*

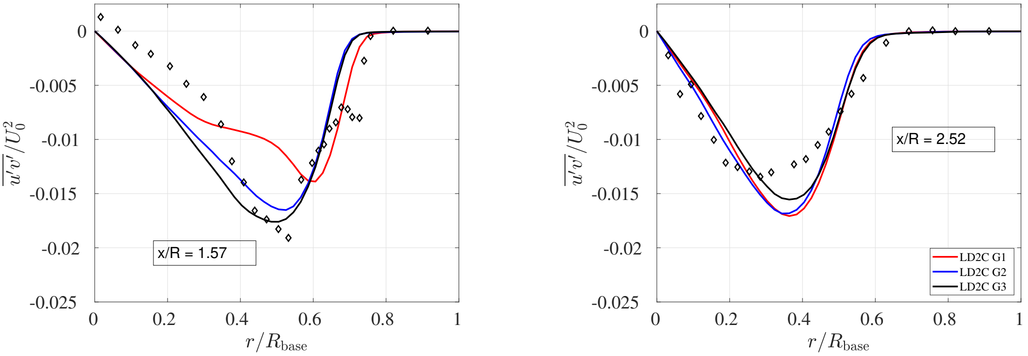

(c) *Resolved shear stress, $x/R = 1.57$.*

(d) *Resolved shear stress, $x/R = 2.52$.*

Figure 4.6: *Supersonic base flow using Hybrid RANS-LES SA-DDES. Results compared with experiment [89].*

Time- and azimuth-averaged flow properties are shown in Fig. 4.6. The base pressure

---

[1] The grids G2 and G3 were generated using G3D::Mesh with the help of fellow PhD-student Gonzalo Montero Villar. The help is much appreciated.

is presented in Fig. 4.6a, where the experimental results yield a relatively flat profile around $C_p = -0.102$. The simulations show radial variations along the base and in general an under predicted base pressure coefficient. However, a wavy base pressure profile and in general lower base pressure values are also observed in the works of Simone et al. [92] and Guseva et al. [91].

The previous trends can be explained by investigating the behavior of the centerline streamwise velocity component in Fig 4.6b. The simulations predicts the reattachment point fairly well ($x/R \approx 2.9$ on G1 $x/R \approx 2.7$ on G2 and G3) as compared to the experimental value $x/R = 2.67$. On the other hand, the reverse flow inside the recirculation region is in general over predicted, which gives rise to the under predicted base pressure levels in Fig. 4.6a. Figures 4.6c and 4.6d present a comparison of the predicted and measured fields of turbulent shear stresses at locations $x/R = 1.57$ and $x/R = 2.52$ downstream of the cylinder base, respectively. The shear stress magnitude is slightly under predicted on the coarsest grid G1 at $x/R = 1.57$ but is in very good agreement on the finer grids G2 and G3.

4.2 Verification of Gradient Reconstruction

A new method for gradient reconstruction is presented in Paper C. In order to assess the order of accuracy and robustness of the least-squares gradient reconstruction methods given in Section 3.3, the numerical gradient of a known smooth test function is compared to its analytical value on consecutively refined meshes [93, 94]. The function is evaluated for each interior node through several refinement levels for a set of different unstructured, isotropic and high-aspect-ratio grids. The L_1 and L_2 errors in the resulting numerical gradient are calculated as

$$L_1 = \frac{\sum_i^N |\nabla\phi_{i,num} - \nabla\phi_{i,ana}|}{N}, \quad L_2 = \left(\frac{\sum_i^N |\nabla\phi_{i,num} - \nabla\phi_{i,ana}|^2}{N}\right)^{1/2} \tag{4.3}$$

where N is the number of nodes, $\nabla\phi_{i,num}$ and $\nabla\phi_{i,ana}$ are the numerical and analytical gradients, respectively. The reconstruction schemes are implemented in a stand alone MATLAB script.

The implicit least squares (ILSQ) scheme detailed in Section 3.3.2 is evaluated assuming a fourth-order polynomial order. Since the accuracy of interior nodes is the scope in this thesis, it is assumed that the gradient values at the boundary are known. The compact implicit gradient scheme is compared to the standard distance weighted explicit LSQ (ELSQ) gradient reconstruction scheme given by Eq. (3.21). We consider only connecting neighbours in the LSQ formulation according to Fig. 3.1. This limits the ELSQ schemes to maximum second-order schemes. The test function for the first case is given by:

$$f(x, y) = \sin(\pi x)\sin(\pi y) \tag{4.4}$$

The function in Eq. (4.4) is evaluated on a rectangular domain given by $[0, 1] \times [0, 1]$ shown in Fig. 4.7a and is discretized using mixed elements (quadrilaterals and triangles). Note that vertices of the elements are randomly perturbed in order to fully remove any structure in the grid. This is done in order to remove any favorable cancellation of higher-order error terms.

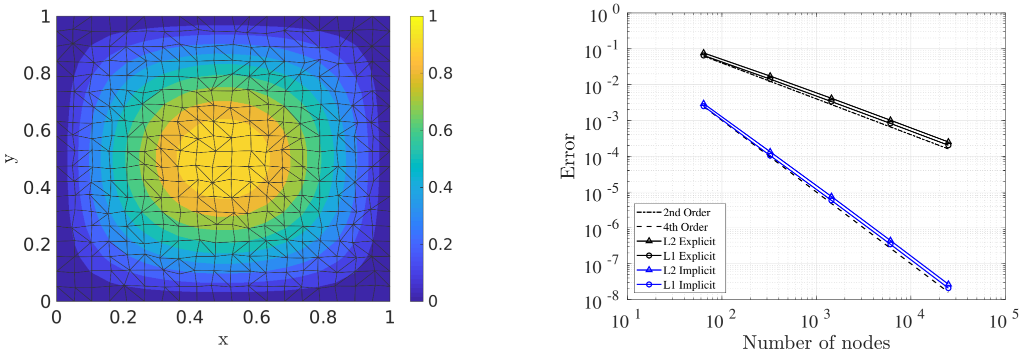

(a) *Function values and grid.* (b) *Error convergence.*

Figure 4.7: *Gradient reconstruction of an analytical function. Mixed elements on isotropic domain size.*

The order of convergence of the error is shown in Fig. 4.7b. The ILSQ scheme yields a robust fourth-order accuracy in the L1 and L2 error norms using a compact stencil, and indicates that the ILSQ gradient reconstruction formulation is insensitive to grids with mixed quadrilaterals and triangles. The ELSQ scheme attains its prescribed second-order scaling using the same compact stencil. In order to evaluate the performance of the gradient reconstruction methods on highly stretched grids, a different problem is considered. The test function is given by:

$$f(x, y) = \sin(\pi x)\sin(4000\pi y) \tag{4.5}$$

Equation (4.5) is evaluated on a rectangular domain given by $[0, 1] \times [0, 0.0005]$. Using this domain size, elements with aspect-ratio of 2000 is considered. This setup models a typical boundary layer problem [94], where the solution variation is predominant in the direction of small grid spacing and an anisotropic grid is specifically tailored to represent the solution anisotropy. The computational domain and the test function are presented in Fig. 4.8. The same mixed element discretization is used as in the previous case.

The order of convergence of the L1 and L2 error norms are shown in Fig. 4.8b. Both methods yield the prescribed accuracy, the ILSQ shows fourth-order convergence and the ELSQ scheme shows second-order convergence. Note that the error levels are higher compared to the case with the isotropic domain size in Fig. 4.7. This is due to the resulting error of the gradient in the direction of the anisotropic scaling being much higher than in the other direction with no stretching. Nevertheless, the ILSQ scheme shows the correct fourth-order scaling on both test cases and are several orders of magnitude more accurate than the standard ELSQ scheme. For example, to reach a similar order of error, the standard ELSQ scheme need to use a discretization of approximately $2.5 \cdot 10^4$ nodes compared to $3.0 \cdot 10^2$ nodes used by the ILSQ scheme.

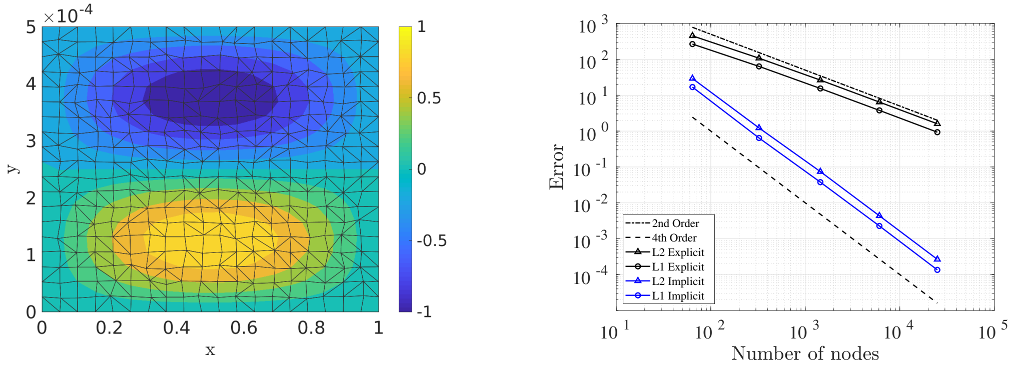

(a) *Function values and grid.* (b) *Error convergence.*

Figure 4.8: *Gradient reconstruction of an analytical function. Mixed elements on highly anisotropic domain size. Aspect ratio* $AR = 2000$*.*

4.3 Examination of Turbulence Injection Methods

This section evaluates the performance of the zonal hybrid RANS-LES approach outlined in Section 2.3.2. The purpose of this section is to assess the injection methods (M1-M3) used in combination with the SEM and STG synthetic turbulence methods. The zonal methodology is evaluated in a hybrid RANS-LES of the spatially developing zero-pressure-gradient (ZPG) turbulent boundary layer. This test case was evaluated in Paper B, where the developing turbulent channel flow at $Re_\tau = 5200$ was also evaluated.

4.3.1 Spatially Developing Boundary Layer Flow

Simulations of spatially developing boundary layers are essential in the aeronautical industry in order to achieve accurate predictions of aircraft drag. The spatially developing zero-pressure-gradient (ZPG) turbulent boundary layer over a smooth flat plate is therefore simulated using the SA-IDDES with a prescribed wall-normal RANS-LES interface (see Fig. 2.1) located inside the boundary layer. A RANS region is prescribed by forcing $l_{IDDES} = l_{RANS}$ in Eq. (2.44) between $0 \leq x/\delta_0 \leq 4$, and an embedded interface is prescribed at $x/\delta_0 = 4$, where δ_0 is the initial boundary layer thickness. Downstream of this interface, the IDDES length scale in Eq. (2.44) is unmodified. Synthetic turbulent fluctuations and an eddy viscosity treatment for the SA-model described in Paper B are imposed at the embedded interface in order to obtain a rapid development of downstream turbulence-resolving LES flow.

The Reynolds number range covered by the simulation is approximately $3000 \leq Re_\theta \leq 6000$, where θ is the momentum thickness computed according to

$$Re_\theta = \frac{U_0 \theta}{\nu}, \quad \theta = \int_0^\delta \frac{u}{U_0}\left(1 - \frac{u}{U_0}\right) \mathrm{d}y \tag{4.6}$$

where U_0 is the free stream velocity and ν is the dynamic viscosity. The Mach number based on the free stream velocity is $M_0 = 0.2$. Profiles of u, v and ν_t from a precursor RANS simulation using the SA model are prescribed at the inlet boundary. Adiabatic conditions are applied at the bottom wall boundary and characteristic Riemann boundary conditions is applied at the top and outlet boundaries. Periodic boundary conditions are applied in the spanwise direction.

The grid used for the simulation is designed by Onera and used in the EU-FP7 Go4Hybrid [95], the Garteur AG54 projects and in Deck et al. [96]. The dimensions of the computational domain in the streamwise, spanwise and in the wall-normal directions are, respectively, $L_x = 113\delta_0$, $L_z = 5\delta_0$ and $L_y = 52\delta_0$. Note that for $x/\delta_0 > 77$, grid cells are stretched in the streamwise direction in order to progressively damp the turbulent fluctuations. This procedure is common to ensure that the domain of interest is free from wave reflections from the outlet. Details about the grid used are given in Table 4.4.

Table 4.4: Grid parameters of the ZPG turbulent boundary layer. Re_{θ_0} and Re_{τ_0} are computed with the initial boundary layer thickness δ_0.

Re_{θ_0}	Re_{τ_0}	M_∞	n_x	n_y	n_z	Δx^+	Δy^+_{min}	Δz^+
3030	1065	0.2	587	127	103	100-200	2	50

The injection methods M1-M3 (see Section 2.3.2) are assessed by imposing synthetic fluctuations from either the STG given by Eq. (2.58) or the SEM given by Eq. (2.50) at the wall-normal RANS-LES interface. The fluctuations are scaled with the Cholesky tensor given by Eq. (2.66), where the Reynolds stress tensor is taken as the RANS stresses from a precursor RANS simulation.

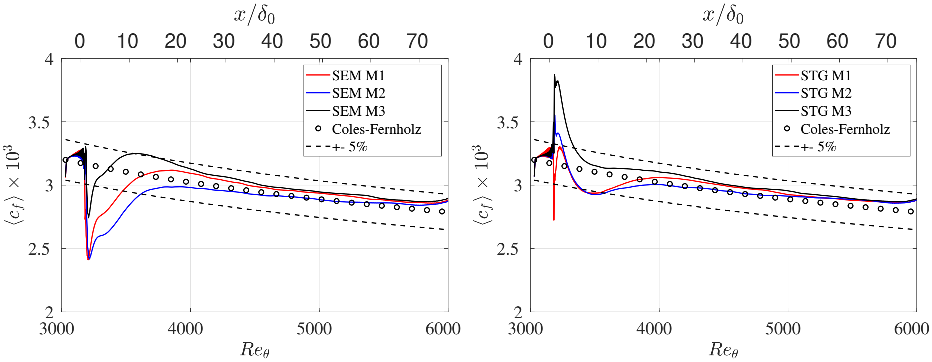

(a) *Skin friction, SEM.* (b) *Skin friction, STG.*

Figure 4.9: *Developing turbulent boundary layer at* $Re_\theta = 3030$ *using Hybrid RANS-LES SA-IDDES. Synthetic turbulence model and turbulence injection method sensitivity. Results compared with Coles-Fernholz correlation [97]. Prescribed wall-normal RANS-LES interface is located at* $\tilde{x}/\delta_0 = 0$.

Figure 4.9 shows the resulting skin friction coefficient in comparison with the Coles-Fernholz correlation [97]. It can be concluded that the proposed method M3, which is the combination of M1 and M2, performs best for both the SEM and STG. The initial sudden decrease of the skin friction coefficient is characteristic for the SEM, but this effect seems to be mitigated by using method M3. On the other hand, the initial skin friction is over predicted for the STG in combination with M3, but the correct asymptotic behavior is reached quicker compared to M1 and M2. The correct trend of M3 is reached after roughly $5\delta_0$ when using either the SEM or the STG, a clear improvement compared to M1 and M2. However, it is important to highlight that all simulations are within a 5% margin after $10\delta_0$ from the reference correlation, and give a correct decay of the skin friction further downstream in the boundary layer, as shown in Fig. 4.9.

The difference between the methods with respect to the mean velocity profile and resolved stresses measured at $Re_\theta = 4060$ are very small and yield similar small deviation from DNS [98], as shown in Figs. 4.10a and 4.10b. Here, only the results are shown for the STG, the results for the SEM are very similar.

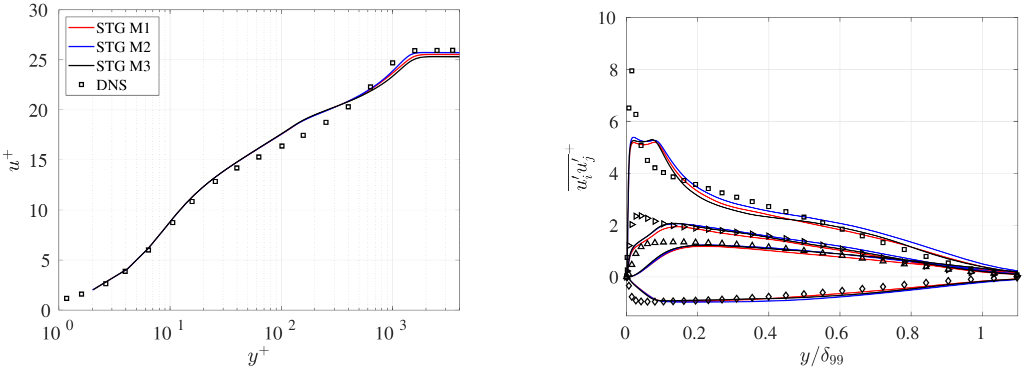

(a) *Velocity profile, STG.*

(b) *Resolved stresses, STG.*

Figure 4.10: *Developing turbulent boundary layer using Hybrid RANS-LES SA-IDDES. Synthetic turbulence model and turbulence injection method sensitivity. Profiles are measured at at Re_θ = 4060 and compared with DNS data [98]:* $\square : \overline{u'u'}^+$, $\triangle : \overline{v'v'}^+$, $\triangleright$: $\overline{w'w'}^+$, $\diamond : \overline{u'v'}^+$.

4.4 Verification of Seamless GAM Methodology

This section reports results from Paper D, which evaluate the proposed seamless Grey-Area Mitigation (GAM) methodology outlined in Section 2.3.3. The seamless methodology is evaluated for a mixing shear layer flow case using hybrid RANS-LES. Additional results of flow over a wall-mounted hump (Hump flow) is presented in Paper D. A baseline formulation is considered, the $k-\omega$ SST DDES model (Eqs.(2.28) and (2.41)) using the filter width $\Delta = \tilde{\Delta}_\omega$. The length scale based commutation term (CT) is implemented as a source term in the k and ω equations through Eq. (2.71). The contribution to the resolved Eqs.(2.11) - (2.13) is implemented as a modified eddy viscosity μ_t^* (see Eq. (2.73)), which replaces μ_t in Eq. (2.18). In addition to the length scale based commutation term, the

σ-DDES model by Mocket et al. [99] is evaluated in combination with the commutation term or as a stand-alone GAM methodology.

4.4.1 Mixing Shear Layer Flow

Mixing layer flows and free shear flows are often encountered in aeronautical applications, for example jet flows and flows downstream of aircraft wings after the trailing edge. The free shear layer flow evaluated in this Section was investigated experimentally by Delville [100]. The computational domain includes a very thin flat plate, with turbulent boundary layers on each side. A mixing layer is formed in the region downstream of the flat plate trailing edge. The experimental boundary layer properties at the trailing edge are presented in Table 4.5.

Table 4.5: Flow parameters of mixing-layer case. Data from experiment [100].

Measure	Notation	High vel. BL	Low vel. BL
Velocity	U_∞	41.54 m/s	22.40 m/s
Thickness	δ	9.6 mm	6.3 mm
Displ. thick.	δ_1	1.4 mm	1.0 mm
Mom. thick.	θ	1.0 mm	0.73 mm
Shape factor	H	1.35	1.37
Re based on θ	Re_θ	2900	1200
Turbulence level	u'/U_∞	~ 0.3 %	~ 0.3 %

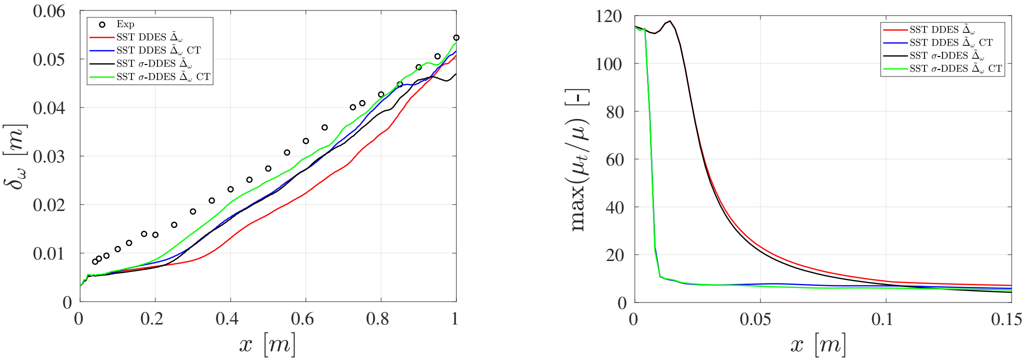

(a) *Vorticity thickness.*

(b) *Maximum eddy viscosity.*

Figure 4.11: *Mixing shear layer flow using Hybrid RANS-LES SST-DDES. Commutation term is indicated by CT. Results compared with experiment [100].*

The focus region, i.e. the region from the flat plate trailing edge at $x = 0$ to $x = 1$ m, is meshed with $(n_x, n_y, n_z) = (640, 196, 96)$ cells. The grid is equidistant in the streamwise x-direction and spanwise z-direction, $\Delta x = \Delta z = 1.5625$ mm. The total number of hexahedral grid cells are 13.7 million. A timestep of $\Delta t = 2.5 \times 10^{-5}$ seconds is used. The upstream boundary layers are treated in RANS mode and the DDES model automatically switches to LES after the trailing edge. The growth of the mixing layer, the vorticity thickness, computed as

$$\delta_\omega = \frac{U_a - U_b}{(\partial U/\partial y)_{y=0}} \tag{4.7}$$

is presented in Fig. 4.11a. The baseline case clearly underpredicts the growth of the shear layer. By applying the the commutation term, the σ-DDES model or a combination of those gives improved results, where the agreement with the experimental result is significantly improved for after $x > 0.2$ m. The maximum eddy viscosity at the initial part of the shear layer is shown in Fig. 4.11b. The effect of the commutation term is large, where the eddy viscosity is rapidly reduced. Without the commutation term, such a reduction is relatively slow. The lower eddy viscosity levels contributes to a rapid growth of resolved turbulence, which is visualised in Fig. 4.12. As shown, the resolved shear stress is better predicted at station $x = 0.2$ m, where the prediction incorporating both the commutation terms combined with σ-DDES gives the best result.

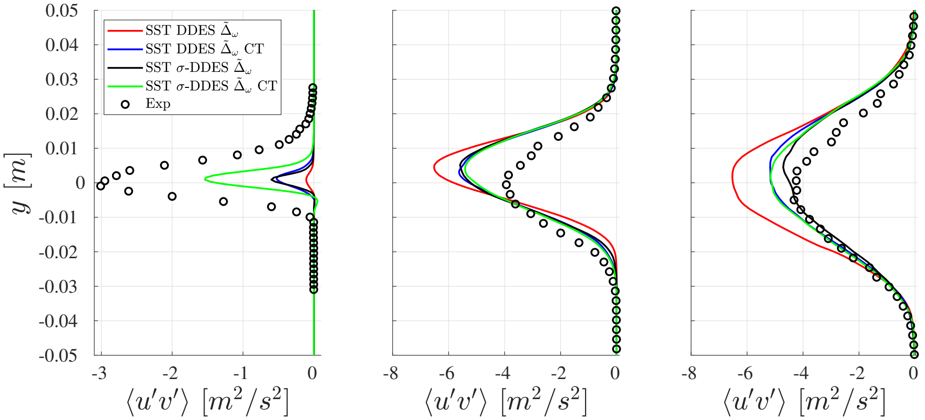

Figure 4.12: *Mixing shear layer flow using Hybrid RANS-LES SST-DDES. Commutation term is indicated by CT. Resolved shear stress at locations $x = 0.2$ m (left), $x = 0.65$ m (middle) and $x = 0.95$ m (right). Results compared with experiment [100].*

Chapter 5

Summary of Papers

The main contribution and the major work done for each paper appended in the thesis are presented in this chapter. Comments are given to highlight possible improvement and future work.

5.1 Paper A

"Investigation of Low-dissipation Low-dispersion Schemes for Incompressible and Compressible Flows in Scale-Resolving Simulations"

In Paper A, a numerical scheme suitable for unstructured grids was investigated and developed. The numerical scheme is an essential part of a CFD code and will determine the capabilities of resolving the turbulent scales in the LES mode of hybrid RANS-LES. A low-dispersive, low-dissipative (LD2) scheme developed by Löwe et al. [42] and Probst et al. [43] was found suitable, since the scheme requires little modification to the second-order scalar valued Jameson-Schmidt-Turkel (JST) scheme already present in M-Edge. The scheme exploits a matrix valued dissipation operator to reduce the added numerical dissipation while maintaining numerical stability. Numerical dispersion is reduced and controlled by using higher order central reconstruction of the face values, using the local nodal gradients on each side of the cell face.

The work in Paper A is a continuation of the work in Carlsson et al. [74], in which the numerical scheme was evaluated in incompressible LES of the turbulent channel flow at $Re_\tau = 395$ and decaying isotropic turbulence (DIT). In Paper A, the LD2 scheme was examined and modified for compressible flow cases involving shock discontinuities, LD2-Compressible (LD2C), and verified in a shock-tube problem. The scheme was then further verified in hybrid RANS-LES of DIT, and the turbulent channel flow for a wide range of Reynolds numbers in both subsonic and supersonic conditions. It is reported that the LD2C scheme can accurately predict the correct decay of the turbulent energy spectrum in DIT and the mean velocity profile and turbulent stresses in the turbulent channel flow cases.

Moreover, a supersonic base flow was simulated using hybrid RANS-LES. The LD2C scheme exploits a shock sensor incorporating vorticity and was shown to improve the prediction of the resolved shear stress in the shear layer of compression in comparison with the conventional scheme. However, the predicted base pressure was shown to be underestimated in comparison with experiments, which was also reported in the works by Simone et al. [92] and Guseva et al. [91]. This was caused by an overprediction of the back flow inside the recirculation bubble.

5.2 Paper B

"Turbulence Injection Methods at RANS-LES Interfaces or Inlets for Scale-Resolving Simulations"

The purpose of Paper B was to develop and demonstrate a methodology for injecting synthetic turbulence in a fully coupled embedded hybrid RANS-LES. Three different methods for imposing velocity fluctuations in a compressible finite-volume solver were evaluated for zonal hybrid RANS-LES applications using the SA-IDDES model. The methods were derived from an expansion of the governing equations, resulting in additional source terms stemming from the time derivative, the convective operator and a combination thereof. Additionally, following the work by Hamba [20], a commutation term was derived for the convection term in the SA turbulence model in order rapidly reduce the turbulent viscosity across the RANS-LES interface. The three injection methods and the commutation term was verified in embedded RANS-LES using SA-IDDES in a turbulent channel flow at $Re_\tau = 5200$ and zero-pressure-gradient boundary layer flow at $Re_\theta \geq 3000$, where the synthetic fluctuations were computed according to the Synthetic Turbulence Generator (STG) formulation by Shur et al. [28].

It is reported that the commutation term is able to effectively reduce the upstream RANS levels of turbulent viscosity to LES levels of turbulent viscosity across the embedded interface for both considered cases. The transition occurs over a distance much shorter than δ, where δ is the channel half width or the local boundary layer thickness. The formulation is expressed as a source term, and is free from model dependent parameters.

It is concluded that all the three injection methods perform very well for the turbulent channel flow case, and are able to reproduce reference simulation friction velocity (within a 5% margin) within 1δ downstream from the interface. In the simulations of the boundary layer flow, the discrepancy between the different injection methods are relatively large. The shortest recovery length with a well predicted skin friction level is produced by the combined approach. The other two approaches yield similar recovery lengths, considerably longer compared to the combined approach. However, all the simulations that are presented predict a skin friction distribution within 5% compared to the Coles-Fernholz correlation, which is used as a reference. Good agreement with DNS data further downstream is achieved for all simulation, with respect to mean velocity profile and resolved Reynolds stresses.

5.3 Paper C

"Higher-Order Gradients on Unstructured Meshes Using Compact Formulation for Node-Centered Schemes"

In Paper C, a new approach for gradient computations on node-centered unstructured grids was introduced. This was done in order to improve the numerical scheme in Paper A, which use nodal gradient for reconstructing the cell face values in the convective flux computations. The proposed approach derives a gradient algorithm from a least squares

(LSQ) approximation, where a local equation system is solved to introduce connectivity between neighbouring nodes. The resulting scheme forms a globally coupled linear system of equations for the gradients. The implicit LSQ (ILSQ) allows a higher-order gradient reconstruction using a compact formulation, i.e. using only nearest neighbours. This may greatly simplify implementations of higher-order schemes in unstructured CFD codes.

The ILSQ scheme was assessed in the capability of reconstructing the gradient of a known analytical function, and was implemented in a standalone MATLAB script. It is reported that the ILSQ scheme shows a fourth-order scaling on all grids considered, including highly irregular quadrilateral grids, triangular grids, mixed element grids and high-aspect-ratio grids ($AR = 2000$). Using the same compact stencil, it is shown that a standard distance weighted explicit LSQ (ELSQ) can at most achieve a second-order scaling.

Comments

The new gradient-reconstruction algorithm in Paper C considers only interior nodes and it was assumed that the gradient was known on the boundaries, i.e. a Neumann boundary condition. The proposed gradient scheme needs to be closed with a suitable boundary condition for cases when the gradient is unknown, e.g. a Dirichlet boundary condition, in order to maintain the fourth-order accuracy and be applicable for general CFD purposes.

While the overall accuracy of the numerical scheme in Paper A may be improved using the new gradient reconstruction scheme, a higher-order evaluation of the surface integral in the flux evaluation needs to be considered in order to raise the overall order of accuracy of a finite-volume scheme, as is shown by Gooch [93]. This can e.g. be achieved by using additional quadrature points in the surface integral [93] or an iterative k-exact reconstruction strategy by Setzwein et al. [101].

5.4 Paper D

"Seamless Interface Methods for Grey-Area Mitigation in Scale-Resolving Hybrid RANS-LES"

A new Grey-Area Mitigation (GAM) method was proposed in Paper D. A commutation residue term formulation by Girimaji and Wallin [21] for PANS modeling was further expanded to DES-type modeling aiming for a more rapid transition between modeled and resolved turbulent scales in the vicinity of a RANS-LES interface. The proposed GAM method, aiming to mitigate the grey area over the RANS-LES interface, is based on a commutation term stemming from the variation of the local hybrid length scale. Furthermore, a sub-grid model enabling to reduce the eddy viscosity in a shear layer, the σ-DDES model by Mocket et al [99], was also evaluated. Both methods require no additional manipulation of, or explicitly defining, the RANS-LES interface and are applied in a global manner.

Paper D reports hybrid RANS-LES computations undertaken in the verification of GAM formulations incorporated into the SST DDES model. Two test cases, namely, the flow over a wall-mounted hump and a mixing shear layer was computed. It was shown that the effect of both the commutation term and the $\sigma - DDES$ model improve the results for the mixing shear layer and are able to trigger a rapid transition of modeled to resolved turbulence. This indicated improved predictions of both vorticity thickness and resolved shear stress. The effect of commutation term and the $\sigma - DDES$ model is less pronounced for the hump flow, however, where the recovery of the skin friction coefficient is only slightly better predicted.

Comments

The commutation term presented in Paper D effectively reduces the modeled kinetic energy and eddy viscosity further in the vicinity of a RANS-LES interface. We believe that this is necessary but not enough, and synthetic turbulence could be added to further mitigate the grey area in flow cases where resolved fluctuations are not triggered by strong shear. The commutation term, which is a measure of the energy transfer between the modeled and resolved scales, can be used to scale the intensity of the synthetic fluctuations. The Anisotropic Linear Forcing (ALF) method by de Laage de Meux et al. [102] offers an interesting combination with the commutation term, due to its relatively small computational overhead, which is necessary since the commutation term is computed in the entire computational domain, and that it requires no explicit RANS-LES interface to be defined.

5.5 Paper E

"Implementation of Nonreflecting Inlet and Outlet Boundary Conditions in the Subsonic Regime for a Node-Based Compressible Solver"

With the experience gained from the work in Paper B, it was concluded that synthetic turbulent fluctuations may produce spurious pressure reflections in the vicinity of inlet or outlet boundaries. This is caused by an improper treatment of the incoming and outgoing characteristic waves at truncated computational domains, which is not accounted for in standard inlet/outlet boundary conditions. Paper E presents a survey on the implementation of the Navier-Stokes characteristic boundary conditions (NSCBC) by Lele et al. [103]. Special attention paid to node-centered finite volume schemes, with the aim to mitigate the reflected waves from the boundaries. Two different implementations were investigated of the NSCBC, the first sets the primitive variables at the boundary from the NSCBC equations, the other implements the NSCBC as a source term. The NSCBC implementations were compared to conventional boundary conditions.

A subsonic inlet was tested to evaluate the boundary conditions in their capability to inject an analytical isentropic vortex. The boundary conditions was verified in examining how well the analytical solution is preserved. A Dirichlet boundary condition was capable of injecting the vortex with minimal distortion and give accurate results. The strong implementation of setting the primitive variables at the boundary was capable of injecting the vortex, although significant checkerboard pattern is observed in the pressure. The source term implementation failed to inject the vortex in a reasonable form unless a high value of a penalty parameter σ is chosen. The value had to be chosen much larger than the recommended value (50 vs. 0.25), although a zero value of this parameter has been reported in the literature to give satisfactory results.

A subsonic outlet was evaluated to assess the boundary conditions of their capability of transporting out an analytical vortex through the exit boundary. No reflections and minimal distortion of the vortex condition is expected. The NSCBC was compared to a conventional outlet condition with a static pressure specified. The static pressure outlet condition is reflective, and reflection in the pressure field is observed. The source term implementation of the NSCBC gives the best result with minimal reflections observed. The strong implementation of setting the primitive variables manages to transport out the vortex with checkerboard pattern observed.

Chapter 6

Conclusions and Outlook

The thesis work has dedicated to improvements of modelling and simulation methodologies for robust use in scale-resolving computations of turbulent flows of industry relevance. These concern of developing and examining both improved modelling approaches and feasible modelling-related numerical issues.

6.1 Concluding Remarks

A low-dissipative low-dispersive scheme (LD2) by Löwe et al. has been investigated in in order to reduce the dissipative and dispersive numerical errors connected to the convective term. The scheme controls added artificial dissipation through a matrix dissipation operator and is adapted to low speed flows with a low Mach number preconditioner. The scheme exploits a higher order central reconstruction of the face fluxes to reduce the dispersive numerical error. In Paper A, the numerical scheme was applied in hybrid RANS-LES of turbulent channel flow and the decaying isotropic turbulence (DIT) for calibration purposes. The scheme was then further adopted to and assessed in compressible flows involving shock waves, such a shock tube case. Additional hybrid RANS-LES of supersonic flow over a cylindrical base further verifies the scheme and give good agreement with reference data.

A sensitivity study on the implementation of the Synthetic-Eddy Method (SEM) and the Synthetic Turbulence Generator (STG), to inject synthetic turbulence at the RANS-LES interface in order to mitigate the grey-area problem in the LES region has been made. Three methods have been implemented in Paper B, where the synthetic turbulent fluctuations is numerically represented by means of, respectively, a volumetric source term or a virtual flux term, or the combination of both methods, where the three methods were implemented through imposing the fluctuations (in the form of a source term) at the inlet boundary or in a plane further downstream of the inlet boundary. The methods have been verified in hybrid RANS-LES of developing turbulent channel flow and developing boundary layer.

In Paper C, an implicit least squares gradient (ILSQ) reconstruction scheme with a compact formulation has been derived. A detailed study of two-dimensional gradient calculation for node-centered unstructured data on regular and highly irregular grids has been made. Compared to a standard compact LSQ scheme, which uses only nearest neighbours in the stencil, the implicit scheme also includes information from neighbouring gradients, leading to a linear system to be solved. This allows the assumed polynomial or Taylor expansion in the least squares approach to be of higher order. In this study, a third-order polynomial is assumed for the ILSQ scheme. The ILSQ shows a fourth-order scaling on highly irregular mixed-element grids (quadrilaterals and triangles) with large variation in number of nearest neighbours.

In Paper D, a new seamless hybrid RANS-LES approach was derived and evaluated for free shear layer flows. The method exploits the commutation error at RANS-LES interfaces, where a commutation error term based on the hybrid length-scale is applied to reduce the grey-area in the vicinity of the RANS-LES interface. Improved results with respect to experiment is achieved in hybrid RANS-LES of the mixing shear layer flow.

The Navier-Stokes characteristic boundary conditions (NSCBC) has been implemented in Paper E and evaluated in order to reduce numerical and physical wave reflections from simulation boundaries. The implementation was assessed by the transport of an analytical vortex in the subsonic regime. The current implementation of the boundary condition give satisfactory results for a subsonic outlet, where the vortex is effectively transported with minimal reflections. For a subsonic inlet, the implementation deviates from results reported in the literature and will be further examined.

The numerical scheme, the synthetic turbulence generator, and the characteristic boundary conditions were implemented and evaluated in M-Edge, a node-centered second-order unstructured compressible finite-volume Navier-Stokes solver. The new gradients scheme was implemented in a stand-alone script, where an implementation of the gradient scheme in the aforementioned flow solver is planned.

6.2 Outlook

The work presented in this thesis and in the appended papers is by no means considered the end of research effort dedicated to these topics. The numerical scheme will be further assessed and improved in verification and validation of additional hybrid RANS-LES flow cases. The performance of the numerical scheme will be examined and evaluated on true unstructured grids, i.e. grids containing mixed elements of hexahedra, prisms and tetrahedrons, which often is encountered in industrial applications of complex aeronautical flow cases.

The implementation of the characteristic boundary conditions will be further explored. A combination of the synthetic turbulent inlet boundary condition and the characteristic boundary condition is of special interest. The ability to inject synthetic turbulence while not producing unphysical pressure waves and reflections will be examined.

The current study of the new gradient-reconstruction algorithm is planned to be followed up by an implementation in the M-Edge flow solver, where the accuracy, feasibility and robustness will be further evaluated on relevant flow cases. The gradient scheme will be extended to three dimensions and applied to scale-resolving simulations for hybrid RANS-LES applications.

References

[1] *European Aviation: A vision for 2020.* acare4europe.org.

[2] European Commission, Directorate-General for Mobility, Transport, Directorate-General for Research, and Innovation. *Flightpath 2050 : Europe's vision for aviation : maintaining global leadership and serving society's needs.* Publications Office, 2011. DOI: `doi/10.2777/50266`.

[3] Jeffrey P. Slotnick, A. Khodadoust, J. Alonso, D. Darmofal, W. Gropp, Elizabeth Lurie, and D. Mavriplis. "CFD Vision 2030 Study: A Path to Revolutionary Computational Aerosciences, NASA/CR–2014-218178". 2014.

[4] P. Spalart, W-H Jou, M. Strelets, and S. Allmaras. "Comments on the Feasibility of LES for Wings, and on a Hybrid RANS/LES Approach". *Advanced in DNS/LES.* Jan. 1997.

[5] A. Travin, M. Shur, M. Strelets, and P. Spalart. Detached-Eddy Simulations Past a Circular Cylinder. *Flow Turbulence and Combustion* **63** (Jan. 2000), 293–313. DOI: `10.1023/A:1009901401183`.

[6] P.R Spalart. Strategies for turbulence modelling and simulations. *International Journal of Heat and Fluid Flow* **21**.3 (2000), 252 –263. DOI: `https://doi.org/10.1016/S0142-727X(00)00007-2`.

[7] P. Spalart, S. Deck, M. Shur, K. Squires, M. Strelets, and A. Travin. A New Version of Detached-eddy Simulation, Resistant to Ambiguous Grid Densities. *Theoretical and Computational Fluid Dynamics* **20** (July 2006), 181–195. DOI: `10.1007/s00162-006-0015-0`.

[8] M. L. Shur, P. R. Spalart, M. Kh. Strelets, and A. K. Travin. A hybrid RANS-LES approach with delayed-DES and wall-modelled LES capabilities. *International Journal of Heat and Fluid Flow* **29**.6 (2008), 1638 –1649. ISSN: 0142-727X. DOI: `https://doi.org/10.1016/j.ijheatfluidflow.2008.07.001`.

[9] R. Schiestel and A. Dejoan. Towards a new partially integrated transport model for coarse grid and unsteady turbulent flow simulation. *Theoretical and Computational Fluid Dynamics* **18(6)** (2005), 443–468.

[10] B. Chaouat and R. Schiestel. Progress in subgrid-scale transport modelling for continuous hybrid non-zonal RANS/LES simulations. *International Journal of Heat and Fluid Flow* **30**.4 (2009), 602–616. ISSN: 0142-727X. DOI: `https://doi.org/10.1016/j.ijheatfluidflow.2009.02.021`.

[11] *PANS Turbulence Model for Seamless Transition Between RANS and LES: Fixed-Point Analysis and Preliminary Results.* Vol. Volume 2: Symposia, Parts A, B, and C. Fluids Engineering Division Summer Meeting. July 2003, pp. 1901–1909.

[12] S. S. Girimaji. Partially-Averaged Navier-Stokes Model for Turbulence: A Reynolds-Averaged Navier-Stokes to Direct Numerical Simulation Bridging Method. *Journal of Applied Mechanics* **73**.3 (Nov. 2005), 413–421.

[13] Florian M. and Yury E. "A Scale Adaptive Simulation Model using Two-Equation Models". *43rd AIAA Aerospace Sciences Meeting and Exhibit.* DOI: `10.2514/6.2005-1095`.

[14] S. H. Peng. Hybrid RANS-LES modeling based on zero- and one-equation models for turbulent flow simulation. *4th International Symposium on Turbulence and Shear Flow Phenomena* **3** (Jan. 2005), 1159–1164.

[15] S. H. Peng. "Algebraic Hybrid RANS-LES Modelling Applied to Incompressible and Compressible Turbulent Flows". Vol. 4. June 2006. DOI: `10.2514/6.2006-3910`.

[16] Sebastien Deck. Recent improvements in the Zonal Detached Eddy Simulation (ZDES) formulation. *Theoretical and Computational Fluid Dynamics* **26** (Dec. 2011), 1–28. DOI: `10.1007/s00162-011-0240-z`.

[17] Sébastien Deck and Nicolas Renard. Towards an enhanced protection of attached boundary layers in hybrid RANS/LES methods. *Journal of Computational Physics* **400** (2020), 108970. ISSN: 0021-9991. DOI: `https://doi.org/10.1016/j.jcp.2019.108970`.

[18] Tabor G. Fureby C. Mathematical and Physical Constraints on Large-Eddy Simulations. *Theoretical Computation Fluid Dynamics* **9** (1997), 85–102. DOI: `https://doi.org/10.1007/s001620050034`.

[19] M. Germano. Properties of the hybrid RANS/LES filter. *Theoretical Computation Fluid Dynamics* **17** (2004), 225–231. DOI: `https://doi.org/10.1007/s00162-004-0116-6`.

[20] Fujihiro Hamba. Analysis of filtered Navier–Stokes equation for hybrid RANS/LES simulation. *Physics of Fluids* **23**.1 (2011), 015108.

[21] Sharath S. Girimaji and Stefan Wallin. Closure modeling in bridging regions of variable-resolution (VR) turbulence computations. *Journal of Turbulence* **14**.1 (2013), 72–98. DOI: `10.1080/14685248.2012.754893`.

[22] L. Davidson. Zonal PANS: evaluation of different treatments of the RANS–LES interface. *Journal of Turbulence* **17**.3 (2016), 274–307.

[23] L. Davidson. Two-equation hybrid RANS–LES models: a novel way to treat k and at inlets and at embedded interfaces. *Journal of Turbulence* **18**.4 (2017), 291–315.

[24] S. Arvidson, L. Davidson, and S.-H. Peng. Interface methods for grey-area mitigation in turbulence-resolving hybrid RANS-LES. *International Journal of Heat and Fluid Flow* **73** (2018), 236–257. ISSN: 0142-727X. DOI: `https://doi.org/10.1016/j.ijheatfluidflow.2018.08.005`.

[25] Nitin S. Dhamankar, Gregory A. Blaisdell, and Anastasios S. Lyrintzis. Overview of Turbulent Inflow Boundary Conditions for Large-Eddy Simulations. *AIAA Journal* **56**.4 (2018), 1317–1334. DOI: `10.2514/1.J055528`.

[26] Robert H. Kraichnan. Diffusion by a Random Velocity Field. *Physics of Fluids* **13** (1970), 22–31. DOI: `10.1063/1.1692799`.

[27] P. Batten, U. Goldberg, and S. Chakravarthy. Interfacing Statistical Turbulence Closures with Large-Eddy Simulation. *AIAA Journal* **42**.3 (2004), 485–492. DOI: `10.2514/1.3496`.

[28] M.L. Shur, P.R. Spalart, M.K. Strelets, and A.K. Travin. Synthetic Turbulence Generators for RANS-LES Interfaces in Zonal Simulations of Aerodynamic and Aeroacoustic Problems. *Flow, Turbulence and Combustion* **93** (2014), 63–92. DOI: `10.1007/s10494-014-9534-8`.

[29] L. Davidson and M. Billson. Hybrid LES-RANS using synthesized turbulent fluctuations for forcing in the interface region. *International Journal of Heat and Fluid Flow* **27** (2006), 1028–1042.

[30] N. Jarrin, S. Benhamadouche, D. Laurance, and R. Prosser. A synthetic-eddy-method for generating inflow conditions for large-eddy simulations. *International Journal of Heat and Fluid Flow* **27** (2006), 585–593.

[31] N. Jarrin, R. Prosser, J.-C. Uribe, S. Benhamadouche, and D. Laurance. Reconstruction of turbulent fluctuations for hybrid RANS/LES simulations using a Synthetic-Eddy Method. *International Journal of Heat and Fluid Flow* **30** (2009), 435–442.

[32] R. Poletto, A. Revell, T. Craft, and N. Jarrin. Divergence free synthetic eddy method for embedded LES inflow boundary conditions. *Seventh international Symposium On Turbulence and Shear Flow Phenomena (TSFP-7)* (2011).

[33] A. Skillen, A. Revell, and T. Craft. Accuracy and efficiency improvements in synthetic eddy methods. *International Journal of Heat and Fluid Flow* **62** (2016), 386–394. DOI: `https://doi.org/10.1016/j.ijheatfluidflow.2016.09.008`.

[34] X.-D. Liu, S. Osher, and T. Chan. Weighted Essentially Non-oscillatory Schemes. *Journal of Computational Physics* **115**.1 (1994), 200–212. ISSN: 0021-9991. DOI: `https://doi.org/10.1006/jcph.1994.1187`.

[35] R. Abgrall. On Essentially Non-oscillatory Schemes on Unstructured Meshes: Analysis and Implementation. *Journal of Computational Physics* **114**.1 (1994), 45–58. ISSN: 0021-9991. DOI: `https://doi.org/10.1006/jcph.1994.1148`.

[36] B. Cockburn and C.-W. Shu. TVB Runge-Kutta Local Projection Discontinuous Galerkin Finite Element Method for Conservation Laws II: General Framework. *Mathematics of Computation* **52**.186 (1989), 411–435. ISSN: 00255718, 10886842.

[37] Z.J. Wang. Spectral (Finite) Volume Method for Conservation Laws on Unstructured Grids. Basic Formulation: Basic Formulation. *Journal of Computational Physics* **178**.1 (2002), 210–251. ISSN: 0021-9991. DOI: `https://doi.org/10.1006/jcph.2002.7041`.

[38] Z.J. Wang and Yen Liu. Spectral (Finite) Volume Method for Conservation Laws on Unstructured Grids: II. Extension to Two-Dimensional Scalar Equation. *Journal of Computational Physics* **179**.2 (2002), 665–697. ISSN: 0021-9991. DOI: `https://doi.org/10.1006/jcph.2002.7082`.

[39] Y. Liu, M. Vinokur, and Z. J. Wang. "Discontinuous Spectral Difference Method for Conservation Laws on Unstructured Grids". *Computational Fluid Dynamics 2004*. Ed. by C. Groth and D. W. Zingg. Berlin, Heidelberg: Springer Berlin Heidelberg, 2006, pp. 449–454.

[40] G. Lodato, P. Castonguay, and A. Jameson. Structural Wall-modeled LES Using a High-order Spectral Difference Scheme for Unstructured Meshes. *Flow, Turbulence and Combustion* **92**.1-2 (Jan. 2014). WOS:000328844400028, 579–606. DOI: `10.1007/s10494-013-9523-3`.

[41] A. Probst and S. Reuß. "Scale-Resolving Simulations of Wall-Bounded Flows with an Unstructured Compressible Flow Solver". *Progress in Hybrid RANS-LES Modelling*. Vol. 130. Springer, 2015, pp. 481–491.

[42] J. Löwe, A. Probst, T. Knopp, and R. Kessler. Low-Dissipation Low-Dispersion Second-Order Scheme for Unstructured Finite-Volume Flow Solvers. *AIAA Journal* **54** (2016). DOI: `10.2514/1.J054956`.

[43] Axel Probst, Johannes Löwe, Silvia Probst, Tobias Knopp, and Roland Kessler. Scale-Resolving Simulations with a Low-Dissipation Low-Dispersion Second-Order Scheme for Unstructured Flow Solvers. *AIAA Journal* **54** (July 2016), 1–15. DOI: `10.2514/1.J054957`.

[44] A. Jameson. Time-dependent calculations using multigrid with applications to unsteady flows past airfoils and wings. *AIAA Paper* 91-1596 (1991).

[45] F Ducros, Valerie Ferrand, Nicoud Franck, C Weber, Denis Darracq, C Gacherieu, and Thierry Poinsot. LES of the Shock/Turbulence Interaction. *Journal of Computational Physics* **152** (July 1999), 517–549. DOI: `10.1006/jcph.1999.6238`.

[46] P.R Spalart. Strategies for turbulence modelling and simulations. *International Journal of Heat and Fluid Flow* **21**.3 (2000), 252–263. ISSN: 0142-727X. DOI: `https://doi.org/10.1016/S0142-727X(00)00007-2`.

[47] A. Favré. "Problems of Hydrodynammics and Continuum Mechanics". *Society for Industrial and Applied Mathematics*. 1969, pp. 231–266.

[48] P. Spalart and S. Allmaras. "A one-equation turbulence model for aerodynamic flows". *30th Aerospace Sciences Meeting and Exhibit*. DOI: `10.2514/6.1992-439`.

[49] B. Aupoix and P.R. Spalart. Extensions of the Spalart–Allmaras turbulence model to account for wall roughness. *International Journal of Heat and Fluid Flow* **24**.4 (2003). Selected Papers from the Fifth International Conference on Engineering Turbulence Modelling and Measurements, 454–462. ISSN: 0142-727X.

[50] Florian Menter, M. Kuntz, and RB Langtry. Ten years of industrial experience with the SST turbulence model. *Heat and Mass Transfer* **4** (Jan. 2003).

[51] W.P Jones and Brian Launder. The prediction of laminarization with a two-equation model of turbulence. *International Journal of Heat and Mass Transfer* **15** (Feb. 1972), 301–314. DOI: `10.1016/0017-9310(72)90076-2`.

[52] D. Wilcox. *Turbulence Modeling for CFD (Third Edition)*. Jan. 2006.

[53] J. Smagorinsky. General circulation experiments with the primitive equations: I. The basic experiment. *Monthly Weather Review* **91**.3 (Mar. 1963), 99–164. DOI: `10.1175/1520-0493(1963)091<0099:GCEWTP>2.3.CO;2`.

[54] F. Nicoud and F. Ducros. Subgrid-scale stress modelling based on the square of the velocity gradient tensor. *Flow, Turbulence and Combustion* **63** (1999), 183–200.

[55] Franck Nicoud, Hubert Baya Toda, Olivier Cabrit, Sanjeeb Bose, and Jungil Lee. Using singular values to build a subgrid-scale model for large eddy simulations. *Physics of Fluids* **23**.8 (2011), 085106. DOI: `10.1063/1.3623274`.

[56] P. Spalart, W-H Jou, M. Strelets, and S. Allmaras. "Comments on the Feasibility of LES for Wings, and on a Hybrid RANS/LES Approach". Jan. 1997, pp. 137–147.

[57] Mikhail Gritskevich, Andrey Garbaruk, Jochen Schütze, and Florian Menter. Development of DDES and IDDES Formulations for the k- Shear Stress Transport Model. *Flow, Turbulence and Combustion* **88** (Apr. 2012). DOI: `10.1007/s10494-011-9378-4`.

[58] Michael Shur, Philippe Spalart, Michael Strelets, and Andrey Travin. An Enhanced Version of DES with Rapid Transition from RANS to LES in Separated Flows. *Flow, Turbulence and Combustion* **95** (Dec. 2015). DOI: `10.1007/s10494-015-9618-0`.

[59] Thomas S. Lund, Xiaohua Wu, and Kyle D. Squires. Generation of Turbulent Inflow Data for Spatially-Developing Boundary Layer Simulations. *Journal of Computational Physics* **140**.2 (1998), 233–258. ISSN: 0021-9991. DOI: `https://doi.org/10.1006/jcph.1998.5882`.

[60] M. Carlsson, L. Davidson, S.H. Peng, and S. Arvidson. "Investigation of Turbulence Injection Methods in Compressible Flow Solvers in Large Eddy Simulation". *2022 AIAA SciTech Forum*. Jan. 2022. DOI: `10.2514/6.2022-0483`.

[61] F. Mathey. Aerodynamic noise simulation of the flow past an airfoil trailing-edge using a hybrid zonal RANS-LES. *Computers & Fluids* **37** (2007), 836–843.

[62] S. Schmidt and M Breuer. Source term based synthetic turbulence inflow generator for eddy-resolving predictions of an airfoil flow including a laminar separation bubble. *Computer & Fluids* **146** (2017), 1–22.

[63] A. Probst. Implementation and assesment of the Synthetic-Eddy Method in an unstructured compressible flow solver. *Progress in Hybrid RANS-LES Modelling. NNFMMD* **137** (2018), 91–101.

[64] Donald P. Rizzetta and Daniel J. Garmann. Wall-Resolved Large-Eddy Simulation of Smooth-Body Separated Flow. *International Journal of Computational Fluid Dynamics* **36**.1 (2022), 1–20. DOI: `10.1080/10618562.2022.2087873`.

[65] M. Carlsson, S. Wallin, L. Davidson, S.H. Peng, and S. Arvidson. "Seamless Interface Methods for Grey-Area Mitigation in Scale-Resolving Hybrid RANS-LES". *DLES13 2022*. 2022.

[66] P. Eliasson. "Edge, a Navier–Stokes solver for unstructured grids". *Finite Volumes for Complex Applications*. Vol. III. CP849. 2002, pp. 527–534.

[67] P. Eliasson and P. Weinerfelt. "Recent applications of the flow solver Edge". *7th Asian CFD Conference*. CP849. 2007.

[68] J. C. Kok. A high-order low-dispersion symmetry-preserving finite volume method for compressible flow on curvilinear grids. *Journal of Computational Physics* **228** (2009), 6811–6832. DOI: `https://doi.org/10.1016/j.jcp.2009.06.015`.

[69] R. C. Swanson and E. Turkel. On the central-difference and upwind schemes. *Journal of Computational Physics* **101** (1992), 292–306. DOI: `https://doi.org/10.1016/0021-9991(92)90007-L`.

[70] Antony Jameson. Origins and Further Development of the Jameson–Schmidt–Turkel Scheme. *AIAA Journal* **55**.5 (2017), 1487–1510. DOI: `10.2514/1.J055493`.

[71] P. Eliasson, S. Eriksson, and J. Nordström. The influence of weak and strong solid wall boundary conditions on the convergence to steady-state of the navier-stokes equations. *AIAA Paper* 2009-3551 (2009).

[72] A. Jameson, W. Schmidt, and E. Turkel. "Numerical solution of the Euler equations by finite volume methods using Runge Kutta time stepping schemes". *14th Fluid and Plasma Dynamics Conference*. 1981. DOI: `10.2514/6.1981-1259`.

[73] S. Langer. Investigations of a compressible second order finite volume code towards the incompressible limit. *Computer and Fluids* **149** (2017), 119–137.

[74] M. Carlsson, L. Davidson, S.H. Peng, and S. Arvidson. “Parametric Investigation of Low-dissipation Low-dispersion Schemes for Unstructured Flow Solvers in Large Eddy Simulation”. *2020 AIAA SciTech Forum.* 2020.

[75] S. K. Godunov and I. Bohachevsky. Finite difference method for numerical computation of discontinuous solutions of the equations of fluid dynamics. *Matematičeskij sbornik* **47(89)**.3 (1959), 271–306.

[76] E. Turkel, R. Radespiel, and N. Kroll. Assessment of preconditioning methods for multidimensional aerodynamics. *Computer and Fluids* **26** (1997), 613–643. DOI: `https://doi.org/10.1016/S0045-7930(97)00013-3`.

[77] M. Carlsson, L. Davidson, S.H. Peng, and S. Arvidson. “Higher Order Gradients on Unstructured Meshes Using Compact Formulation for Node-Centered Schemes”. *2022 AIAA Aviation Forum.* June 2022. DOI: `10.2514/6.2022-4156`.

[78] Dimitri Mavriplis. “Revisiting the Least-Squares Procedure for Gradient Reconstruction on Unstructured Meshes”. *16th AIAA Computational Fluid Dynamics Conference.* DOI: `10.2514/6.2003-3986`.

[79] Fan Zhang. *A vertex-weighted-Least-Squares gradient reconstruction.* 2017. DOI: `10.48550/ARXIV.1702.04518`.

[80] Hiroaki Nishikawa and Jeffery A. White. An efficient cell-centered finite-volume method with face-averaged nodal-gradients for triangular grids. *Journal of Computational Physics* **411** (2020), 109423. ISSN: 0021-9991. DOI: `https://doi.org/10.1016/j.jcp.2020.109423`.

[81] Hong Luo, Joseph D. Baum, and Rainald Löhner. A discontinuous Galerkin method based on a Taylor basis for the compressible flows on arbitrary grids. *Journal of Computational Physics* **227**.20 (2008), 8875–8893. ISSN: 0021-9991. DOI: `https://doi.org/10.1016/j.jcp.2008.06.035`.

[82] G. Comte-Bellot and S. Corrsin. Simple eulerian time correlation of full- and narrow-band velocity signals in grid-generated "isotropic" turbulence. *Journal of Fluid Mechanics* **48** (1971), 943–13. DOI: `10.1017/S0022112071001599`.

[83] E. Fares and W. Schröder. A general one-equation turbulence model for free shear and wall-bounded flows. *Flow, Turbulence and Combustion* **73** (2005), 187–215. DOI: `https://doi.org/10.1007/s10494-005-8625-y`.

[84] R. Moser, J. Kim, and N. Mansour. Direct numerical simulation of turbulent channel flow up to $Re = 590$. *Physics of Fluids* **11**.4 (1999), 943–13. DOI: `10.1006/1.869966`.

[85] Davide Modesti and Sergio Pirozzoli. Reynolds and Mach number effects in compressible turbulent channel flow. *International Journal of Heat and Fluid Flow* **59** (2016), 33–49. DOI: `https://doi.org/10.1016/j.ijheatfluidflow.2016.01.007`.

[86] G. N. Coleman, J. Kim, and R. D. Moser. A numerical study of turbulent supersonic isothermal-wall channel flow. *Journal of Fluid Mechanics* **305** (1995), 159–183. DOI: `10.1017/S0022112095004587`.

[87] H. Reichardt. Vollständige Darstellung der turbulenten Geschwindigkeitsverteilung in glatten Leitungen. *ZAMM - Journal of Applied Mathematics and Mechanics / Zeitschrift für Angewandte Mathematik und Mechanik* **31**.7 (1951), 208–219. DOI: `https://doi.org/10.1002/zamm.19510310704`.

[88] E. R. Van Driest. Turbulent Boundary Layer in Compressible Fluids. *Journal of the Aeronautical Sciences* **18**.3 (1951), 145–160. DOI: `10.2514/8.1895`.

[89] J. L. Herrin and J. C. Dutton. Supersonic base flow experiments in the near wake of a cylindrical afterbody. *AIAA Journal* **32**.1 (1994), 77–83. DOI: `10.2514/3.11953`.

[90] Werner Haase, Marianna Braza, and Alistair Revell. *DESider: A European effort on hybrid RANS-LES Modelling (Notes on numerical fluid mechanics multidisciplinary design, Vol. 103).* Vol. 103. Jan. 2009. ISBN: 978-3-540-92772-3. DOI: `10.1007/978-3-540-92773-0`.

[91] Ekaterina Guseva, Andrey Garbaruk, and Michael Strelets. Assessment of Delayed DES and Improved Delayed DES Combined with a Shear-Layer-Adapted Subgrid Length-Scale in Separated Flows. *Flow, Turbulence and Combustion* **98** (Mar. 2017). DOI: `10.1007/s10494-016-9769-7`.

[92] Franck Simon, Sébastien Deck, Philippe Guillen, and Pierre Sagaut. Reynolds-Averaged Navier-Stokes/Large-Eddy Simulations of Supersonic Base Flow. *AIAA Journal* **44**.11 (2006), 2578–2590. DOI: `10.2514/1.21366`.

[93] C. Ollivier-Gooch, A. Nejat, and Krzysztof M. Obtaining and Verifying High-Order Unstructured Finite Volume Solutions to the Euler Equations. *AIAA Journal* **47**.9 (2009), 2105–2120. DOI: `10.2514/1.40585`.

[94] H. Nishikawa. From hyperbolic diffusion scheme to gradient method: Implicit Green–Gauss gradients for unstructured grids. *Journal of Computational Physics* **372** (2018), 126–160. ISSN: 0021-9991. DOI: `https://doi.org/10.1016/j.jcp.2018.06.019`.

[95] Charles Mocket, W Haase, and F Thiele. "Go4hybrid: An European Initiative for Improved Hybrid RANS-LES Modelling". *Progress in Hybrid RANS-LES Modelling.* Ed. by S Girimaji, W Haase, Shia-Hui Peng, and Dieter Schwamborn. Vol. 130. Cham: Springer International Publishing, 2015, pp. 299–303.

[96] Sébastien Deck, Pierre-Elie Weiss, and Nicolas Renard. A rapid and low noise switch from RANS to WMLES on curvilinear grids with compressible flow solvers. *Journal of Computational Physics* **363** (2018), 231–255. ISSN: 0021-9991. DOI: `https://doi.org/10.1016/j.jcp.2018.02.028`.

[97] Hassan M Nagib, Kapil A Chauhan, and Peter A Monkewitz. Approach to an asymptotic state for zero pressure gradient turbulent boundary layers. *Philosophical Transactions of the Royal Society A: Mathematical, Physical and Engineering Sciences* **365**.1852 (2007), 755–770.

[98] Philipp Schlatter and Ramis Örlü. Assessment of direct numerical simulation data of turbulent boundary layers. *Journal of Fluid Mechanics* **659** (Sept. 2010), 116 –126.

[99] Charles Mockett, Marian Fuchs, Andrey Garbaruk, Michael Shur, Philippe Spalart, Michael Strelets, Frank Thiele, and Andrey Travin. "Two Non-zonal Approaches to Accelerate RANS to LES Transition of Free Shear Layers in DES". *Progress in Hybrid RANS-LES Modelling.* Ed. by Sharath Girimaji, Werner Haase, Shia-Hui Peng, and Dieter Schwamborn. Cham: Springer International Publishing, 2015, pp. 187–201. ISBN: 978-3-319-15141-0. DOI: `https://doi.org/10.1007/978-3-319-15141-0_15`.

[100] Delville J. “La décomposition orthogonale aux valeurs propres et l’analyse de l’organisation tridimensionnelle des écoulements turbulents ci saillés libre”. PhD thesis. Université de Poitier, 1995.

[101] Florian Setzwein, Peter Ess, and Peter Gerlinger. An implicit high-order k-exact finite-volume approach on vertex-centered unstructured grids for incompressible flows. *Journal of Computational Physics* **446** (2021), 110629. ISSN: 0021-9991. DOI: `https://doi.org/10.1016/j.jcp.2021.110629`.

[102] B. de Laage de Meux, B. Audebert, R. Manceau, and R. Perrin. Anisotropic linear forcing for synthetic turbulence generation in large eddy simulation and hybrid RANS/LES modeling. *Physics of Fluids* **27**.3 (2015), 035115. DOI: `10.1063/1.4916019`.

[103] Sanjiva K. Lele. Compact finite difference schemes with spectral-like resolution. *Journal of Computational Physics* **103**.1 (1992), 16–42. ISSN: 0021-9991. DOI: `https://doi.org/10.1016/0021-9991(92)90324-R`.

[104] M. Carlsson, L. Davidson, S.H. Peng, and S. Arvidson. “Investigation of Low-dissipation Low-dispersion Schemes for Incompressible and Compressible Flows in Scale-Resolving Simulations”. Submitted for journal publication.

[105] M. Carlsson, L. Davidson, S.H. Peng, and S. Arvidson. *Implementation of Non-reflecting Inlet and Outlet Boundary Conditions in the Subsonic Regime for a Node-Based Compressible Solver*. Tech. rep. Chalmers University of Technology, Göteborg, Sweden, Technical Report, 2021.

[106] S. Arvidson, M. Carlsson, and S. Nilsson. “Effect of LES Length Scale and Numerical Scheme in Hybrid RANS-LES of Free Shear Layer Flows”. *International Council of Aeronauutical Sciences (ICAS), Stockholm*. 2022.

Part II
Appended Papers

Paper A

Investigation of Low-dissipation Low-dispersion Schemes for Incompressible and Compressible Flows in Scale-Resolving Simulations

M. Carlsson, L. Davidson, S.H. Peng, and S. Arvidson. "Investigation of Low-dissipation Low-dispersion Schemes for Incompressible and Compressible Flows in Scale-Resolving Simulations". Submitted for journal publication

Investigation of Low-dissipation Low-dispersion Schemes for Incompressible and Compressible Flows in Scale-Resolving Simulations

Magnus Carlsson[a], Lars Davidson[a], Shia-Hui Peng[a,b], Sebastian Arvidson[a,c]

[a]*Division of Fluid Dynamics and Maritime Sciences, Chalmers University of Technology, Gothenburg, SE-412 96, SWEDEN*
[b]*Swedish Defence Research Agency, FOI, Stockholm, SE-16490, SWEDEN*
[c]*Propulsion Systems, Saab Aeronautics, Linkoping, SE-581 88, SWEDEN*

Abstract

A comprehensive study is conducted on a second-order low-dissipation low-dispersion (LD2) scheme in scale-resolving simulations of both incompressible and compressible flows, using a node-based unstructured CFD solver. The scheme deploys a higher order central reconstruction of the face values (up to fourth-order on structured meshes) and a matrix dissipation formulation to reduce the dispersive and dissipative numerical errors. The LD2 scheme is examined for compressible flow cases involving shock discontinuities, LD2-Compressible (LD2C), and is verified in a classical shock-tube problem. The scheme is then further verified in Large-Eddy Simulations (LES) of decaying isotropic turbulence (DIT) in comparison with available experimental data. It is shown that in scale-resolving simulations, the LD2C scheme is able to significantly improve the prediction as compared to a conventional second-order central scheme. The scheme is then further assessed and verified in hybrid Reynolds-Averaged Navier-Stokes (RANS)-LES computations for the subsonic and supersonic turbulent channel flow, where excellent agreement with reference DNS and correlations are observed. Moreover, a supersonic base flow is simulated using hybrid RANS-LES, where improved predictions are observed. The LD2C scheme exploits a shock sensor incorporating vorticity and is shown to improve the prediction of the resolved shear stress in the shear layer of compression.

Keywords:
Low-dissipation low-dispersion scheme, Scale-resolving simulations,

Turbulent flows, Compressible flows

1. Introduction

Hybrid RANS-LES modeling (HRLM) is a computational technique considered to be more accurate than RANS and computationally more affordable than LES for the aeronautical industry. The key feature of HRLM is the RANS-type behavior in the vicinity of a solid boundary combined with LES in regions far away from the wall. Commonly used HRLM methods stem from the Detached Eddy Simulation (DES) by Spalart et. al [1] and extended by boundary-layer shielding, e.g. Delayed DES, which is considered to be the most mature for industrial use. A wide variety of additional methods exist such as Improved DDES (IDDES) [2], HYB0 [3, 4], PANS [5] and ZDES [6].

The turbulence-resolving capability in LES mode of DES and hybrid RANS-LES approaches depends strongly on the choice of the LES length scale. In flows involving free shear layers, the choice of LES length scale is crucial in order to mitigate the "grey-area" problem, which delays the development of LES-resolved turbulence in the initial LES region adjacent to the RANS-LES interface. As a result, the accuracy of scale-resolving simulation in the focusing LES region may become significantly degraded. In order to have effective transition between the RANS and the LES region in free shear layers, Grey-Area Mitigation (GAM) methods modifying the LES-length scale may be employed [6, 7].

To accurately capture resolved turbulent fluctuations, proper resolution of LES requires a minimal dissipative and minimal dispersion numerical scheme. A low-dissipative finite-volume scheme suitable for unstructured compressible solvers was developed by Probst et. al [8], where the added numerical dissipation was effectively reduced and demonstrated for wall-bounded scale resolving flow. The numerical dissipation of the scheme is controlled by a Jameson matrix dissipation scheme [9], in order to reduce the level of added numerical dissipation suitable for scale-resolving simulations. To further improve the capabilities of the numerical scheme, a low-dissipation and low-dispersion (LD2) scheme was formulated by Löwe et al. [10], where a higher order extrapolation of the face values is used to control and reduce the numerical dispersion errors.

A thorough study similar to [8, 10] was conducted in Carlsson et al. [11] using the LD2 scheme in the compressible flow solver M-Edge [12] (former CFD solver Edge), which is an unstructured finite-volume Navier-Stokes solver used to investigate complex aeronautical flows. A number of previous examples of aeronautical relevant cases using HRLM simulated with the solver have been well demonstrated, e.g. the flow over rudimentary landing gear [13], transonic duct flow [14, 15] and flow around a three-element airfoil in high-lift configuration [16]. In the previous work [11], the LD2 scheme was applied to low-speed (nearly incompressible) turbulent flows, showing good results in LES of the turbulent channel flow case for a moderate Reynolds number and the decaying isotropic turbulence (DIT) in comparison to DNS and experiments.

In this work, we seek to adapt the LD2 scheme for scale-resolving of compressible flows. In addition to a verification of the LD2 scheme in hybrid RANS-LES of subsonic turbulent channel flow and DIT, three compressible flow cases are also considered here. The Sod shock tube case, hybrid RANS-LES of the super sonic channel flow and the supersonic base flow (experimentally investigated by Herrin and Dutton [17]). These test cases are chosen to adapt and evaluate the numerical scheme in compressible scale-resolving simulations.

The shock capturing capabilities of the numerical scheme is important, and should not interfere with the scale-resolving properties. In the original formulation by Jameson, a sensor similar to the second derivative of the pressure was formulated to identify shock-waves [9]. A different variant of sensor targeting to minimize excessive dissipation in shock/turbulence interaction in LES was formulated by Ducros [18]. The sensor is a slight modification to Jameson's sensor and involves the local flow vorticity to identify regions with resolved turbulence.

The paper is organized as follows. The numerical method is outlined in Section 2 and the turbulence models used in the paper is presented in Section 3. Results and evaluation of the numerical test are then presented in Section 4. Finally, the work is summarized and concluded in Section 5.

2. Numerical Methods

The CFD solver used in the computations is the M-Edge code, which is an edge- and node-based Navier-Stokes flow solver applicable for both structured and unstructured grids [12, 19]. The finite volume discretization is obtained by applying the integral formulation of the governing equations to a control volume surrounding node i,

$$\Delta V_i \frac{\mathrm{d}q_i}{\mathrm{d}t} + \sum_{j=1}^{nb_i} F_{ij} S_{ij} + \sum_{j=1}^{nb_i} G_{ij} S_{ij} = 0, \tag{1}$$

where ΔV_i is the volume surrounding node i, $q_i = (\rho, \rho u, \rho v, \rho w, \rho E)$ are the unknown conservative variables at the node, F_{ij} and G_{ij} are the cell face convective and viscous fluxes between nodes i and j, and S_{ij} is the cell face area connecting the dual control volumes of the nodes. The number of neighbours adjacent to node i is denoted by nb_i. Equation (1) is integrated in time using a 2nd-order backward Euler scheme, together with a dual-time stepping methodology using an explicit low-storage multistage Runge-Kutta scheme accelerated further by full-approximation storage (FAS) multigrid [9]. The boundary conditions have a weak formulation in which a set of temporary flow variables are computed and used in the calculations of the boundary flux added to the residual. The residual then updates all unknown variables including the boundary values [20].

Since the dispersion and dissipation, due to the convective term, are of interest, a detailed description of the theory and implementation follows below. The convective fluxes are discretized according to the central skew-symmetric energy preserving formulation of Kok [21], together with a Jameson-Schmidt-Turkel (JST) artifical matrix dissipation [22, 23]

$$F_{ij} = \tilde{F}_{ij}(q_L, q_R) - D_{ij}(q), \tag{2}$$

where q_L, q_R are extrapolated face values according to a central scheme for reducing dispersion errors [10], and the subscripts L and R refer to the left and right states at the cell face ij. The matrix dissipation D_{ij} is the JST artificial viscosity term included for increased numerical stability on hybrid grids, since the central skew-symmetric formulation by Kok does not provide any numerical dissipation to the scheme.

2.1. Numerical Dispersion

The skew-symmetric energy preserving formulation by Kok [21] relies on a particular discretization of the convective terms in the mean flow equations such that good dispersion properties are obtained. The averaged cell face values in the convective numerical flux are formulated as

$$\tilde{F}_{ij} = \begin{bmatrix} (\overline{\rho u})_{ij} \\ (\overline{\rho u}\bar{u} + \bar{p}I)_{ij} \\ (\overline{\rho u}\tilde{E} + \widetilde{pu})_{ij} \end{bmatrix} = \begin{bmatrix} \frac{1}{2}(\rho_L u_L + \rho_R u_R) \\ \frac{1}{2}(\rho_L u_L + \rho_R u_R)\frac{1}{2}(u_L + u_R) + \frac{1}{2}(p_L + p_R)I \\ \frac{1}{2}(\rho_L u_L + \rho_R u_R)\left[\frac{1}{2}(u_L u_R) + \frac{C_L C_R}{\gamma(\gamma-1)}\right] + \frac{1}{2}(u_L p_R + u_R p_L) \end{bmatrix} \tag{3}$$

The reader is referred to [10, 21] for the particular choice of averaging ($(\bar{\cdot})$ and $(\tilde{\cdot})$) in Eq. (3). For the conventional central flux the subscripts L, R are given by the respective nodal values. In the low-dispersion scheme by Löwe et al. [10], the left and right face values of the velocity and pressure are extrapolated from the left and right node values, respectively, by using the gradient of the variable in the nodes, i.e.

$$\begin{aligned} u_L =& u_i + \alpha \nabla u_i \cdot \mathbf{d}_{ij}, \quad u_R = u_j - \alpha \nabla u_j \cdot \mathbf{d}_{ij} \\ p_L =& p_i + \alpha \nabla p_i \cdot \mathbf{d}_{ij}, \quad p_R = p_j - \alpha \nabla p_j \cdot \mathbf{d}_{ij} \end{aligned} \tag{4}$$

where $\mathbf{d}_{ij}$ is the distance vector between the two nodes. In this work, the gradients are evaluated with a Green-Gauss' approximation. α is a parameter that can be chosen to reduce the dispersion error for a specific range of wave numbers. Note that the speed of sound and density is not extrapolated in the original scheme, since the effects of extrapolation of these quantities were argued to be small as reported by Löwe et al. [10]. However, Löwe's formulation was only evaluated for subsonic flow cases. For compressible flow cases involving shock waves, see Section 4, we evaluate further the extrapolation of density and speed of sound as well in the following form,

$$\begin{aligned} \rho_L = \rho_i + \alpha \nabla \rho_i \cdot \mathbf{d}_{ij}, \quad \rho_R = \rho_j - \alpha \nabla \rho_j \cdot \mathbf{d}_{ij} \\ c_L = c_i + \alpha \nabla c_i \cdot \mathbf{d}_{ij}, \quad c_R = c_j - \alpha \nabla c_j \cdot \mathbf{d}_{ij} \end{aligned} \tag{5}$$

A theoretical analysis of the dispersion properties of α for an analytical case is given in Section 2.3.

2.2. Numerical Dissipation

2.2.1. Matrix Dissipation

The artificial matrix dissipation [22] in Eq. (2) is given by

$$D_{ij}(q) = \left|\frac{\partial F}{\partial q}\right|_{ij} [\varepsilon_{ij}^{(2)}(q_i - q_j) + \varepsilon_i^{(4)} L(q_i) - \varepsilon_j^{(4)} L(q_j)], \tag{6}$$

where L is the undivided Laplacian and the convective flux Jacobian $|\frac{\partial F}{\partial q}|_{ij} = R_{ij}|\Lambda|_{ij}R_{ij}^{-1}$ is computed and diagonalized according to Langer [24]. A Harten type entropy fix [25] is employed to prevent vanishing eigenvalues of $|\Lambda|_{ij}$, and are limited so that they are larger than 30% of the spectral radius. The second order dissipation scaling parameter $\varepsilon_{ij}^{(2)}$ in Eq. (6) is only active in the presence of strong discontinuities (i.e. for high speed flows with shocks) and can be omitted when low Mach number flow cases are considered. The parameters $\varepsilon_i^{(4)}$ and $\varepsilon_j^{(4)}$ are given by, respectively,

$$\begin{aligned} \varepsilon_i^{(4)} &= \varepsilon^{(4)}\left(\frac{\lambda_i}{2\lambda_{0ij}}\right)^p, \quad \varepsilon_j^{(4)} = \varepsilon^{(4)}\left(\frac{\lambda_j}{2\lambda_{0ij}}\right)^p, \\ \lambda_i &= \sum_{k=1}^{nb_i}(u_{ik}n_{ik} + c_{ik})S_{ik}, \quad \lambda_{0ij} = (|u_{ij}n_{ij}| + c_{ij})S_{ij}, \end{aligned} \tag{7}$$

where $u_{ij} = (u_i + u_j)/2$ and $c_{ij} = (c_i + c_j)/2$ denote, respectively, the flow velocity and speed of sound at the control volume face. The normal direction of the control surface to the edge between nodes i and j is denoted by n_{ij}. The purpose of the additional scaling with the local convective eigenvalues (λ_i, λ_j and λ_{0ij}) in Eq. (7) is to apply extra dissipation for highly stretched cells in direction of the cell stretching, for example in near wall boundary layer flows or free shear layer flows resolved by an anisotropic grid. This is a desired effect to improve the robustness of the discretization [26]. The factor p is chosen to have a close resemblance with the Martinelli [27] eigenvalue scaling for structured grids ($p = 0.3$). Note that by setting $p = 0$ we have $\varepsilon_i^{(4)} = \varepsilon_j^{(4)} = \varepsilon^{(4)}$. The fourth-order scaling parameter

$$\varepsilon^{(4)} = \max[0, \kappa^{(4)} - \varepsilon_{ij}^{(2)}] \tag{8}$$

is deactivated in the vicinity of shocks. Here, $\kappa^{(4)}$ is a global scaling parameter, where a typical value of $\kappa^{(4)}$ used in RANS simulations varies often with a value set between $1/128 - 1/64$ [24]. These values gives extra numerical dissipation to dampen numerical errors and converge to a steady state simulation quickly. However, as shown by Probst et al. [8, 28] and Carlsson et al. [11], these values are not suitable for scale-resolving simulations and will severely dissipate resolved turbulence. LES of decaying grid turbulence and turbulent channel flow indicate that 1/512 to 1/1024 is a suitable range for $\kappa^{(4)}$ to allow a good trade off between convergence and numerical accuracy in scale-resolving simulations. The dissipation properties of this parameter is theoretically analyzed in Section 2.3 and is further explored in hybrid RANS-LES simulations in Section 4.

2.2.2. Low Mach Number Preconditioning

To enhance the convergence properties and accuracy for low Mach number flows the convective flux Jacobian in Eq. (6) is modified,

$$\left|\frac{\partial F}{\partial q}\right|_{ij} \longrightarrow P_{ij}^{-1}\left|\frac{\partial PF}{\partial q}\right|_{ij} \tag{9}$$

where the preconditioning matrix P_{ij} is based on Turkel's formulation [29]. The matrix $\left|\frac{\partial PF}{\partial q}\right|_{ij}$ in Eq. (9) is approximated by $\left|\frac{\partial \tilde{F}}{\partial q}\right|_{ij}$ [24], where the local speed of sound c in $\left|\frac{\partial F}{\partial q}\right|_{ij}$ has been replaced with an artificial speed of sound

$$\tilde{c} = \frac{c}{2}\sqrt{(1+\beta)^2 M^2 + 4\beta(1-M^2)}. \tag{10}$$

where M is the local Mach number on the cell face. Both the precondtioning matrix and the convective flux Jacobian are functions of the local speed of sound given in Eq. (10), where the rescaled speed of sound decreases the difference between the largest and the smallest eigenvalues of the convective flux Jacobian in Eq. (9) for low Mach number flows. The function of preconditioning is controlled by

$$\beta = \min[\max(M^2, KM_\infty^2), 1] \tag{11}$$

where $\beta = 1$ gives no preconditioning, M_∞ is the free-stream Mach number and K is a tuning coefficient. In Eq. (9) the preconditioning can be turned off by setting K to a very large value ($K \to \infty$) to ensure $\beta = 1$. Typical values of K previously used in M-Edge vary between 1 and 4 for RANS simulations [30].

2.2.3. Shock Capturing Methods

For high speed flows the flow solver needs to be able to identify discontinuities in the presence of shock waves. A standard pressure-based sensor by Jameson [31] is often deployed, reading

$$\varepsilon_{ij}^{(2)} = \min[\kappa^{(2)} \max(\Psi_i, \Psi_j), 0.5] \tag{12}$$

where the sensor

$$\Psi_i = \frac{\left|\sum_{k=1}^{nb_i}(p_i - p_k)\right|}{\sum_{k=1}^{nb_i}(p_i + p_k)} \tag{13}$$

identifies regions with large pressure differences, e.g. shock waves, and returning a value close to unity. The numerical scheme is then reduced to a first-order scheme through Eqs. (12), (8) and (6). This is necessary since according to the work by Godunov [32], any monotonicity preserving numerical scheme in the presence of shock waves can be at most first-order accurate. For regions with a smooth continuously varying flow field the sensor given by Eq. (13) tends to be switched off and the scheme follows the fourth-order dissipation in Eq. (6). The value 0.5 in Eq. (12) limits the scheme to behave as a first-order upwind scheme in shock regions. The sensitivity of the sensor is modified through $\kappa^{(2)}$, where the value is tuned in a shock-tube case (Section 4.1) in this work.

A different sensor targeted for minimizing excessive dissipation in shock-turbulence interaction in LES was formulated by Ducros as [18]

$$\Phi_i = \frac{(\nabla \cdot \mathbf{u})^2}{(\nabla \cdot \mathbf{u})^2 + (\nabla \times \mathbf{u})^2 + \epsilon} \tag{14}$$

where the sensor includes the dilation and the magnitude of vorticity of the flow field. Here, ϵ is a small number (10^{-30}) in order to avoid singularities. This limiter reduces the added dissipation in regions with resolved turbulence where the vortex motion becomes intensive. However, Eq. (14) alone is not capable of separating large dilatations (shocks) from small dilatational disturbances. Also, in flow regions where vorticity is negligible even very small dilatations will activate the switch. This can add dissipation where it is not wanted and can also introduce spurious oscillations, which both can degrade the accuracy of the solution. In order to mitigate these problems, the sensor given by Eq. (14) was multiplied [18] by the standard Jameson's sensor given by Eq. (13)

$$\varepsilon_{ij}^{(2)} = \min[\kappa^{(2)} \max(\Psi_i \Phi_i, \Psi_j \Phi_j), 0.5] \tag{15}$$

which was shown to effectively distinguish between shocks and compressible turbulence [18].

2.3. Analysis of Numerical Scheme

The dispersion and dissipation relations for the convective scheme can be analyzed by performing a semi-discrete stability analysis of a one-dimensional convection equation as discussed by Hirsch [33]. The numerical error of the discretization due to the convective term can be cast into a purely dissipative term, ε_D, and a purely dispersive term, ε_Φ, as a function of the wave numbers that the grid can resolve, $\phi \in [0, \pi]$. Here, values $\varepsilon_D < 1$ correspond to physical waves being dissipated by the convective scheme, and deviations from $\varepsilon_\Phi = 1$ corresponds to physical waves being transported with a negative ($\varepsilon_\Phi < 1$) or positive ($\varepsilon_\Phi > 1$) group velocity. The contribution to the dissipative error for smooth flows is a function of the fourth-order dissipation scaling parameter $\kappa^{(4)}$ (Eq. (8)), and the contribution to the dispersive error is a function of α (Eq. (4)). The corresponding errors for a set of chosen values are presented in Fig. 1.

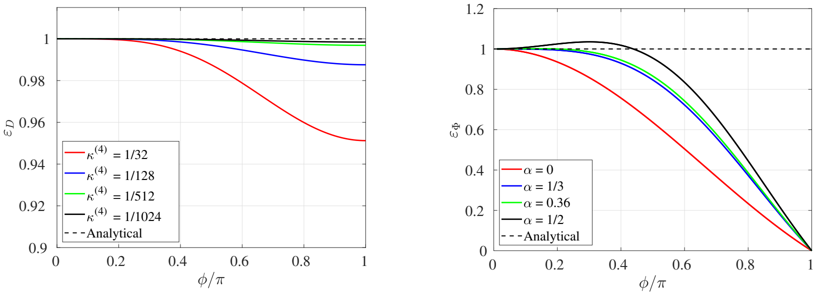

(a) Dissipation.

(b) Dispersion.

Figure 1: Dissipation and dispersion relations.

The added numerical dissipation can effectively be lowered by reducing the value of $\kappa^{(4)}$, as indicated in Fig. 1(a). If one assumes that the added dissipation to the simulation should be only due to the SGS scales, it is therefore desirable to use as low value as possible of $\kappa^{(4)}$ in order to avoid dissipation of the smaller scales that the grid can resolve. However, in practical application some amount of numerical dissipation is often needed ($\kappa^{(4)} > 0$) in order to reach convergence.

The dispersion error is presented in Fig. 1(b). Taylor expansion shows that one has to choose $\alpha = 1/3$ to achieve fourth-order approximation of the derivative, which is the theoretically highest order for any α. The value

$\alpha = 0$ yields a pure second-order central approximation. In [10], Löwe et al. investigated the values of $\alpha = 0.36$ and $\alpha = 0.4$, which showed better performance than $\alpha = 1/3$ in resolving features on a coarse grid for an analytical case, while admitting higher dispersion errors on finer grids compared to $\alpha = 1/3$. They concluded that $\alpha = 0.36$ gave the most favorable cancellation properties [10] and used it in a set of studies [28, 34, 35] for scale-resolving simulations. However, the dispersion relation in Fig. (1) indicates that there is a small difference between $\alpha = 0.36$ optimized by Löwe et al. [10] and the value $\alpha = 1/3$ that gives the theoretically highest order. In Carlsson et al. [11], LES of fully developed channel flow and DIT using the LD2 scheme showed that in practical applications there is little difference between the values of $\alpha > 0$ shown in Fig. 1. Therefore, $\alpha = 1/3$ is chosen in the following analysis.

3. Turbulence Modeling

For the hybrid RANS-LES computations of attached boundary layers with flow induced separation, we use the DDES approach [36]. The blending function between the RANS mode and the LES mode reads:

$$l_{DDES} = l_{RANS} - f_d \max(0, l_{RANS} - l_{LES}) \tag{16}$$

where the enhanced boundary layer shielding function f_d blends between l_{RANS} and l_{LES}, the RANS and LES length scales, respectively. The RANS-model then works as a hybrid RANS-LES model by replacing l_{RANS} by the hybrid length scale given by l_{DDES}. The LES length scale in (16) is given by

$$l_{LES} = C_{DES} \Psi \Delta \tag{17}$$

Here, C_{DES} is the modeling constant and is code dependent, and Ψ is a correction function to avoid (an unphysical) low Reynolds number damping in the LES region [36]. In the original formulation of the DDES model, the length scale in Eq. (17) is set to the maximum cell dimension Δ_{max}. In an edge-based code like M-Edge, it is defined as the maximum edge length of a dual control volume cell.

For scale-resolving simulation of wall bounded flows, the IDDES [2] is employed. The IDDES blends two branches, the DDES-like branch which should become active only when the inflow conditions do not have any turbulent content, and the WMLES-like branch intended to be active only when the inflow conditions used in the simulation are unsteady and impose some turbulent content and if the grid is fine enough to resolve boundary-layer dominant eddies. The blending function between the RANS mode and the LES mode reads:

$$l_{IDDES} = \tilde{f}_d(1 + f_e)l_{RANS} + (1 - \tilde{f}_d)l_{LES} \tag{18}$$

Here, $\tilde{f}_d$ is a function that blends between DDES and WMLES, and f_e is a function to enhance the RANS length scale in the vicinity of the RANS-LES interface in order to reduce the log-layer mismatch [2]. The LES length scale in Eq. (18) is given by Eq. (17) but the the local filter-width Δ is replaced by

$$\Delta_{dw} = \min(\max[C_{dw}d_w, C_{dw}\Delta_{max}, \Delta_{wn}], \Delta). \tag{19}$$

The purpose of Δ_{dw} in Eq. (19) is to give a correct log-layer behaviour in WMLES without the need to alter the value of the modeling constant C_{DES} adapted to decaying grid turbulence. In Eq. (19), $C_w = 0.15$ and Δ_{wn} is the characteristic wall-normal cell size. For an unstructured edge-based solver as M-Edge, this quantity is not defined in a straightforward way. In this work, it is approximated by taking the difference between the maximum and the minimum cell face value of the wall distance d_w for a given cell. The cell face value is computed by the average of the two connecting nodes for a given edge. As underlying RANS models, the Spalart-Allmaras (SA) RANS model [37] and the Menter Shear-Stress Transport (SST) [38] are considered in this work. Note that the damping function in Eq. 17 is not needed for the SST model ($\Psi = 1$). The Δ_{max} length scale is used in Eqs. (17) and (19) unless otherwise stated.

3.1. Improved LES Length Scale

It has been shown in several studies that Δ_{max} often gives an excess SGS viscosity for flow cases involving free shear layers in LES mode (e.g. [7, 39, 40]). An alternative length scale to alleviate this problem was formulated by Shur et. al [7], where the length scale in Eq. (17) is replaced by $\tilde{\Delta}_\omega$ which is based on the local vorticity direction in the flow. For a hexahedral cell $\tilde{\Delta}_\omega$ is formulated as in Eq. (20)

$$\tilde{\Delta}_\omega = \frac{1}{\sqrt{3}} \max_{n,m} \|\mathbf{I}_n - \mathbf{I}_m\|, \quad \mathbf{I}_n = \mathbf{n}_\omega \times (\mathbf{r}_n - \mathbf{r}), \quad \mathbf{n}_\omega = \frac{\boldsymbol{\omega}}{\|\boldsymbol{\omega}\|} \tag{20}$$

where $\mathbf{n}_\omega$ is the unit vector aligned with the vorticity vector. This approach adapts the filter width to the local orientation of eddies, thus helping to reduce the well-known problem of delayed transition from RANS to LES modeling (”grey area”) in the initial region of the shear layer. The factor $\frac{1}{\sqrt{3}}$ is needed to recover Δ_{max} for cubic cells in isotropic turbulence.

However, as pointed out in [7], replacing Δ_{max} with $\tilde{\Delta}_{\omega}$ is not enough to fully unlock the Kelvin-Helmholtz instability. To further force the reduction of the turbulent SGS viscosity in free shear layers the F_{KH} function is added to $\tilde{\Delta}_{\omega}$ to give

$$\Delta_{SLA} = \tilde{\Delta}_{\omega} F_{KH}(\langle VTM \rangle) \tag{21}$$

The F_{KH} function is based on a Vortex Tilting Measure (VTM) with the aim to detect Kelvin-Helmholtz like structures and rapidly reduce the LES filter width. Local VTM values are averaged over the current and closest neighboring cells, in order to make Δ_{SLA} behave as Δ_{max} in developed 3D turbulence. The averaged VTM quantity denoted $\langle VTM \rangle$ is close to zero in the quasi-2D regions of the flow, whereas in regions with fully developed turbulence it is of the order of 1.0. The Vortex Tilting Measure $\langle VTM \rangle$ in our implementation is computed as a volume average of the neighbouring cells. The function F_{KH} takes values between zero and one, where one is its natural value and a reduction towards zero takes place in flows where Kelvin-Helmholtz like structures are detected. By achieving this additional reduction of the turbulent SGS viscosity, the two dimensional Kelvin-Helmholtz structures are able to break up and form three dimensional turbulent structures. For further information about F_{KH} and VTM, the reader is referred to Shur et al. [7].

4. Results and Discussion

In this section, computations of several test cases are reported to investigate the effect of numerical dispersion (Section 2.1) and dissipation (Section 2.2) on resolved turbulence. In the present study we have examined a certain range of values of different parameters in test case computations. A summary of the optimal values for each parameter is shown in Table 1, which in the present study give the optimal performance, numerical stability and numerical accuracy in the computation of both incompressible and compressible flows. For reference, the LD2-related parameters adopted for incompressible flows by Probst et al. [28] and the values for the conventional second-order central scheme often used in RANS applications [26, 24] are also shown in Table 1.

To establish the value of the shock capturing parameter $\kappa^{(2)}$ and the impact of the extrapolation parameter α in Eqs. (4) and (5) in the compress-

Table 1: Optimized parameters in numerical dissipation and dispersion for incompressible (LD2) and compressible (LD2C) flows.

Scheme	$\kappa^{(2)}$	Shock Sensor	$\kappa^{(4)}$	$\alpha_u,\ \alpha_p$	$\alpha_\rho,\ \alpha_c$
Ref	5	Ψ_i	1/128	0	0
LD2 [28]	0	-	1/1024	1/3	0
LD2C	5	$\Psi_i \Phi_i$	1/512	1/3	1/3

ible flow adapted scheme, LD2-Compressible (LD2C), the Sod shock tube test case is evaluated in Section 4.1. The turbulence-resolving properties of the numerical scheme and calibration of the modeling constant C_{DES} are then investigated in simulation of DIT in Section 4.2.

The turbulence-resolving capabilities of the numerical scheme in wall-bounded flows in subsonic and supersonic conditions are investigated in Section 4.3 using IDDES. Having established the shock capturing and the turbulence resolving capabilities in supersonic flow, the LD2C scheme is further evaluated in hybrid RANS-LES of the supersonic base flow case in Section 4.4. In the supersonic base flow, the optimized numerical parameters using the test cases in Sections 4.1, 4.2 and 4.3 are evaluated, together with the length scale Δ_{SLA} (Eq. (21)).

4.1. Sod shock tube

The Sod Shock tube [41] is a Riemann problem commonly used to test the accuracy of computational methods for flow cases involving discontinuities. The problem consists of propagation of a shock wave, a contact discontinuity (surface that separates zones of different density and temperature), and an expansion fan. The Euler equations are solved to measure how well the numerical scheme can resolve the propagation speed of the rarefaction wave, the contact discontinuity and the shock discontinuity without introducing nonphysical oscillations. The test case is chosen to evaluate the effects of the second-order dissipation parameter $\kappa^{(2)}$ and the extrapolation (dispersion) parameter α. All simulations in this section exploit the standard Jameson sensor given by Eq. (13). In order to detect the contact discontinuity (since the pressure is continuous here), the sensor is modified to include the density as well, i.e.

$$\Psi_i = \max[\Psi_{i,p}, \Psi_{i,\rho}] \tag{22}$$

where $\Psi_{i,p}$ and $\Psi_{i,\rho}$ are the sensors of Eq. 13 evaluated with pressure and density, respectively.

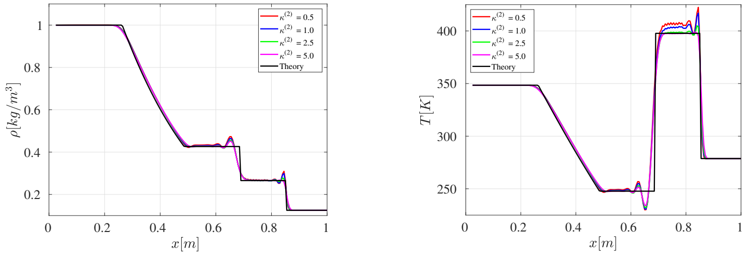

(a) Density, $\alpha = 0$.

(b) Temperature, $\alpha = 0$.

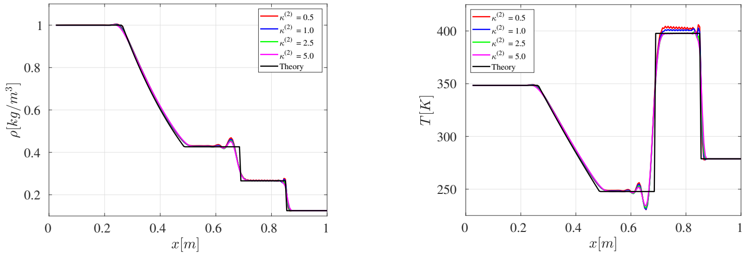

(c) Density, $\alpha_u, \alpha_p = 1/3$, α_ρ, $\alpha_c = 0$

(d) Temperature, $\alpha_u, \alpha_p = 1/3$, $\alpha_\rho, \alpha_c = 0$

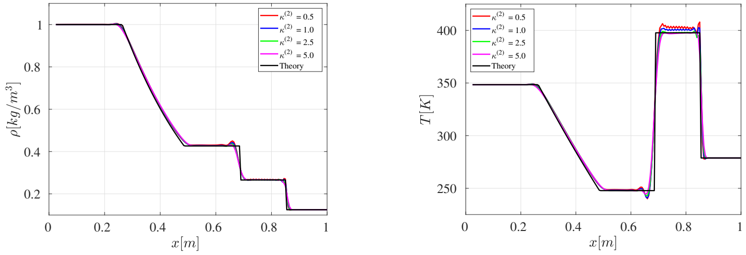

(e) Density, $\alpha_u, \alpha_p, \alpha_\rho, \alpha_c = 1/3$.

(f) Temperature, $\alpha_u, \alpha_p, \alpha_\rho, \alpha_c$= 1/3.

Figure 2: Sod shock tube [41] problem at $\tilde{t} = 0.2$ using different schemes.

The initial conditions are given by:

$$(p\ [bar], u\ [m/s], \rho\ [kg/m^3]) = \begin{cases} (1, 0, 1), & x \leq 0.5 \\ (0.125, 0, 0.1), & x > 0.5. \end{cases} \tag{23}$$

The computational domain is given by $x \in [0, 1]$ m. Simulations are performed with constant time steps $\Delta t = 3.162 \cdot 10^{-6}$ s on a uniform grid composed of 200 grid points where $\Delta x = 0.005$ m, comparison between the exact solution and the numerical solution is made after 200 time steps (non-dimensional time $\tilde{t} = 0.2$).

Figure 2 presents the density and temperature profiles. Figures 2(a) and 2(b) shows the result for no extrapolation ($\alpha = 0$, see Ref scheme in Table 1), and Figures 2(c) and 2(d) for the LD2 scheme ($\alpha_p, \alpha_u = 1/3$, see Eq. (4) and Table 1). Somewhat surprisingly, the oscillations at the normal shock location ($x \approx 0.85$ m) are slightly reduced when using the higher order extrapolation for the pressure and velocity. The oscillations are effectively dampened by increasing the value of the second-order dissipation parameter $\kappa^{(2)}$ from 1 to 5. However, the oscillation around the contact discontinuity ($x \approx 0.7$ m) remains mainly unaffected by this treatment.

This deficiency can effectively be mitigated by including the density and the speed of sound in the extrapolation scheme ($\alpha_\rho, \alpha_c = 1/3$, see Eq. (5)). Figures 2(e) and 2(f) present the density and temperature profiles for the LD2-Compressible (LD2C) scheme (see Table 1), where oscillations around the contact discontinuity are effectively dampened by increasing $\kappa^{(2)}$. The value $\kappa^{(2)} = 5$ was chosen for the LD2C scheme as a good trade off between shock sensitivity and not adding too much numerical dissipation. The Ducros sensor (Eq. (15)) was verified as well for the LD2C scheme (not shown), and showed similar results as in Figs. 2(e) and 2(f).

4.2. Decaying isotropic turbulence

To asses the scale-resolving properties of the numerical scheme for nearly incompressible isotropic turbulence using the LES versions of the SA and SST turbulence models, the isotropic grid-generated turbulence experiment of Comte-Bellot and Corssin [42] is simulated as a temporal decay on an equidistant isotropic mesh. The incoming velocity field in the experiment was $U_0 = 10$ m/s, the grid spacing $M_g = 0.0508$ m, with a resulting Reynolds number $Re = \frac{U_0 M_g}{\nu} = 34\ 000$. The kinetic energy and the turbulent spectra were reported for dimensionless times $\frac{tU_0}{M_g} \in \{42, 98, 171\}$. The reported spectra and wave number are made dimensionless to correspond to computational times of $\tilde{t} \in \{0, 0.87, 2.0\}$ [43].

The computational domain is a $2\pi \times 2\pi \times 2\pi$ cube discretized with N^3 equal sized Cartesian control volumes. Three grids have been considered with $N \in \{32, 64, 128\}$. The flow field is initialised with a prescribed velocity field of zero mean velocity. The initial fluctuating velocity distribution is obtained from the experimental energy distribution for $\tilde{t} = 0$ using an inverse

Fourier transformation in a tool provided by Prof. Strelets at St. Petersburg Technical University. The other thermodynamic variables are initiated to uniform fields to simulate an initial turbulent Mach number of $M_t = 0.1$.

The chosen physical time step Δt corresponds to $CFL = 0.2$ based on the maximum initial velocity in the domain. A timestep of $\Delta t/2$ (namely $CFL = 0.1$) was tested for a couple of cases and gave no deviation in the result. Periodic boundary conditions are applied in all directions. The computed results are compared with the experiment by comparing the three dimensional spectra at times $\tilde{t} \in \{0.87, 2.0\}$. The results on three different grids for the LES models of SA and SST are shown in Fig. 3, where a sensitivity study on the different numerical settings given in Table 1 is made.

The modeling constant for the SA LES model is set to the standard value $C_{DES} = 0.65$ [36], the results are presented in Figs. 3(a), 3(c) and 3(e). For this test case the LD2 scheme is examined with two different values of $\kappa^{(4)}$, namely 1/512 and 1/1024. The results indicate that a relatively large value of $\kappa^{(4)}$ is only slightly more dissipative on the higher wave number for each grid. Nevertheless, the effect is very small and does not affect the overall performance of the scheme in this case. The results also show that the reference scheme (see Table 1) applies too much numerical dissipation, where the energy spectrum shows a too steep decay for the higher wave number on all three grids.

Results for the SST LES model is shown in Figs. 3(b), 3(d) and 3(f). Here, the model is run in its $k - \varepsilon$ mode using the standard value $C_{DES,k-\varepsilon} = 0.61$ [38]. Similar trends can be seen compared to the results of the SA model, the experimental spectra is well captured on all three grids for the LD2 scheme. The SST model was also run in its $k - \omega$ mode with $C_{DES,k-\omega} = 0.78$ (not shown), giving nearly identical results as in Figs. 3(b), 3(d) and 3(f).

The results shown in Fig. 3 indicate that the LD2 scheme with a value $\kappa^{(4)} = 1/512$ can accurately predict the correct decay of isotropic turbulence without the need to recalibrate the standard values of the modeling constant C_{DES} for the underlying turbulence models.

4.3. Fully developed channel flow

The fully-developed turbulent channel flow is a very useful test case for examining the capabilities of resolving turbulence in wall-bounded flows. The test case is employed for the implementation, examination and validation

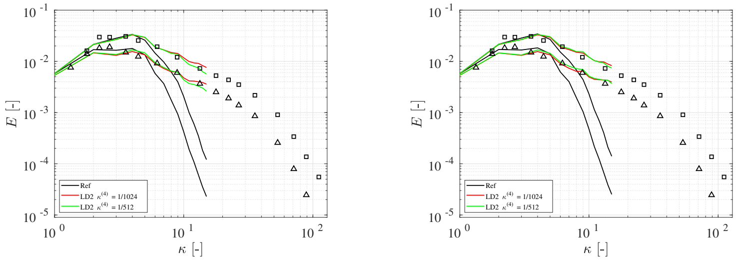

(a) SA LES, $N = 32$.

(b) SST LES, $N = 32$.

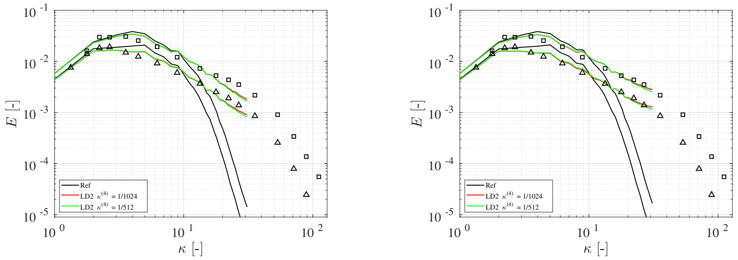

(c) SA LES, $N = 64$.

(d) SST LES, $N = 64$.

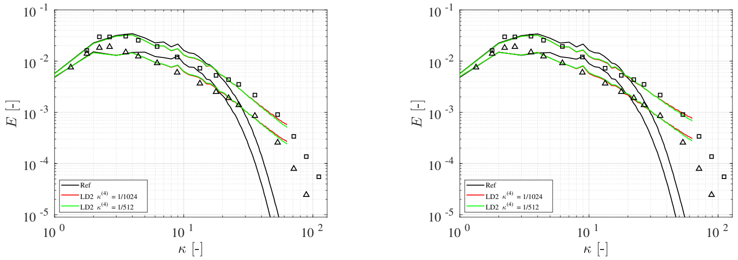

(e) SA LES, $N = 128$.

(f) SST LES, $N = 128$.

Figure 3: DIT. Prediction of energy spectra in comparison with experimental data at non-dimensional times $\tilde{t} = 0.87$ ($\square$) and $\tilde{t} = 2.0$ ($\triangle$). Effects of numerical scheme. The legend is referred to Table 1.

of the numerical scheme for wall-bounded turbulence resolving simulations using IDDES (see Eq. (18)). In order to evaluate the methodology for aeronautical applications both subsonic and supersonic conditions and a wide Reynolds number range of the fully-developed turbulent channel flow are simulated.

The computational domain is a rectangular box of height 2δ (y), a length of $2\pi\delta$ (x), and a width of $\pi\delta$ (z), where δ is the half-channel height. Periodic boundary conditions are applied in the streamwise (x) and the spanwise (z) directions. To replicate the same wall boundary conditions as the reference DNS [44, 45], no-slip adiabatic conditions are applied in the subsonic cases and no-slip isothermal conditions are applied in the supersonic cases.

To compensate for the lack of a pressure gradient $\partial p/\partial x$ driving the flow in the streamwise direction, the flow is driven by a forcing term, which enforces a specific massflow through the channel in order to achieve a target Reynolds number based on the bulk velocity Re_b. The target bulk Reynolds number is chosen to satisfy a corresponding Reynolds number based on the friction velocity Re_τ, where the target Re_τ is taken from DNS results or correlations. Subsonic or supersonic conditions are controlled by specifying the bulk Mach number M_b. The operating Re_b, Re_τ and M_b are defined as in Coleman et al. [46]

$$Re_b = \frac{\overline{\rho}_b \overline{u}_b \delta}{\overline{\mu}_w}, \quad M_b = \frac{\overline{u}_b}{\overline{c}_w}, \quad Re_\tau = \frac{\overline{\rho}_w u_\tau \delta}{\overline{\mu}_w} \tag{24}$$

where $\overline{\mu}_w$ is dynamic viscosity at the wall, $\overline{c}_w$ is the speed of sound at the wall and $u_\tau = \sqrt{\tau_w/\overline{\rho}_w}$ is the friction velocity. Details on the computational arrangement of the turbulent channel flow simulations are given in Table 2.

Table 2: Summary of channel flow test cases and corresponding grid properties.

Case	Re_b	M_b	Re_τ	n_x	n_y	n_z	r	Δx^+	Δy^+	Δz^+
INC-395	6875	0.15	395	64	75	64	1.14	40	0.47-38	20
INC-2400	52500	0.15	2400	64	102	64	1.14	239	0.45-219	120
INC-18000	483000	0.15	18000	64	132	64	1.14	1795	0.45-1697	898
CMP-500	7667	1.5	500	64	78	64	1.14	50	0.45-46	25
CMP-1015	17000	1.5	1015	64	90	64	1.14	101	0.47-97	51
CMP-1015F	17000	1.5	1015	128	118	128	1.11	50	0.5-40	25
CMP-5000	100000	1.5	5000	64	112	64	1.14	518	0.5-515	259

The different numerical settings (using low Mach number preconditioning, see Eq. (9)) in Table 1 are evaluated in the nearly incompressible regime ($M_b = 0.15$, cases INC-395, INC-2400 and INC-18000 in Table 2), where the meshing strategy follows WMLES practice according to Shur et al. [2].

The first off wall-normal node is placed at $y^+ \approx 0.5$ and a stretching factor $r = 1.14$ is used. A time step of $\Delta t^+ = 0.4$ is chosen in accordance to Probst et al. [28]. A random velocity field is generated by imposing synthetic fluctuations (STG by Shur et al. [47]) in a $y - z$ plane in the middle of the channel for one convective time units (CTU $= \delta/U_b$). The flow is then allowed to develop for two CTU and then averaged over ten CTU. Time averaged quantities are then averaged in the streamwise and and spanwise directions.

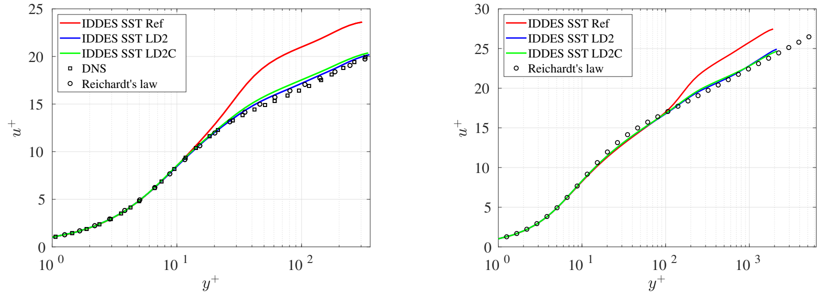

(a) Velocity profile, INC-395.

(b) Velocity profile, INC-2400.

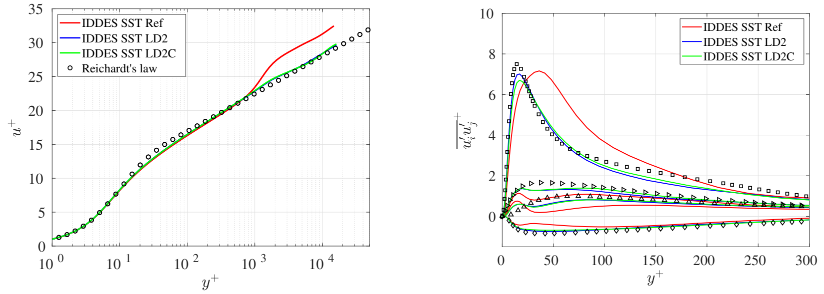

(c) Velocity profile, INC-18000.

(d) Total stresses, INC-395.

Figure 4: Fully developed turbulent channel flow with bulk Mach number $M_b = 0.15$ using SST-IDDES. Effects of numerical scheme. Results compared with Reichardt's law [48] and DNS [44]: $\square : \overline{u'u'}^+$, $\triangle : \overline{v'v'}^+$, $\triangleright$: $\overline{w'w'}^+$, $\diamond : \overline{u'v'}^+$.

Figure 4 presents the mean velocity profile for the cases INC-395, INC-2400 and INC-18000 and the total stresses (modeled plus resolved stresses) for INC-395 using the SST version of IDDES. For comparison in this case, we have also included additional simulations with the LD2 scheme and the second-order dissipation activated by setting $\kappa^{(2)} = 5$, as in the LD2C scheme. This is to verify that the shock capturing scheme is automatically switched off for low speed incompressible flows. The results using the SA model are very similar (not shown). Excellent agreement with reference DNS [44] for the velocity profile (Fig. 4(a)) and the total stresses (Fig. 4(d)) is achieved for the LD2 and LD2C schemes at $Re_\tau = 395$, where the peak of the streamwise stress $\overline{u'u'}^+$ is very well captured.

The velocity profile for the higher Reynolds number are in general well captured in comparison with the correlation by Reichardt [48], where a small log-layer mismatched can be observed at the RANS-LES interface (at around $y^+ \approx 200$ for $Re_\tau = 2400$ as shown in Fig. 4(b) and $y^+ \approx 2000$ for $Re_\tau = 18000$ as shown in Fig. 4(b)). On the other hand, the reference scheme (see Table 1) shows a significant log-layer mismatch for all Reynolds number. The velocity profile are well captured in the viscous sub-layer, buffer layer and the part of the log-layer where the IDDES operates in RANS mode, but fails as soon as the model switches to LES due to adding to much numerical dissipation. Overall, the results for the LD2 scheme are in line with previously reported results by Probst et al. [28].

In the supersonic channel flow simulations the bulk Mach number is set to $M_b = 1.5$. No low Mach number preconditioning is used. A time step $\Delta t^+ = 0.0015$ was chosen according to [49]. The same meshing strategy, initialization of flow field and averaging as in the incompressible cases are used. The Reynolds numbers for cases CMP-500 and CMP-1015 in Table 2 are chosen according to the DNS data available by Modesti et al. [45]. The Reynolds number for CMP-5000 was estimated using fully developed RANS to establish the relation between Re_b and Re_τ, since no reference DNS data was found by the author for this combination of higher Reynolds number and Mach number. However, by using proper velocity profile transformation the accuracy of the simulation can be estimated by using incompressible scaling laws.

As discussed by Coleman et al. [46], the so-called Van Driest transformation [50] can be employed for supersonic boundary layers in accounting for mean property variations in compressible turbulent wall-bounded flows. That means that, the density weighted velocity profile and Reynolds stresses

$$u^+_{vD} = \int_0^{u^+} \sqrt{\frac{\overline{\rho}}{\overline{\rho}_w}} \mathrm{d}\tilde{u}^+, \quad \overline{u'_i u'_j}^+_{vD} = \frac{\overline{\rho}}{\overline{\rho}_w} \overline{u'_i u'_j}^+, \tag{25}$$

are expected to follow their incompressible counterparts. However, it has been shown in several studies, for example in [51, 45, 52], that the velocity transformation in Eq. (25) is inaccurate for non-adiabatic walls. Trettel and Larsson [52] proposed a different velocity transformation according to

$$u_T^+ = \int_0^{u^+} \sqrt{\frac{\overline{\mu}}{\overline{\mu}_w}} \frac{\mathrm{d}y_T^+}{\mathrm{d}y^+} \mathrm{d}\tilde{u}^+, \quad y_T^+ = \frac{\overline{\rho}(\tau_w/\overline{\rho})^{1/2} y}{\overline{\mu}}, \tag{26}$$

which was found to produce a good collapse of the mean velocity profile in comparison to standard incompressible scaling laws at different Reynolds numbers and Mach numbers of supersonic channel flows with iso-thermal walls. The velocity transformation in Eq. (26) is adopted in this work.

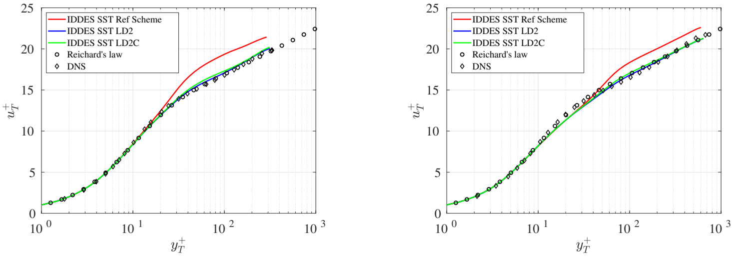

(a) Velocity profile, CMP-500.

(b) Velocity profile, CMP-1015.

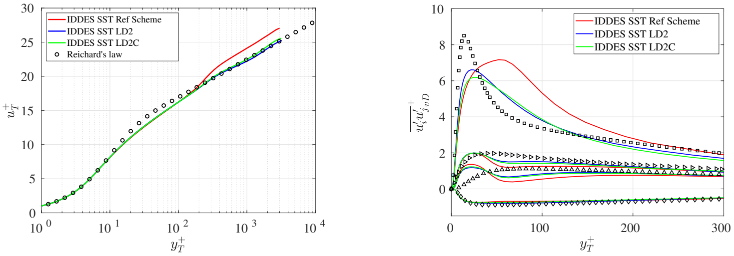

(c) Velocity profile, CMP-5000.

(d) Total stresses, CMP-1015.

Figure 5: Fully developed turbulent channel flow with bulk Mach number $M_b = 1.5$ at different Re_b using SST-IDDES. Effects of numerical scheme. Compared with Reichardt's law [48] and DNS data [45]: $\square$: $\overline{u'u'}^+_{vD}$, $\triangle$: $\overline{v'v'}^+_{vD}$, $\triangleright$: $\overline{w'w'}^+_{vD}$, $\diamond$: $\overline{u'v'}^+_{vD}$.

Figure 5 presents the mean velocity profile for the cases CMP-500, CMP-1015 and CMP-5000 and the total stresses for CMP-5000 using SST-IDDES.

Details about the grids used are given in Table 2. The results are similar to the subsonic case, the LD2 and LD2C schemes predicts the velocity profile very well in comparison to DNS data for cases CMP-500 and CMP-1015 (Figs. 5(a) and 5(b)), which collapses onto Reichardt's incompressible scaling law. Thus, the good agreement for the LD2 and LD2C schemes with the aforementioned law for the higher Reynolds number in CMP-5000 (Fig. 5(c)) is considered accurate. The reference scheme shows similar behavior as in the incompressible cases, the velocity profile is accurately predicted in the RANS part but is overestimated in the LES region.

However, the Reynolds stresses shown in Fig. 6(b) are not captured as well as in the incompressible case (Fig. 4(d)) for the LD2 and LD2C schemes using the same meshing strategy. For example, the peak value of the streamwise normal stress $\overline{u'u'}^{+}_{vD}$ is under predicted in comparison to the DNS result. In order to investigate the grid sensitivity, a finer grid is generated (see CMP-1015F in Table 2) with double grid resolution in the streamwise and spanwise directions, and a slightly finer resolution in the wall normal direction ($r = 1.11$).

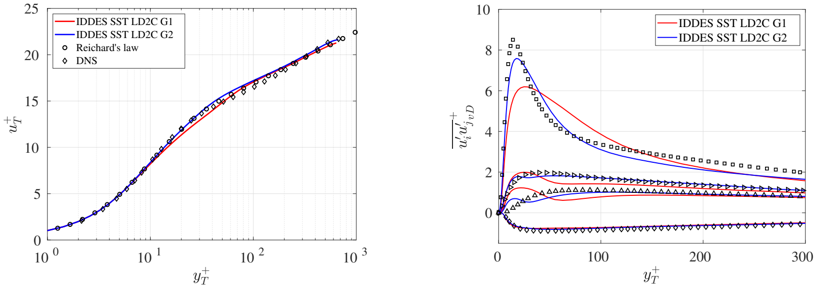

(a) Velocity profile.

(b) Total stresses.

Figure 6: Fully developed supersonic channel flow with bulk Mach number $M_b = 1.5$ using SST-IDDES and LD2C. Effects of grid resolution, cases CMP-1015 (G1) and CMP-1015F (G2). Results compared with Reichardt's law [48] and DNS [45]: $\square$: $\overline{u'u'}^{+}_{vD}$, $\triangle$: $\overline{v'v'}^{+}_{vD}$, $\triangleright$: $\overline{w'w'}^{+}_{vD}$, $\diamond$: $\overline{u'v'}^{+}_{vD}$.

The results for the LD2C scheme are shown in Fig. 6. The improved grid resolution yields a better match with the DNS velocity profile in the buffer layer (Fig 6(a)) and the peak value of the streamwise stress is better predicted (Fig. 6(b)).

4.4. Supersonic Base Flow

A supersonic flow downstream of a blunt-based cylinder is characterized by expansion waves triggered due to the sharp turn of the flow over the base corner. A separation bubble with a low pressure recirculation region contained by a shear layer is formed behind the base. The shear layer undergoes recompression and reattachment at the downstream end of the separation bubble along the symmetry axis. Due to the recompression, a shock wave is formed. An illustration of the flow field is shown in Fig. 7. This kind of flow is commonly found behind high speed projectiles, and the low pressure region behind the base causes drag which is a major part of the total drag. Thus, the modelling needs to be able to accurately predict the base pressure, along with other relevant properties such as the size of the recirculation bubble and turbulent properties subject to strong compressibility effects. For this flow, experimental data is available from the study by Herrin and Dutton [17].

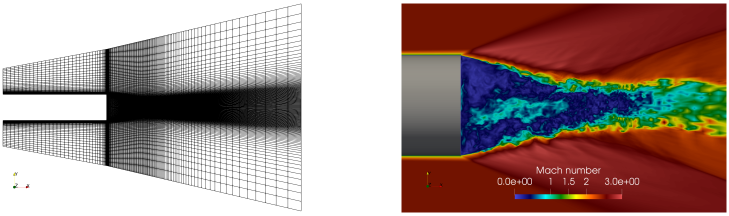

Figure 7: Supersonic base flow. Illustration of computational domain (left) and visualization of flow field in the near wake of the cylinder (right). Simulation results acquired using LD2C on the finest grid.

The base flow has been employed in a number of modelling validations for compressible turbulent flows. The case was one of the test cases in the in the DESider EU Project [53]. Most of the contributors used SA-DES [54] with the standard length scale Δ_{max} and standard value of modeling constant $C_{DES} = 0.65$. Different grid resolution (0.9 - 3.6 Million cells) and grid type (structured and unstructured) were investigated but a common trend was identified: good prediction of the base pressure with a flat profile as in the experiment, an over-estimated size of the recirculation bubble and underpredicted shear stress levels in the initial part of the separated shear layer. This was mainly attributed to the excessive levels of μ_t produced by Δ_{max} in the separated shear layer, which severely delayed the development of resolved turbulence. Simone et al. used the ZDES in two different studies

[55, 56], which employs the cubic root length scale $\Delta_{vol} = (\Delta_x \Delta_y \Delta_z)^{1/3}$ and a slightly lower value of the model constant ($C_{DES} = 0.55$). The studies included very fine grids (13.5 and 20.7 Million cells) and they reported very good agreement with experiment with regards to length of recirculation zone and the shear stress profiles. However, the backflow magnitude inside the bubble was greatly overpredicted yielding a wavy base pressure profile with the azimuth averaged pressure level significantly lower than that in the experiment. More recently, similar results was reported by Guseva et al. [57], where they employed the SA-DDES and the Δ_{SLA} length scale (Eq. (21)) on a relatively coarse mesh (2 Million cells) using $C_{DES} = 0.65$. They reported a considerable acceleration of the shear layer instability (due to the reduced levels of μ_t stemming from Δ_{SLA}) and a better general turbulence resolution in general, but did not capture a flat radial distribution of the base pressure. Nevertheless, the length scale was able to trigger resolved turbulence on a relatively coarse grid, which motivated the use of Δ_{SLA} to evaluate the impact of the numerical scheme in this study.

The Reynolds number based on the freestream velocity U_∞, base radius $R = 0.03175$ m and kinematic viscosity ν is $Re_R = 1.632 \cdot 10^6$, with a freestream Mach number of $M_\infty = 2.46$. In the computation, we have used a computational domain (shown in Fig. 7) of size $L_x \times L_r = 23R \times 8R$ in the axial and radial direction, respectively. The length of the cylinder is set to $8R$, in order to match the upstream boundary layer momentum thickness with the experimental measurement at a distance of 1 mm up the base [53]. The downstream extension of the domain is $15R$ after the cylinder base. Characteristic Riemann conditions are imposed on all no-wall boundaries, and adiabatic wall conditions on the cylinder surfaces.

Three different grids are considered. A baseline grid with $N_{cells} = 1.82 \times 10^6$ cells (G1) is used, which was designed by FOI in the DESider project [53], see Figs. 8(a) and 8(b). Two new grids were generated, a grid with improved resolution in the shear layer consisting of $N_{cells} = 2.06 \times 10^6$ cells (G2), which was designed to match the resolution used in Guseva et al. [57]. An illustration of the grid is shown in Figs. 8(c) and 8(d). The third grid considered contains $N_{cells} = 8.51 \times 10^6$ cells (G3), where several cells in the axial and radial directions have also been added in the recirculation region downstream the base, see Figs. 8(e) and 8(f). A time step of $\Delta t = 1.0 \times 10^{-6}$ s (or equivalently $\Delta t = 0.018R/U_\infty$) is used, and the time sample for accumulation of turbulence statistics after a transient period of $90R/U_\infty$ is equal to $350R/U_\infty$. It is observed that for some of the simulations, the mean

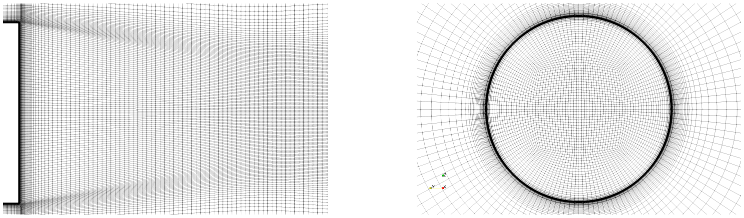

(a) Zoomed mesh on the plane $y = 0$, G1. (b) Zoomed mesh over the base plane, G1.

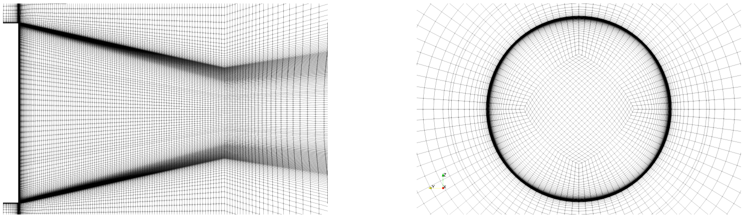

(c) Zoomed mesh on the plane $y = 0$, G2. (d) Zoomed mesh over the base plane, G2.

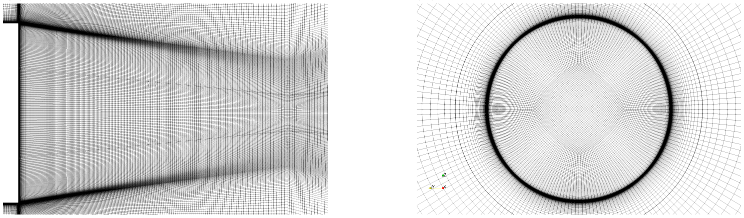

(e) Zoomed mesh on the plane $y = 0$, G3. (f) Zoomed mesh over the base plane, G3.

Figure 8: Supersonic base flow. Illustration of computational grids adopted to highlight grid sensitivity of resolving critical flow regions.

flow is still slightly asymmetric after time averaging, which is diminished by further averaging the solution over the azimuthal direction ϕ. The hybrid RANS-LES method SA-DDES (Eq. (16)) using DES model constant $C_{DES} = 0.65$ is employed, as determined in the DIT case in Section 4.2. The length scale Δ_{SLA} (Eq. (21)) is used as the filter width for the LES length scale in Eq. (17), where it was verified in DIT that the same spectra is acquired as for Δ_{max} (see Figs. 3(a), 3(c) and 3(e)) using the same value of the modeling constant.

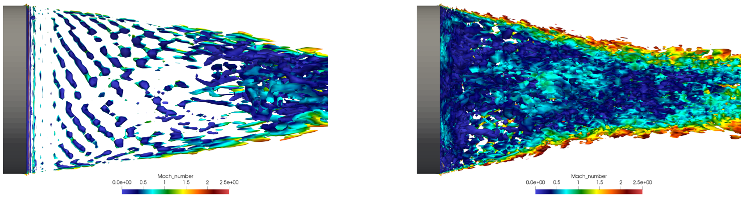

(a) Reference scheme, G1.

(b) LD2C, G1.

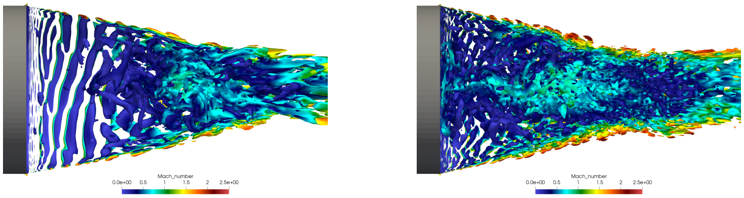

(c) Reference scheme, G2.

(d) LD2C, G2.

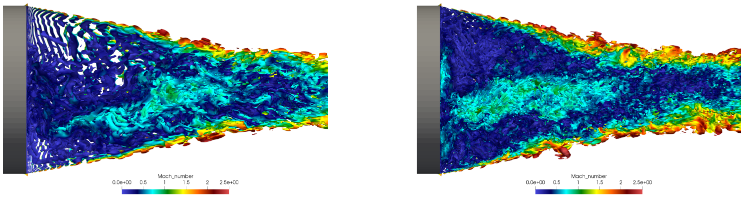

(e) Reference scheme, G3.

(f) LD2C, G3.

Figure 9: Supersonic base flow. Resolved turbulent structures visualized using iso-surfaces of Q-criterion $Q(D/U_\infty)^2 = 10$. Colorbar indicates Mach number.

Resolved instantaneous flow structures

In Figure 9 the resolved turbulent structures are visualized using iso-surfaces of the Q-criterion at $Q(D/U_\infty)^2 = 10$. Similarly as reported by Guseva et al. [57], the Δ_{SLA} length scale reduces the eddy viscosity μ_t in the initial part of the shear layer to relatively small levels as in comparison to the upstream RANS modeled boundary layer. This allows unsteady turbulent motion to be triggered due to the strong shear. Thus, the creation of turbulent structures in the initial part of the shear layer using Δ_{SLA} is mainly governed by the amount of numerical dissipation introduced by the numerical scheme and the resolution of the grid.

The results of using the reference scheme for the three different grids are presented in Figs. 9(a) (G1), 9(c) (G2) and 9(e) (G3). There is a strong delay in the creation of the resolved structures in the vicinity of the trailing edge due to the high levels of numerical dissipation. Kelvin-Helmholtz (KH) like structures with large azimuthal coherence just downstream the base can be observed, where the two-dimensional structures break up into three-dimensional structures further downstream of the reattachment point. By refining the grid in the separated shear layer (G2), the delay is mitigated and hence the length of the recirculation bubble is reduced. The richness of the small scale turbulence is further increased by further refining the grid in the axial and azimuthal directions (G3), where an earlier breakup of the KH structures can be observed.

However, the effect of using the low dissipative LD2C scheme (Figs. 9(b), 9(d) and 9(f)) has a drastic effect on the flow field. A reduction in numerical dissipation from the shock capturing sensor (Ducros sensor in Eq. (14)) and the reduced overall dissipation unlocks the KH instability and substantially accelerates the transition to 3D turbulence in the separated shear layer. The overall richness of small scale turbulence on the coarse grid G1 is comparable to the fine grid G3 using the reference scheme.

Mean flow statistics

Time- and azimuth-averaged flow properties are shown in Fig. 10. The base pressure is presented in Fig. 10(a), where the experimental results yield a relatively flat profile around $C_p = -0.102$. The reference scheme is able to predict a flat profile on all three grids, but show a large variation of the mean value between G1 and the two other grids. The C_p values are in quite close agreement with the experiment on the axis for grids G2 and G3, but deviates more further away from the center. The simulations using the LD2C scheme show radial variations along the base and in general an under predicted base pressure coefficient. The difference between G1 and the other grids is smaller as compared to the reference scheme, but predicts too low pressure levels compared to the experimental data. However, a wavy base pressure profile and in general lower base pressure values are also observed in the works of Simone et al. [55] and Guseva et al. [57] as previously mentioned.

The previous trends can be explained by investigating the behavior of the centerline streamwise velocity component in Fig 10(c). The reattachment point is poorly predicted using the reference scheme, which is $x/R \approx 4.0$ on

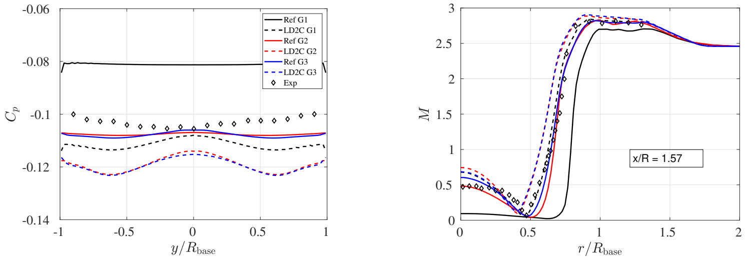

(a) Base pressure.

(b) Mach number at $x/R = 1.57$.

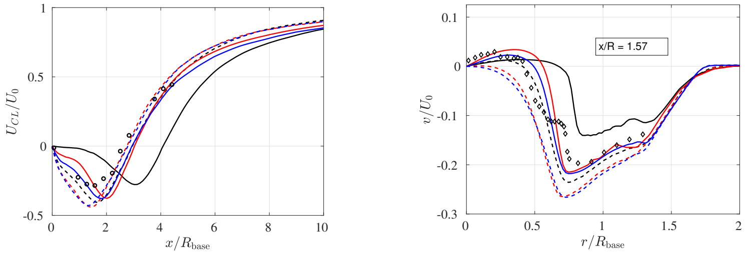

(c) Centerline velocity.

(d) Radial velocity at $x/R = 1.57$.

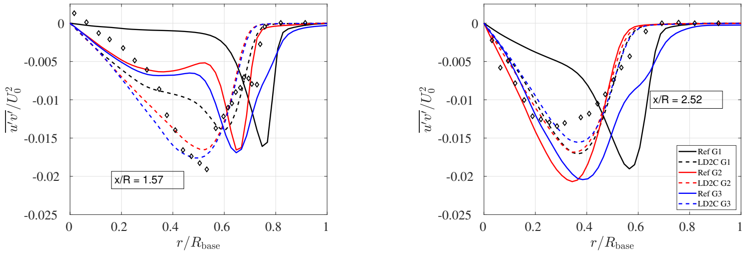

(e) Resolved shear stress at $x/R = 1.57$.

(f) Resolved shear stress at $x/R = 2.52$.

Figure 10: Supersonic base flow. Effect of numerical scheme on SA-DDES prediction of the ϕ-averaged mean flow. Experiment by Herrin and Dutton [17] ($\diamond$).

G1 and $x/R \approx 3.0$ on G2 and G3, as compared to the experimental value $x/R = 2.67$. By using the LD2C scheme, the reattachment point ($x/R \approx 2.7$ on G2 and G3) and the flow downstream of $x/R > 2$ is much better predicted. On the other hand, the reverse flow is in general over predicted for the simulations using LD2C, which give rise to the under predicted base pressure levels in Fig. 10(a). The average Mach number and radial velocity at $x/R = 1.57$ are shown in Figs. 10(b) and 10(d). In general, the radial size of the recirculation bubble is under predicted for the simulations using LD2C scheme compared to the reference scheme, which indicates that the strength of the shear layer is under predicted.

Figures 10(e) and 10(f) present a comparison of the predicted and measured fields of turbulent shear stresses at locations $x/R = 1.57$ and $x/R = 2.52$, respectively. The LD2C scheme is able to provide a much better agreement with the experimental data at $x/R = 1.57$, where the peak value of the shear stress is improved (which is further verifies the smaller resolved structures shown in Figs. 9(b), 9(d), 9(f)). A great over prediction of the shear stress at $x/R = 2.52$ can be observed for the simulations using the reference scheme, as is shown in Fig. 10(f). However, this effect is mitigated when using the LD2C scheme.

A general conclusion based on the simulations of the supersonic base flow is that improved numerics in the initial shear layer does not produce a better prediction of the base pressure profile, where a wavy pattern can be observed. However, the results are in line with what is reported in Simone et al. [55] (where they use the AUSM + (P) numerical scheme and the ZDES model [55] on a much finer grid than G3) and in Guseva et al. [57] (where they use a blended fourth-order centered/third-order upwind biased convective scheme, the same length scale Δ_{SLA} and similar grid resolution as G2). A much better prediction of the resolved shear stress, both in the initial part of the shear layer and close to the attachment point, is achieved with the LD2C scheme.

5. Summary and Conclusions

The low-dissipative low-dispersive scheme (LD2) by Löwe et al. [28] has been investigated in scale-resolving simulations. The original formulation considered only subsonic flow cases, but in this work the numerical scheme was investigated in and adapted to compressible flow cases, with the updated abbreviation LD2-Compressible (LD2C). The scheme reduces the dissipative and dispersive numerical errors connected to the convective term. The scheme controls added artificial dissipation through the matrix dissipation operator by Swanson and Turkel and can be adapted to low speed flows with a low Mach number preconditioner. The shock capturing parameter $\kappa^{(2)}$ and the global scaling parameter $\kappa^{(4)}$ are important parameters incorporated in the artificial dissipation formulation. The scheme exploits a shock sensor (formulated by Ducros [18]) targeting to minimize numerical dissipation in shock/turbulence interaction in scale-resolving simulations. Furthermore, the scheme employs a higher order central reconstruction to reduce the dispersive numerical error, controlled by an extrapolation parameter α.

The LD2C scheme was verified in scale-resolving simulations of two fundamental incompressible flows, the decaying isotropic turbulence (DIT) and the subsonic turbulent channel flow. Furthermore, the LD2C scheme has been calibrated and evaluated in an inviscid fundamental test case involving a contact discontinuity and a normal shock wave. Further validation has been made in scale-resolving simulations of fully developed supersonic turbulent channel flow and supersonic base flow using hybrid RANS-LES modeling.

The first test case is the Sod shock tube. Validation against analytical solution showed that it is important to extrapolate both density and speed of sound to cell face using the extrapolation parameter α, in addition to only velocities and pressure as formulated in the LD2 scheme. This was needed to properly capture and mitigate oscillations in the vicinity of the normal shock wave and the contact discontinuity. The oscillation could effectively be reduced by setting the shock capturing parameter $\kappa^{(2)}$ to 5.

The second test case is decaying homogeneous isotropic turbulence with a turbulent Mach number of 0.1. It was shown that numerical dissipation associated to the convection term dominates the decay of turbulent kinetic energy, which becomes too strong at higher wave numbers. This could effectively be controlled by employing a low Mach number preconditioner and using a reduced value of $\kappa^{(4)}$ in the range of 1/512 or smaller. Results acquired on 32^3, 64^3, 128^3 grids give good agreement with reference experimental data using standard values of the modeling constant C_{DES} for the Spalart-Allmaras (SA) and Menter Shear Stress Transport (SST) as underlying turbulence models.

The third test case is the fully developed turbulent channel flow, investigated in subsonic and supersonic conditions at a wide range of Reynolds numbers. In validation against DNS data and correlation using SST-IDDES, the prediction of the mean velocity profile and the resolved turbulent stresses for $Re_\tau = \{395, 2400, 18000\}$ is excellent using the LD2C scheme, and is significantly improved as compared to a conventional second-order scheme. The results are consistent with previously reported results in [10] for the subsonic channel flow case. Moreover, the LD2C scheme shows good agreement with reference DNS using SST-IDDES in supersonic channel flow ($M_b = 1.5$) for $Re_\tau = \{500, 1015, 5000\}$, where the mean velocity profile and the Reynolds stresses are accurately predicted.

The final test case is the supersonic base flow. Hybrid RANS-LES simulations using SA-DDES showed a substantial improvement in the resolved turbulent structures triggered by the initial shear layer downstream the base, using the LD2C scheme and using the shear layer adapting LES length scale Δ_{SLA}. It is shown that the parameters optimized for the previous test cases remain suitable. The prediction agrees reasonably well with the measured data, but yield similar results to previously reported studies [55, 57]. A shock-capturing scheme appropriately incorporating vorticity in the sensor formulation, e.g. by Ducros [18], was shown to improve capabilities in resolving the shear stress and contributing to grey-area mitigation in the initial part of the shear layer behind the base, compared to a standard scheme using the sensor formulation by Jameson [9].

Acknowledgments

This work has been funded by the Swedish Governmental Agency for Innovation Systems (VINNOVA), the Swedish Defence Materiel Administration (FMV) and the Swedish Armed Forces within the National Aviation Research Programme (NFFP, Contract No. 2017–04887) and Saab Aeronautics. The simulations were performed on resources provided by the Swedish National Infrastructure for Computing (SNIC) at the National Supercomputer Centre (NSC).

References

[1] P. Spalart, W.-H. Jou, M. Strelets, S. Allmaras, Comments on the feasibility of LES for wings, and on a hybrid RANS/LES approach, in: Advanced in DNS/LES, 1997.

[2] M. L. Shur, P. R. Spalart, M. K. Strelets, A. K. Travin, A hybrid RANS-LES approach with delayed-DES and wall-modelled LES capabilities, International Journal of Heat and Fluid Flow 29 (6) (2008) 1638 – 1649. doi:https://doi.org/10.1016/j.ijheatfluidflow.2008.07.001.

[3] S. H. Peng, Hybrid RANS-LES modeling based on zero- and one-equation models for turbulent flow simulation, 4th International Symposium on Turbulence and Shear Flow Phenomena 3 (2005) 1159–1164.

[4] S. H. Peng, Hybrid RANS-LES modelling with an energy backscatter function incorporated in the LES mode, 2012, p. 9. doi:10.1615/ICHMT.2012.ProcSevIntSympTurbHeatTransfPal.260.

[5] S. S. Girimaji, S. Wallin, Closure modeling in bridging regions of variable-resolution (vr) turbulence computations, Journal of Turbulence 14 (1) (2013) 72–98. doi:10.1080/14685248.2012.754893.

[6] S. Deck, Recent improvements in the zonal detached eddy simulation (zdes) formulation, Theoretical and Computational Fluid Dynamics 26 (2011) 1–28. doi:10.1007/s00162-011-0240-z.

[7] M. Shur, P. Spalart, M. Strelets, A. Travin, An enhanced version of des with rapid transition from RANS to LES in separated flows, Flow, Turbulence and Combustion 95 (12 2015). doi:10.1007/s10494-015-9618-0.

[8] A. Probst, S. Reuß, Scale-resolving simulations of wall-bounded flows with an unstructured compressible flow solver, in: Progress in Hybrid RANS-LES Modelling, Vol. 130, Springer, 2015, pp. 481–491.

[9] A. Jameson, Time-dependent calculations using multigrid with applications to unsteady flows past airfoils and wings, AIAA Paper (91-1596) (1991).

[10] J. Löwe, A. Probst, T. Knopp, R. Kessler, Low-dissipation low-dispersion second-order scheme for unstructured finite-volume flow solvers, AIAA Journal 54 (2016). doi:10.2514/1.J054956.

[11] M. Carlsson, L. Davidson, S. Peng, S. Arvidson, Parametric investigation of low-dissipation low-dispersion schemes for unstructured flow solvers in large eddy simulation, in: 2020 AIAA SciTech Forum, 2020.

[12] P. Eliasson, Edge, a navier–stokes solver for unstructured grids, in: Finite Volumes for Complex Applications, Vol. III of CP849, 2002, pp. 527–534.

[13] S. H. Peng, Hybrid RANS-LES computations of turbulent flow over rudimentary landing gear, 2013. doi:10.2514/6.2013-2913.

[14] S. Arvidson, S.-H. Peng, L. Davidson, Feasibility of hybrid RANS-LES modeling of shock/boundary-layer interaction in a duct, Notes on Numerical Fluid Mechanics and Multidisciplinary Design 117 (2012) 245–256. doi:10.1007/978-3-642-31818-4_21.

[15] S. Arvidson, S.-H. Peng, L. Davidson, Prediction of transonic duct flow using a zonal hybrid RANS-LES modeling approach, Notes on Numerical Fluid Mechanics and Multidisciplinary Design 130 (2015) 229–241. doi:10.1007/978-3-319-15141-0_18.

[16] B. Nebenführ, H. Yao, S. H. Peng, L. Davidson, Hybrid RANS/LES simulations for aerodynamic and aeroacoustic analysis of a multi-element airfoil, 2013. doi:10.2514/6.2013-2066.

[17] J. L. Herrin, J. C. Dutton, Supersonic base flow experiments in the near wake of a cylindrical afterbody, AIAA Journal 32 (1) (1994) 77–83. doi:10.2514/3.11953.

[18] F. Ducros, V. Ferrand, N. Franck, C. Weber, D. Darracq, C. Gacherieu, T. Poinsot, LES of the shock/turbulence interaction, Journal of Computational Physics 152 (1999) 517–549. doi:10.1006/jcph.1999.6238.

[19] P. Eliasson, P. Weinerfelt, Recent applications of the flow solver edge, in: 7th Asian CFD Conference, CP849, 2007.

[20] P. Eliasson, S. Eriksson, J. Nordström, The influence of weak and strong solid wall boundary conditions on the convergence to steady-state of the navier-stokes equations, AIAA Paper (2009-3551) (2009).

[21] J. C. Kok, A high-order low-dispersion symmetry-preserving finite volume method for compressible flow on curvilinear grids, Journal of Computational Physics 228 (2009) 6811–6832. doi:https://doi.org/10.1016/j.jcp.2009.06.015.

[22] R. C. Swanson, E. Turkel, On the central-difference and upwind schemes, Journal of Computational Physics 101 (1992) 292–306. doi:https://doi.org/10.1016/0021-9991(92)90007-L.

[23] A. Jameson, Origins and further development of the jameson–schmidt–turkel scheme, AIAA Journal 55 (5) (2017) 1487–1510. doi:10.2514/1.J055493.

[24] S. Langer, Investigations of a compressible second order finite volume code towards the incompressible limit, Computer and Fluids 149 (2017) 119–137.

[25] J. Harten A., Hyman, Self adjusting grid methods for one-dimensional hyperbolic conservation laws, Journal of Computational Physics 50 (1983) 235–269.

[26] S. Langer, Agglomeration multigrid methods with implicit runge–kutta smoothers applied to aerodynamic simulations on unstructured grids, Journal of Computational Physics 277 (2014) 72–100. doi:https://doi.org/10.1016/j.jcp.2014.07.050.

[27] L. Martinelli, Calculation of viscous flows with multigrid methods, Ph.D. thesis, Princeton University (1987).

[28] S. Probst, T. Knopp, D. Francois, C. Grabe, T. Landa, R. Radespiel, Scale-resolving simulations of the streamwise sortex downstream of a delta wing, AIAA Journal 54 (2016). doi:10.2514/1.J054957.

[29] E. Turkel, R. Radespiel, N. Kroll, Assessment of preconditioning methods for multidimensional aerodynamics, Computer and Fluids 26 (1997) 613–643. doi:https://doi.org/10.1016/S0045-7930(97)00013-3.

[30] S.-H. Peng, On the implementation of local preconditioning methods in EURANUS, Tech. Rep. FOI-R–0332–SE, Swedish Research Agency, FOI (2001).

[31] A. Jameson, W. Schmidt, E. Turkel, Numerical solution of the Euler equations by finite volume methods using Runge Kutta time stepping schemes. doi:10.2514/6.1981-1259.

[32] S. K. Godunov, I. Bohachevsky, Finite difference method for numerical computation of discontinuous solutions of the equations of fluid dynamics.

[33] C. Hirsch, Numerical Computation of Internal External Flows: Fundamentals of Numerical Discretization, John Wiley Sons, Inc., USA, 1988.

[34] A. Probst, Scale-resolving simulations on unstructured meshes with a low-dissipation low-dispersion scheme, in: New Results in Numerical and Experimental Fluid Mechanics XI, Springer International Publishing, Cham, 2018, pp. 489–498.

[35] S. Probst, T. Knopp, D. Francois, C. Grabe, T. Landa, R. Radespiel, Scale-resolving simulations of the streamwise vortex downstream of a delta wing, in: AIAA Scitech 2019 Forum, 2019. doi:10.2514/6.2019-0331.

[36] P. Spalart, S. Deck, M. Shur, K. Squires, M. Strelets, A. Travin, A new version of detached-eddy simulation, resistant to ambiguous grid densities, Theoretical and Computational Fluid Dynamics 20 (2006) 181–195. doi:10.1007/s00162-006-0015-0.

[37] B. Aupoix, P. Spalart, Extensions of the spalart–allmaras turbulence model to account for wall roughness, International Journal of Heat and Fluid Flow 24 (4) (2003) 454–462, selected Papers from the Fifth International Conference on Engineering Turbulence Modelling and Measurements.

[38] M. Gritskevich, A. Garbaruk, J. Schütze, F. Menter, Development of ddes and iddes formulations for the k- shear stress transport model, Flow, Turbulence and Combustion 88 (04 2012). doi:10.1007/s10494-011-9378-4.

[39] Interface methods for grey-area mitigation in turbulence-resolving hybrid RANS-LES, International Journal of Heat and Fluid Flow 73 (2018) 236–257. doi:https://doi.org/10.1016/j.ijheatfluidflow.2018.08.005.

[40] S. Arvidson, M. Carlsson, S. Nilsson, Effect of LES length scale and numerical scheme in hybrid RANS-LES of free shear layer flows, in: International Council of Aeronauutical Sciences (ICAS), Stockholm, 2022.

[41] G. A. Sod, A survey of several finite difference methods for systems of nonlinear hyperbolic conservation laws, Journal of Computational Physics 27 (1) (1978) 1–31. doi:https://doi.org/10.1016/0021-9991(78)90023-2.

[42] G. Comte-Bellot, S. Corrsin, Simple eulerian time correlation of full- and narrow-band velocity signals in grid-generated ”isotropic” turbulence, Journal of Fluid Mechanics 48 (1971) 943–13. doi:10.1017/S0022112071001599.

[43] C. M. Yan J., F. Thiele, Investigation of alternative length scale substitutions in detached-eddy simulation, Flow, Turbulence and Combustion 74 (2005) 85–102. doi:10.1007/s10494-005-6916-y.

[44] R. Moser, J. Kim, N. Mansour, Direct numerical simulation of turbulent channel flow up to $re = 590$, Physics of Fluids 11 (4) (1999) 943–13. doi:10.1006/1.869966.

[45] D. Modesti, S. Pirozzoli, Reynolds and mach number effects in compressible turbulent channel flow, International Journal of Heat and Fluid Flow 59 (2016) 33–49. doi:https://doi.org/10.1016/j.ijheatfluidflow.2016.01.007.

[46] G. N. Coleman, J. Kim, R. D. Moser, A numerical study of turbulent supersonic isothermal-wall channel flow, Journal of Fluid Mechanics 305 (1995) 159–183. doi:10.1017/S0022112095004587.

[47] M. Shur, P. Spalart, M. Strelets, A. Travin, Synthetic turbulence generators for RANS-LES interfaces in zonal simulations of aerodynamic and aeroacoustic problems, Flow, Turbulence and Combustion 93 (2014) 63–92. doi:10.1007/s10494-014-9534-8.

[48] H. Reichardt, Vollständige darstellung der turbulenten geschwindigkeitsverteilung in glatten leitungen, ZAMM - Journal of Applied Mathematics and Mechanics / Zeitschrift für Angewandte Mathematik und Mechanik 31 (7) (1951) 208–219. doi:https://doi.org/10.1002/zamm.19510310704.

[49] G. Gerolymos, I. Vallet, Pressure, density, temperature and entropy fluctuations in compressible turbulent plane channel flow, Journal of Fluid Mechanics 757 (2014) 701–746. doi:10.1017/jfm.2014.431.

[50] E. R. Van Driest, Turbulent boundary layer in compressible fluids, Journal of the Aeronautical Sciences 18 (3) (1951) 145–160. doi:10.2514/8.1895.

[51] P. G. Huang, G. N. Coleman, P. Bradshaw, Compressible turbulent channel flows: Dns results and modelling, Journal of Fluid Mechanics 305 (1995) 185–218. doi:10.1017/S0022112095004599.

[52] A. Trettel, J. Larsson, Mean velocity scaling for compressible wall turbulence with heat transfer, Physics of Fluids 28 (2) (2016) 026102. doi:10.1063/1.4942022.

[53] W. Haase, M. Braza, A. Revell, DESider: A European effort on hybrid RANS-LES Modelling (Notes on numerical fluid mechanics multidisciplinary design, Vol. 103), Vol. 103, 2009. doi:10.1007/978-3-540-92773-0.

[54] P. Spalart, Strategies for turbulence modelling and simulations, International Journal of Heat and Fluid Flow 21 (3) (2000) 252 – 263. doi:https://doi.org/10.1016/S0142-727X(00)00007-2.

[55] F. Simon, S. Deck, P. Guillen, P. Sagaut, Reynolds-averaged navier-stokes/large-eddy simulations of supersonic base flow, AIAA Journal 44 (11) (2006) 2578–2590. doi:10.2514/1.21366.

[56] F. Simon, S. Deck, P. Guillen, P. Sagaut, A. Merlen, Numerical simulation of the compressible mixing layer past an axisymmetric trailing edge, Journal of Fluid Mechanics 591 (2007) 215–253. doi:10.1017/S0022112007008129.

[57] E. Guseva, A. Garbaruk, M. Strelets, Assessment of delayed des and improved delayed des combined with a shear-layer-adapted subgrid length-scale in separated flows, Flow, Turbulence and Combustion 98 (03 2017). doi:10.1007/s10494-016-9769-7.

Paper B

Investigation of Turbulence Injection Methods in Compressible Flow Solvers in Large Eddy Simulation

M. Carlsson, L. Davidson, S.H. Peng, and S. Arvidson. "Investigation of Turbulence Injection Methods in Compressible Flow Solvers in Large Eddy Simulation". ***2022 AIAA SciTech Forum*****. Jan. 2022. DOI:** `10.2514/6.2022-0483`

Investigation of Turbulence Injection Methods in Large Eddy Simulation using a Compressible Flow Solver

Magnus Carlsson *[1], Lars Davidson †[1], Shia-Hui Peng ‡ §[1,2], and Sebastian Arvidson ¶ ‖[1,3]
[1]*Division of Fluid Dynamics and Maritime Sciences, Chalmers University of Technology, SE-412 96, Gothenburg, SWEDEN*
[2]*Swedish Defence Research Agency, FOI, SE-16490 Stockholm, SWEDEN*
[3]*Propulsion Systems, Saab Aeronautics, SE-581 88, Linköping, SWEDEN*

Three different methods for imposing velocity fluctuations in a compressible finite-volume solver are evaluated for zonal hybrid RANS-LES applications using the SA-IDDES model. The first method is a volume source term derived from an expansion of the time discretization of the fluctuating velocity component, suitable for an unstructured solver. The second method stems from an expansion of the convective flux of the fluctuating velocity component normal to the flow direction. The third methods considers a combination of both aforementioned methods. Additionally, a commutation term is derived for the convection term in the SA turbulence model in order rapidly reduce the turbulent viscosity across the RANS-LES interface. Good agreement with reference data is obtained with the investigated interface methods for the evaluated flow cases, which includes the turbulent channel flow and the zero-pressure-gradient boundary layer flow.

I. Introduction

Computational Fluid Dynamics (CFD) is a powerful tool for the aeronautical industry in predicting complex turbulent flows. Reynolds-averaged Navier–Stokes (RANS) is an industry standard computational technique, where temporal and spatial turbulent length scales are completely modeled. The method have been proven to effectively estimate turbulent flows in attached boundary layers at an affordable computational cost. However, RANS based methods are rather inaccurate in predicting turbulent flows around bluff bodies that produce massively separated flow regions. Scale-resolving methods such as Large-Eddy-Simulation (LES), where the turbulent scales are partly resolved have been shown to be much more accurate than RANS in estimating separated flow regions. However, LES is much more computationally demanding than RANS and is expected to remain unfeasible for complex engineering computations in the foreseeable future.

Hybrid RANS-LES modeling (HRLM) is a computational technique considered to be more accurate than RANS and computationally more affordable than LES for the aeronautical industry. The key feature of HRLM is the RANS-type behavior inside the near wall boundary layer coupled with a LES-type behavior further away from the wall. The most commonly used HRLM methods are based on Detached Eddy Simulation (DES) by Spalart et. al [1] and extended by boundary-layer shielding, e.g. Delayed DES (DDES), which is considered to be the most mature for industrial use. A wide variety of additional methods exist such as Improved DDES (IDDES) [2], HYB0 [3, 4], SAS and PANS (e.g. [5]).

In zonal RANS-LES approaches, zonal scale-resolving simulations are enabled using a LES mode embedded in an overall RANS computation. The embedded coupling often leads to the so-called "grey-area" problem, which delays the development of LES-resolved turbulence in association to the RANS-modeling over the RANS-LES interface. As a result, the accuracy of scale-resolving simulation in the focusing LES region may become significantly degraded or might even generate nonphysical predictions. In order to have effective transition between the RANS mode and the LES mode, Synthetic Turbulence (ST) have been often employed at the RANS-LES interface. The synthetic turbulent fluctuations are often superimposed on the mean flow over the RANS-LES interface to mitigate the grey-area problem.

Common ST methods are usually based on Fourier reconstruction techniques [6–8], where Fourier series is used as a mean to introduce spatial correlation. Time correlation can be introduced through imposing a time filter [7] or

---

[*] PhD. student, Division of Fluid Dynamics and Maritime Sciences, Chalmers University of Technology.

[†] Professor, Division of Fluid Dynamics and Maritime Sciences, Chalmers University of Technology.

[‡] Professor, Division of Fluid Dynamics and Maritime Sciences, Chalmers University of Technology.

[§] Research Director, Division of Defense Technology, FOI. peng@foi.se, AIAA associate fellow.

[¶] PhD. Systems Engineer, Propulsion Aerodynamics and Performance, Saab Aeronautics

[‖] PhD. Visiting Researcher, Department of Mechanics and Maritime Sciences, Chalmers University of Technology.

using a modified position vector [8], where time correlation is imposed in the streamwise direction of the flow using mean flow quantities. An alternative approach is the Synthetic Eddy methods (SEM) [9, 10], where the flow field is superimposed by virtual vortical structures. These vortical structures or eddies are randomly generated and convected through a fictional domain giving both spatial and temporal correlation to the fluctuations, which are allowed to induce perturbations to cells in their neighbourhood. Further improvement was made to the original SEM, where it was extended to give a divergence-free (DF-SEM) [11] fluctuating velocity field.

For grey-area mitigation in zonal hybrid RANS-LES computations, different methods to inject the artificial velocity fields into the flow domain have been proposed. In scale-resolving simulations, for example in LES, a Dirichlet boundary condition can be readily used for the velocities by directly imposing the fluctuations at the inlet boundary. In the work by Mathey [12] and Davidson [13], they imposed the fluctuations as an embedded approach where virtual fluxes are added to the momentum equations. The virtual fluxes are derived from an expansion of the convective flux term and were added to an interface plane between a RANS and a LES region. However, these studies were using the incompressible flow equations. Other approaches are based on the expansion of the time-derivative term, where in the works by Schmidt et al. [14] and Probst [15], they investigated a volumetric source term to impose the fluctuations. The expansion is based on the time derivative of the momentum equations, the fluctuations in the continuity and total energy equations are assumed to be small and are neglected.

In order to provide a rapid development of the turbulence-resolving LES flow, excess modeled turbulence (i.e. turbulent viscosity) need to be reduced across the RANS-LES interface. If not, the resolved turbulence imposed by the ST methods might be dampened and further delay the development of resolved turbulence. Hamba [16] identified a commutation error, owing to the non-commutivity of the spatial derivative and the filter applied in RANS and LES, at the RANS-LES interface. It was found that the commutation error can be large across the RANS-LES interface and should be considered. Following the work by Hamba, Davidson [17] and Arvidson et al. [18] explored the combination of the commutation term with synthetic fluctuations at interfaces in hybrid RANS-LES simulations, with the aim to reduce the turbulent viscosity across the RANS-LES interface. Commutation terms were derived for the k and ω equations used for the hybrid RANS-LES model and successively applied to embedded hybrid simulations, such as turbulent channel flow, zero-pressure-gradient boundary layer and mixing boundary layers.

In this work, we further explore the effects of the aforementioned injection methods using the Synthethic Turbulence Generator (STG) by Shur et al. [8]. A virtual flux term suitable for a compressible solver is derived and compared to the source term based on the time derivative. In order to provide a more complete description of the injected fluctuations, a combination of the two methods are evaluated. We apply the proposed methodology to embedded LES simulations of turbulent channel flow and boundary layer flow, using the SA-IDDES hybrid RANS-LES turbulence model [2, 19]. Hence, a commutation term suitable for the SA-model is also derived and evaluated. The efficiency and performance of the proposed methodology are evaluated and implemented into a compressible flow solver, M-Edge [20, 21].

The paper is organized as follows. In Sections II and III the synthetic turbulence methods and turbulence models used in this paper are outlined. The numerical method, injection methods and the commutation term are presented in Section IV. In Section V, the performance of these methods are assessed by their capabilities of mitigating grey area, by comparing the resolved turbulent statistics and the skin friction coefficient. Finally, some conclusions are made with a proposed continuation of the work in Section VI.

II. Synthetic Turbulence Method

The synthetic turbulence method considered in this paper is the Synthetic Turbulence Generator (STG) by Shur et al. [8]. The velocity fluctuations are computed by superimposing N Fourier modes:

$$\mathbf{v}'(\mathbf{r},t) = \sqrt{6}\sum_{k=1}^{N}\sqrt{q^n}\,\left[\boldsymbol{\sigma}^n \cos(k^n \mathbf{d}^n \cdot \mathbf{r}' + \phi^n)\right] \tag{1}$$

Here, the fluctuating field $\mathbf{v}'$ is computed from random quantities (mode direction vectors $\mathbf{d}^n$, $\boldsymbol{\sigma}^n \cdot \mathbf{d}^n = 0$ and mode phase ϕ^n), and statistical quantities such as the wave number amplitude k^n, which is computed from upstream RANS statistics and grid metrics. A modified von Karman spectrum is used to compute the mode amplitude q^n. An important note is that the random numbers used in (1) is only computed once. Unlike in [7], where a time-filter is introduced to impose a temporal correlation between the fluctuations, a modified position vector $\mathbf{r}'$ is introduced and linked with the actual quantities $\mathbf{x}$ and t using Taylor's frozen velocity hypothesis [8].

The velocity fluctuations $\mathbf{v}'(\mathbf{r},t)$ in (1) satisfies the restrictions $\langle v_i' \rangle = 0$ and $\langle v_i' v_j' \rangle = \delta_{ij}$, where $\langle \cdot \rangle$ denotes time averaging. In order to impose the correct Reynolds stress statistics at the interface, the actual fluctuations $\mathbf{u}'(\mathbf{x},t)$ are computed from

$$\mathbf{u}'(\mathbf{x},t) = a_{ij}\mathbf{v}'(\mathbf{r},t) \tag{2}$$

where a_{ij} is the Cholesky-decomposed Reynolds stress tensor:

$$a_{ij} = \begin{bmatrix} \sqrt{R_{11}} & 0 & 0 \\ R_{21}/a_{11} & \sqrt{R_{22} - a_{21}^2} & 0 \\ R_{31}/a_{11} & (R_{32} - a_{21}a_{31})/a_{22} & \sqrt{R_{33} - a_{31}^2 - a_{32}^2} \end{bmatrix} \tag{3}$$

a_{ij} determines the magnitude of the velocity fluctuation as a function of the estimated Reynolds stresses $R_{ij} =< u_i'u_j' >$, taken from upstream RANS modeled stresses in the hybrid RANS-LES simulation.

III. Turbulence Modeling

For the simulation of wall bounded flows with synthetic turbulence (ST) injection, the Improved Delayed DES (IDDES) [2] based on the SA-model [19] is employed. The IDDES blends two branches, the DDES-like branch which should become active only when the inflow conditions do not have any turbulent content, and the WMLES-like branch intended to be active only when the inflow conditions used in the simulation are unsteady and impose some turbulent content and if the grid is fine enough to resolve boundary-layer dominant eddies. The blending function between the RANS mode and the LES mode reads:

$$l_{hyb} = \tilde{f}_d(1 + f_e)l_{RANS} + (1 - \tilde{f}_d)l_{LES} \tag{4}$$

where l_{RANS} for the SA-model is the wall distance d. The SA-model can then work as a hybrid RANS-LES model by replacing the wall distance d by the hybrid length scale given by l_{hyb}. The LES length scale in (4) is given by

$$l_{LES} = C_{DES}\Psi\Delta, \quad \Delta = \min(\max[C_{dw}d, C_{dw}\Delta_{max}, \Delta_{min}], \Delta_{max}) \tag{5}$$

Here, $C_{DES} = 0.65$ and Ψ is a damping function [2]. In the edge-based solver (further outlined in Section IV), Δ_{max} and Δ_{min} in Eq. (5) are approximated as the maximum and minimum edge length of a dual-cell, respectively.

In an zonal approach, a RANS region upstream of the ST-injection interface can be enforced by setting the hybrid length scale to the RANS length scale of the underlying turbulence model, $l_{hyb} = l_{RANS}$. Then, further downstream of the interface Eq. (4) can be used without any modification. In this way, no assumptions are made about the downstream region. A schematic of a zonal approach is presented in Fig. 1.

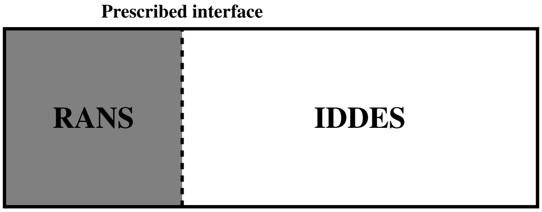

Fig. 1 Schematic of RANS and LES regions in zonal hybrid RANS-LES (embedded LES) with wall-normal RANS-LES interfaces indicated.

An alternative method is to modify the switching function f_{dt} [22]

$$\tilde{f}_d = \max(1 - f_{dt}, f_B), \quad f_{dt} = 1 - \tanh[(8r_{dt})^3] \tag{6}$$

where f_{dt} is set to 0 in the upstream RANS region, driving the length scale to $l_{hyb} = l_{RANS}$. Downstream of the interface the WMLES mode is enforced by setting $f_{dt} = 1$. This was necessary since without manual switch to WMLES mode, the large (RANS-level) eddy viscosity resulted in too strong damping of the injected fluctuations [22]. In Section IV.B, a method to reduce the upstream RANS-level eddy viscosity at the interface is presented, which does not require a manual switch to WMLES mode.

The turbulent stresses used in Eq. (3) needs to be approximated by the RANS-model. This can be achieved by the eddy viscosity assumption:

$$-\rho < u_i' u_j' >= 2\mu_t S_{ij} - \frac{2}{3}\rho k \delta_{ij} \tag{7}$$

The modeled kinetic energy k in Eq. (7) is usually not computed in the SA-model but at a RANS-LES interface where synthetic turbulence is to be generated by Eq. (1), non-zero normal stresses $< u_i' u_i' >$ have to be provided. The turbulent kinetic energy is estimated as [23]

$$k \approx \frac{\mu_t S}{\rho \sqrt{C_\mu}} \tag{8}$$

where $S = \sqrt{2 S_{ij} S_{ij}}$ is the magnitude of the strain rate tensor. It is reported in [24] that the ratio between the Reynolds shear stress $- < u_1' u_2' >$ and the turbulent kinetic energy k is nearly the same for a wide range of flows, including boundary layers, wakes and mixing layers. This constant is fixed to 0.3 and Eq. (8) agrees well with this relationship for a zero pressure gradient boundary layer where $\sqrt{C_\mu} = 0.3$ and $S \approx - < u_1' u_2' >$. The reconstructed isotropic normal stresses are then evaluated as

$$< u'^2 >=< v'^2 >=< w'^2 >= \frac{2}{3} k \tag{9}$$

where k is computed according to Eq. (8). In order to take into account the turbulence anisotropy, a more realistic distribution of the normal shear stresses can be employed. The anisotropic Reynolds stress tensor can be computed by the Wallin and Johansson EARSM model [25], which requires the modeled kinetic energy k and specific dissipation ω at the interface. However, in the work by Wilcox [26], it is shown that in the case of a zero pressure gradient turbulent boundary layer (ZPG), the following expression provide a good approximations throughout the log layer and most of the defect layer:

$$< u'^2 >= \frac{4}{9} 2k, \quad < v'^2 >= \frac{2}{9} 2k, \quad < w'^2 >= \frac{3}{9} 2k. \tag{10}$$

Equation (10) is only a slight modification to Eq. (9), where the spanwise stresses remain unaffected. The robustness and efficiency of Eq. (10) was further verified by Deck et al. [24] for the ZPG boundary layer in case hybrid RANS-LES, when used for reconstruction stresses from the SA-model in combination with synthetic turbulence (the ST model used in [24] was the SEM [10], but it uses the same expression as Eq. (3) for anisotropic stresses). In this paper, the anisotropic normal stresses given by Eq. (10) is used.

IV. Numerical Method

The flow solver used in this paper is the M-Edge code, which is an edge- and node-based Navier-Stokes flow solver applicable for both structured and unstructured grids [20, 27]. The compressible Navier-Stokes equations are discretized with a finite-volume approximation and is integrated in time using a 2nd-order backward difference scheme, together with a dual-time stepping methodology using an explicit low-storage multistage Runge-Kutta scheme accelerated by local-timestepping and full-approximation storage (FAS) multigrid [28]. The boundary conditions are based on a weak formulation in which a set of temporary flow variables are computed and used in the calculations of the boundary flux added to the residual. The residual is then used to update all unknown variables including the boundary values [21]. The viscous fluxes are discretized with a 2nd-order central scheme. The inviscid fluxes are based on the LD2 scheme, which combines a low-dissipative convection operator with a low-dispersive reconstruction of the face values [29]. The LD2-scheme was successfully applied to reduce the numerical dissipation and dispersion for fully developed turbulent channel flow and decaying homogenous isotropic turbulence [30].

A. Synthetic Turbulence Injection

The velocity fluctuations provided by the STG in Eq. (2) are injected by considering three different methods. A forcing region is defined at the RANS-LES interface, which is a plane perpendicular to the general flow direction, where cells that intersect this plane are identified by manual input. This is visualized in Fig. 1. The velocity fluctuations are then added to the flow solver using three different methods outlined below.

The first method represents the injected fluctuations by means of a flux [12] added to the momentum residuals

$$F_i = \rho S_n \left(u_n u_i' + u_n' u_i + u_n' u_i' \right) \tag{11}$$

where $u_n = u_i n_i$, $u'_n = u'_i n_i$, u'_i is taken from Eq. (2) and n_i denotes the unit vector normal to the interface S_n. The expression (11) is derived for an incompressible solver. The extension of Eq. (11) suitable for a compressible solver is straightforward. Consider a convective flux projected in the plane (n_x, n_y, n_z)

$$\vec{F}_c = S_n \begin{bmatrix} \rho V \\ \rho u V + n_x p \\ \rho v V + n_y p \\ \rho w V + n_z p \\ \rho H V \end{bmatrix} \tag{12}$$

where $V = n_x u + n_y v + n_z w$ is the projected normal velocity and $H = E + p/\rho = e + u_i u_i/2 + p/\rho$ is the total enthalpy. By letting $u_i \rightarrow \tilde{u}_i + u'_i$ in Eq. (12), where $\tilde{u}_i$ is the instantaneous velocity, and identifying all terms that contain a fluctuating part, an additional flux associated to the fluctuations is derived in the following form:

$$\vec{F}_c^{\text{virt}} = S_n \begin{bmatrix} \rho V' \\ \rho(\tilde{u} V' + u'(\tilde{V} + V')) \\ \rho(\tilde{v} V' + v'(\tilde{V} + V')) \\ \rho(\tilde{w} V' + w'(\tilde{V} + V')) \\ \rho H V' + \rho(\frac{1}{2}(2\tilde{u}_i u'_i + u'_i u'_i))(\tilde{V} + V') \end{bmatrix} \tag{13}$$

where $V' = n_x u' + n_y v' + n_z w'$ and $\tilde{V} = n_x \tilde{u} + n_y \tilde{v} + n_z \tilde{w}$. If the interface coincides with an inlet boundary, adding the velocity fluctuations as Eq. (13) would be equivalent to a Dirichlet boundary condition, where $\tilde{u}_i$ is the inlet mean flow. This method is denoted M1.

The second method is a volume source term [31] derived from an expansion of the implicit time discretization for the fluctuating velocity components u'_i at different time levels consistent with the 2nd-order difference scheme. The contribution to the momentum residuals reads

$$Q_i = \frac{\partial(\rho u'_i)}{\partial t}\Delta V \approx \frac{3(\rho u'_i)^{n+1} - 4(\rho u'_i)^n + (\rho u'_i)^{n-1}}{2\Delta t}\Delta V \tag{14}$$

where ΔV is the cell volume and Δt is the physical time step. The fluctuating velocity $u_i'^{n+1}$ is taken from Eq. (2) but the values at previous times are computed as the predicted fluctuations, namely $u_i'^{n} = u_i^n - \langle u_i \rangle$ and $u_i'^{n-1} = u_i^{n-1} - \langle u_i \rangle$, respectively. This treatment prevents decoupling of the predicted flow solution from the target synthetic field, and adds the requirement of incorporating the time-averaged mean values $\langle u_i \rangle$ [31], which is computed as running-time average. Note that the contribution from Eq. (11) are added to the continuity, momentum and total energy equations, whereas the contribution from Eq. (14) are only added to the momentum equations. The turbulent fluctuations of other solution variables are expected to be reflected through the injection of velocity fluctuations. This method is denoted M2.

The third method introduces fluctuations by superimposing both previous methods. That is, the contribution from the source term given by Eq. (14) are added to the momentum equations. In addition, the contribution from the virtual flux term given by Eq. (11) is added to the continuity, momentum and total energy equations. This method is denoted M3.

B. Eddy Viscosity Treatment at Interface

A commutation error occurs in hybrid RANS-LES simulations since the hybrid filter width does not commute with the spatial derivative. Additional terms appears when computing the spatial derivative of a physical quantity f, as shown in Eq. (15)

$$\overline{\frac{\partial f}{\partial x_i}} = \frac{\partial \overline{f}}{\partial x_i} - \frac{\partial \Delta}{\partial x_i}\frac{\partial \overline{f}}{\partial \Delta} \tag{15}$$

where $(\bar{\cdot})$ denotes filter operation. It has been shown that the commutation error (second term on RHS in Eq. (15)) can be large at RANS-LES interfaces [16]. The effects of adding the commutation term in hybrid RANS-LES simulations has been explored by Arvidson et al. [18] and by Davidson [17]. It was shown that by introducing commutation terms in the k and ω equations for a $k - \omega$ based hybrid model at zonal RANS-LES wall normal interfaces, the upstream RANS modeled kinetic energy levels could effectively be reduced to downstream SGS levels of modeled kinetic energy without using any model dependent parameters. In this paper, the underlying RANS model considered is the SA-model which solves the transport equation for the modeled eddy viscosity $\tilde{\nu}$. Using Eq. (15), the commutation term for the convection term in the SA-model can be formulated as

$$\overline{\frac{\partial u_i\tilde{\nu}}{\partial x_i}} = \frac{\partial \overline{u}_i\tilde{\nu}}{\partial x_i} - \frac{\partial \Delta}{\partial x_i}\frac{\partial \overline{u}_i\tilde{\nu}}{\partial \Delta} \tag{16}$$

If one then considers a wall normal interface in the $x-$direction, the second term on the RHS in Eq. (16) can be disctretized as

$$\begin{aligned} S^c_{\tilde{\nu}} = \frac{\partial \Delta}{\partial x}\frac{\partial \overline{u}\tilde{\nu}}{\partial \Delta} &\approx \left(\frac{\Delta_{Hyb} - \Delta_{RANS}}{\Delta x}\right)\frac{\overline{u}_{RANS}\tilde{\nu}_{RANS} - \overline{u}_{Hyb}\tilde{\nu}_{Hyb}}{\Delta_{RANS} - \Delta_{Hyb}} \\ &= \frac{\overline{u}_{Hyb}\tilde{\nu}_{Hyb} - \overline{u}_{RANS}\tilde{\nu}_{RANS}}{\Delta x} \end{aligned} \tag{17}$$

where Δx is the length of the region in which the commutation terms are used for the $\tilde{\nu}_t$ equation. The RANS properties in Eq. (17) can either be taken from a precursor steady RANS simulation or upstream RANS values. The value of $\tilde{\nu}_{Hyb}$ is estimated from a Smagorinsky model expression [2]

$$\nu_{t,Hyb} = \min[(\kappa d)^2, (C_S\Delta)^2]S, \quad \nu_{t,Hyb} = f_{v1}\tilde{\nu}_{Hyb} \tag{18}$$

in order to provide a rapid transition form pure RANS levels of $\tilde{\nu}_t$, to a $\tilde{\nu}_t$-profile given by the hybrid length scale in Eq. (4). In Eq. (18), the modeling constant is set to $C_S = 0.2$, the length scale Δ is given by Eq. (5) and f_{v1} is the near-wall scaling function for the SA-model. The non-linear relationship between $\nu_{t,Hyb}$ and $\tilde{\nu}_{Hyb}$ is solved using a few iterations of a Newton-Rhapson solver.

The influence of the distance Δx, which is the length of the region in which the commutation terms are used in the equations for modeled turbulence, has been analyzed by Davidson [17], where he concluded that the larger the distance, the weaker the effect of the commutation terms. In this paper, Δx is taken as the characteristic cell size in the direction of the mean flow. For an unstructured code like M-Edge, Δx is approximated as the maximum edge length of the cell.

V. Results

The different injection methods defined in Section IV are evaluated in embedded hybrid RANS-LES simulations for developing turbulent plane channel flow and zero-pressure-gradient boundary layer. A set of cells coinciding with a plane defining the forcing-region are chosen manually, where the fluctuations from the STG in Eq. (2) are added by the methods defined by Eq. (13) (referred to as M1), Eq. (14) (referred to as M2) or the combination of both methods (referred to as M3).

The effect of the commutation term outlined in Section IV.B for the SA equation is evaluated for developing turbulent plane channel flow. The commutation given by Eq. (17) is added to the same cells where the fluctuations are added.

A. Turbulent channel flow at $Re_\tau = 5200$

Hybrid RANS-LES simulations of the turbulent flow in a plane channel are performed at $Re_\tau = 5200$. A hexahedral grid of dimensions $9\delta \times 2\delta \times 1.6\delta$ is discretized using $96 \times 96 \times 32$ cells. The resolution in wall units is set to $\Delta x^+ = 500$, $\Delta z^+ = 250$, and $\Delta y^+ \leq 1$ at the wall. Periodic boundary conditions are applied in the spanwise direction and adiabatic wall boundary conditions are used. Standard inlet and outlet boundary conditions are applied in the streamwise direction. The bulk Mach number M_b is set to 0.15. A baseline simulation is performed for a fully developed turbulent channel flow with periodic boundary condition in the streamwise direction using the SA-IDDES model which is used as reference. Emphasis will be put on how quickly the different methods outlined in Sections II and IV can re-establish fully developed turbulent conditions with the same grid and conditions. A precursor RANS simulation using the SA-model is used to generate initial conditions for the embedded simulation. Fluctuations are added at the interface at $\tilde{x}/\delta \approx 1.92$, where the IDDES is forced to be in RANS mode upstream of the interface. Reynolds stress statistics used by the STG are generated from the RANS SA-model using Eqs. (8) and (10).

The first test case evaluates the effect of the commutation term (17). The IDDES length scale in Eq. (4) is manipulated to work either in WMLES mode, by setting $f_{dt} = 1$, or by using the standard definition without any modification. Fluctuations are imposed at the interface using method M1. The effect of the commutation term is shown in Figs. 2 -4. The response in friction velocity is shown in Fig. 2(a), and the velocity profile at 2δ downstream of the interface is shown in Fig. 2(b).

As can be observed in the Fig.2(a), the upstream RANS friction velocity deviates from the developed IDDES friction velocity, where the developed IDDES result underpredicts the target $u_\tau = 1$ by approximately 4%. This is due to a too short simulation domain in the spanwise direction, another developed IDDES simulation was performed with twice the domain size (3.2δ) in spanwise direction with the same resolution $\Delta z^+ = 250$, which yielded the desired value of $u_\tau = 1$ (not shown).

When the commutation term is applied, the IDDES is able to rapidly switch from RANS to hybrid mode, as the friction velocity reaches the developed results within 1δ and are almost spot on for the entire channel length. This is also achieved without forcing the IDDES to be in WMLES mode. The mean velocity profile agrees very well with the reference simulation after 2δ, as shown in Fig. 2(b). When no commutation term is applied, the results are different. If the IDDES is forced to be in WMLES mode, a longer adaption length is observed in the friction velocity, but are still within 5% after 1δ. When no commutation term is applied and not forcing the IDDES to be in WMLES, a slight over prediction of the friction velocity and an under prediction of the velocity profile is observed.

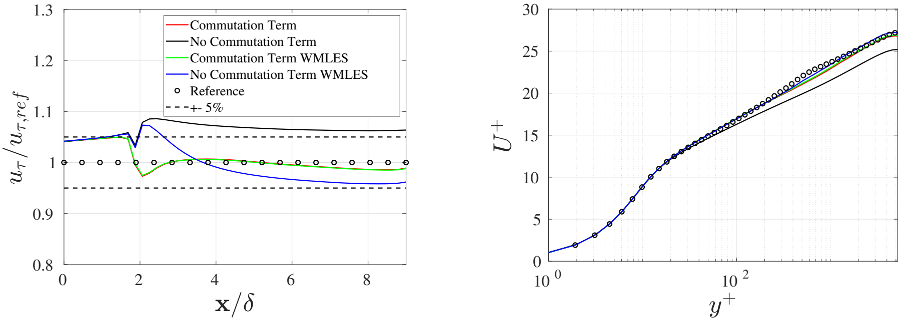

(a) Normalized friction velocity

(b) Mean velocity profile

Fig. 2 Effect of commutation term applied at RANS-LES interface using M1 to inject fluctuations. Friction velocity and mean velocity profile for turbulent channel flow at $Re_\tau = 5200$. Velocity profile taken at 2δ downstream of interface. Green and red lines are on top of each other. Red and black lines are computed with no modification of l_{hyb} in Eq. (4), blue and green lines are computed with $f_{dt} = 1$ in the IDDES region.

The impact of the commutation term on the modeled eddy viscosity is shown in Fig. 3. A quick reduction of the turbulent viscosity is obtained across the interface due to the commutation term, where the reduced eddy viscosity levels reaches the downstream developed levels within 1δ. If no commutation term is applied, the IDDES has to be forced to WMLES mode in order to reduce the upstream RANS level viscosity. However, the reduction is relatively much slower compared to using the commutation term, where the fully developed levels are reached within 6δ. If no commutation term is applied and the model is not forced to be WMLES, the modeled eddy viscosity is not reduced at all across the interface, but rather slightly increased compared to the upstream RANS levels. The reason is that the excessive upstream RANS viscosity hinders the model to switch from the RANS length scale to the hybrid length scale, since f_{dt} remains unmodified across the interface. By using the commutation term, f_{dt} is modified implicitly with the reduced eddy viscosity, and can quickly switch to the hybrid length scale.

The positive impact of the commutation term is further verified in the response of the resolved shear stress (Fig. 4(a)) and resolved normal stresses (Fig. 4(b). When no commutation term is applied and without forcing the downstream domain to be in WMLES mode, most of the fluctuations from the STG are damped within 2δ. A slight difference is observed when using the commutation term for both zonal methods (i.e. setting f_{dt} to 1 in Eq. (6) or using the standard expression given by Eq. (4)), but both agree very well with the stresses from the reference simulation. When no commutation term is applied in the forced WMLES mode, a minor under prediction of the resolved stresses is observed.

In general, it is concluded that the positive response of using the commutation term at the wall-normal RANS-LES interface together with the synthetic fluctuations from the STG are large and greatly improves the transition from modeled RANS turbulence partly resolved turbulence in the downstream hybrid RANS-LES domain. Hence, the

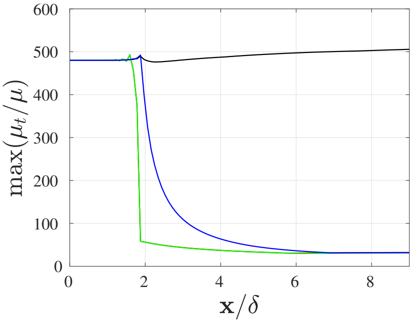

Fig. 3 Effect of commutation term applied at RANS-LES interface using M1 to inject fluctuations. Maximum turbulent eddy viscosity for turbulent channel flow at $Re_\tau = 5200$. Colors correspond to legend in Fig. 2(a). Green and red lines are on top of each other. Red and black lines are computed with no modification of l_{hyb} in Eq. (4), blue and green lines are computed with $f_{dt} = 1$ in the IDDES region.

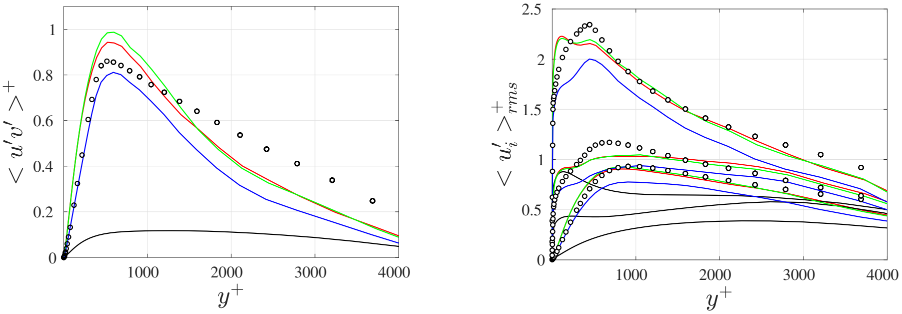

(a) Resolved shear stress

(b) RMS of resolved normal stresses

Fig. 4 Effect of commutation term applied at RANS-LES interface using M1 to inject fluctuations. Resolved shear stress and RMS of resolved normal stresses for turbulent channel flow at $Re_\tau = 5200$. Profiles are taken 2δ downstream of interface. Colors correspond to legend in Fig. 2(a). Red and black lines are computed with no modification of l_{hyb} in Eq. (4), blue and green lines are computed with $f_{dt} = 1$ in the IDDES region.

commutation term given by Eq. (17) for the $\tilde{\nu}_t$-equation is important and is used at the interface for the remaining test cases of this paper. f_{dt} is not forced to one but is computed from Eq. (6).

The second part to evaluate is considering the effects of imposing fluctuations at a wall-normal RANS-LES interface using the different injection methods (M1 - M3) outlined in Section IV.A. The results are shown in Figs. 5 and 6. Fig. 5(a) shows the response in friction velocity across the interface. All three methods experiences a sudden decrease in friction velocity across the interface, but remain within 5% for the entire downstream region. M2 experiences the largest decrease and does not reach the developed conditions. Closest to the reference simulation is M3, which is a superposition of the source term based on the time derivative and the virtual flux term based on the convective flux. The mean velocity profile shown in Fig. 5(b), where all methods show similar agreement with the reference simulation, measured 2δ downstream of the interface.

The effect of the different injection methods on the resolved stresses is shown in Fig. 6(a) and 6(b), where the profiles are measured 2δ downstream of the interface. A slight overestimation of the maximum value of resolved shear stress is observed for M1 and M3, but similar results are also reported in the work by Shur et al. [2], where the fluctutations are imposed at an inlet. M2 captures the near wall shear stress quite good but deviates more from the reference simulation further away from the wall. The same trends can be observed in the resolved normal stresses in Fig.

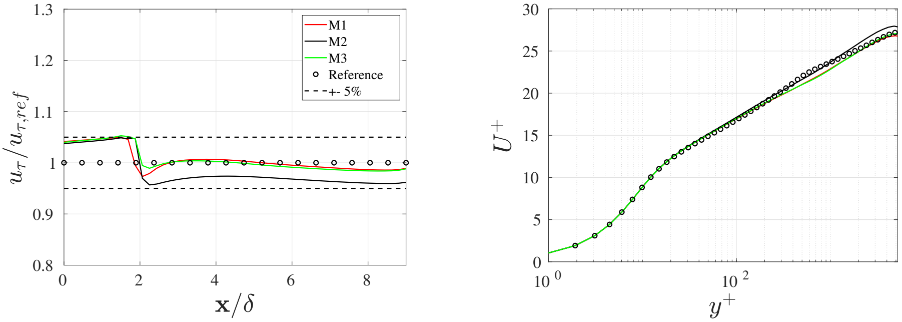

(a) Normalized friction velocity **(b) Mean velocity profile**

Fig. 5 Effect of different injection methods applied at RANS-LES interface. Friction velocity and mean velocity profile for turbulent channel flow at $Re_\tau = 5200$. Velocity profile taken at 2δ downstream of interface.

6(b), where M2 under predicts all normal stresses, M1 captures the streamwise stress very good and M3 gives a slight over estimation of the streamwise stress.

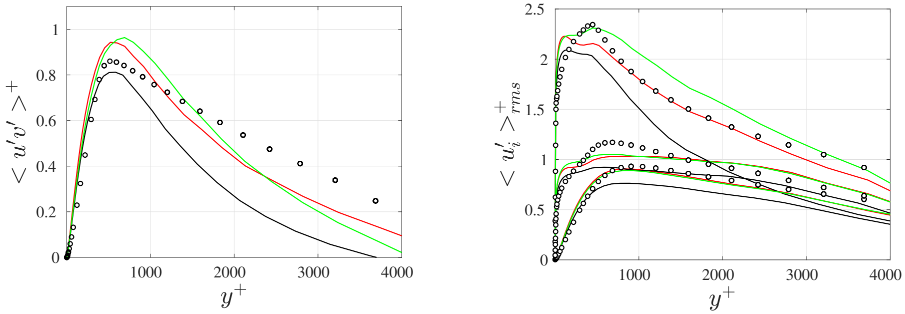

(a) Resolved shear stress **(b) RMS of resolved normal stresses**

Fig. 6 Effect of different injection methods applied at RANS-LES interface. Resolved shear stress and RMS of resolved normal stresses for turbulent channel flow at $Re_\tau = 5200$. Profiles are taken 2δ downstream of interface. Colors correspond to legend in Fig. 5(a).

B. Zero-Pressure-Gradient Turbulent Boundary Layer at $Re_\theta \geq 3000$

The spatially developing zero-pressure-gradient (ZPG) turbulent boundary layer over a smooth flat plate is simulated using an zonal RANS-LES approach. The Reynolds number range covered by the simulation is approximately $3000 \leq Re_\theta \leq 6000$, where θ is the momentum thickness. The Mach number based on the free stream velocity is $M_0 = 0.2$. Profiles of u, v and ν_t from a precursor RANS simulation using the SA model is prescribed at the inlet boundary. An initial RANS region is prescribed by forcing $l_{hyb} = l_{RANS}$ in Eq. (4), and an embedded interface is prescribed at $x/\delta_0 = 4$, where δ_0 is the initial boundary layer thickness. Downstream of this interface, the IDDES length scale in Eq. (4) is unmodified. Synthetic turbulent fluctuations from the STG given by Eq. (2) and the commutation term given by Eq. (17) for the SA-model are imposed at the embedded interface to obtain a rapid development of downstream turbulence-resolving LES flow.

The grid used for the simulation is designed by Onera in the EU-FP7 Go4Hybrid and the Garteur AG54 projects. The dimensions of the computational domain in the streamwise, spanwise and in the wall-normal directions are, respectively,

$L_x = 113\delta_0$, $L_z = 5\delta_0$ and $L_y = 52\delta_0$. The computational domain is discretized using $587 \times 127 \times 103$ cells, which gives $7.8M$ cells. The wall units are $(\Delta x^+, \Delta y^+, \Delta z^+) = (100 - 200, 2, 50)$. Note that for $x/\delta_0 > 77$, grid cells are stretched in the streamwise direction in order to progressively damp the turbulent fluctuations. This procedure is common to ensure that the domain of interest is free from wave reflections from the outlet.

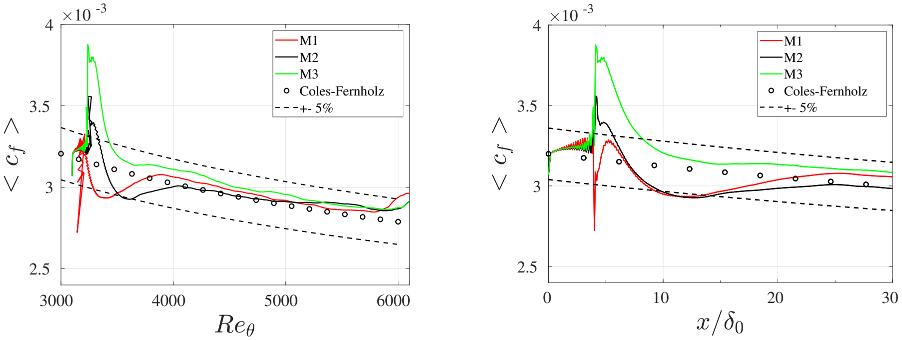

(a) $C_f(Re_\theta)$ **(b)** $C_f(x)$

Fig. 7 Effect of different injection methods applied at RANS-LES interface. Skin friction coefficient for ZPG boundary layer at $Re_\theta \geq 3000$. Results compared with Coles-Fernholz correlation [32].

The injection methods M1-M3 are assessed by imposing the fluctuations from the STG at the wall-normal RANS-LES interface. Fig. 7 shows the resulting skin friction coefficient in comparison with the Coles-Fernholz correlation [32]. Compared to results for the developing channel flow case 5(a), the methods show larger differences for this flow case. M1 gives a drop in the skin friction, a rapid increase and then a transition region to reach the correct trend according to the correlation after approximately $20\delta_0$ from the interface. On the other hand, M2 experiences a sudden increase across the interface, but shows a similar adaption trend as M2. M3 over estimates the skin friction initially but reaches developed flow conditions much quicker than the other two methods. The correct trend of M3 is reached after $7\delta_0$, a clear improvement compared to M1 and M2. However, it is important to highlight that all methods are within a 5% margin after $5\delta_0$ from the reference correlation, and give a correct decay of the skin friction further downstream in the boundary layer, as shown in Fig. 7(a).

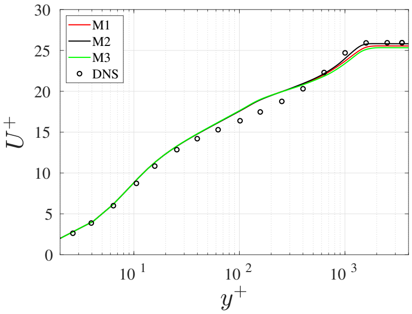

Fig. 8 Effect of different injection methods applied at RANS-LES interface. Mean velocity profile compared with DNS data [33] for ZPG boundary layer at $Re_\theta \geq 3000$.

The difference between the methods with respect to the mean velocity profile and resolved stresses measured at $Re_\theta = 4060$ are very small and yield similar small deviation from DNS [33], as shown in Figs. 8 and 9.

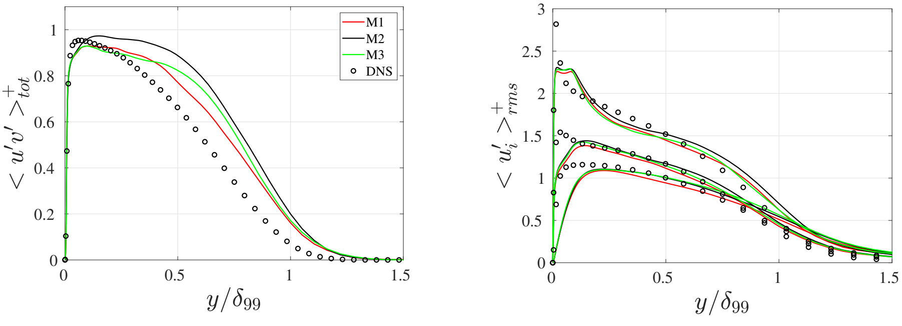

(a) Total shear stress **(b) RMS of resolved normal stresses**

Fig. 9 Effect of different injection methods applied at RANS-LES interface. Total shear stress and RMS of resolved normal stresses compared with DNS data [33] for ZPG boundary layer at $Re_\theta \geq 3000$.

VI. Summary and Conclusions

A sensitivity study on different formulations of synthetic turbulence has been conducted, which is imposed at the RANS-LES interface for zonal RANS-LES computations in order to mitigate the grey-area problem in the LES region, has been made in a compressible flow solver. Three injection methods have been implemented, where the synthetic turbulent fluctuations is numerically represented by means of, respectively, a volumetric source term, a virtual flux term, or a combination of thereof. The three methods were implemented by imposing the fluctuations (in the form of a source term, a flux term or a combination thereof) at an embedded wall-normal RANS-LES interface. Additionally, a formulation based on the commutation error for the convective term at the RANS-LES interface has been derived for the Spalart-Allmaras turbulence model, in order to reduce the modeled turbulent viscosity across the RANS-LES interface. This formulation is expressed as a source term, and is free from model dependent parameters. The three injection methods and the commutation term have been verified in embedded RANS-LES using SA-IDDES in a turbulent channel flow at $Re_\tau = 5200$ and zero-pressure-gradient boundary layer at $Re_\theta \geq 3000$.

The commutation term is able to effectively reduce the upstream RANS levels of turbulent viscosity to LES levels of turbulent viscosity across the embedded interface for the turbulent channel flow case. The transition occurs over a distance shorter than 1δ, where δ is the channel half width. The same effect can be achieved by forcing the IDDES to be in WMLES mode, however, this delays the transition length to above 4δ. If no commutation term is applied, or no explicit forcing of the IDDES to WMLES mode, the turbulent viscosity remains in RANS levels across the interface and dampens the fluctuations imposed by the STG, effectively driving the IDDES towards the RANS mode. Thus, it is concluded that the commutation term works very well and does not require any manual manipulation of the IDDES to force it to WMLES mode.

All the three injection methods perform very well for the turbulent channel flow case, where the virtual flux based method and the combination of the virtual flux term and the source term give nearly identical results. The two methods are able to reproduce reference simulation friction velocity within 1δ downstream from the interface. By using only the source term, the friction velocity does not fully recover for the downstream computational domain. The deviation is although very small (less than 5%) compared to the reference simulation.

In the simulation of the boundary layer flow, the discrepancy between the different injection methods are relatively large. The shortest recovery length with a well predicted skin friction level is produced by the combined flux and source term method. The other two approaches yield similar recovery lengths, considerably longer compared to the combined approach ($7\delta_0$ compared to $20\delta_0$, where δ_0 is the initial boundary layer thickness). However, all the simulations that are presented predict a skin friction distribution within 5% compared to the Coles-Fernholz correlation, which is used as a reference. Good agreement with DNS data further downstream is achieved for all simulation, with respect to mean velocity profile and resolved Reynolds stresses.

Acknowledgement

This work has been funded by the Swedish Governmental Agency for Innovation Systems (VINNOVA), the Swedish Defence Materiel Administration (FMV) and the Swedish Armed Forces within the National Aviation Research Programme (NFFP, Contract No. 2017–04887) and Saab Aeronautics. The simulations were performed on resources provided by the Swedish National Infrastructure for Computing (SNIC) at the Chalmers Centre for Computational Science and Computing (C3SE).

References

[1] Spalart, P., Jou, W.-H., Strelets, M., and Allmaras, S., "Comments on the Feasibility of LES for Wings, and on a Hybrid RANS/LES Approach," *Advanced in DNS/LES*, 1997.

[2] Shur, M. L., Spalart, P. R., Strelets, M. K., and Travin, A. K., "A hybrid RANS-LES approach with delayed-DES and wall-modelled LES capabilities," *International Journal of Heat and Fluid Flow*, Vol. 29, No. 6, 2008, pp. 1638 – 1649.

[3] Peng, S. H., "Hybrid RANS-LES modeling based on zero- and one-equation models for turbulent flow simulation," *4th International Symposium on Turbulence and Shear Flow Phenomena*, Vol. 3, 2005, pp. 1159–1164.

[4] Peng, S. H., "Hybrid RANS-LES modelling with an energy backscatter function incorporated in the LES mode," 2012, p. 9. https://doi.org/10.1615/ICHMT.2012.ProcSevIntSympTurbHeatTransfPal.260.

[5] Girimaji, S. S., and Wallin, S., "Closure modeling in bridging regions of variable-resolution (VR) turbulence computations," *Journal of Turbulence*, Vol. 14, No. 1, 2013, pp. 72–98. https://doi.org/10.1080/14685248.2012.754893.

[6] Batten, P., Goldberg, U., and Chakravarthy, S., "Interfacing Statistical Turbulence Closures with Large-Eddy Simulation," *AIAA Journal*, Vol. 42, No. 3, 2004, pp. 485–492. https://doi.org/10.2514/1.3496.

[7] Davidson, L., and Billson, M., "Hybrid LES-RANS using synthesized turbulent fluctuations for forcing in the interface region," *International Journal of Heat and Fluid Flow*, Vol. 27, 2006, pp. 1028–1042.

[8] Shur, M., Spalart, P., Strelets, M., and Travin, A., "Synthetic Turbulence Gnerators for RANS-LES Interfaces in Zonal Simulations of Aerodynamic and Aeroacoustic Problems," *Flow, Turbulence and Combustion*, Vol. 93, 2014, pp. 63–92.

[9] Jarrin, N., Benhamadouche, S., Laurance, D., and Prosser, R., "A synthetic-eddy-method for generating inflow conditions for large-eddy simulations," *International Journal of Heat and Fluid Flow*, Vol. 27, 2006, pp. 585–593.

[10] Jarrin, N., Prosser, R., Uribe, J.-C., Benhamadouche, S., and Laurance, D., "Reconstruction of turbulent fluctuations for hybrid RANS/LES simulations using a Synthetic-Eddy Method," *International Journal of Heat and Fluid Flow*, Vol. 30, 2009, pp. 435–442.

[11] Poletto, R., Revell, A., Craft, T., and Jarrin, N., "Divergence free synthetic eddy method for embedded LES inflow boundary conditions," *Seventh international Symposium On Turbulence and Shear Flow Phenomena (TSFP-7)*, 2011.

[12] Mathey, F., "Aerodynamic noise simulation of the flow past an airfoil trailing-edge using a hybrid zonal RANS-LES," *Computers & Fluids*, Vol. 37, 2007, pp. 836–843.

[13] Davidson, L., "Zonal PANS: evaluation of different treatments of the RANS–LES interface," *Journal of Turbulence*, Vol. 17, No. 3, 2016, pp. 274–307.

[14] Schmidt, S., and Breuer, M., "Source term based synthetic turbulence inflow generator for eddy-resolving predictions of an airfoil flow including a laminar separation bubble," *Computer & Fluids*, Vol. 146, 2017, pp. 1–22.

[15] Probst, A., "Scale-Resolving Simulations on Unstructured Meshes with a Low-Dissipation Low-Dispersion Scheme," *New Results in Numerical and Experimental Fluid Mechanics XI*, Springer International Publishing, Cham, 2018, pp. 489–498.

[16] Hamba, F., "Analysis of filtered Navier–Stokes equation for hybrid RANS/LES simulation," *Physics of Fluids*, Vol. 23, No. 1, 2011, p. 015108.

[17] Davidson, L., "Two-equation hybrid RANS–LES models: a novel way to treat k and at inlets and at embedded interfaces," *Journal of Turbulence*, Vol. 18, No. 4, 2017, pp. 291–315.

[18] Arvidson, S., Davidson, L., and Peng, S.-H., "Interface methods for grey-area mitigation in turbulence-resolving hybrid RANS-LES," *International Journal of Heat and Fluid Flow*, Vol. 73, 2018, pp. 236–257.

[19] Aupoix, B., and Spalart, P., “Extensions of the Spalart–Allmaras turbulence model to account for wall roughness,” *International Journal of Heat and Fluid Flow*, Vol. 24, No. 4, 2003, pp. 454–462. Selected Papers from the Fifth International Conference on Engineering Turbulence Modelling and Measurements.

[20] Eliasson, P., “Edge, a Navier–Stokes solver for unstructured grids,” *Finite Volumes for Complex Applications*, CP849, Vol. III, 2002, pp. 527–534.

[21] Eliasson, P., Eriksson, S., and Nordström, J., “The influence of weak and strong solid wall boundary conditions on the convergence to steady-state of the navier-stokes equations,” *AIAA Paper*, , No. 2009-3551, 2009.

[22] Probst, A., and Ströer, P., “Comparative Assessment of Synthetic Turbulence Methods in an Unstructured Compressible Flow Solver,” *Progress in Hybrid RANS-LES Modelling*, edited by Y. Hoarau, S.-H. Peng, D. Schwamborn, A. Revell, and C. Mockett, Springer International Publishing, Cham, 2020, pp. 193–202.

[23] Rung, T., Bunge, U., Schatz, M., and Thiele, F., “Restatement of the Spalart-Allmaras Eddy-Viscosity Model in Strain-Adaptive Formulation,” *AIAA Journal*, Vol. 41, No. 7, 2003, pp. 1396–1399. https://doi.org/10.2514/2.2089.

[24] Laraufie, R., and Deck, S., “Assessment of Reynolds stresses tensor reconstruction methods for synthetic turbulent inflow conditions. Application to hybrid RANS/LES methods,” *International Journal of Heat and Fluid Flow*, Vol. 42, 2013, pp. 68–78.

[25] Wallin, S., and Johansson, A. V., “An explicit algebraic Reynolds stress model for incompressible and compressible turbulent flows,” *Journal of Fluid Mechanics*, Vol. 403, 2000, p. 89–132. https://doi.org/10.1017/S0022112099007004.

[26] Wilcox, D., *Turbulence Modeling for CFD (Third Edition)*, 2006.

[27] Eliasson, P., and Weinerfelt, P., “Recent applications of the flow solver Edge,” *7th Asian CFD Conference*, 2007.

[28] Jameson, A., “Time-dependent calculations using multigrid with applications to unsteady flows past airfoils and wings,” *AIAA Paper*, , No. 91-1596, 1991.

[29] Löwe, J., Probst, A., Knopp, T., and Kessler, R., “Low-Dissipation Low-Dispersion Second-Order Scheme for Unstructured Finite-Volume Flow Solvers,” *AIAA Journal*, Vol. 54, 2016. https://doi.org/10.2514/1.J054956.

[30] Carlsson, M., Davidson, L., Peng, S., and Arvidson, S., “Parametric Investigation of Low-dissipation Low-dispersion Schemes for Unstructured Flow Solvers in Large Eddy Simulation,” *2020 AIAA SciTech*, 2020.

[31] Probst, A., “Implementation and assesment of the Synthetic-Eddy Method in an unstructured compressible flow solver,” *Progress in Hybrid RANS-LES Modelling. NNFMMD*, Vol. 137, 2018, pp. 91–101.

[32] Nagib, H. M., Chauhan, K. A., and Monkewitz, P. A., “Approach to an asymptotic state for zero pressure gradient turbulent boundary layers,” *Philosophical Transactions of the Royal Society A: Mathematical, Physical and Engineering Sciences*, Vol. 365, No. 1852, 2007, pp. 755–770.

[33] Schlatter, P., and Örlü, R., “Assessment of direct numerical simulation data of turbulent boundary layers,” *Journal of Fluid Mechanics*, Vol. 659, 2010, pp. 116 – 126.

Paper C

Higher Order Gradients on Unstructured Meshes Using Compact Formulation for Node-Centered Schemes

M. Carlsson, L. Davidson, S.H. Peng, and S. Arvidson. "Higher Order Gradients on Unstructured Meshes Using Compact Formulation for Node-Centered Schemes". *2022 AIAA Aviation Forum.* June 2022. DOI: `10.2514/6.2022-4156`

Higher Order Gradients on Unstructured Meshes using Compact Formulation for Node-Centered Schemes

Magnus Carlsson *[1], Lars Davidson †[1], Shia-Hui Peng ‡ §[1,2], and Sebastian Arvidson ¶ ‖[1,3]
[1]*Chalmers University of Technology, SE-412 96, Gothenburg, SWEDEN*
[2]*Swedish Defence Research Agency, FOI, SE-16490 Stockholm, SWEDEN*
[3]*Saab Aeronautics, SE-581 88, Linköping, SWEDEN*

This paper introduces a new approach for gradient computations on node-centered unstructured grids. The proposed approach is to derive a gradient algorithm from a least squares approximation, where a local system is solved to introduce connectivity between neighbouring nodes. The resulting scheme forms a globally coupled linear system of equations for the gradients which can be solved efficiently by iterative techniques. Fourth-order gradient accuracy for interior nodes can be obtained on isotropic quadrilateral and mixed elements (quadrilaterals and triangles) grids. The same accuracy is achieved on quadrilateral and mixed elements grids with high-aspect-ratio. Additionally, a different formulation to the standard distance weighted least squares node-centered gradients is proposed, which shows robust second-order accuracy on grids with high-aspect-ratio compared to the standard formulation. The paper concludes with a proposed continuation for future developments.

I. Introduction

COMPUTATIONAL Fluid Dynamics (CFD) tools are now routinely used for direct support/guidance of fast-paced engineering design processes in the aerodynamic industry. The gradient reconstruction scheme is a crucial part in a CFD analysis, which is closely associated to computational accuracy and efficiency, where the finite-volume methods is an industry standard. Finite volume discretizations are usually divided into cell-centered and node-centered approaches [1, 2]. In the cell-centered approach, the solution is defined at the centers of the grid elements, where the cell center coordinates are typically defined as the averages of the coordinates of the cell's vertexes. In the node-centered approach, the solutions are defined at the grid nodes. Control volumes are constructed around the grid nodes by a dual-grid, where the faces between control volumes are located at the midpoints between nodes. Since this study is focused towards a Node-centered finite-volume solver [3, 4], the focus is placed on a node-centered gradient reconstruction scheme.

Two common gradient reconstruction methods for unstructured finite-volume schemes are the Green-Gauss (GG) (see for example [5]) and Least Squares (LSQ) methods (see for example [6]). The LSQ method is a very popular method for unstructured grids, where the gradients are computed as a solution to a LSQ problem of fitting a polynomial over solution values in nearby cells. The LSQ method is more flexible than the GG method in that it is designed to be exact for linear functions on any type of grid, and also can be extended to high-order by fitting high-order polynomials. A drawback is, however, that high-order LSQ methods require large stencils, thus being less attractive for parallel implementation and for the construction of effective implicit solvers.

A recent approach called the variational reconstruction (VR) [7] method was proposed. In this method, a globally coupled system of linear equations for the gradients is found by minimizing the solution jumps at cell faces. The system is iteratively solved along with a finite-volume solver. In case that only one iteration is performed for the gradients per solver iteration, the cost per iteration is almost the same as the explicit methods suchs as the GG or LSQ methods. A similar approach, the Implicit Green-Gauss (IGG) gradient method [8], was derived from a second-order finite-volume discretization of a hyperbolic diffusion model. A common feature shared among these methods is that higher order can be achieved while still retaining a compact formulation. However, both methods were designed for cell-centered schemes, where the high accuracy gradients are assumed to be stored at the cell centers. Inspired by the these methods, we have explored a similar implicit gradient methodology, but targeted towards a node-centered scheme.

---

[*] PhD. student, Division of Fluid Dynamics, Department of Mechanics and Maritime Sciences, Chalmers University of Technology.
[†] Professor, Division of Fluid Dynamics, Department of Mechanics and Maritime Sciences, Chalmers University of Technology.
[‡] Guest Professor, Division of Fluid Dynamics, Department of Mechanics and Maritime Sciences, Chalmers University of Technology.
[§] Research Director, Division of Defense Technology, FOI. peng@foi.se, AIAA associate fellow.
[¶] PhD. Senior Engineer, Propulsion Aerodynamics and Performance, Saab Aeronautics
[‖] PhD. Visiting Researcher, Division of Fluid Dynamics, Department of Mechanics and Maritime Sciences, Chalmers University of Technology.

The presented work shares many similarities with high-order implicit finite difference (FD) methods called compact difference (CD) methods, also known as Padé schemes [9, 10]. The main difference between the CD and classical FD schemes is the computational stencil employed in the formulation of the discretization formulas. In the CD methods, the derivatives approximations are the results of solving linear systems of equations formulated based on coefficients calculated for all grid points along particular node lines. It makes the CD schemes much more accurate than FD methods. The CD schemes have been successfully applied on non-uniform meshes and in irregular domains, e.g. see [11–16]. However, in these works, the CD schemes are implemented with an underlying structure (Cartesian or curvilinear coordinate system) assumed. In the present work, we seek to extend the CD framework to fully unstructured grids, containing quadrilaterals, triangles or mixed elements.

The paper starts with the mathematical formulation of the implicit gradient scheme. A detailed investigation of the performance of the scheme to reproduce a known function on unstructured grids is then presented. Finally, some conclusions are made with a proposed continuation of the work.

II. Compact Gradient Reconstruction

A compact finite difference Padé scheme for approximating a derivative on a 1D grid can be written [9, 10, 17] as

$$\beta_{i+1}\left(\frac{\partial\phi}{\partial x}\right)_{i+1} + \beta_i\left(\frac{\partial\phi}{\partial x}\right)_i + \beta_{i-1}\left(\frac{\partial\phi}{\partial x}\right)_{i-1} = \gamma_{i+1}\phi_{i+1} + \gamma_i\phi_i + \gamma_{i-1}\phi_{i-1}, \tag{1}$$

where the coefficients $\{\beta_{i-1}, \beta_i, \beta_{i+1}, \gamma_{i+1}, \gamma_i, \gamma_{i-1}\}$ will set the order of the scheme. To obtain an approximation for the first derivative at node i, a polynomial can be fitted to pass through nodes $i-1, i, i+1$, where both the variable values at nodes $i-1, i, i+1$ and the first derivatives at nodes $i-1, i+1$ will be used. Using this compact formulation as in Eq. (1), a polynomial of fourth-degree can be constructed. Note that for a non-equidistant grid spacing, the coefficients in Eq. (1) need to depend on grid metrics to maintain a high order. The gradient scheme in Eq. (1) can be written as

$$P_{1D}\frac{\partial\boldsymbol{\phi}}{\partial x} = Q_{1D}\boldsymbol{\phi}, \tag{2}$$

which has to be solved each iteration if not the inverse solution $\frac{\partial\boldsymbol{\phi}}{\partial x} = P_{1D}^{-1}Q_{1D}\boldsymbol{\phi}$ can be easily found. To extend the compact scheme for higher dimensions, Eq. (1) can readily be applied along grid lines if the grid is structured (see e.g. Visbal et al. [11] for application in a curvilinear coordinate system). However, for an unstructured grid containing mixed elements (quadrilaterals and triangles) considered in this work, Eq. (1) can not be applied in a straight forward manner. In this work, we seek to derive an expression similar to Eq. (1) which is valid for higher dimensions on unstructured grids.

The derivation is made in 2D, the extension to 3D is straight forward. Consider a node i with a nearest neighbouring node j separated by a distance vector $\mathbf{d}_{ij}$, as shown in Fig. 1. Here, an unstructured grid containing mixed elements of quadrilaterals and triangles is considered, where only nodes j sharing an element with node i are included to maintain the compact formulation. The nodal value and the gradients of an arbitrary function ϕ at node j can be expressed from a polynomial expansion around node i:

$$\begin{aligned}
\phi_j &= \phi_i + \sum_{l=1}^{K}\sum_{m=0}^{l} a_k \Delta x_{ij}^{l-m}\Delta y_{ij}^{m},\\
\left(\frac{\partial\phi}{\partial x}\right)_j &= \frac{1}{L_{i,x}}\sum_{l=1}^{K}\sum_{m=0}^{l} a_k (l-m)\Delta x_{ij}^{l-m-1}\Delta y_{ij}^{m},\\
\left(\frac{\partial\phi}{\partial y}\right)_j &= \frac{1}{L_{i,y}}\sum_{l=1}^{K}\sum_{m=0}^{l} a_k \Delta x_{ij}^{l-m} m\Delta y_{ij}^{m-1}
\end{aligned} \tag{3}$$

where a_k is the unknown coefficients of the polynomial, $k = \frac{l(l+1)}{2} + m$ and K is the polynomial order. M is the number of terms in the polynomial expansion, where the relation between M and K is $M = \frac{K(K+3)}{2}$ in 2D. The normalized distances are expressed as

$$\Delta x_{ij} = \frac{x_j - x_i}{L_{i,x}}, \quad \Delta y_{ij} = \frac{y_j - y_i}{L_{i,y}} \tag{4}$$

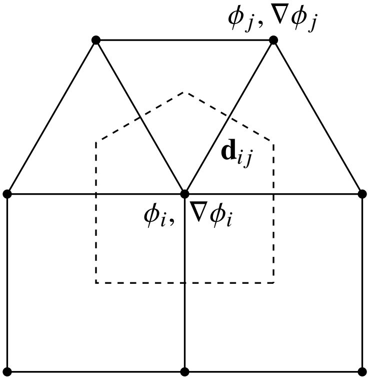

Fig. 1 Notation for dual grid control-volumes for a finite-volume discretization. The dual grid is generated from a node-centered unstructured grid.

where $L_{i,x}, L_{i,y}$ are normalization factors for node i. The choice of these factors are crucial to avoid growth of the condition number of the reconstruction matrix with grid refinement [18]. A natural choice is to choose the normalization according to the maximum distance to a neighbouring node j

$$L_{i,x} = L_{i,y} = \max_j d_{ij} \tag{5}$$

where

$$d_{ij} = |\mathbf{d}_{ij}| = \sqrt{(x_j - x_i)^2 + (y_j - y_i)^2} \tag{6}$$

is the distance between node i and neighbouring node j. In the work by Lou et al. [18] they tested a different normalization according to:

$$L_{i,x} = (x_{max} - x_{min})/2, \;\; L_{i,y} = (y_{max} - y_{min})/2, \tag{7}$$

which uses the local grid spacing in each coordinate direction. Here, $x_{max}, y_{max}, x_{min}$ and y_{min} are the maximum and minimum coordinates of node i and neighbouring nodes j in $x-$ and $y-$direction, respectively. This is helpful and important to remove the stiffness of the system matrices (Eqs. (9) and (13)) for higher-order approximations [18]. In this work, we also investigate a slightly different formulation, which can be seen as a combination of Eqs. (5) and (7), and is given by

$$L_{i,x} = \max_j |x_j - x_i|, \;\; L_{i,y} = \max_j |y_j - y_i|. \tag{8}$$

The coefficients a_k in Eq. (3) are estimated by summing over $j \in \{1, ..., N_b\}$ nearest neighbours to node i. This leads to the following set of equations:

$$\begin{bmatrix} \Delta x_{i1} & \Delta y_{i1} & \Delta x_{i1}^2 & \Delta x_{i1}\Delta y_{i1} & \Delta y_{i1}^2 & \cdots \\ \vdots & \vdots & \vdots & \vdots & \vdots & \ddots \\ \Delta x_{iN_b} & \Delta y_{iN_b} & \Delta x_{iN_b}^2 & \Delta x_{iN_b}\Delta y_{iN_b} & \Delta y_{iN_b}^2 & \cdots \\ 1 & 0 & 2\Delta x_{i1} & \Delta y_{i1} & 0 & \cdots \\ \vdots & \vdots & \vdots & \vdots & \vdots & \ddots \\ 1 & 0 & 2\Delta x_{iN_b} & \Delta y_{iN_b} & 0 & \cdots \\ 0 & 1 & 0 & \Delta x_{i1} & 2\Delta y_{i1} & \cdots \\ \vdots & \vdots & \vdots & \vdots & \vdots & \ddots \\ 0 & 1 & 0 & \Delta x_{iN_b} & 2\Delta y_{iN_b} & \cdots \end{bmatrix} \begin{bmatrix} a_1 \\ a_2 \\ a_3 \\ a_4 \\ a_5 \\ \vdots \\ a_M \end{bmatrix} = \begin{bmatrix} \phi_i(\mathbf{x_i}) - \phi(\mathbf{x_1}) \\ \vdots \\ \phi_i(\mathbf{x_i}) - \phi(\mathbf{x_{N_b}}) \\ L_{i,x}\frac{\partial\phi}{\partial x}(\mathbf{x_1}) \\ \vdots \\ L_{i,x}\frac{\partial\phi}{\partial x}(\mathbf{x_{N_b}}) \\ L_{i,y}\frac{\partial\phi}{\partial y}(\mathbf{x_1}) \\ \vdots \\ L_{i,y}\frac{\partial\phi}{\partial y}(\mathbf{x_{N_b}}) \end{bmatrix} \tag{9}$$

where $a_1 = L_{i,x}\frac{\partial\phi}{\partial x}(\mathbf{x_i})$ and $a_2 = L_{i,y}\frac{\partial\phi}{\partial y}(\mathbf{x_i})$ by construction. Equation (9) can be expressed as $Ax = b$, where A has the size $3N_b \times M$, x has the size $M \times 1$ and b has the size $3N_b \times 1$. The solution to Eq. (9) is found in a least squares sense, since the local system may be overdetermined, upon the number of neighbours N_b to node i and the polynomial order K assumed. Note that for a quadrilateral grid where each interior node has 8 neighbours sharing an element, we have $3N_b > M$ for a fourth-order polynomial.

The least square solution for Eq. (9) is found by minimising $||Ax - b||_2^2$, where the matrix A is decomposed using QR factorization via the Householder transformation [19]:

$$A = QR;\;\; Q^{-1} = Q^T;\;\; C = (A)^{-1} = R^{-1}Q^T, \tag{10a}$$

$$\Rightarrow x = Cb, \tag{10b}$$

where Q is an orthonormal matrix and R is an upper triangular, non singular matrix. Since we are only interested in the gradients, only the first two rows of C are kept. The higher order terms contribute to an increased accuracy of the gradients. The first two rows of C now contains the connectivity coefficients between the gradient at node i, nodal values at neighbouring nodes j and gradients at neighbouring nodes j. This can be seen from the the first two rows of Eq. (10b):

$$\begin{bmatrix} L_{i,x}\frac{\partial\phi}{\partial x}(\mathbf{x_i}) \\ L_{i,y}\frac{\partial\phi}{\partial y}(\mathbf{x_i}) \end{bmatrix} = \begin{bmatrix} C_{1j}b_j \\ C_{2j}b_j \end{bmatrix} \tag{11}$$

By expanding the terms on the right hand side of Eq. (11) and moving the terms which contains coefficients from neighbouring gradient values at nodes j to node i to the left hand side, we get the following linear system for node i:

$$\begin{aligned} L_{i,x}\left[\left(\frac{\partial\phi}{\partial x}\right)_i - \sum_{j=N_b+1}^{2N_b} C^i_{1j}\left(\frac{\partial\phi}{\partial x}\right)_j\right] - L_{i,y}\left[\sum_{j=2N_b+1}^{3N_b} C^i_{1j}\left(\frac{\partial\phi}{\partial y}\right)_j\right] &= \sum_{j=1}^{N_b} C^i_{1j}\phi_j - \phi_i\sum_{j=1}^{N_b} C^i_{1j} \\ L_{i,y}\left[\left(\frac{\partial\phi}{\partial y}\right)_i - \sum_{j=2N_b+1}^{3N_b} C^i_{2j}\left(\frac{\partial\phi}{\partial y}\right)_j\right] - L_{i,x}\left[\sum_{j=N_b+1}^{2N_b} C^i_{2j}\left(\frac{\partial\phi}{\partial x}\right)_j\right] &= \sum_{j=1}^{N_b} C^i_{2j}\phi_j - \phi_i\sum_{j=1}^{N_b} C^i_{2j} \end{aligned} \tag{12}$$

Equation (12) is then evaluated for all nodes N in the grid, which results in the following global sparse block linear system:

$$\begin{bmatrix} C_{1,dx} & C_{1,dy} \\ C_{2,dx} & C_{2,dy} \end{bmatrix} \begin{bmatrix} \frac{\partial\phi}{\partial x}(\mathbf{x_1}) \\ \vdots \\ \frac{\partial\phi}{\partial x}(\mathbf{x_N}) \\ \frac{\partial\phi}{\partial y}(\mathbf{x_1}) \\ \vdots \\ \frac{\partial\phi}{\partial y}(\mathbf{x_N}) \end{bmatrix} = \begin{bmatrix} C_{1,x} & 0 \\ 0 & C_{2,dy} \end{bmatrix} \begin{bmatrix} \phi(\mathbf{x_1}) \\ \vdots \\ \phi(\mathbf{x_N}) \\ \phi(\mathbf{x_1}) \\ \vdots \\ \phi(\mathbf{x_N}) \end{bmatrix} \tag{13}$$

expressed as

$$P_{2D}\begin{bmatrix} \frac{\partial\boldsymbol{\phi}}{\partial x} \\ \frac{\partial\boldsymbol{\phi}}{\partial y} \end{bmatrix} = Q_{2D}\begin{bmatrix} \boldsymbol{\phi} \\ \boldsymbol{\phi} \end{bmatrix} \tag{14}$$

The order of the solution of Eq. (14), depend on the polynomial order K in Eq. (3). In the current formulation, the order of the scheme is increased by including connectivity from neighbouring gradients, allowing a higher polynomial order K in Eq. (3) while maintaining the compact formulation of only including neighbours according to the stencil in Fig. 1. The effective stencil however, incurred in Eq, (13), then span over the entire grid. This method will be referred to implicit LSQ (ILSQ).

The coefficients of P_{2D} and Q_{2D} only depend on grid metrics, if the grid is stationary these can be computed in preprocessing step. The appearance of the off-diagonal block elements $C_{1,dy}, C_{2,dx}$ in Eq. (13) is a result due to the formulation of the two-dimensional polynomial expansion in Eq. (3) and the solution of the least square system in Eq. (10). For a uniform cartesian grid, the resulting coefficients in $C_{1,dy}$ and $C_{2,dx}$ are zero. The coefficients in P_{2D} and Q_{2D} then reduce to the 1D case in Eq. (1) in each coordinate direction, with coefficients according to the classical compact fourth-order formula [9, 10]

$$\frac{1}{4}\left(\frac{\partial\phi}{\partial x}\right)_{i+1} + \left(\frac{\partial\phi}{\partial x}\right)_i + \frac{1}{4}\left(\frac{\partial\phi}{\partial x}\right)_{i-1} = \frac{3}{4}\frac{\phi_{i+1} - \phi_{i-1}}{\Delta x} \tag{15}$$

A. Boundary Conditions

In this paper, the high-order compact gradient scheme is only considered for interior nodes. For a Neumann boundary condition, the gradients are specified at the boundary and the coefficients in Eq. (14) may be moved to the right hand side. For a Dirichlet boundary condition, the boundary nodes requires special care. According to Gustafsson [20], the global order of the scheme is conserved if the boundary nodes are closed with one order less than the interior nodes. For the ILSQ scheme with target fourth-order accuracy, the boundaries need to be closed with at least third-order accuracy. Methods of deriving appropriate high-order boundary schemes are e.g. based on one-sided formulas [9, 10, 21] or the so-called Summation-By-Parts [22] which can be also applied for high-order compact gradients schemes.

B. Solution of Linear System

The size of the matrices P_{2D} and Q_{2D} in Eq. (14) are $4N^2$, the corresponding system in 3D have size $9N^2$. As the compact discretisation leads to a non-symmetric matrix P_{2D} for unstructured grids, Eq. (14) is solved with ILU preconditioned biconjugate gradient stabilized method (BiCGStab) [23]. In the test cases considered in Section IV, the BiCGStab solver requires only a couple of iterations to reach the set tolerance of 10^{-8} of the linear solver. If there is enough memory space available the solution of Eq. (14), $P_{2D}^{-1}Q_{2D}$, may be precomputed and stored in a preprocessing step.

III. Explicit Gradient Reconstruction

The implicit gradient scheme is compared to an explicit LSQ (ELSQ), which for a second-order polynomial can be formulated as

$$\begin{bmatrix} w_{i1}\Delta x_{i1} & w_{i1}\Delta y_{i1} & w_{i1}\Delta x_{i1}^2 & w_{i1}\Delta x_{i1}\Delta y_{i1} & w_{i1}\Delta y_{i1}^2 \\ \vdots & \vdots & \vdots & \vdots & \vdots \\ w_{ij}\Delta x_{ij} & w_{ij}\Delta y_{ij} & w_{ij}\Delta x_{ij}^2 & w_{ij}\Delta x_{ij}\Delta y_{ij} & w_{ij}\Delta y_{ij}^2 \\ \vdots & \vdots & \vdots & \vdots & \vdots \\ w_{iN_b}\Delta x_{iN_b} & w_{iN_b}\Delta y_{iN_b} & w_{iN_b}\Delta x_{iN_b}^2 & w_{iN_b}\Delta x_{iN_b}\Delta y_{iN_b} & w_{iN_b}\Delta y_{iN_b}^2 \end{bmatrix} \begin{bmatrix} L_{i,x}\frac{\partial\phi}{\partial x}(\mathbf{x_i}) \\ L_{i,y}\frac{\partial\phi}{\partial y}(\mathbf{x_i}) \\ \vdots \end{bmatrix} = \begin{bmatrix} w_{i1}(\phi_i(\mathbf{x_i}) - \phi(\mathbf{x_1})) \\ \vdots \\ w_{ij}(\phi_i(\mathbf{x_i}) - \phi(\mathbf{x_j})) \\ \vdots \\ w_{iN_b}(\phi_i(\mathbf{x_i}) - \phi(\mathbf{x_{N_b}})) \end{bmatrix} \tag{16}$$

where $\Delta x_{ij}, \Delta y_{ij}$ are given in Eq. (4). The explicit least-squares problem in Eq. (16) is solved using QR-decomposition according to Eq. (10). We investigate two different variants of Eq. (16). The first one is according to the standard distance weighted LSQ [24–26] (WLSQ) scheme, where the following weights and normalization factors are chosen as:

$$w_{ij} = \frac{1}{d_{ij}},\ L_{i,x} = 1,\ L_{i,y} = 1 \tag{17}$$

where d_{ij} is defined in Eq. (6). It is shown in Section IV that the order and accuracy of this formulation deteriorates on grids with high-aspect-ratio. In order to alleviate this problem, we propose a similar but different variant by choosing the following weights and normalization factors:

$$w_{ij} = 1,\ L_{i,x},\ L_{i,y} \tag{18}$$

where $L_{i,x},\ L_{i,y}$ can be either of the normalization methods defined by Eqs. (5), (7) or (8). This method will be referred to as modified LSQ (MLSQ). By choosing normalization method according to Eq. (7) or (8), the local grid spacing in each coordinate direction is used instead of the maximum length method given by Eq. (5), which should intuitively be more valid in regions with high-aspect-ratio elements. In order to increase the order and accuracy of an ELSQ gradient reconstruction scheme, one can increase the amount of node candidates by including neighbours to nearest neighbours. However, the compact formulation is then lost and the implementations on an unstructured grid may become increasingly complicated.

IV. Analysis and Assessment of Gradient Reconstruction

In order to assess the order, accuracy and robustness of the gradient reconstruction schemes, the numerical gradient of a known smooth test function is compared to its analytical value on consecutively refined meshes [6, 8]. The function is evaluated for each interior node repeatedly through several refinement levels for a set of different structured, unstructured, isotropic and high-aspect-ratio grids. The L_1 and L_2 errors in the resulting numerical gradient are calculated as

$$L_1 = \frac{\sum_i^N |\nabla\phi_{i,num} - \nabla\phi_{i,ana}|}{N}, \quad L_2 = \left(\frac{\sum_i^N |\nabla\phi_{i,num} - \nabla\phi_{i,ana}|^2}{N}\right)^{1/2}, \tag{19}$$

where $\nabla\phi_{i,num}$ and $\nabla\phi_{i,ana}$ are the numerical and analytical gradients, respectively. The implicit (ILSQ) scheme is evaluated for a polynomial order $K = 4$ in Eq. (3) using the normalization given by Eq. (8), unless otherwise stated. We set the tolerance of the BiCGStab solver to 10^{-8} measured in the L_2 norm of the residual. Since the accuracy of interior nodes of in the scope of this work, it is assumed that the gradient values at the boundary are known. The compact implicit gradient scheme is compared to the standard distance weighted explicit LSQ (WLSQ) gradient reconstruction scheme (Eq. (16)), with weighting and normalization factors according to Eq. (17). The modified LSQ (MLSQ) scheme is also considered, with weighting and normalization factors according to Eq. (18). We consider only neighbours included in the LSQ formulation according to Fig. 1. This limits the ELSQ schemes to maximum second-order schemes.

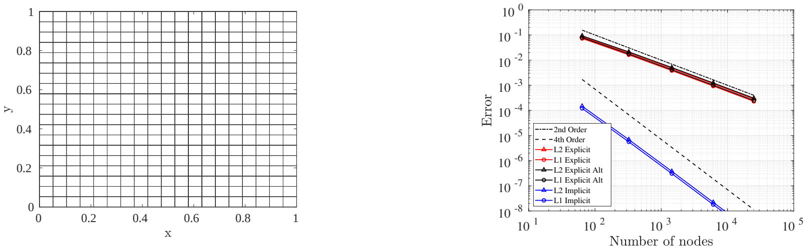

(a) Uniform quadrilaterals. **(b) Error on grid Fig. 2(a).**

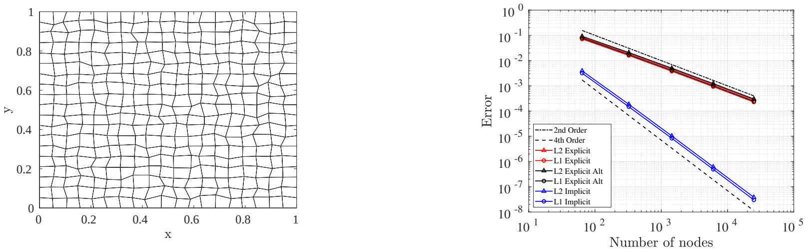

(c) Perturbed quadrilaterals. **(d) Error on grid Fig. 2(c).**

Fig. 2 Error convergence of gradient reconstruction of the function given by Eq. (20)**, using WLSQ (red), MLSQ (black) and ILSQ (blue) gradients on isotropic quadrilateral grids.**

A. Isotropic Grids

The test function is given by:

$$f(x, y) = \sin(\pi x)\sin(\pi y) \tag{20}$$

Function (20) is evaluated on a rectangular domain given by $[0, 1] \times [0, 1]$, discretized with quadrilaterals or mixed elements (quadrilaterals and triangles).

Results on the isotropic quadrilateral set of grids are shown in Fig. 2. Error convergence results for the interior nodes are given in Figs. 2(b) and 2(d). The ILSQ scheme yields fourth-order accuracy on both the uniform and the perturbed quadrilateral grids. The vertices of the grid in Fig. 2(c) are randomly disturbed compared to the grid Fig. 2(a), and as a result, the underlying structure is lost. This produces a one order of magnitude larger error level for the ILSQ scheme, however, the fourth-order scaling is still preserved. The two different ELSQ schemes show the expected second-order accuracy on both grids, where the two different formulations show a negligible difference in error.

We consider uniform and perturbed mixed element grids for the same function. The two different grids are shown in Figs. 3(a) and 3(c). The grids are generated from a quadrilateral grid, where for each element, there is a 50 % probability that the quadrilateral element will be split into two triangles. The error convergence are given in Figs. 3(b) and 3(d).

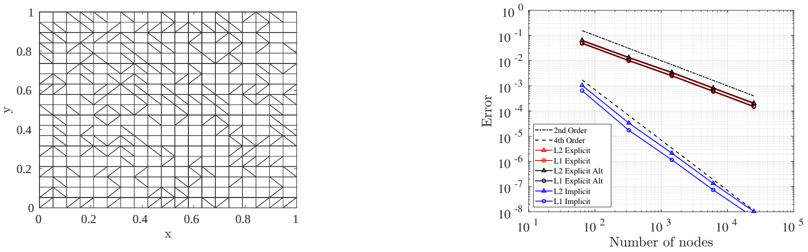

(a) Uniform mixed elements.

(b) Error on grid Fig. 3(a).

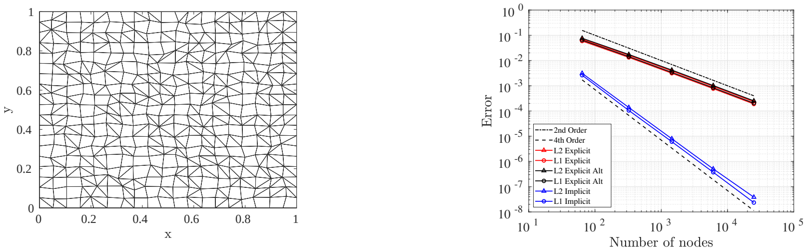

(c) Perturbed mixed elements.

(d) Error on grid Fig. 3(c).

Fig. 3 Error convergence of gradient reconstruction of the function given by Eq. (20)**, using WLSQ (red), MLSQ (black) and ILSQ (blue) gradients on isotropic mixed element grids.**

All methods yield the prescribed accuracy, the ILSQ shows fourth-order convergence and the two different ELSQ schemes show second-order convergence, on both the uniform and perturbed grids. The error levels are comparable to the quadrilateral grids considered in Fig. 2, which indicates that the LSQ gradient reconstruction formulation is insensitive to grids with mixed quadrilaterals and triangles.

B. High-aspect-ratio-grids

The test function is given by:

$$f(x, y) = \sin(\pi x)\sin(4000\pi y) \tag{21}$$

Equation (21) is evaluated on a rectangular domain given by $[0, 1] \times [0, 0.0005]$. Using this domain size, elements with aspect-ratio of 2000 is considered. This setup models a typical boundary layer problem [8], where the solution variation is predominant in the direction of small grid spacing and an anisotropic grid is specifically tailored to represent the solution anisotropy. Five types of grids are considered: uniform quadrilateral, perturbed quadrilateral, uniform mixed elements, perturbed mixed elements and perturbed fully triangular grids.

The quadrilateral grids are shown in Figs. 4(a) and 4(c), error convergence results on these grids are shown in Figs. 4(b) and 4(d). The error convergence results are similar to the isotropic quadrilateral grids, the ISLQ scheme yields fourth-order accuracy, the two ELSQ schemes yield second-order accuracy. However, on the perturbed quadrilateral grid, the WLSQ method breaks down and even yields larger errors with increased grid refinement. On the same grid, the ILSQ and MLSQ methods yield the prescribed accuracy, fourth-order for ILSQ and second-order for MLSQ.

Results for the mixed element grids are shown in Figs. 5(a). and 5(c), error convergence results on these grids are shown in Figs. 5(b) and 5(d). The error convergence results are similar to the isotropic mixed element grids, the ISLQ scheme yields fourth-order accuracy, the two ELSQ schemes yield second-order accuracy. Similar to the high-aspect-ratio uniform quadrilateral grid, the WLSQ method fails to recover second-order on the perturbed mixed element grids, as can be seen in Fig. 5(d). On the same grid, the ILSQ and MLSQ methods yield the prescribed

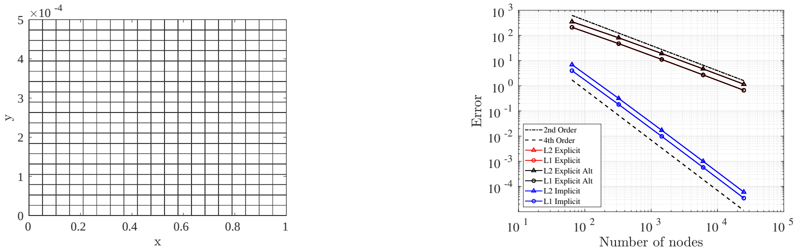

(a) Uniform quadrilaterals.

(b) Error on grid Fig. 4(a).

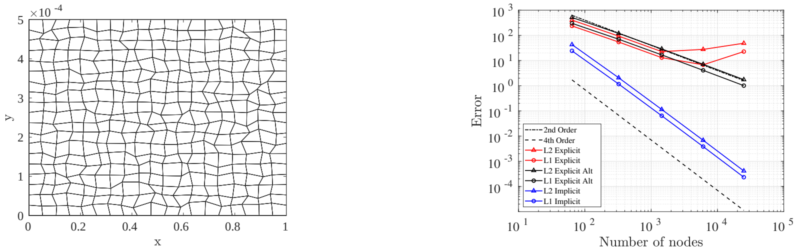

(c) Perturbed quadrilaterals.

(d) Error on grid Fig. 4(c).

Fig. 4 Error convergence of gradient reconstruction of the function given by Eq. (21)**, using WLSQ (red), MLSQ (black) and ILSQ (blue) gradients on high-aspect-ratio quadrilateral grids.**

accuracy, fourth-order for ILSQ and second-order for MLSQ. Remarkably, the accuracy is preserved for the ILSQ and MLSQ although these grids are irregular and involve two different types of cell stencils.

Finally, the effects of using different normalization given by Eqs. (5), (7), (8) are investigated for the ILSQ and the MLSQ. A perturbed triangular grid is considered (Fig. 6). Results for the error convergence are shown in Figs. 6(b), 6(c) and 6(d). Similar to WLSQ, the ILSQ using the length based normalization according to Eq. (5) completely fails to reconstruct the gradients. However, this is not observed for the MLSQ using the same normalization method. This can be attributed to that the MLSQ only assumes a second-order polynomial, whereas the ILSQ assumes a fourth-order polynomial, which should be more sensitive to specific choice of normalization. The ILSQ is able to recover the fourth-order accuracy by using the normalization according to Eqs. (8) or (7). These methods take the local grid spacing in each direction into account and is thus more accurate and robust compared to the length based approach given by Eq. (5) on grids with high-aspect-ratio.

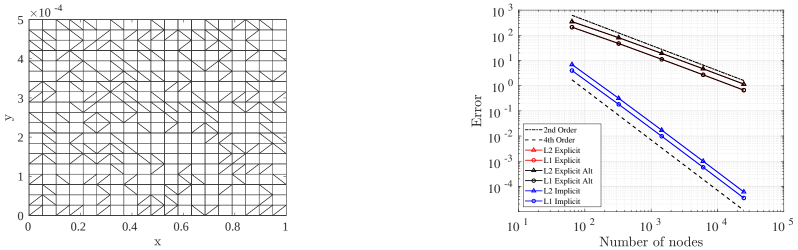

(a) Mixed elements. **(b) Error on grid Fig. 5(a).**

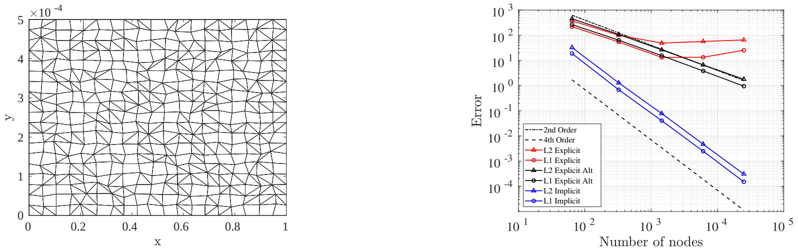

(c) Uniform quadrilaterals. **(d) Error on grid Fig. 5(c).**

Fig. 5 Error convergence of gradient reconstruction of the function given by Eq. (21)**, using WLSQ (red), MLSQ (black) and ILSQ (blue) gradients on high-aspect-ratio mixed elements grids.**

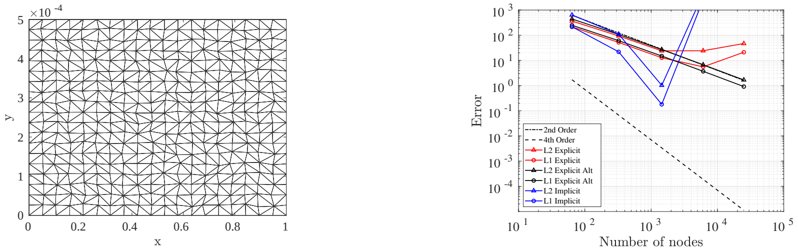

(a) Perturbed triangles. **(b) Normalization given by Eq.** (5)**.**

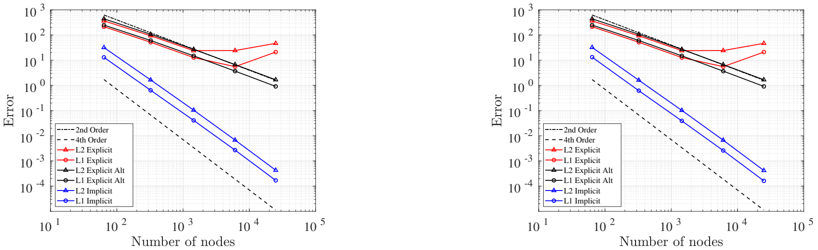

(c) Normalization given by Eq. (8)**.** **(d) Normalization given by Eq.** (7)**.**

Fig. 6 Error convergence of gradient reconstruction of the function given by Eq. (21)**, using WLSQ (red), MLSQ (black) and ILSQ (blue) gradients on high-aspect-ratio triangular grids. Effects of using different normalizations given by Eqs.** (5), (7) **or** (8)**.**

V. Conclusions and future work

An implicit least squares gradient reconstruction scheme with a compact formulation is derived and compared with a standard distance weighted explicit least squares scheme. Additionally, a modified explicit least squares scheme is formulated, which uses different weighting compared to the standard method. The schemes only use neighbouring nodal values and can be viewed as unstructured finite difference schemes. A detailed study of gradient calculation for node-centered unstructured data on regular, highly irregular and high-aspect-ratio ($AR = 2000$) grids is presented.

Compared to a standard distance weighted LSQ scheme, which uses only nodal values of nearest neighbours in the stencil, the implicit scheme also includes information from neighbouring gradient values, leading to a linear system to be solved. This allows the assumed polynomial or Taylor expansion in the least squares approach to be of higher order. In this study, a fourth-order polynomial is assumed for the implicit LSQ scheme, and a second-order polynomial is assumed for the explicit LSQ schemes.

The schemes are assessed in the capability of reconstructing the gradient of a known analytical function. The implicit LSQ shows a fourth-order scaling on all grids considered, including highly irregular quadrilateral grids, triangular grids, mixed element grids and high-aspect-ratio grids. The standard distance weighted LSQ scheme, on the other hand, fails to achieve the prescribed second-order accuracy on high-aspect-ratio grids, where even the error is increased with grid refinement. The modified explicit least squares scheme, which uses the local grid spacing in each coordinate direction in the weighting procedure, is able to achieve second-order accuracy on high-aspect-ratio grids.

The current study is planned to be followed up by an implementation of the new scheme in an unstructured compressible finite-volume flow solver, where the accuracy, feasibility and robustness will be investigated on relevant flow cases.

Acknowledgement

This work has been funded by the Swedish Governmental Agency for Innovation Systems (VINNOVA), the Swedish Defence Materiel Administration (FMV) and the Swedish Armed Forces within the National Aviation Research Programme (NFFP, Contract No. 2017–04887) and Saab Aeronautics.

References

[1] Diskin, B., T., J. L., Nielsen, E. J., Nishikawa, H., and White, J. A., "Comparison of Node-Centered and Cell-Centered Unstructured Finite-Volume Discretizations: Viscous Fluxes," *AIAA Journal*, Vol. 48, No. 7, 2010, pp. 1326–1338. https://doi.org/10.2514/1.44940.

[2] Diskin, B., and T., J. L., "Comparison of Node-Centered and Cell-Centered Unstructured Finite-Volume Discretizations: Inviscid Fluxes," *AIAA Journal*, Vol. 49, No. 4, 2011, pp. 836–854. https://doi.org/10.2514/1.J050897.

[3] Eliasson, P., "Edge, a Navier–Stokes solver for unstructured grids," *Finite Volumes for Complex Applications*, CP849, Vol. III, 2002, pp. 527–534.

[4] Eliasson, P., and Weinerfelt, P., "Recent applications of the flow solver Edge," *7th Asian CFD Conference*, 2007.

[5] Moukalled, F., Mangani, L., and Darwish, M., *The Finite Volume Method in Computational Fluid Dynamics: An Advanced Introduction with OpenFOAM and Matlab*, 1^{st} ed., Springer Publishing Company, Incorporated, 2015.

[6] Ollivier-Gooch, C., Nejat, A., and M., K., "Obtaining and Verifying High-Order Unstructured Finite Volume Solutions to the Euler Equations," *AIAA Journal*, Vol. 47, No. 9, 2009, pp. 2105–2120. https://doi.org/10.2514/1.40585.

[7] Wang, Q., Ren, Y.-X., Pan, J., and Li, W., "Compact high order finite volume method on unstructured grids III: Variational reconstruction," *Journal of Computational Physics*, Vol. 337, 2017, pp. 1–26. https://doi.org/https://doi.org/10.1016/j.jcp.2017.02.031.

[8] Nishikawa, H., "From hyperbolic diffusion scheme to gradient method: Implicit Green–Gauss gradients for unstructured grids," *Journal of Computational Physics*, Vol. 372, 2018, pp. 126–160. https://doi.org/https://doi.org/10.1016/j.jcp.2018.06.019.

[9] Lele, S. K., "Compact finite difference schemes with spectral-like resolution," *Journal of Computational Physics*, Vol. 103, No. 1, 1992, pp. 16–42. https://doi.org/https://doi.org/10.1016/0021-9991(92)90324-R.

[10] Carpenter, M. H., Gottlieb, D., and Abarbanel, S., "Stable and accurate boundary treatments for compact, high-order finite-difference schemes," *Applied Numerical Mathematics*, Vol. 12, No. 1, 1993, pp. 55–87. https://doi.org/https://doi.org/10.1016/0168-9274(93)90112-5, sPECIAL ISSUE.

[11] Visbal, M. R., and Gaitonde, D. V., "High-Order-Accurate Methods for Complex Unsteady Subsonic Flows," *AIAA Journal*, Vol. 37, No. 10, 1999, pp. 1231–1239. https://doi.org/10.2514/2.591.

[12] Shukla, R. K., and Zhong, X., "Derivation of high-order compact finite difference schemes for non-uniform grid using polynomial interpolation," *Journal of Computational Physics*, Vol. 204, No. 2, 2005, pp. 404–429. https://doi.org/https://doi.org/10.1016/j.jcp.2004.10.014.

[13] Shukla, R. K., Tatineni, M., and Zhong, X., "Very high-order compact finite difference schemes on non-uniform grids for incompressible Navier–Stokes equations," *Journal of Computational Physics*, Vol. 224, No. 2, 2007, pp. 1064–1094. https://doi.org/https://doi.org/10.1016/j.jcp.2006.11.007.

[14] Pandit, S. K., Kalita, J. C., and Dalal, D., "A transient higher order compact scheme for incompressible viscous flows on geometries beyond rectangular," *Journal of Computational Physics*, Vol. 225, No. 1, 2007, pp. 1100–1124. https://doi.org/https://doi.org/10.1016/j.jcp.2007.01.016.

[15] Pandit, S. K., and Chattopadhyay, A., "A robust higher order compact scheme for solving general second order partial differential equation with derivative source terms on nonuniform curvilinear meshes," *Computers Mathematics with Applications*, Vol. 74, No. 6, 2017, pp. 1414–1434. https://doi.org/https://doi.org/10.1016/j.camwa.2017.06.031.

[16] Fishelov, D., "A new fourth-order compact scheme for the Navier–Stokes equations in irregular domains," *Computers Mathematics with Applications*, Vol. 74, No. 1, 2017, pp. 6–25. https://doi.org/https://doi.org/10.1016/j.camwa.2016.10.020, 5th European Seminar on Computing ESCO 2016.

[17] Ferziger, J. H., and P., M., *Computational Methods for Fluid Dynamics*, 2nd ed., Springer, Berlin, 1999.

[18] Luo, H., Baum, J. D., and Löhner, R., "A discontinuous Galerkin method based on a Taylor basis for the compressible flows on arbitrary grids," *Journal of Computational Physics*, Vol. 227, No. 20, 2008, pp. 8875–8893. https://doi.org/https://doi.org/10.1016/j.jcp.2008.06.035.

[19] Strang, G., *Linear Algebra and its Application*, 2nd ed., Academic Press, 1980. https://doi.org/https://doi.org/10.1016/B978-0-12-673660-1.50003-4.

[20] Gustafsson, B., "The Convergence Rate for Difference Approximations to Mixed Initial Boundary Value Problems," *Mathematics of Computation*, Vol. 29, No. 130, 1975, pp. 396–406.

[21] Svärd, M., and Nordström, J., "On the order of accuracy for difference approximations of initial-boundary value problems," *Journal of Computational Physics*, Vol. 218, No. 1, 2006, pp. 333–352. https://doi.org/https://doi.org/10.1016/j.jcp.2006.02.014.

[22] Svärd, M., and Nordström, J., "Review of summation-by-parts schemes for initial–boundary-value problems," *Journal of Computational Physics*, Vol. 268, 2014, pp. 17–38. https://doi.org/https://doi.org/10.1016/j.jcp.2014.02.031.

[23] van der Vorst, H. A., "Bi-CGSTAB: A Fast and Smoothly Converging Variant of Bi-CG for the Solution of Nonsymmetric Linear Systems," *SIAM Journal on Scientific and Statistical Computing*, Vol. 13, No. 2, 1992, pp. 631–644. https://doi.org/10.1137/0913035.

[24] Mavriplis, D., *Revisiting the Least-Squares Procedure for Gradient Reconstruction on Unstructured Meshes*, ???? https://doi.org/10.2514/6.2003-3986.

[25] Zhang, F., "A vertex-weighted-Least-Squares gradient reconstruction," , 2017. https://doi.org/10.48550/ARXIV.1702.04518.

[26] Nishikawa, H., and White, J. A., "An efficient cell-centered finite-volume method with face-averaged nodal-gradients for triangular grids," *Journal of Computational Physics*, Vol. 411, 2020, p. 109423. https://doi.org/https://doi.org/10.1016/j.jcp.2020.109423.

Paper D

Seamless Interface Methods for Grey-Area Mitigation in Scale-Resolving Hybrid RANS-LES

M. Carlsson, S. Wallin, L. Davidson, S.H. Peng, and S. Arvidson. "Seamless Interface Methods for Grey-Area Mitigation in Scale-Resolving Hybrid RANS-LES". ***DLES13 2022.*** **2022**

Seamless interface methods for grey- area mitigation in scale-resolving hybrid RANS-LES

Magnus Carlsson[1], Stefan Wallin[2] Lars Davidson[1], Shia-Hui Peng[3], and Sebastian Arvidson[4,1]

[1] Chalmers University of Technology, Gothenburg, Sweden,
[2] KTH Royal Institute of Technology, Stockholm, Sweden,
[3] Swedish Defence Research Agency, Stockholm, Sweden
[4] Saab Aeronautics, Linköping, Sweden

1 Introduction

A new Grey-Area Mitigation (GAM) method for hybrid RANS-LES is presented. In regions of variable resolution, the transfer of turbulence energy between RANS-modeled and LES-resolved turbulence are quantified by a commutation residue term, as proposed by for PANS modeling [1]. Girimaji and Wallin showed that the commutation residue term needs to be accounted for in regions with a variable PANS parameter, f_k, which is a ratio of modeled and total turbulence energy, in order to have a proper transition from modeled to resolved turbulence. A model was proposed for this term in PANS, of which an extension was also indicated for other hybrid RANS-LES formulation based on length scales [1].

Commutation residue stemming from length scale variation was quantified by Hamba [2] for fully developed turbulent channel flow, by a filtering operation with the filter width varying between RANS and LES length scales in different regions. The magnitude of the commutation term was found in the same order as the turbulence production term. This was further investigated by Arvidson et al. in their hybrid RANS-LES method based on the $K-\omega$ model [3]. It was shown that the commutation residue term can significantly accelerate the transition from modeled to resolved turbulence, and thus effectively mitigating the grey area.

In this work, an effort has been made to exploit the formulation proposed by Girimaji and Wallin and expand it further in DES-type modeling aiming for a more rapid transition between modeled and resolved turbulent scales in the vicinity of a RANS-LES interface.

2 Mathematical formulation

The turbulence energy cascade in the spectral space is illustrated in Fig. 1 with $\kappa_c \propto 1/L_{ref}$ as the spectral cut-off wave number dividing the turbulence energy into the resolved and modeled turbulence energy, denoted by K_r and K_u, respectively. It is noted further that L_{ref} is a reference length scale. For constant resolution, where κ_c is constant in space, the energy cascade σ is responsible for

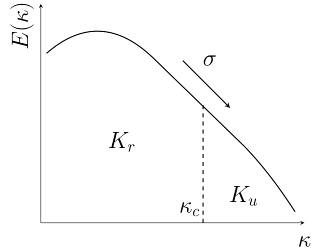

Fig. 1. Illustration of energy spectrum with cut-off wave number.

the energy exchange between the resolved and unresolved scales. With variable L_{ref}, κ_c can vary in time or space and, correspondingly, the position of the interface between K_r and K_u will change. This leads to an additional mechanism of energy exchange between K_r and K_u. Following Girimaji and Wallin [1], this energy exchange can be described by integrating the unresolved turbulent kinetic energy in spectral space

$$\frac{\mathrm{d}K_u}{\mathrm{d}t} = \frac{\mathrm{d}}{\mathrm{d}t}\int_{\kappa_c}^{\infty} E(\kappa,t)\mathrm{d}\kappa = \int_{\kappa_c}^{\infty} \frac{\mathrm{d}E}{\mathrm{d}t}\mathrm{d}\kappa - E(\kappa_c,t)\frac{\mathrm{d}\kappa_c}{\mathrm{d}t}. \tag{1}$$

The first term on the RHS represents the balance between the unresolved and dissipation considering non-varying κ_c. The second term on the RHS corresponds to energy exchange between K_r and K_u in the vicinity of κ_c, denoted by P_{Tr}. By assuming a standard spectrum in the Kolmogorov inertial subrange, $E(\kappa) = C\varepsilon^{2/3}\kappa^{-5/3}$, one can show that

$$P_{Tr} = -E(\kappa_c,t)\frac{\mathrm{d}\kappa_c}{\mathrm{d}t} = ... = -\frac{2}{3}\frac{K_u}{\kappa_c}\frac{\mathrm{d}\kappa_c}{\mathrm{d}t}, \tag{2}$$

where $\frac{d}{dt}$ is the material derivative, or advection by the resolved flow field. Using the relation $\kappa_c \propto 1/L_{ref}$, one can express the commutation residue in terms of the variation of the hybrid length scale L_{ref}:

$$P_{Tr} = \frac{2}{3}\frac{K_u}{L_{ref}}\frac{\mathrm{d}L_{ref}}{\mathrm{d}t}. \tag{3}$$

The commutation residue term P_{Tr} in Eq. (3) acts as a source/sink term in the equation for K_u. If a $K-\omega$ based hybrid model is used, as in this work, it can be shown that a corresponding term has to be added to the ω-equation, namely $-(K_u/\omega_u)P_{Tr}$ [1]. In the case of decreasing L_{ref}, energy is transferred from the RANS-modeled to the LES-resolved scales and $P_{Tr} < 0$. Energy conservation dictates that the energy transfer rate, P_{Tr}, removed from the unresolved scales must be added to the resolved scales. The energy transfer to/from the resolved scales is modelled as a diffusion term in the momentum equation [1]

$$\nu_{Tr} = \frac{P_{Tr}}{S^2}, \tag{4}$$

where $S = \sqrt{2S_{ij}S_{ij}}$. It must be emphasized that ν_{Tr} and ν_t represent different physics and should not be mixed up. For the numerical solution they can be added as:

$$\nu^* = \nu_t + \nu_{Tr}. \tag{5}$$

With increasingly refined resolution in space/time, energy is transferred from unresolved to resolved turbulence. This will bring up a negative ν_{Tr}. Decreasing resolution will, on the other hand, transfer energy from resolved to unresolved scales through positive ν_{Tr} and P_{Tr}. We limit $\nu_{Tr} \geq -\nu_t$ to ensure positive total turbulent diffusion for numerical stability. Note that Eqs. (3) and (4) are deployed in the whole computational domain.

3 Numerical setup

The computations have been conducted using the M-Edge code, which is an edge- and node-based Navier-Stokes flow solver applicable for both structured and unstructured grids [4]. The compressible Navier-Stokes equations are discretized with a finite-volume approximation and integrated in time using a 2nd-order backward difference scheme. The viscous fluxes are estimated with a 2nd-order central scheme. The inviscid fluxes are based on the low-dispersive and low-dissipative (LD2) scheme, which combines a low-dissipative convection operator with a low-dispersive reconstruction of the face values [5].

All computations have been carried out using the $K-\omega$ SST DDES model [6, 7] as base model in combination with the proposed GAM formulation. The hybrid length scale in Eq. (3) is computed as

$$L_{ref} = L_{RANS} - f_d \max(0, L_{RANS} - L_{LES}), \tag{6}$$

where $L_{RANS} = \beta^* K_u \omega_u$ and $L_{LES} = C_{DES}\mathit{\Delta}$ are the RANS and LES length scales, respectively, and f_d is the DDES shielding function. The LES filter width is computed as $\mathit{\Delta} = \tilde{\mathit{\Delta}}_\omega$ [8], which adapts the subgrid-scale based on the local vorticity direction of the flow. Furthermore, another modification of the sub-grid model aiming at acceleration of the RANS-LES transition in separated shear layers for the DDES method is evaluated. The σ-DDES model [9, 10] replaces the standard strain rate invariant S in the production term by a blended variant

$$S_{\sigma-DDES} = S - f_d \ \mathrm{pos}(L_{RANS} - L_{LES})(S - B_\sigma S_\sigma), \tag{7}$$

where $\mathrm{pos}(a) = 1$ if $a > 0$, otherwise 0. The subgrid model of SST σ-DDES then performs as the algebraic σ-model [11] instead of the Smagorinsky model in the LES domain, and the empirical constant $B_\sigma = 60$ is calibrated in decaying grid turbulence. In quasi two-dimensional flow regions, S_σ, which is the strain rate operator in the σ-model, is close to zero and ensures the decrease of the eddy viscosity in shear layers by rapidly reducing the production term in the LES mode of DDES.

4 Results and discussion

The commutation term is evaluated and verified for two different flow cases with geometry induced flow separating and mixing, the flow over a wall-mounted hump and mixing shear layer. The upstream boundary layers are treated in RANS mode, and the DDES automatically switches to LES in the separated region. Simulations using the commutation term (i.e. Eqs. (3) and (4)) are indicated by CT. The baseline case is the SST DDES version with length scale $\tilde{\Delta}_\omega$, while the variations with GAM methods are made by incorporating $\sigma - DDES$ and/or the commutation term. Figure 2 presents the Q-criterion for the two flow cases, highlighting the resolved flow features.

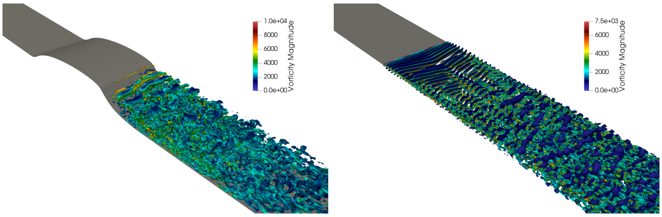

Fig. 2. Q-criterion coloured by vorticity magnitude contours for flow over wall-mounted hump (left) and mixing shear layer (right). Results are acquired using SST σ-DDES with commutation terms.

4.1 Flow over a wall-mounted hump

This flow was experimentally studied by Greenblatt et al. [12]. The Reynolds number based on the hump length c and a reference velocity U_0 (maximum free stream velocity at the inlet of the domain) is $Re_c = 9.36 \cdot 10^5$, the height of the hump is $h = 0.128c$. The flow is characterized by a large-scale separation on the downstream lean of a wall-mounted hump as well as a free shear layer emanating from the crest of the hump. The flow over the hump separates at $x/c = 0.65$ and is reattached at $x/c = 1.1$. The grid adopted in all computations has $(n_x, n_y, n_z) = (520, 128, 80)$ cells in x-, y- and z-directions, respectively, resulting in a total grid size of about $5.3 \cdot 10^6$ cells. The size of the domain in the spanwise direction is $0.4c$ and the grid-spacing is $\Delta z = 5.0 \cdot 10^{-3}c$. The time step in the simulation is $0.002c/U_0$, which ensures that the CFL number, based on the streamwise spacing δx, less than one in the entire domain.

The effect of the commutation term is presented in Fig. 4. The commutation decreases modeled K_u by activating negative P_{Tr} (see Eq. (3), which is further amplified by a positive contribution to the production term in the ω_u-equation. As a result, the modeled eddy viscosity in the free shear layer is dramatically

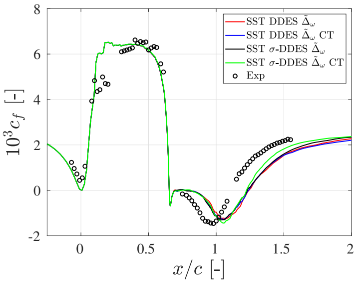

Fig. 3. Skin friction.

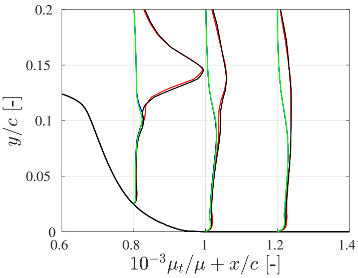

Fig. 4. Eddy viscosity.

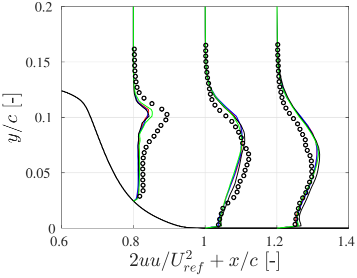

Fig. 5. Resolved streamwise stress.

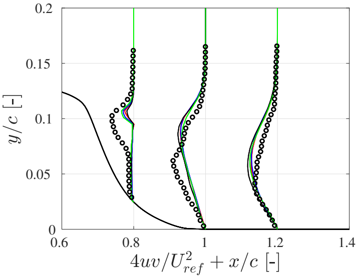

Fig. 6. Resolved shear stress.

reduced at station $x/c = 0.8$. This effect is not captured by the $\sigma - DDES$ model solely, since the $\sigma - DDES$ model only modifies the production of K_u in the LES region and does not provide an additional mechanism for reducing upstream RANS modeled eddy viscosity entering the LES domain.

The response in the resolved stresses are presented in Figs. 5 and 6. A slight increase in the streamwise stress and shear stresses can be observed at $x/c = 0.8$ for the $\sigma - DDES$ model using the commutation term, but only marginal difference is observed further downstream for the different settings. The skin friction is shown in Fig. 3, where the reattachment region is slightly better predicted by the $\sigma - DDES$ model in combination with the commutation term. However, the reattachment is located too much downstream for all cases, which implies that a reduced eddy viscosity in the LES-region due to the commutation term is not sufficient to fully trigger resolved turbulence for this flow case.

4.2 Mixing Shear Layer

The free shear layer flow was investigated experimentally by Delville [13]. The computational domain includes a very thin flat plate, with turbulent boundary layers on each side, a mixing layer is formed in the region downstream of the flat plate trailing edge. The experimental boundary layer properties at the trailing edge are presented in Table 1. The focus region, i.e. the region from the flat plate trailing edge at $x = 0$ to $x = 1$ m, is meshed with $(n_x, n_y, n_z) = (640, 196, 96)$ cells. The grid is equidistant in the streamwise x-direction and spanwise z-direction, $\mathit{\Delta} x = \mathit{\Delta} z = 1.5625$ mm. The total number of hexahedral grid cells are 13.7 million. A timestep of $\mathit{\Delta} t = 2.5 \times 10^{-}5$ second is used. The upstream boundary layers are treated in RANS mode and the DDES automatically switches to LES after the trailing edge.

Table 1. Flow parameters of mixing-layer case. Data from experiment [13].

Measure	Notation	High vel. BL	Low vel. BL
Velocity	U_∞	41.54 m/s	22.40 m/s
Thickness	δ	9.6 mm	6.3 mm
Displ. thick.	δ_1	1.4 mm	1.0 mm
Mom. thick.	θ	1.0 mm	0.73 mm
Shape factor	H	1.35	1.37
Re based on θ	Re_θ	2900	1200
Turbulence level	u'/U_∞	~ 0.3 %	~ 0.3 %

The growth of the mixing layer, the vorticity thickness, is presented in Fig. 7. The baseline model clearly underpredicts the growth of the shear layer. With either of the two GAM methods considered the results are improved. By using a combination of both $\sigma - DDES$ and the commutation term the agreement with the experimental result is significantly improved for $x > 0.2$ m. The maximum eddy viscosity at the initial part of the shear layer is shown in Fig. 8. The effect of the commutation term is large, as indicated by a rapidly reduced eddy viscosity. Without the commutation term, such a reduction is relatively slow. A reduced eddy viscosity level contributes to a rapid growth of resolved turbulence, which is visualised in Fig. 9. As shown, the resolved shear stress is better predicted at station $x = 0.2$ m, where the prediction incorporating both the commutation terms combined with σ-DDES gives the best result.

5 Conclusions

A new Grey-Area Mitigation (GAM) method is proposed in this paper. The work presents hybrid RANS-LES computations undertaken in the verification of GAM formulations incorporated into the SST DDES model. Two test cases, namely, the flow over a wall-mounted hump and a mixing shear layer have been computed. The proposed GAM method, aiming to mitigate the grey area over the RANS-LES interface, is based on a commutation term stemming from the variation of the local hybrid length scale. Furthermore, a sub-grid model enabling to reduce the eddy viscosity in a shear layer, the σ-DDES model, is also evaluated in the

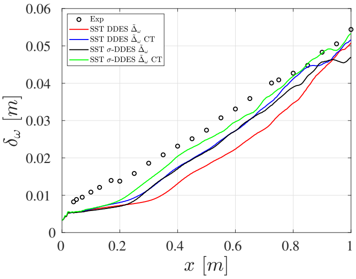

Fig. 7. Vorticity thickness.

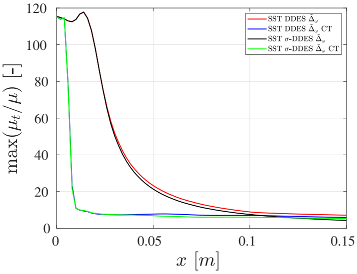

Fig. 8. Maximum eddy viscosity.

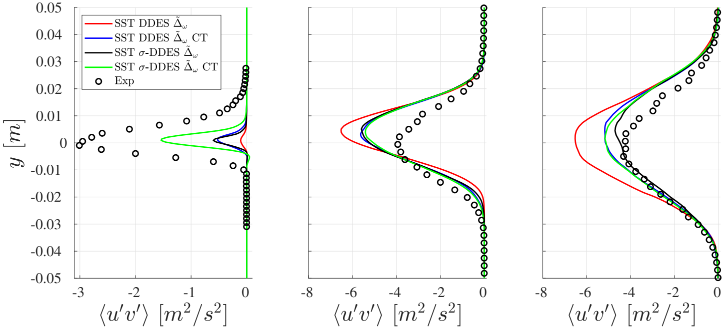

Fig. 9. Resolved shear stress at locations $x = 0.2$ m (left), $x = 0.65$ m (middle) and $x = 0.95$ m (right).

comparison. Both methods require no additional manipulation of, or explicitly defining, the RANS-LES interface and are applied in a global manner.

It is shown that the effect of both the commutation term and the $\sigma - DDES$ model improve the results for the mixing shear layer and are able to trigger a rapid transition of modeled to resolved turbulence. This is indicated improved predictions of both vorticity thickness and resolved shear stress. The effect of commutation term and the $\sigma - DDES$ model is less pronounced for the hump flow, however, where the recovery of the skin friction coefficient is only slightly better predicted.

Acknowledgement

This work has been funded by the Swedish Governmental Agency for Innovation Systems (VINNOVA), the Swedish Defence Materiel Administration (FMV) and the Swedish Armed Forces within the National Aviation Research Programme (NFFP, Contract Number 2017-04887) and Saab Aeronautics. The 2nd author (S. Wallin) would like to acknowledge all the early discussions with Prof. Sharath Girimaji on this and related topics.

References

1. Girimaji S., Wallin S.: Closure modeling in bridging regions of variable-resolution (VR) turbulence computations, *Journal of Turbulence.*, **14:1**, 72–98 (2014).
2. Hamba, F.: Analysis of filtered Navier–Stokes equation for hybrid RANS/LES simulation. *Physics of Fluids* **23:1**, 015108 (2011).
3. Arvidson S., Davidson L., Peng S.: Interface methods for grey-area mitigation in turbulence-resolving hybrid RANS-LES, *International Journal of Heat and Fluid Flow.*, **73**, 236–257 (2018).
4. Eliasson, P. : Edge, a Navier–Stokes solver for unstructured grids, *Finite Volumes for Complex Applications*, **3**, 527–534 (2002)
5. Löwe, J., Probst, A., Knopp, T., Kessler, R. : Low-Dissipation Low-Dispersion Second-Order Scheme for Unstructured Finite-Volume Flow Solvers. *AIAA Journal*, **54**, 2016.
6. Spalart, P.R., Deck, S., Shur, M.L. et al. :A New Version of Detached-eddy Simulation, Resistant to Ambiguous Grid Densities, *Theoret. Comput. Fluid Dynamics.*, **20**, 181 (2006).
7. Gritskevich, M., Garbaruk, A., Schütze, J., Menter, F. : Development of DDES and IDDES Formulations for the k-ω Shear Stress Transport Model. *Flow, Turbulence and Combustion.* **88**, (2012).
8. Shur, M.L., Spalart, P.R., Strelets, M.K. et al.: An Enhanced Version of DES with Rapid Transition from RANS to LES in Separated Flows, *Flow Turbulence Combust.*, **95**, 709–737 (2015).
9. Mockett, C., Fuchs, M., Garbaruk, A., Shur, M., Spalart, P., Strelets, M., Thiele, F., Travin, A. : Two non-zonal approaches to accelerate RANS to LES transition of free shear layers in DES Notes. *Numer. Fluid Mech. Multidiscip. Des.* **130**, 187–201, (2015).
10. Guseva, E. K. et al : Assessment of two approaches to accelerate RANS to LES transition in shear layers in the framework of ANSYS-FLUENT. *J. Phys.: Conf. Ser.*, 1038 012134, (2018).
11. Nicoud, F., Toda, H. B., Cabrit, O., Bose, S., Lee, J. : Using singular values to build a subgrid-scale model for large eddy simulations. *Phys. Fluids* **23**, 1–12, (2011).
12. Greenblatt, D., Paschal, K., Yao, C. S., Harris, J. :A Separation Control CFD Validation Test Case Part 2. Zero-Efflux Oscillatory Blowing, AIAA 2005-485. 43rd AIAA Aerospace Sciences Meeting and Exhibit. January 2005.
13. Delville J.: *La décomposition orthogonale aux valeurs propres et l'analyse de l'organisation tridimensionnelle des écoulements turbulents ci saillés libre.* PhD Thesis, Université de Poitier (1995)

Paper E

Implementation of Nonreflecting Inlet and Outlet Boundary Conditions in the Subsonic Regime for a Node-Based Compressible Solver

M. Carlsson, L. Davidson, S.H. Peng, and S. Arvidson. *Implementation of Nonreflecting Inlet and Outlet Boundary Conditions in the Subsonic Regime for a Node-Based Compressible Solver.* Tech. rep. Chalmers University of Technology, Göteborg, Sweden, Technical Report, 2021

Verification of Nonreflecting Inlet and Outlet Boundary Conditions in the Subsonic Regime for a Node-Based Compressible Solver

Magnus Carlsson[1], Lars Davidson[1], Shia-Hui Peng[1,2], and Sebastian Arvidson[1,3]

[1] *Chalmers University of Technology, SE-412 96, Gothenburg, Sweden*
[2] *Swedish Defence Research Agency, FOI, SE-16490, Stockholm, Sweden*
[3] *Saab Aeronautics, SE-581 88, Linköping, Sweden*

This paper examines the implementation of the Navier-Stokes characteristic boundary equations in a node-centered edge based compressible code. The boundary conditions are tested for injecting and transporting an analytical vortex through a subsonic inlet and a subsonic outlet, respectively. Since the analytical solution is known, any distortion from this is an error in the boundary condition. Two different implementations are evaluated, an implementation which modifies the convective flux at the boundary and a method that sets the primitive vector at the boundary. The current implementations of the non-reflecting boundary conditions does not give results comparable to results reported in the literature. The non-reflective inlet implementation performs worse than a standard incompressible dirichlet inlet, but the results are improved compared to standard incompressible static pressure oulet.

1 Introduction

Boundary conditions are an important part of a compressible solver to ensure well-posed numerical problem with unique solution of flow variables, especially for large eddy simulation (LES) and direct numerical simulation (DNS) in addressing flow-induced aero-acoustic problems. For external flows around, for example, an air vehicle immersed in a fresstream, a truncated computational domain is often taken where special attention should be paid to handling possible reflections of pressure waves at the boundaries. The nonreflecting characteristic boundary condition was initially introduced by Hedstrom [1] and Thompson [2] in solving the Euler equations, which was then further extended to the Navier-Stokes equations by Poinsot and Lele [3], namely, the Nacier-Stokes characterisc boundary conditions (NSCBC). The NSCBC approach decomposes the Navier-Stokes equations at the boundary to identitfy the contribution of waves going into the domain and waves leaving the domain. The outgoing waves are computed using one-sided derivatives and are not modified, whereas the waves leaving the domain are changed according to the boundary condition imposed. The original NSCBC approach solves a local one-dimensional inviscid (LODI) problem [3] to impose the wave amplitudes for the outgoing waves.

For outlet boundaries, it was found that including transverse terms [4, 5] in the analysis for multidimensional problems provide better damping than the one-dimensional LODI formulation. However, at in inlet these terms play a limited role and can be omitted. In LES and DNS applications, imposing turbulent fluctuations to a mean velocity profile while being nonreflecting to acoustic and numerical waves is a challenge in specifying relevant inlet boundary conditions. The vortical-flow characteristic boundary condition (VFCBC) [6] by Guézennec and Poinsot was proven to successfully be able to impose an analytical isentropic vortex and homogeneous isentropic turbulent flow into a two-dimensional domain for low speed flows, based on a Mach number expansion, as detailed in Prosser [7].

The implementation of the NSCBC is straightforward task for codes using structured (i, j, k) grids, while it may become more challenging on a unstructured grid, as exampled in previous work, see e.g. [6, 8]. In this paper, we have investigated the implementation of the NSCBC for a node-centered finite-volume solver. In Section 2, the theory for the NSCBC is outlined along with the conditions for subsonic non-reflecting inflow and outflow boundaries. The numerical methods adopted in the computation are introduced in Section 3. Results are then presented and analyzed in Section 4. The work is concluded in Section 5.

2 Navier-Stokes Characteristic Boundary Conditions

When solving the compressible Navier-Stokes equations, five characteristic waves are introduce into the domain. In case of an inflow boundary, four waves are entering the domain while one is leaving the domain. In case of an outflow boundary, four are leaving the domain while one is entering. It is crucial to introduce dampening factors at the boundaries to mitigate the numerical and physical waves leaving the domain.

The NSCBC approach [3] uses the Navier-Stokes equations in the characteristic form in which outgoing and incoming waves can be identified. The outgoing waves can be computed from interior points. The incoming waves which come from outside of the domain must be prescribed to close the boundary problem. The characteristic equations of a boundary with a normal in the x_1-direction are:

$$
\begin{aligned}
\frac{\partial \rho}{\partial t} + d_1 + \frac{\partial \rho u_2}{\partial x_2} + \frac{\partial \rho u_3}{\partial x_3} &= 0, & (1)\\
\frac{\partial \rho u_1}{\partial t} + u_1 d_1 + \rho d_3 + \frac{\partial \rho u_1 u_2}{\partial x_2} + \frac{\partial \rho u_1 u_3}{\partial x_3} &= \frac{\partial t_{1j}}{\partial x_j} + \rho b_1, & (2)\\
\frac{\partial \rho u_2}{\partial t} + u_2 d_1 + \rho d_4 + \frac{\partial \rho u_2 u_2}{\partial x_2} + \frac{\partial \rho u_2 u_3}{\partial x_3} &= -\frac{\partial p}{\partial x_2} + \frac{\partial t_{2j}}{\partial x_j} + \rho b_2, & (3)\\
\frac{\partial \rho u_3}{\partial t} + u_3 d_1 + \rho d_5 + \frac{\partial \rho u_3 u_2}{\partial x_2} + \frac{\partial \rho u_3 u_3}{\partial x_3} &= -\frac{\partial p}{\partial x_3} + \frac{\partial t_{3j}}{\partial x_j} + \rho b_3, & (4)\\
\frac{\partial \rho E}{\partial t} + \frac{1}{2} u_i u_i d_1 + \frac{d_2}{\gamma - 1} + \rho u_1 d_3 + \rho u_2 d_4 + \rho u_3 d_5 + \frac{\partial \rho u_2 H}{\partial x_2} + \frac{\partial \rho u_3 H}{\partial x_3} &= \frac{\partial \left(-q_{Lj} + t_{ij} u_i\right)}{\partial x_j} & (5)
\end{aligned}
$$

The system of Eqs. (1) - (5) contains derivatives normal to the x_1-boundary (d_1 to d_5). The d_i are functions of the characteristic wave amplitudes [3]

$$
\mathbf{d} = \begin{bmatrix} d_1 \\ d_2 \\ d_3 \\ d_4 \\ d_5 \end{bmatrix} = \begin{bmatrix} \frac{1}{c^2}\left[\mathcal{L}_2 + \frac{1}{2}\left(\mathcal{L}_5 + \mathcal{L}_1\right)\right] \\ \frac{1}{2}\left[\mathcal{L}_5 + \mathcal{L}_1\right] \\ \frac{1}{2\rho c}\left[\mathcal{L}_5 - \mathcal{L}_1\right] \\ \mathcal{L}_3 \\ \mathcal{L}_4 \end{bmatrix} = \begin{bmatrix} \frac{\partial \rho u_1}{\partial x_1} \\ \rho c^2 \frac{\partial u_1}{\partial x_1} + u_1 \frac{\partial p}{\partial x_1} \\ u_1 \frac{\partial u_1}{\partial x_1} + \frac{1}{\rho}\frac{\partial p}{\partial x_1} \\ u_1 \frac{\partial u_2}{\partial x_1} \\ u_1 \frac{\partial u_3}{\partial x_1} \end{bmatrix} \tag{6}
$$

where c is the local speed of sound given by $c^2 = \gamma p/\rho$ and the $\mathcal{L}_i$ are the amplitude variation of the i'th characteristic wave crossing the boundary

$$
\mathcal{L} = \begin{bmatrix} \mathcal{L}_1 \\ \mathcal{L}_2 \\ \mathcal{L}_3 \\ \mathcal{L}_4 \\ \mathcal{L}_5 \end{bmatrix} = \begin{bmatrix} \lambda_1 \left(\frac{\partial p}{\partial x_1} - \rho c \frac{\partial u_1}{\partial x_1}\right) \\ \lambda_2 \left(c^2 \frac{\partial \rho}{\partial x_1} - \frac{\partial p}{\partial x_1}\right) \\ \lambda_3 \frac{\partial u_2}{\partial x_1} \\ \lambda_4 \frac{\partial u_3}{\partial x_1} \\ \lambda_5 \left(\frac{\partial p}{\partial x_1} + \rho c \frac{\partial u_1}{\partial x_1}\right) \end{bmatrix} \tag{7}
$$

propagating at the characteristic velocities:

$$
\begin{aligned}
\lambda_1 &= u_1 - c & (8)\\
\lambda_2 =\lambda_3 &= \lambda_4 = u_1 & (9)\\
\lambda_5 &= u_1 + c & (10)
\end{aligned}
$$

λ_1 and λ_5 are the velocities of sound waves moving either in the negative or positive direction. All the other characteristic velocities are convection velocities. For the outgoing waves, the $\mathcal{L}_i's$ may be computed using one sided differences with interior points and values from previous time steps using (7). The incoming waves can be determined from the LODI assumption. Once all waves are computed, balance equations are used to advance the sytem in time. Under the LODI assumption, the flow is assumed to be locally one-dimensional and inviscid. The equations of the primitive variables on the boundary become [3] (diffusive terms and source terms are neglected):

$$\frac{\partial \mathbf{U}}{\partial t} = \begin{bmatrix} \frac{1}{c^2}\left[\mathcal{L}_2 + \frac{1}{2}\left(\mathcal{L}_5 + \mathcal{L}_1\right)\right] \\ \frac{1}{2\rho c}\left[\mathcal{L}_5 - \mathcal{L}_1\right] \\ \mathcal{L}_3 \\ \mathcal{L}_4 \\ \frac{1}{2}\left[\mathcal{L}_5 + \mathcal{L}_1\right] \end{bmatrix} + \begin{bmatrix} \frac{1}{c^2}\left[\mathcal{T}_2 + \frac{1}{2}\left(\mathcal{T}_5 + \mathcal{T}_1\right)\right] \\ \frac{1}{2\rho c}\left[\mathcal{T}_5 - \mathcal{T}_1\right] \\ \mathcal{T}_3 \\ \mathcal{T}_4 \\ \frac{1}{2}\left[\mathcal{T}_5 + \mathcal{T}_1\right] \end{bmatrix} = \begin{bmatrix} 0 \\ 0 \\ 0 \\ 0 \\ 0 \end{bmatrix} \tag{11}$$

where $\mathbf{U} = (\rho, u_1, u_2, u_3, p)$ is the primitive variable vector. The extension of the LODI equations to multidimensional problems is achieved by introducing the transverse wave amplitudes:

$$\mathcal{T} = \begin{bmatrix} \mathcal{T}_1 \\ \mathcal{T}_2 \\ \mathcal{T}_3 \\ \mathcal{T}_4 \\ \mathcal{T}_5 \end{bmatrix} = \begin{bmatrix} u_t\left(\frac{\partial p}{\partial x_t} - \rho c \frac{\partial u_1}{\partial x_t}\right) + \gamma p \frac{\partial u_t}{\partial x_t} \\ u_t\left(c^2 \frac{\partial \rho}{\partial x_t} - \frac{\partial p}{\partial x_t}\right) + c^2 \rho \frac{\partial u_t}{\partial x_t} - \gamma p \frac{\partial u_t}{\partial x_t} \\ u_t \frac{\partial u_2}{\partial x_t} + \frac{1}{\rho}\frac{\partial p}{\partial x_2} \\ u_t \frac{\partial u_3}{\partial x_t} + \frac{1}{\rho}\frac{\partial p}{\partial x_3} \\ u_t\left(\frac{\partial p}{\partial x_t} + \rho c \frac{\partial u_1}{\partial x_t}\right) + \gamma p \frac{\partial u_t}{\partial x_t} \end{bmatrix} \quad (t = 2, 3). \tag{12}$$

The inclusion of the transverse terms (12) are essential for estimating incoming waves at an outlet. At an inlet these terms plays a limited role [6] and can be neglected to recover the original LODI assumption. Equation (11) can be written in characteristic form of the so-called effective boundary conditions (Yoo et al. [4]):

$$\begin{bmatrix} \left(\frac{\partial p}{\partial t} - \rho c \frac{\partial u_1}{\partial t}\right) \\ \left(c^2 \frac{\partial \rho}{\partial t} - \frac{\partial p}{\partial t}\right) \\ \frac{\partial u_2}{\partial t} \\ \frac{\partial u_3}{\partial t} \\ \left(\frac{\partial p}{\partial t} + \rho c \frac{\partial u_1}{\partial t}\right) \end{bmatrix} + \begin{bmatrix} \mathcal{L}_1 \\ \mathcal{L}_2 \\ \mathcal{L}_3 \\ \mathcal{L}_4 \\ \mathcal{L}_5 \end{bmatrix} + \begin{bmatrix} \mathcal{T}_1 \\ \mathcal{T}_2 \\ \mathcal{T}_3 \\ \mathcal{T}_4 \\ \mathcal{T}_5 \end{bmatrix} = \begin{bmatrix} 0 \\ 0 \\ 0 \\ 0 \\ 0 \end{bmatrix} \tag{13}$$

Depending on the type of boundary, inflow or outflow which is considered here, the wave amplitudes can be determined by Eq. (13).

2.1 Subsonic non-reflecting outflow

For a subsonic outflow, all waves go out, except the acoustic wave traveling at speed $u_1 - c$ corresponding to $\mathcal{L}_1$. $\mathcal{L}_i$ $(i = 2, \ldots, 5)$ are directly determined by the expression in Eq. (7). $\mathcal{L}_1$ is computed using Eq. (13):

$$\left(\frac{\partial p}{\partial t} - \rho c \frac{\partial u_1}{\partial t}\right) + \mathcal{L}_1 + \mathcal{T}_1 = 0 \tag{14}$$

The outlet pressure is enforced to be p_∞, which is done by introducing a relaxation term and a constant β:

$$\left(\frac{\partial p}{\partial t} - \rho c\frac{\partial u_1}{\partial t}\right) + K(p - p_\infty) + \beta\mathcal{T}_1 = 0 \tag{15}$$

where K is a relaxation term for the pressure. Combining (14) and (15) gives the following expression for the incoming wave amplitude:

$$\mathcal{L}_1 = K(p - p_\infty) + (\beta - 1)\mathcal{T}_1 \tag{16}$$

where $\beta \in [0, 1]$ is a transverse damping parameter. When the parameter β is set to one, the LODI assumption is recovered. It is found in [6] that using the mean Mach number averaged in space over the exit section give good dampening properties:

$$\beta = \beta(t) = \overline{M}(t) = \overline{\left(\frac{u_1(\mathbf{x}, t)}{c(\mathbf{x}, t)}\right)} \tag{17}$$

The pressure relaxation coefficients K is chosen as [9]

$$K = \frac{\sigma c(1 - M^2)}{L} \tag{18}$$

where M is the maximum Mach number on the boundary, L and c are a characteristic length and a typical sound speed of the domain. The factor σ is a reduced scaling factor and is commonly chosen as 0.25 [3,4]. A non-zero relaxation term makes the outlet partially reflecting, but prevents the outlet pressure to drift from its target value p_∞.

2.2 Subsonic non-reflecting inflow

For a subsonic inlet, four incoming waves $\mathcal{L}_2, \ldots, \mathcal{L}_5$ must be imposed, which is equivalent to imposing the three velocity components u_i and the temperature T. The $\mathcal{L}_1$ wave is computed from the interior using Eq. (7). The inlet is imposed to be isentropic, which is achieved by setting $\mathcal{L}_2$ to zero. The remaining incoming waves are determined by Eq. (11), where the transverse terms are omitted since they play a insignificant role at an inlet. For injecting a velocity signal (u_1^t, u_2^t, u_3^t), we set:

$$\begin{aligned}
\mathcal{L}_2 &= 0 \\
\mathcal{L}_3 &= -\frac{\partial u_2^t}{\partial t} + 2K(u_2 - u_2^t) \\
\mathcal{L}_4 &= -\frac{\partial u_3^t}{\partial t} + 2K(u_3 - u_3^t) \\
\mathcal{L}_5 &= \rho c\left(-\frac{\partial u_1^t}{\partial t} + 2K(u_1 - u_1^t)\right)
\end{aligned} \tag{19}$$

The (u_1^t, u_2^t, u_3^t) are the target velocities, either coming from a steady mean velocity profile or an unsteady velocity signal. The time derivative terms in Eq. (19) are computed with Eq. (22). The relaxation terms like $(u_1 - u_1^t)$ prevent the inlet velocities to drift from their target values. The relaxation coefficients K is chosen as [9, 10]

$$K = \frac{\sigma c}{L} \tag{20}$$

where L, c and σ are chosen as in Eq. (20).

3 Numerical Method

The flow solver used in this paper is the M-Edge code, which is an edge- and node-based Navier-Stokes flow solver applicable for both structured and unstructured grids [11, 12]. The compressible Navier-Stokes equations are discretized with a finite-volume approximation and is integrated in time using a 2nd-order backward difference scheme. A dual-time stepping methodology using an explicit low-storage multistage Runge-Kutta scheme accelerated by local-timestepping and full-approximation storage (FAS) multigrid [13] is used. The boundary conditions are based on a weak formulation in which a set of temporary flow variables are computed and used in the calculations of the boundary flux added to the residual. The residual is then used to update all unknown variables including the boundary values [14]. The inviscid fluxes are based on the LD2 scheme, which combines a low-dissipative convection operator with a low-dispersive reconstruction of the face values [15].

3.1 Implementation for Unstructured Grid

Consider a boundary node (in 2D case for easy demonstration) with a corresponding dual-grid as shown in Fig. 1. Two implementation strategies of the NSCBC are tested. Method 1 computes the vector **d** in Eq. (6) from the known or imposed characteristic waves $\mathcal{L}_i$, and are directly injected as source terms in the system of Equations (1) - (5) at the boundary nodes. Since the convective terms normal to the boundary has been replaced by the **d** vector, the convective contribution in the numerical scheme normal to the boundary from other neighbouring nodes is canceled. This method is similar to the methods reported by Widenhorn et al. [16] and Granet et al. [17].

Method 2 solves the system (11) and sets the primitive variables vector at the boundary

$$\mathbf{U}_b = \begin{bmatrix} \rho_b \\ u_{1,b} \\ u_{2,b} \\ u_{3,b} \\ p_b \end{bmatrix} \tag{21}$$

There is no modification to the numerical scheme at the boundary nodes. In an edge-based solver, the boundary nodes can either be solved for by a weak boundary condition [14], or fixed when using a strong boundary condition. The time derivative is computed using the implicit backwards Euler in M-Edge

$$\frac{\partial \phi}{\partial t} \approx \frac{\beta_{n+1}\phi^{n+1} + \beta_n \phi^n + \beta_{n-1}\phi^{n-1}}{\Delta t} \tag{22}$$

Thus, the updated boundary value for the next time step is computed as:

$$\mathbf{U}_b^{*,n+1} = \frac{1}{\beta_{n+1}} \left(-\beta_n \mathbf{U}_b^n - \beta_{n-1}\mathbf{U}_b^{n-1} + \Delta t \frac{\partial \mathbf{U}_b^{n+1}}{\partial t} \right) \tag{23}$$

To enforce the weak boundary condition, the new boundary value is updated as

$$\mathbf{U}_b^{n+1} = \mathbf{U}_b^{*,n+1} + \alpha(\mathbf{U}_b^n - \mathbf{U}_b^{*,n+1}) \tag{24}$$

where α is a penalty factor and has stability limit of $\alpha \geq 0.5$. The contribution from the boundary values are then added to the residuals through a boundary flux

$$R_{i,b} = R_{i,b}^* + F(\mathbf{U}_b^{n+1}) \tag{25}$$

where F is the convective flux as a function of the primitive variables vector. To enforce a strong boundary condition, the new value is set to the updated boundary value

$$\mathbf{U}_b^{n+1} = \mathbf{U}_b^{*,n+1} \tag{26}$$

with the residuals of the boundary nodes set to zero.

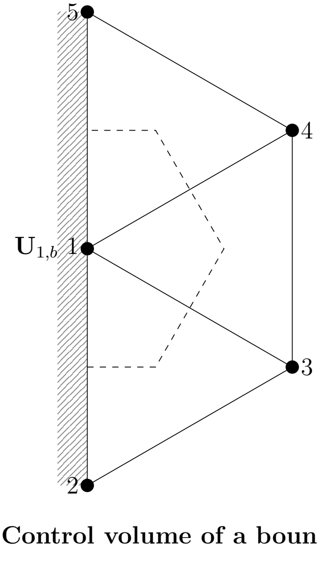

Figure 1. Control volume of a boundary node.

4 Verification in Propagating a 2-D Inviscid Vortex

To evaluate the implementation and functionality of the nonreflecting boundary condition to handle outgoing vortices, a typical convected vortex case [3, 5] is considered. The velocity field of a vortex convected by a steady flow is defined using the stream function:

$$\begin{pmatrix} u_1 \\ u_2 \end{pmatrix} = \begin{pmatrix} \frac{\partial \psi}{\partial X_2} \\ -\frac{\partial \psi}{\partial X_1} \end{pmatrix} \text{ and } \psi = C \exp\left(-\frac{r^2}{2r_v^2}\right) \tag{27}$$

where $r = \sqrt{X_1^2 + X_2^2}$, C is the vortex strength, and r_v is a characteristic radius. From Eq. (27), the radial and tangential velocity fields are given as

$$u_r = 0 \text{ and } u_\theta = \frac{Cr}{r_v^2} \exp\left(-\frac{r^2}{2r_v^2}\right) \tag{28}$$

and the vorticity distribution is given by

$$\omega(r) = C \left[\frac{2r_v^2 - r^2}{r_v^4}\right) \exp\left(-\frac{r^2}{r_v^2}\right] \tag{29}$$

The corresponding analytical pressure field is given as

$$p(r) = p_0 \exp\left(-\frac{\gamma}{2}\left(\frac{C}{r_v c}\right)^2 \exp\left(-\frac{r^2}{r_v^2}\right)\right) \tag{30}$$

These results are expressed in a reference frame of (X_1, X_2) attached to the vortex, which is traveling with the speed of the free stream velocity $(u_\infty, 0)$. The analytical results show that the vortex should propagate undisturbed through the computational domain.

4.1 Test-Case Conditions

The computational domain is a 2-D square box of dimension $L = 1$ mm with a resolution of 64^2 cells. The air flow has the following ambient conditions, $p_0 = 101.3$ kPa, $T_0 = 300$ K. The vortex strength C is set to 5×10^{-3} m^2/s, producing a maximum vortex induced velocity of 30 m/s. r_v is 0.1 mm and the free stream velocity is varied to give locally a boundary condition that varies between an inlet/outlet. The top and bottom boundaries are set to periodic boundaries. The Euler equations are solved and thus all viscous terms are set to zero in Eqs. (1) - (5).

4.2 Subsonic Inlet

The subsonic inlet is tested for two different free stream velocities, $u_\infty = 20$ m/s and $u_\infty = 100$ m/s. Three nonreflecting methods are compared to a standard Dirichlet inlet, where the target velocity

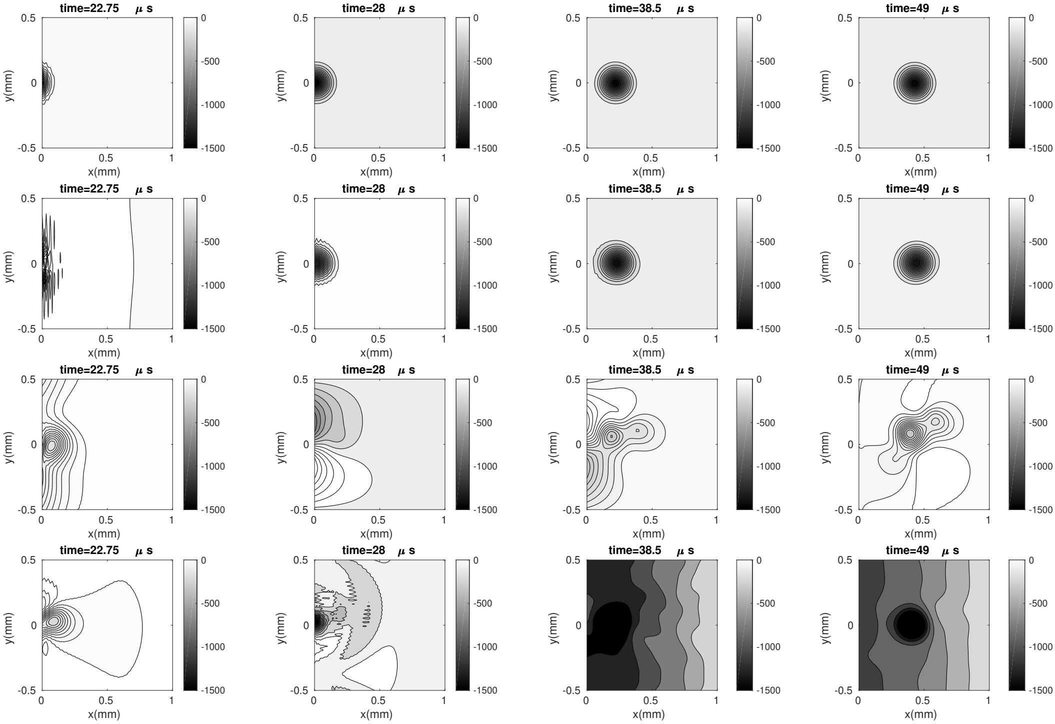

Figure 2. Pressure contours $P - P_0$ for inlet case, $M_\infty = 0.0585$. Rows from top to bottom: Dirichlet inlet, Method 2 strong NSC inlet with $\sigma = 0$, Method 1 with $\sigma = 0$, Method 1 with $\sigma = 50$. σ is used in Eq. (20).

and density are prescribed and the pressure is extrapolated from inside the domain. Method 1 is tested for σ in Eq .(20) set to 0 and 50, Method 2 is tested for $\sigma = 0$ using the strong implementation. Note that for this case, the correct injection of the vortex should be achieved even for $\sigma = 0$, according to results reported in [6]. The results for the weak implementation of Method 2 are not shown since it diverges after a couple of time steps for any values of σ and α tested, the reason is still unknown. The pressure contours, stream wise velocity contours and vorticity contours for $u_\infty = 20$ m/s, which corresponds to a free stream Mach number of 0.0585, are shown in Figs. 2 - 4. Note that for this case the inlet becomes locally an outlet as the vortex pass through the boundary.

The dirichlet inlet injects the vortex reasonably well, the result matches almost perfectly with the analytical results for pressure, stream wise velocity and vorticity. Method 1 fails to inject the vortex for $\sigma = 0$, where the shape of the vortex is completely lost compared to the analytical solution, as shown in Figs. 2 - 4. However, when the target velocity is enforced with a very large relaxation parameter $\sigma = 50$, the velocity and vorticity contours shows some resemblance with the analytical solution, as shown in Figs. 3 and 4, respectively. The pressure field is however heavily distorted, as shown in Fig. 2. Method 2 injects the velocity and vorticity signal fairly well as shown

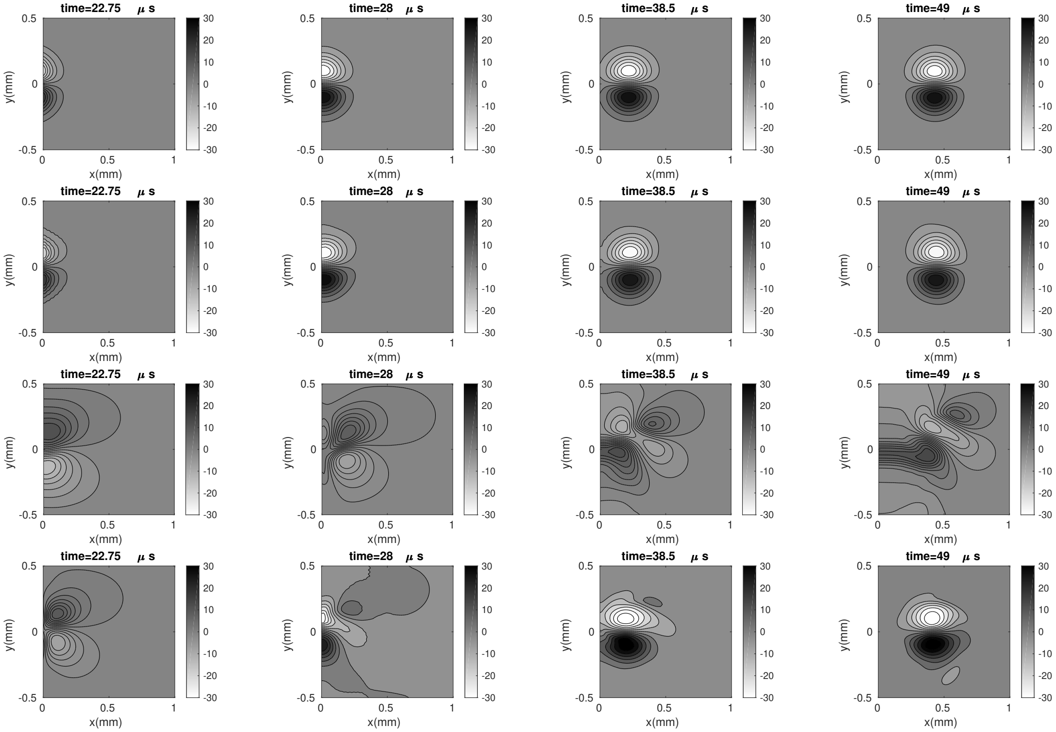

Figure 3. Streamwise velocity contours $u_1 - u_\infty$ for inlet case, $M_\infty = 0.0585$. Rows from top to bottom: Dirichlet inlet, Method 2 strong NSC inlet with $\sigma = 0$, Method 1 with $\sigma = 0$, Method 1 with $\sigma = 50$. σ is used in Eq. (20).

in Figs. 3 and 4. A checkerboard pattern is observed in the pressure field for $t = 22.75\mu s$ when the vortex enters the domain, this effect seems to be disappearing for later simulation times.

The pressure, stream wise velocity and vorticity contours for $u_\infty = 100$ m/s, which corresponds to a free stream Mach number of 0.2924, are shown in Figs. 5 - 7. The dirichlet inlet performs equally well as in the previous case, where the vortex shape is preserved in pressure, velocity and vorticity. Method 1 fails to reproduced the vortex for $\sigma = 0$, but the velocity field in Fig. 6 for $\sigma = 50$ resembles the analytical solution very well. The core of the vortex is well represented in the pressure field, as shown Fig. 5, but slight disturbance is present around the vortex for times $t = 7.35\mu s$ and $t = 10.15\mu s$.

4.3 Subsonic Outlet

The subsonic outlet is tested for two freestream velocities, $u_\infty = 20$ m/s and $u_\infty = 100$ m/s. Two nonreflecting methods are compared with a standard static pressure outlet, where the target pressure is prescribed and the velocity and density are extrapolated from inside the domain. Both Method

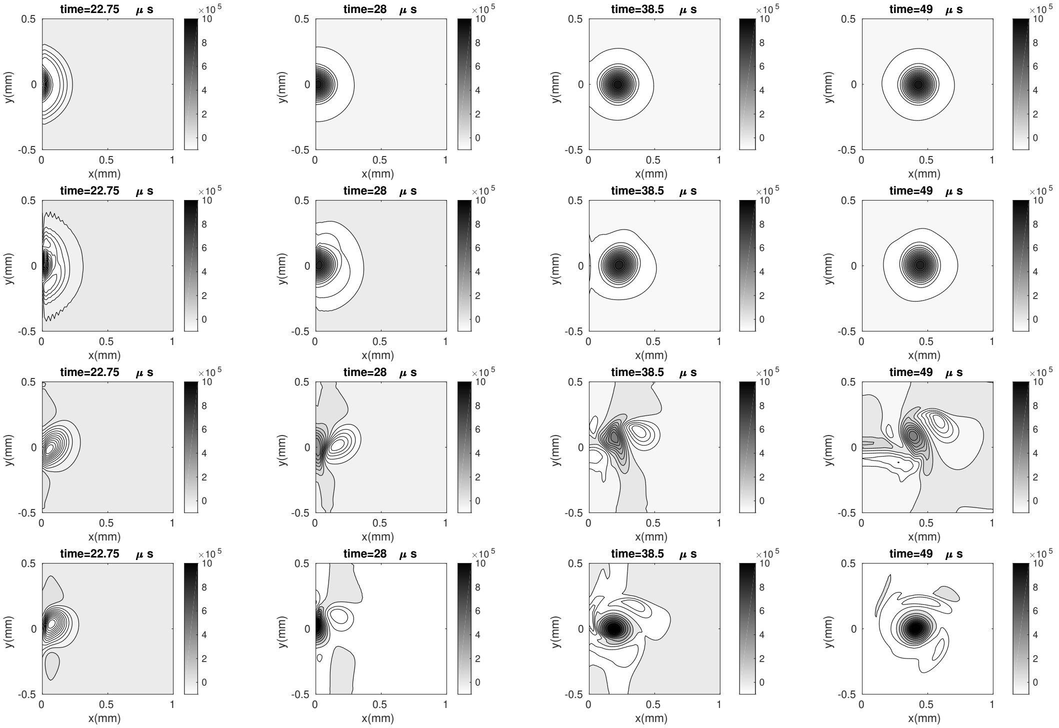

Figure 4. Vorticity contours ω for inlet case, $M_\infty = 0.0585$. Rows from top to bottom: Dirichlet inlet, Method 2 strong NSC inlet with $\sigma = 0$, Method 1 with $\sigma = 0$, Method 1 with $\sigma = 50$. σ is used in Eq. (20).

1 and Method 2 are tested for $\sigma = 0.25$, the recommended value for the relaxation parameter. For Method 2, only the strong implementation is shown since the the weak implementation diverges for any values of σ and α tested after a couple of time steps. The pressure contours, stream wise velocity contours and vorticity contours for $u_\infty = 20$ m/s are shown in Figs. 8 - 10, the same contours are shown in Figs. 11 - 13 for $u_\infty = 100$ m/s.

The first case $u_\infty = 20$ m/s creates a local inlet when the vortex passes through the exit. As shown Fig. 8 , Method 1 creates the least distortion in the pressure contours, the pressure is completely reflected with the static pressure prescribed and there is a strong checkerboard pattern for Method 2. Similar checkerboard patterns are observed for the contours of the stream wise velocity and vorticity in Figs. 9 and 10, the least distortion of the vortex is observed for Method 1.

The last case for $u_\infty = 100$ m/s is shown in Figs. 11 - 13. The static pressure outlet behaves similarly compared to Method 1, with minimal reflections from the outlet. Method 2 is capable of transporting out the vortex but with a strong checkerboard pattern observed in pressure, stream wise velocity and vorticity contours.

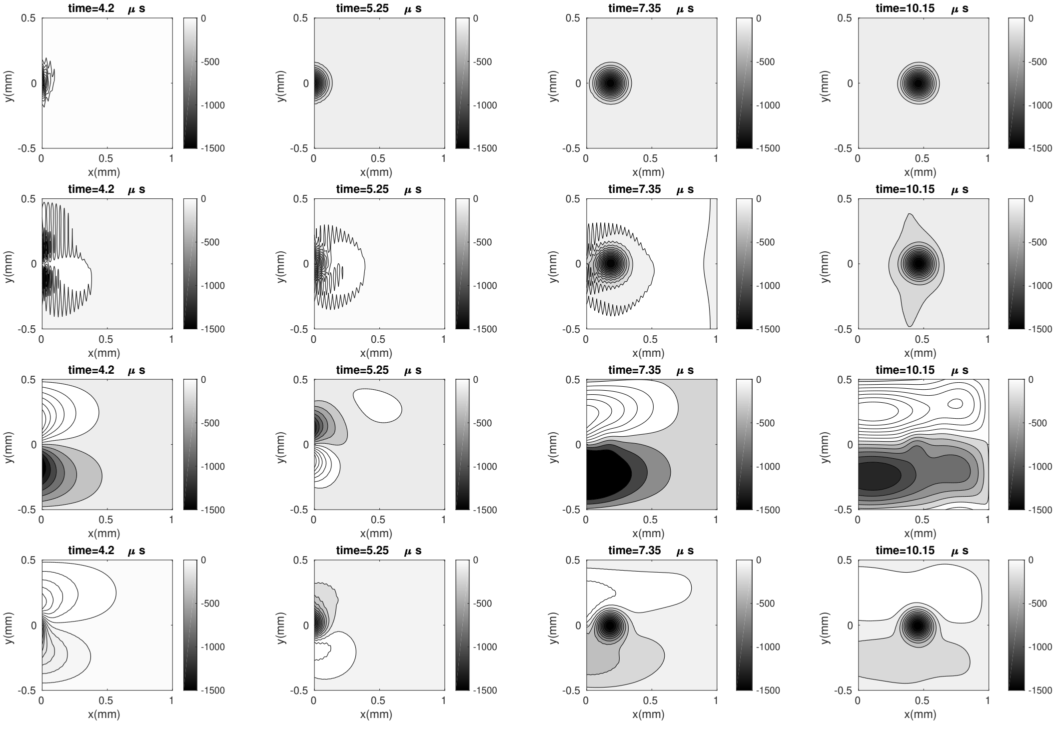

Figure 5. Pressure contours $P - P_0$ for inlet case, $M_\infty = 0.2924$. Rows from top to bottom: Dirichlet inlet, Method 2 strong NSC inlet with $\sigma = 0$, Method 1 with $\sigma = 0$, Method 1 with $\sigma = 50$. σ is used in Eq. (20).

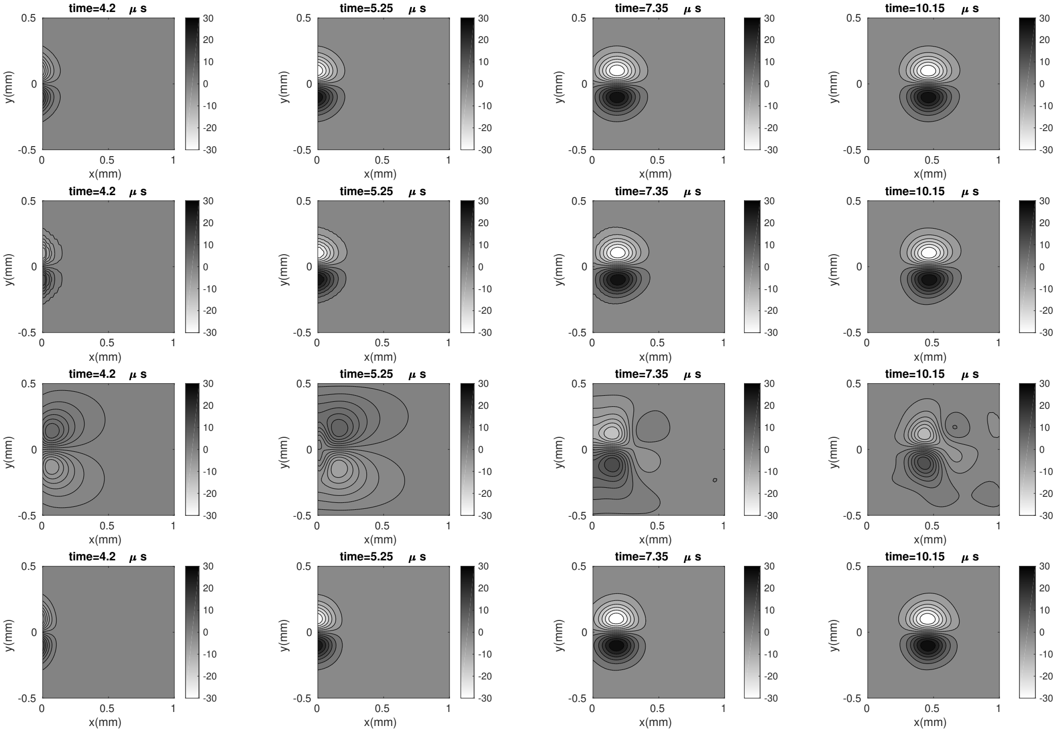

Figure 6. Streamwise velocity contours $u_1 - u_\infty$ for inlet case, $M_\infty = 0.2924$. Rows from top to bottom: Dirichlet inlet, Method 2 strong NSC inlet with $\sigma = 0$, Method 1 with $\sigma = 0$, Method 1 with $\sigma = 50$. σ is used in Eq. (20).

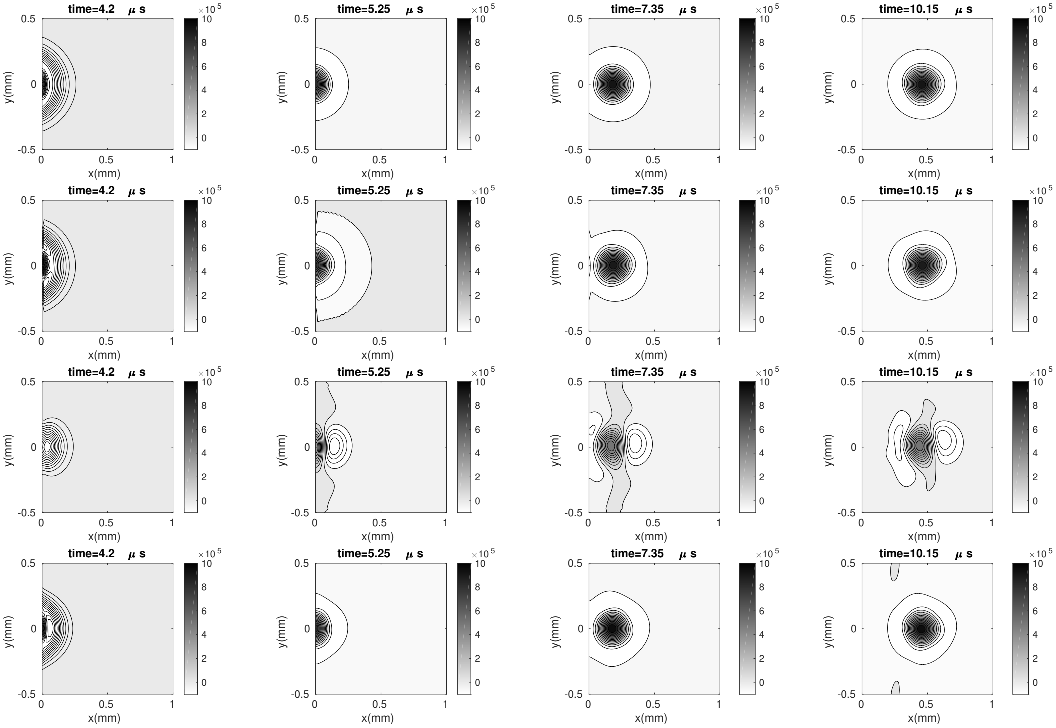

Figure 7. Vorticity contours ω for inlet case, $M_\infty = 0.2924$. Rows from top to bottom: Dirichlet inlet, Method 2 strong NSC inlet with $\sigma = 0$, Method 1 with $\sigma = 0$, Method 1 with $\sigma = 50$. σ is used in Eq. (20).

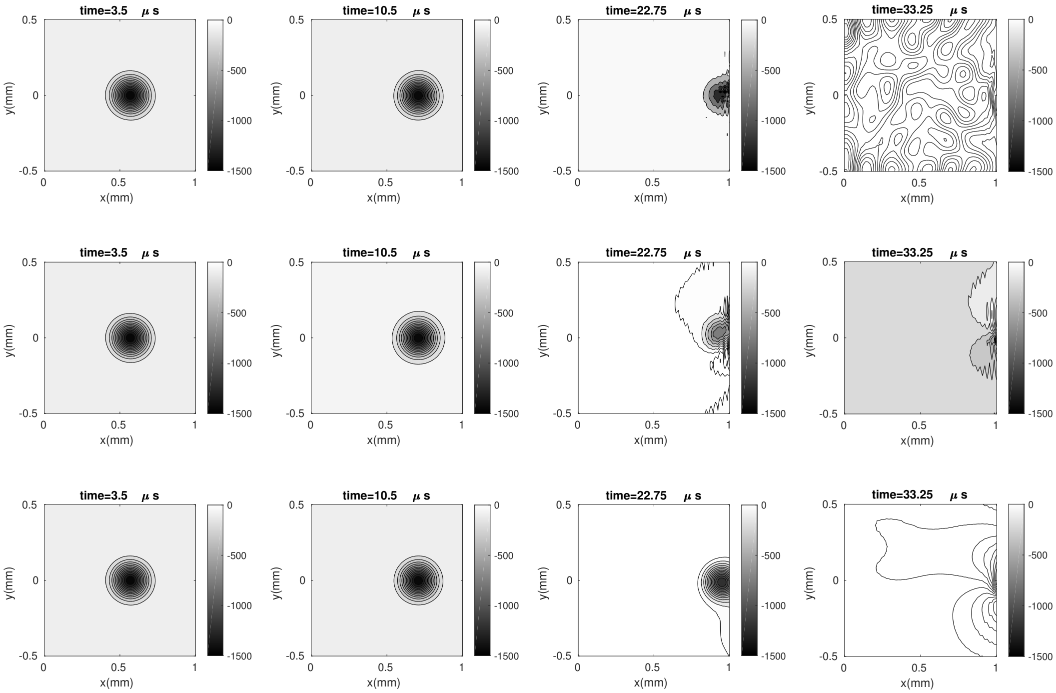

Figure 8. Pressure contours $P - P_0$ for outlet case, $M_\infty = 0.0585$. Rows from top to bottom: Weak static pressure outlet, Method 2 strong NSC inlet with $\sigma = 0.25$, Method 1 with $\sigma = 0.25$, σ is used in Eq. (18).

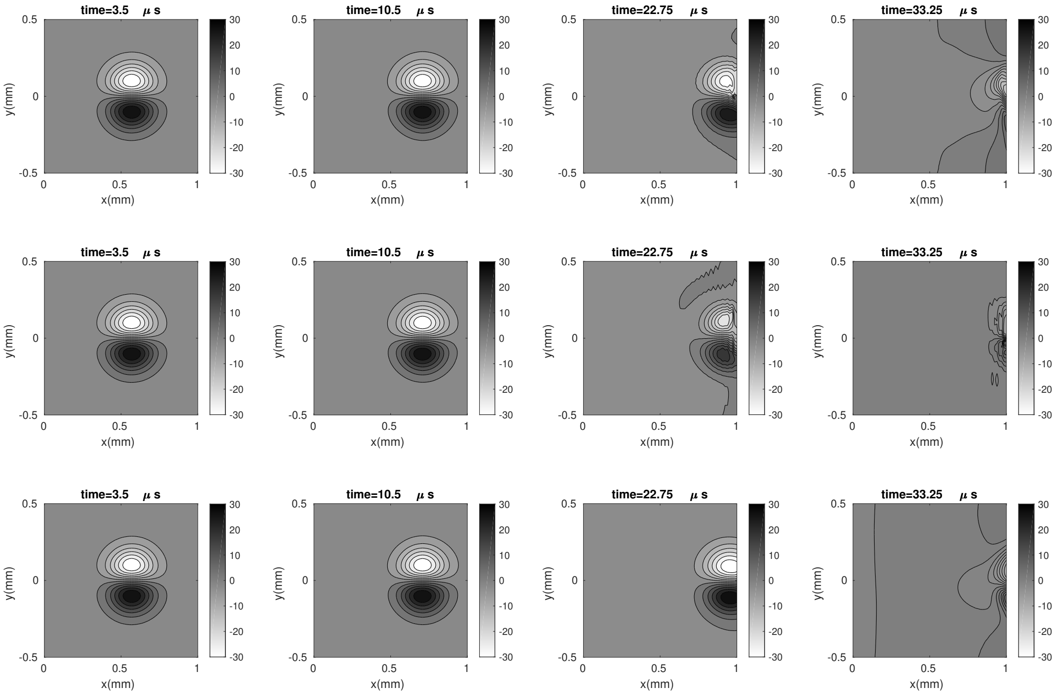

Figure 9. Streamwise velocity contours $u_1 - u_\infty$ for outlet case, $M_\infty = 0.0585$. Rows from top to bottom: Weak static pressure outlet, Method 2 strong NSC inlet with $\sigma = 0.25$, Method 1 with $\sigma = 0.25$, σ is used in Eq. (18).

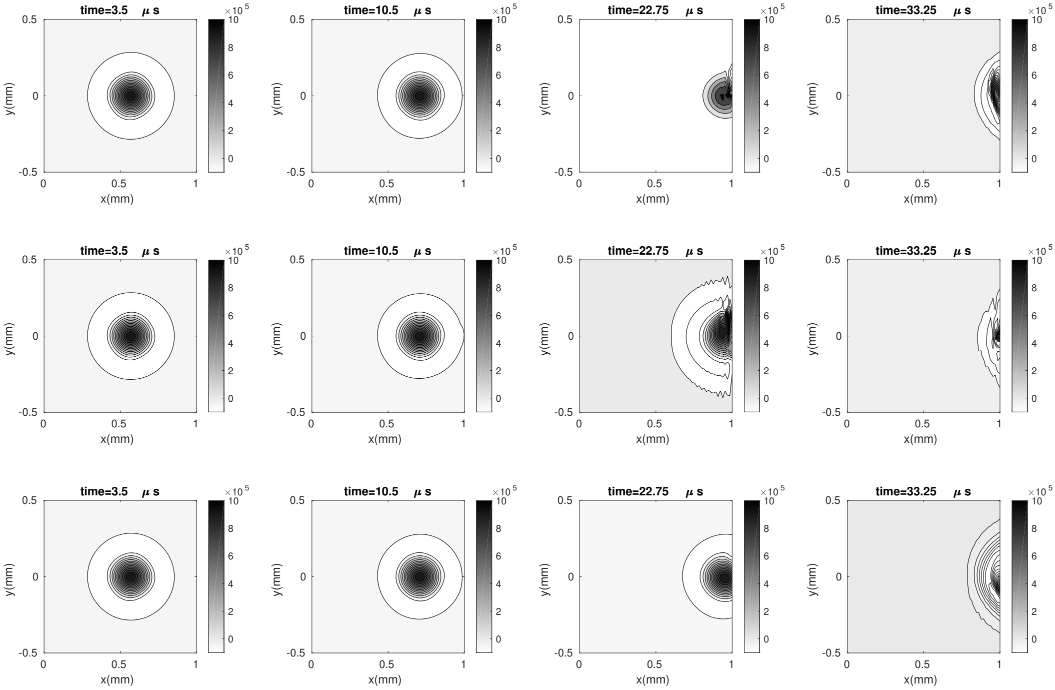

Figure 10. Vorticity contours ω for inlet case, $M_\infty = 0.0585$. Rows from top to bottom: Weak static pressure outlet, Method 2 strong NSC inlet with $\sigma = 0.25$, Method 1 with $\sigma = 0.25$, σ is used in Eq. (18).

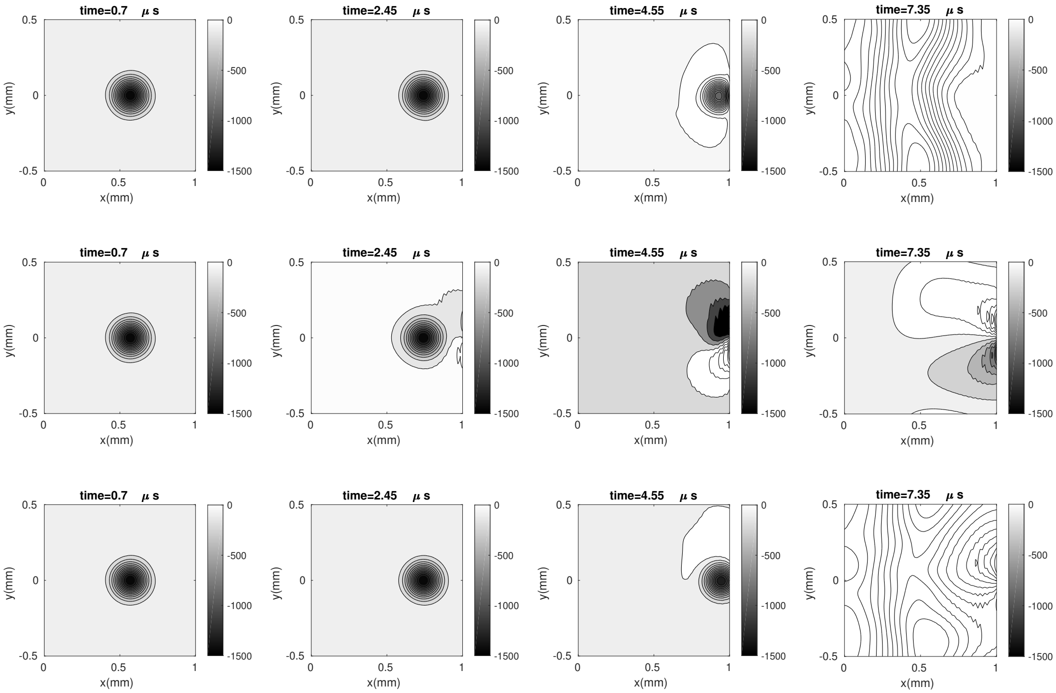
time=0.7 μ s

time=2.45 μ s

time=4.55 μ s

time=7.35 μ s

Figure 11. Pressure contours $P - P_0$ for outlet case, $M_\infty = 0.2924$. Rows from top to bottom: Weak static pressure outlet, Method 2 strong NSC inlet with $\sigma = 0.25$, Method 1 with $\sigma = 0.25$, σ is used in Eq. (18).

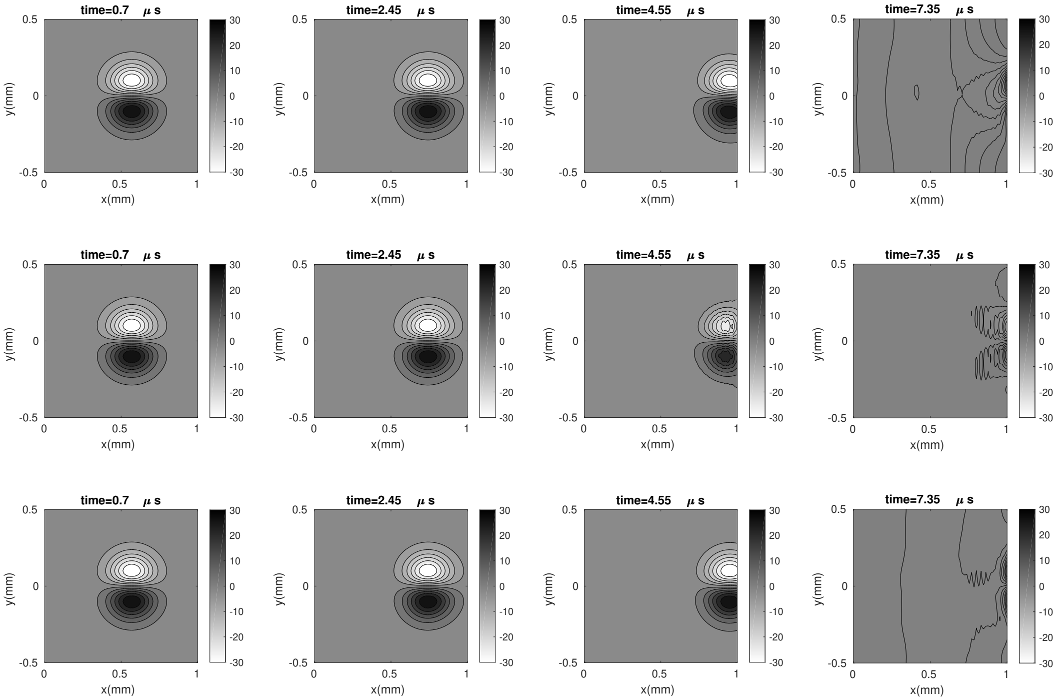

Figure 12. Streamwise velocity contours $u_1 - u_\infty$ for outlet case, $M_\infty = 0.2924$. Weak static pressure outlet, Method 2 strong NSC inlet with $\sigma = 0.25$, Method 1 with $\sigma = 0.25$, σ is used in Eq. (18).

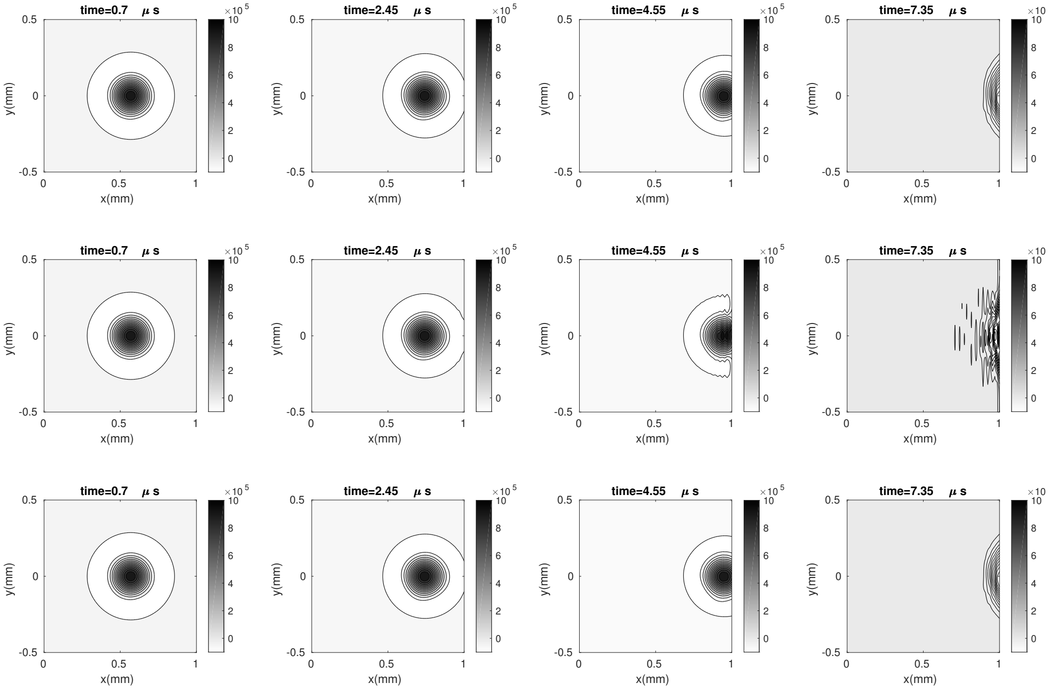

Figure 13. Vorticity contours ω for inlet case, $M_\infty = 0.2924$. Rows from top to bottom: Weak static pressure outlet, Method 2 strong NSC inlet with $\sigma = 0.25$, Method 1 with $\sigma = 0.25$, σ is used in Eq. (18).

5 Conclusions

The Navier-Stokes characteristic boundary conditions (NSCBC) has been tested in a node-centered edge-based compressible flow solver. Three different implementations have been evaluated, the first method imposes the characteristic boundary condition through a source term that is added to the residual, the convective contribution in the numerical scheme has thus been canceled at the boundary nodes. The second method sets the value of the primitive parameters at the boundary nodes. The strong implementation sets the value hard at each iteration, the weak implementation imposes the boundary value through a flux. The NSCBC has been compared to conventional BCs.

A subsonic inlet has been tested to evaluate the boundary conditions in their capability to inject an analytical isentropic vortex. The boundary conditions are verified in examining how well the analytical solution is preserved. A Dirichlet boundary condition is capable of injecting the vortex with minimal distortion and give accurate results. The strong implementation of setting the primitive variables at the boundary is capable of injecting the vortex, although significant checkerboard pattern is observed in the pressure. The source term implementation fails to inject the vortex in a reasonable form unless a high value of a penalty parameter σ is chosen. The value has to be chosen much larger than the recommended value (50 vs. 0.25), although a zero value of this parameter has been reported in the literature to give satisfactory results.

A subsonic outlet has been evaluated to assess the boundary conditions of their capability of transporting out an analytical vortex through the exit boundary. No reflections and minimal distortion of the vortex condition is expected. The NSCBC are compared to a conventional outlet condition with a static pressure specified. The static pressure outlet condition is reflective, and reflection in the pressure field is observed. The source term implementation of the NSCBC gives the best result with minimal reflections observed. The strong implementation of setting the primitive variables manages to transport out the vortex with checkerboard pattern observed.

The implementation of weak boundary conditions both inlet and outlet needs to be further explored in the next step work. Verification with more test cases will be carried out.

Acknowledgement

This work has been funded by the Swedish Governmental Agency for Innovation Systems (VINNOVA), the Swedish Defence Materiel Administration (FMV) and the Swedish Armed Forces within the National Aviation Research Programme (NFFP, Contract No. 2017–04887) and Saab Aeronautics. The simulations were performed on resources provided by the Swedish National Infrastructure for Computing (SNIC) at the National Supercomputer Centre (NSC).

References

[1] G.W Hedstrom. Nonreflecting boundary conditions for nonlinear hyperbolic systems. *Journal of Computational Physics*, 30(2):222–237, 1979.

[2] K. W. Thompson. Time dependent boundary conditions for hyperbolic systems. *Journal of Computational Physics*, 68(1):1–24, 1987.

[3] T. J. Poinsot and S. K. Lele. Boundary conditions for direct simulations of compressible viscous flows. *Journal of Computational Physics*, 101(1):104–129, 1992.

[4] C. S. Yoo, Y. Wang, A. Trouvé, and H. G. Im. Characteristic boundary conditions for direct simulations of turbulent counterflow flames. *Combustion Theory and Modelling*, 9(4):617–646, 2005.

[5] G. Lodato, P. Domingo, and L. Vervisch. Three-dimensional boundary conditions for direct and large-eddy simulation of compressible viscous flows. *J. Comput. Phys.*, 227(10):5105–5143, May 2008.

[6] N. Guezennec and T. Poinsot. Acoustically nonreflecting and reflecting boundary conditions for vortcity injection in compressible solvers. *AIAA Journal*, 47(7):1709–1722, 2009.

[7] R. Prosser. Improved boundary conditions for the direct numerical simulation of turbulent subsonic flows. i. inviscid flows. *Journal of Computational Physics*, 207(2):736–768, 2005.

[8] J. C. Sutherland and C. A. Kennedy. Improved boundary conditions for viscous, reacting, compressible flows. *Journal of Computational Physics*, 191(2):502–524, 2003.

[9] D. H. Rudy and J. C. Strikwerda. Boundary conditions for subsonic compressible navier-stokes calculations. *Computers & Fluids*, 9(3):327–338, 1981.

[10] G. Daviller, G. Oztarlik, and T. Poinsot. A generalized non-reflecting inlet boundary condition for steady and forced compressible flows with injection of vortical and acoustic waves. *Computers Fluids*, 190:503–513, 2019.

[11] P. Eliasson. Edge, a navier–stokes solver for unstructured grids. In *Finite Volumes for Complex Applications*, volume III of *CP849*, pages 527–534, 2002.

[12] P. Eliasson and P. Weinerfelt. Recent applications of the flow solver edge. In *7th Asian CFD Conference*, CP849, 2007.

[13] A. Jameson. Time-dependent calculations using multigrid with applications to unsteady flows past airfoils and wings. *AIAA Paper*, (91-1596), 1991.

[14] P. Eliasson, S. Eriksson, and J. Nordström. The influence of weak and strong solid wall boundary conditions on the convergence to steady-state of the navier-stokes equations. *AIAA Paper*, (2009-3551), 2009.

[15] J. Löwe, A. Probst, T. Knopp, and R. Kessler. Low-dissipation low-dispersion second-order scheme for unstructured finite-volume flow solvers. *AIAA Journal*, 54, 2016.

[16] A. Widenhorn, B. Noll, and M. Aigner. Accurate boundary conditions for the numerical simulation of thermoacoustic phenomena in gas-turbine combustion chambers. In *ASME Turbo Expo 2006: Power for Land, Sea, and Air*, pages 347–356. American Society of Mechanical Engineers Digital Collection, 2006.

[17] V. Granet, O. Vermorel, T. Léonard, L. Gicquel, and T. Poinsot. Comparison of nonreflecting outlet boundary conditions for compressible solvers on unstructured grids. *AIAA Journal*, 48(10):2348–2364, 2010.

Other Publications

Paper F

Effect of LES Length Scale and Numerical Scheme in Hybrid RANS-LES of Free Shear Layer Flows